Development of ^{89}Zirconium-PET Tracers for Immune Cell Imaging

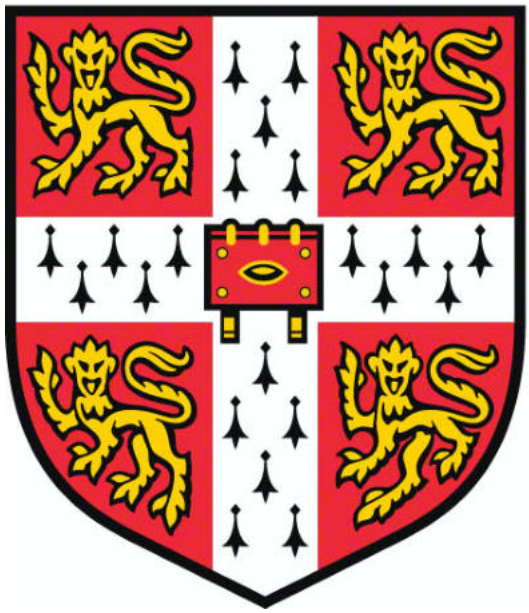

Laura Melanie Tessa Lechermann

This dissertation is submitted for the degree of Doctor of Philosophy

University of Cambridge

Department of Radiology

Clare Hall College

June 2021

Declaration

This dissertation is the result of my own work and includes nothing which is the outcome of work done in collaboration except as declared in the preface of each chapter and specified in the text.

It is not substantially the same as any that I have submitted, or, is being concurrently submitted for a degree or diploma or other qualification at the University of Cambridge or any other University or similar institution except as declared in the Preface and specified in the text. I further state that no substantial part of my dissertation has already been submitted, or, is being concurrently submitted for any such degree, diploma or other qualification at the University of Cambridge or any other University or similar institution except as declared in the Preface and specified in the text. It does not exceed the prescribed word limit of 60 000 words for the relevant Degree Committee.

Cambridge, June 2021
Laura Melanie Tessa Lechermann

Abstract

Development of ^{89}Zirconium-PET Tracers for Immune Cell Imaging

Laura Melanie Tessa Lechermann

The use of cell-based therapies as a living drug have gained considerable attention for the treatment of a range of conditions such as genetic diseases, autoimmune disorders and cancer. The emergence of genetically engineered T cells expressing chimeric antigen receptors (CAR T-cells), together with modulations of immune checkpoints have brought the rapidly advancing field of immunotherapy into a new, revolutionary spotlight with a renewed interest in cell-based therapies.

In vivo imaging and tracking of cells can be used to non-invasively improve the accuracy, efficacy and safety of novel immune-modulatory treatments and cell therapies. Positron Emission Tomography (PET) is a powerful non-invasive imaging technique that can be utilised for spatial and longitudinal tracking of different cell types. The long half-life PET isotope zirconium-89 ($t_{1/2}$ = 78.4 h) has become increasingly available and [^{89}Zr]Zr-Oxine has recently emerged as a promising candidate for direct cell labelling and longitudinal cell tracking. However, the water insolubility and synthesis method of [^{89}Zr]Zr-Oxine may limit its implementation as a routine clinical imaging tool and little work has been performed looking at alternatives to this compound.

The aim of this thesis was to investigate alternative approaches and methods for the direct labelling of cells using zirconium-89. This work also describes the first use of zirconium-89 in Cambridge and the set-up of the infrastructure and methods. First, the sensitivity of detecting ^{89}Zr-labelled cells on clinical PET systems was investigated that can inform on the minimal cellular radioactivity needed for detection in prospective clinical studies. Secondly, a peptide-based approach was developed whereby cell penetrating peptides were tested for ^{89}Zr-labelling, purification, quality control and their *in vitro* properties. ^{89}Zr-labelled peptides were subsequently employed for direct cell labelling in comparison to [^{89}Zr]Zr-Oxine in preparation for preclinical studies.

Dedication

To my beloved mother Ina for nursing me with affection, love, support, and all the lessons for the success in my life while becoming a better person every day.

Acknowledgments

When I applied for this PhD, I started my motivation letter with a statement from Frederick Sanger (1918 - 2013) from his Nobel banquet speech in 1980 when he said: '*Scientific research is one of the most exciting and rewarding of occupations. It is like a voyage of discovery into unknown lands, seeking not for new territory but for new knowledge. It should appeal to those with a good sense of adventure*'. Four and a half years later I can say that the PhD voyage has been a tremendously exciting adventure that I will miss dearly but that I will always remember fondly. Cambridge for me has been a great place for personal and professional growth and learning. It may have been a journey with strong side- and headwinds at times with Brexit and a pandemic sweeping in as well but the voyage always continued under full canvas which has certainly laid the foundation for many more adventures to come. I am beyond grateful that I was able to continue and finish a PhD during a pandemic that entailed many losses.

This scientific but also personal journey wouldn't have been possible without so many people that built the basis of the project but also contributed significantly to the progress of this work and to where I stand today:

To my supervisor Prof Ferdia Gallagher: there are no words to express my wholehearted gratitude for providing me with this unique opportunity in Cambridge and becoming my PhD supervisor, mentor and teacher. You are like a father to all of us at work. I am indebted to you for this chance, your support and continuous care often going beyond work. Your trust and confidence in all my scientific creativity and ideas has made me become a better scientist and leader. Thank you for being able to have sarcastic, funny, scientific and serious conversations all during one single meeting and in general throughout the years. I am the first chemist and one of the few students that you supervised who experienced two of your promotions while I was pursing my PhD. I am glad that we could share a considerable part of our voyage together.

To the Cambridge-GlaxoSmithKline (GSK) project team: Prof Ferdia Gallagher, Dr Bristi Basu, Dr Luigi Aloij, Dr Dmitri Soloviev, Prof Franklin Aigbirhio (Cambridge); Dr Matthew Cleveland, Dr Neel Patel (GSK) – I had a fantastic time with all of you on board of this project while working in such a multidisciplinary team over nearly 5 years. It am deeply grateful for this truly rewarding experience and also the fun times we shared together. Without the generous support from CRUK (C19212/A16628, C19212/A911376) and the GSK project grant this work and my funding extension during a pandemic and beyond the PhD would not

have been possible. Matt and Neel – thank you for such an active involvement in the project and for the warm welcome in Stevenage. Franklin – thank you for hosting me in your chemistry labs. Bristi – thank you for your care and all the casual (coffee) meetings where we spoke about other things apart from work.

To Prof Guus van Dongen and Dr Danielle Vugts at the UMC Amsterdam: thank you for being so welcoming, kind and generous during my ^{89}Zr-training in Amsterdam and beyond.

To colleagues and collaborators in the Clifford Albutt Building: Dr Dan Hodson – thanks to your cooperation and support I was able to set up the hot cell for the ^{89}Zr-work for this PhD. Dr Joanne Jo's research group, in particular Dr Lorna Jarvis, Dr Sarah Howlett, Lou Ellis, Dr Zoya Georgieva, Dr Hani Mousa and Dr Valeria Radjabova – you have all been incredibly accommodating and taught me many things during your own precious working hours. Without all of you, a big part of the work here would not have been possible. Dr Jonathan Clarke – thank you for all your work, support and guidance as an RPS for my project especially with the necessary radiation safety paper work.

To my PET colleagues Dr Roie Manavaki and Dr Tim Fryer: thank you for all your support, time and dedication to the ^{89}Zr-phantom scans and my work. I am grateful that we could work together and for all the PET physics that I picked up while working with you. I will never forget the late night PET scanning session and Costa visit at 2 am in the morning during the experiment that later led to my first first-author publication. Roie – thank you so much for your continuous support and care with various things not only as a colleague, but also as a friend.

To Dr Nick Bird, and Dan Gillet from Nuclear Medicine and the whole team at PET/CT: thank you for all the support throughout the years and for being so accommodating with my work. A significant part of this project would not have been possible without you.

To Chandra Solanki, Fackson Mutambo and the team at Radiopharmacy: thank you for the interest in my research and providing me with support and the facility to undertake quality control of my tracers.

To the research team and support in both the NHS and University Departments of Radiology, in particular Catherine Munn, Sarah Perkins, Wendy Phillips, Gavin Mortimer, Ralph Ball, Candice Anderson, Sarah Hilborne and Jackie Mason: thank you for your continual and essential support with various aspects of our work. Special thanks to Carlos Coutinho for all zirconium-89 and lab purchases especially during the last months of my PhD that helped me significantly in not experiencing any delays.

To Libby Yates and Dr Simon Hoer from the safety office: thank you for your trust and cooperation with setting up the ^{89}Zr-project and making the first use of zirconium-89 in Cambridge possible.

To my friends and colleagues Bala, Doreen, Ines, Julia, Leonardo, Lorena, Maria and Vlad: you have all joined me at different time points throughout my PhD journey. Thank you for your kindness, care and encouragement especially towards the end of my PhD and during the last lockdown. I hope we share many more moments filled with laughter and joy. Julia – we started this PhD journey from our very first day onwards together. We may not have finished this journey together in the end but several moves to the same house in Cambridge, being part of each other's ups and downs during the PhD but also sharing parts of our private lives together have made this voyage memorable filled with learning.

To Rosana, the cleaner in our department: thank you for all the casual conversations we had and the time you took to stop by my office and see how I was doing especially when there was no one else on level 5 in the offices. I enjoyed listening to your family stories, everything you told me about Brazil and all your plans in life.

To my neighbours Rosie and Mike on Alpha Road: you have been like family to me in Cambridge ever since I moved to Alpha Road. Thank you for all the care, support and great conversations throughout the whole time and especially for our almost weekly dinners when this was possible. It was a pleasure spending Christmas with you especially when I couldn't go home for a long time and mostly lived on my own.

To mum: thank you for letting me build my own tiny chemistry 'lab' in my childhood bedroom, you have not only nurtured my sense for discovery but you also let me make mistakes and then we laughed about it afterwards. You let me go away for any wild and adventurous trip abroad and you came to visit me whenever it was possible (even when I moved to Australia). You are my best travel buddy and we had lovely and memorable trips during this PhD. Thanks for all the care packages and boxes you sent, even though we spent 3 lockdowns apart, it made me have a bit of home and yourself as well. You have taught me so many important life skills that really helped me get through the pandemic and several lockdowns by myself. I will be forever indebted to you for the great education you gave me for life, the confidence in all my decisions and the pursuit of my dreams that in the end became reality and that made me come to Cambridge for this PhD.

Nothing in life is to be feared,
it is only to be understood.
Now is the time to understand more,
so that we may fear less.
Marie Curie (1867 – 1934)

Conference presentations arising from this thesis

Oral

BEN GSK Symposium, Stevenage, UK (21st – 22nd of May 2019):
"T cell imaging with Zirconium-89"

DMDG conference, Cambridge (Robinson college, 18th – 20th September 2019):
"*In vitro* detection limit of 89Zr-labelled cells using a human PET system"

GSK-Cambridge Oncology Imaging Meeting (virtual, 22nd June 2020):
Talk and overview about the cell labelling and imaging collaboration project

Poster

Summer School on Translational Medicine, Albufeira, Portugal (7th – 12th of October 2018):
"Zirconium-89 Immuno-PET: Exploring new methods for cellular labelling and imaging" (Poster)

European Molecular Imaging Meeting (EMIM), Glasgow, UK (19th – 22nd of March 2019):
"Detection limit and quantification of ^{89}Zr-labelled cells for cellular tracking: An *in vitro* approach using a human PET system" (Poster with preliminary data)

World Molecular Imaging Congress (WMIC), virtual meeting, 7th – 9th of October 2020):
"Detection limit and quantification of ^{89}Zr-labelled cells for cellular tracking: An *in vitro* approach using a human PET system" (Poster talk with finalised data)

Research visits during the time of this project

VUMC Amsterdam (Radionuclide Centre): 5th – 10th of March 2017 and 21st/22nd of August 2017

Memorial Sloan Kettering Cancer Center New York: 16th – 18th of September 2018

Publications arising from this project

Lechermann LM, Lau D, Attili B, Aloj L, Basu B, Gallagher FA. *In Vivo* Cell Tracking in Oncology using PET: Opportunities and Challenges for Clinical Translation. Cancers 2021 Aug 11, 13(16):4042. doi: 10.3390/cancers13164042

Lau D, **Lechermann LM**, Gallagher FA. Clinical translation of neutrophil imaging and its role in cancer. Mol Imaging Biol. 2021 Oct 12; doi: 10.1007/s11307-021-01649-2

Lechermann LM, Manavaki R, Attili B, Lau D, Jarvis LB, Fryer TD, Bird N, Aloj L, Patel N, Basu B, Cleveland M, Aigbirhio FI, Jones JL, Gallagher FA. Detection limit of ^{89}Zr-labeled T cells for cellular tracking: an in vitro imaging approach using clinical PET/CT and PET/MRI. EJNMMI Res. 2020 Jul 14;10(1):82. doi: 10.1186/s13550-020-00667-5.

Publications arising from other projects

Aloj L, Attili B, Lau D, Caraco C, **Lechermann LM**, Mendichovszky IA, Harper I, Cheow H, Casey RT, Sala E, Gilbert FJ, Gallagher FA. The emerging role of cell surface receptor and protein binding radiopharmaceuticals in cancer diagnostics and therapy. Nucl Med Biol. 2020 Jun 12;S0969-8051(20)30149-9. doi: 10.1016/j.nucmedbio.2020.06.005

Lau D, Garçon F, Chandra A, **Lechermann LM**, Aloj L, Chilvers ER, Corrie PG, Okkenhaug K and Gallagher FA. Intravital Imaging of Adoptive T-Cell Morphology, Mobility and Trafficking Following Immune Checkpoint Inhibition in a Mouse Melanoma Model. Front. Immunol. 2020 Jul; 11:1514. doi: 10.3389/fimmu.2020.01514

Zaccagna F, Grist JT, Deen SS, Woitek R, **Lechermann LM**, McLean MA, Basu B, Gallagher FA. Hyperpolarized carbon-13 magnetic resonance spectroscopic imaging: a clinical tool for studying tumour metabolism. Br J Radiol. 2018 May; 91(1085): 20170688 doi: 10.1259/bjr.20170688

Outline of thesis chapters

Chapter 1 – An introduction to cellular immune therapy and up to date clinical developments in this area are presented together with an overview of cell labelling methods and cell imaging on different imaging modalities.

Chapter 2 – An overview and review of existing and new cell labelling approaches using PET imaging is presented together with a summary of all clinical modalities used for cell tracking. This chapter also presents the thesis objectives and aims in detail.

Chapter 3 – This chapter introduces zirconium-89 in more detail and focuses on the project set-up and preliminary work in preparation for the subsequent cell labelling work.

Chapter 4 – This chapter addresses the sensitivity issue for cell tracking of radiosensitive T-cells directly labelled with [^{89}Zr]Zr-Oxine. An *in vitro* approach was employed with cell viability assessed alongside detection on clinical PET/CT and PET/MRI systems as a function of cell number and radioactivity exposure per cell.

Chapter 5 – The focus of this chapter is put on radiochemistry and the synthesis of ^{89}Zr-labelled cell penetrating peptides including their quality control and properties *in vitro* in comparison to the state-of-the-art tracer [^{89}Zr]Zr-Oxine that was also synthesised throughout all experiments.

Chapter 6 – This chapter describes the investigation of ^{89}Zr-labelled cell penetrating peptides in comparison to [^{89}Zr]Zr-Oxine for direct labelling of cells. Different cell labelling conditions, the short- and long-term cellular retention of zirconium-89 and the subcellular localisation of zirconium-89 inside cells were explored.

Chapter 7 – This chapter is a reflection on the work presented in this dissertation and its contribution to the current knowledge in this field. In addition, some of the limitations during the project but most importantly potential research questions and future directions of this work are described.

Table of Contents

Commonly used abbreviations

ALL	Acute lymphoblastic leukaemia
BLI	Bioluminescence imaging
Bz	Benzyl
CAR	Chimeric antigen receptor
CAB	Clifford Albutt Building
CD3	Cluster of differentiation 3
CD4	Cluster of differentiation 8
CD8	Cluster of differentiation 8
CNR	Contrast-to-noise ratio
CPP	Cell penetrating peptide
CT	Computed tomography
CTLs	cytotoxic T lymphocyte cells
CTLA-4	anti-cytotoxic T-lymphocyte antigen-4
DC	Dendritic Cell
DFO	Desferrioxamine
DNA	Deoxyribonucleic acid
DOTA	1,4,7,10-tetraazacyclododecane-1,4,7,10-tetraacetic acid
DOTAM	1,4,7,10-tetrakis(carbamoylmethyl)-1,4,7,10 tetraazacyclododecane
DOTP	1,4,7,10-tetraazacyclododecane-1,4,7,10-tetra(methylene phosphonic- acid)
EDTA	Ethylenediaminetetraacentic acid
FDA	US Food and Drug Administration
FDG	Fluorodeoxyglucose
GFP	Green fluorescent protein
GMP	Good manufacturing practise
HMPAO	Hexamethylpropyleneamine oxime
HPLC	High performance liquid chromatography
HSV-1	Herpex simplex virus-1
IL	Interleukin
ITLC	Instant thin layer chromatography
IVM	Intravital microscopy
kDa	Kilo Dalton

LLD	Lowest level of detection
mAb	Monoclonal antibody
MAK	Macrophage activation killer
MHC	Major histocompatibility complex
MRI	Magnetic resonance imaging
MPI	Magentic particle imaging
MSC	Mesenchymal stem cell
NCS	Isothiocyonate (chemical group)
NIS	Sodium iodide symporter
NK	Natural killer
NMR	Nuclear magnetic resonance
NSCs	Neural stem cells
NSG	NOD scid gamma mouse
PBS	Phosphate buffered saline
PET	Positron emission tomography
PD-1	Programmed death 1, also known as CD279
PD-L1	Programmed death ligand 1, also known as CD274
PFA	Paraformaldehyde
PSMA	Prostate specific membrane antigen
RNA	Ribonucleic acid
RPMI	Roswell Park Memorial Institute
SDS PAGE	sodium-dodecyl sulfate polyacrylamide gel electrophoresis
SPECT	Single photon emission computed tomography
SPIO	Superparamagnetic iron oxide
SSTR2	Somatostatin receptor 2
T	Tesla (unit for magnetic field strength)
TCR	T-cell receptor
TIL	Tumour infiltrating lymphocyte
TK	Thymidine kinase
TFP	Tetrafluorophenyl
Treg	Regulatory T-cell
US	Ultrasound
WBC	White blood cell

Chapter 1

A roadmap to cell-based immune therapies and cell imaging

1.1 The immunotherapy revolution and cell based therapies

The pharmaceutical industry has historically focused on developing small molecule drugs that heavily rely on the development of synthetic organic chemistry. The molecular biology revolution of monoclonal antibody technology and protein engineering gave a new impetus to the field and biological therapeutics were introduced as a 'second pillar of medicine' [1]. This transformation in drug development spanned many years and was accelerated with the discoveries in the field of cancer immunotherapy [2],[3]. Traditional cancer treatments such as chemotherapy act in a potent way on cancerous cells, whereas cancer immunotherapy utilises the immune system to kill cancer cells. Research on the potential of the immune system to specifically destroy tumours has evolved over more than 40 years of intensive research. Clinical onco-immunology trials have provided solid evidence that tumours are recognised by the immune system and their development can be stopped or controlled long term through a process known as immunosurveillance (**Fig. 1.1**) [4]. A series of stepwise events must be initiated and allowed to proceed in order for an anticancer immune response to lead to effective killing of cancer cells: (1) Release of cancer antigens from tumour cells. (2) Presentation of cancer antigens on the major histocompatibility complex class (MHC) by antigen-presenting cells. (3) Recognition of cancer antigens on the MHC by the T cell receptor, resulting in T-cell activation. (4) Trafficking of activated T-cells. (5) Infiltration into the tumour. (6) Recognition of cancer antigens on the MHC within the tumour. (7) Attack on tumour cells, resulting in tumour cell injury/death. Killing of the cancer cell releases additional tumour-associated antigens. The generation of immunity to cancer is a cyclic process that can be self-propagating leading to an accumulation of immune-stimulatory factors that in principle should amplify and broaden T-cell responses. However the Cancer-Immunity Cycle does not perform optimally in cancer patients which is where cancer immune therapies can step in.

With the success of immune checkpoint inhibitors, i.e. antibodies that can remove the "brake" on the immune system and regulate the ability of T-cells to attack tumours, the field of cancer immunotherapy experienced a renaissance and cancer immunotherapy has gained its place as a 'fourth pillar of cancer treatment', next to surgery, radiotherapy and chemotherapy [2].

The use of immunotherapy can be traced back to the 1890's, when William Coley injected bacteria into patients suffering from a variety of sarcomas in an attempt to encourage a response by the immune system against the cancer where he achieved durable and complete remission in several types of malignancies [5]. In 1908 Paul Ehrlich confirmed Coley's observations reporting several tumours being spontaneously suppressed by the actions of the immune system, however human trials over the following years were unsuccessful and led to the dismissal of the entire idea of cancer immunotherapy for decades. It was not until the mid-twentieth century that the hypothesis of cancer immunosurveillance emerged and it took until almost the end of the twentieth century until it was demonstrated that T-cells were able to perform anti-tumour surveillance and promote anti-tumour immune responses. Further discoveries followed that included the mechanisms for immunoediting, evidence for cancer cell escape and the recognition that immunosuppressed patients have significantly higher risk of cancer development [6].

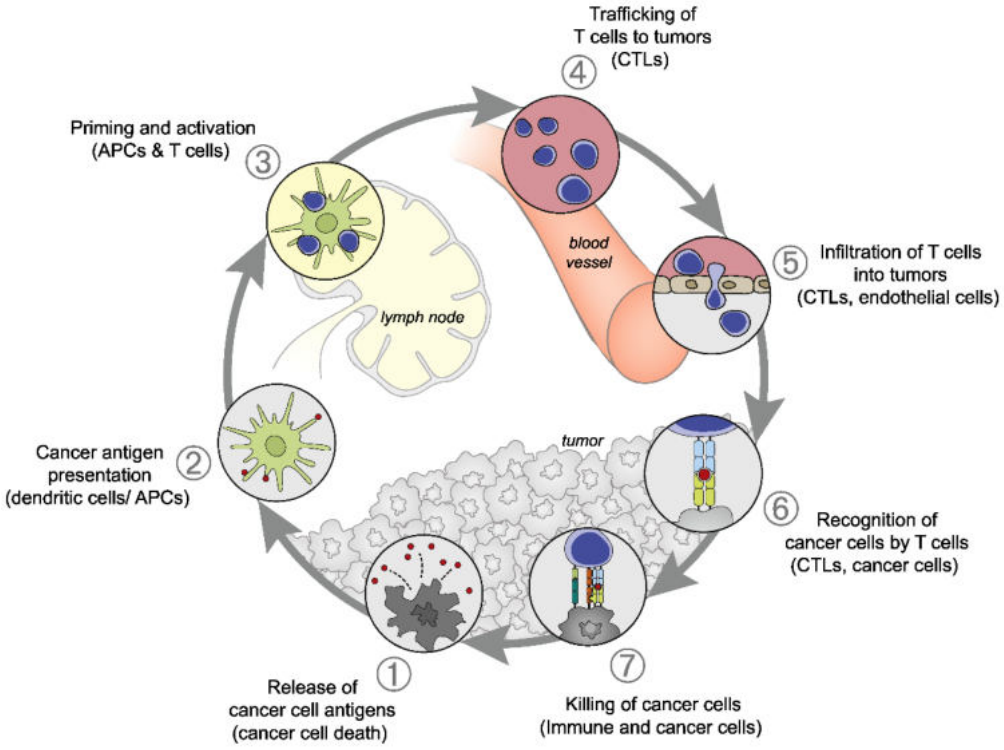

Figure 1.1 Cancer-immunity cycle. This figure was adopted from Chen et al. [4].

To date, several antibodies blocking the cytotoxic T lymphocyte-associated antigen 4 (CTLA-4) and programmed cell death protein 1 (PD-1) on T-cells or its ligand PD-L1 have been approved for clinical use and have demonstrated considerable clinical efficacy [7]. The impact of these achievements were recognised by the 2018 Nobel Prize in Physiology or Medicine awarded to James P Allison and Tasuku Honjo for the development of immune checkpoint blockage [8].

The current immunotherapy landscape is wide reaching and although immunotherapy is commonly associated with the treatment of cancer it has been under extensive and ongoing pre-clinical and clinical research not only for cancer but has also in a wide range of other diseases [9]. Currently, immunotherapy can be broadly divided into five classes: adoptive cell therapy (ACT), vaccines, immunomodulators (*e*.g. checkpoint inhibitors, cytokines, agonists, adjuvants), targeted antibodies (e.g. monoclonal antibodies, antibody-drug conjugates, bispecific antibodies) and oncolytic virus therapy.

The development of adoptive cell therapy has brought the area of immunotherapy to the cusp of using human cells as a 'living drug' for therapy. Cell therapies take advantage of the natural ability to eliminate infected, damaged, or cancerous cells, and can use either cells isolated from the same patient (autologous) or those from a healthy donor (allogeneic). The production process for both autologous and allogeneic cell therapies starts with the collection of peripheral blood mononuclear cells (PBMCs) via a process called leukapheresis, i.e. the removal of blood to collect specific blood cells whereby the remaining blood is returned to the body. Allogeneic cell therapies offer several advantages over autologous cells. Cells from healthy donors confer a more uniform starting material which allows for more predictable manufacturing and performance of generated cell product. Furthermore, allogeneic therapies have the potential to provide a ready to use 'off the shelf' immunotherapeutic product which allows to create an inventory or bank of manufactured immune cells from healthy donors and thereby decreases patient cost while increasing the access to the product. A single manufacturing run would allow dosing for several patients and/or multiple dosing for individual patients. On the other hand, allogeneic cells can have a high risk of causing a graft-versus-host (GvH) effect due to the immunologic mismatch between donor and recipient and the cell therapy may

be rejected in addition, limiting the therapeutic effect. On the opposite, autologous cell therapies are a very personalised, 'custom made' therapy which is labour intensive and time-consuming for each patient which increases cost and manufacturing times and thus lowers access to this form of treatment. Although a cell therapy product can be successfully generated, a proportion can have limited short- or long-term efficacy due to poor autologous immune cell fitness in cancer patients. In addition, there is a risk of contamination with malignant cells during the manufacturing. However, autologous cell transplants have a lower risk of life-threatening complications and there is no risk of GvH disease and there is no need for immunosuppressive therapy to prevent this.

One of the first successful approaches in this field was the use of tumour infiltrating lymphocytes (TILs), which involves the harvesting and selection of naturally occurring T-lymphocytes with anti-tumour activity from resected tumours. TILs are then expanded *ex vivo* in large numbers before being reinfused, often in combination with interleukin 2 (IL2). This approach, pioneered by Rosenberg et al. in the 1980s [10] is currently the most effective treatment for patients with metastatic melanoma [11],[12] and TILs have been successfully produced for other cancers [13]–[16].

However, not all patients have T-lymphocytes with anti-tumour activity, and these may not be capable of being activated and expanded to sufficient numbers to enable rejection of their tumours. Engineered T-cell receptor (TCR) therapy is another option is this case. Just like TILs, the TCR approach also involves taking T-cells from patients, but instead of just activating and expanding the available anti-tumour T-cells, peripheral blood T-cells for genetic modification obtained via leukapheresis are transduced by gamma-retroviral or lentiviral vectors that incorporate the TCR genes into the host genome (**Fig. 1.2**) resulting in high-level expression of the introduced TCR and enabling tumour antigen recognition. Gamma-retroviral vectors are derived from the Moloney Murine Leukemia Virus (MoMLV, MMLV, MuLV, or MLV) or Murine Stem Cell Virus (MSCV) genomes whereas lentiviral vectors are derived from the human immunodeficiency virus (HIV) genome [17].

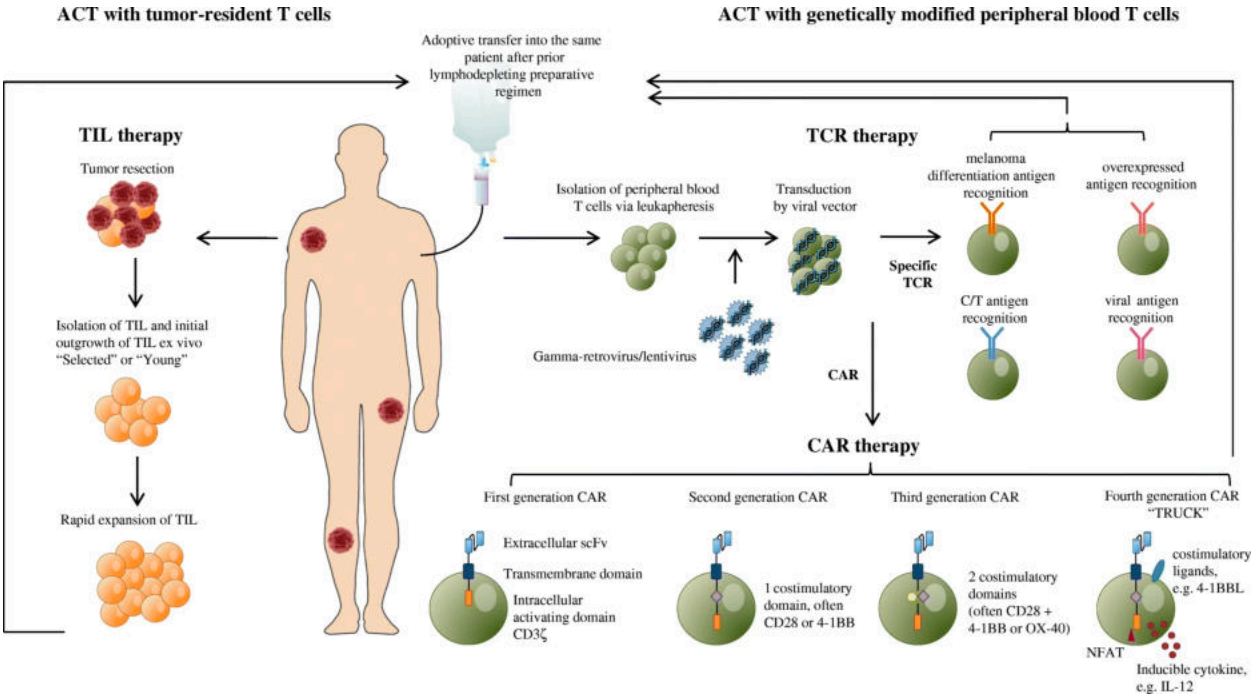

Figure 1.2 Schematic overview of the processes for ACT of tumour-infiltrating lymphocytes (TIL), ACT with T-cell receptor (TCR) gene therapy and ACT with chimeric antigen receptor (CAR)-modified T-cells. Figure adopted from [18].

Similar to TILs, TCR-modified T-cells can only target and eliminate cancer cells when the antigens are bound by the major histocompatibility complex (MHC) also known as MHC restriction. The limited tumour infiltration by adoptively transferred TCR T-cells has been described as a mechanism of malignant relapse [19], suggesting that T-cells lack specific homing and penetration capabilities to the tumour site. In addition, the antigens explored up until now are not solely expressed by the tumour, however the identification of antigens restricted to tumours is essential to further increase the efficacy and safety of TCR therapy. Tumours undergo genetic alterations, some of which can give rise to mutated and non-self peptides presented by human leukocyte antigen (HLA) molecules that elicit T-cell response. Retrospective studies have shown that patients that exhibited complete tumour regression following TIL therapy have a higher tumour mutation burden [20] and that TILs from responders frequently contain neoantigen-specific lymphocytes [21]. These immunogenic mutated peptides or so called neoantigens are foreign in nature and display exquisite tumour specificity giving them a major role in the effectiveness of

various cancer immunotherapies. However, the systematic identification of personalized neoantigens in cancer patients remains challenging and a much desired requisite for the success of targeted immune therapies. Two critical factors in the identification of immunogenic neoantigens are: (1) the identification of candidate neoantigens and (2) the evaluation of their immunogenicity. The process for discovering immunogenic neoantigens starts with the identification of all tumour somatic non-synonymous mutations (NSM) using next generation sequencing (NGS). For each patient, whole genome sequencing (WGS) or whole exome sequencing (WES) data from matched tumour and normal DNA is required. RNA sequencing can also be used in combination to WES to filter out neoantigen candidates before potential neoantigen candidates are then screened for their immunogenicity [22].

In addition, T-cells' homing capacity and tumour infiltration via genetic engineering has been investigated which resulted in the design of hybrid receptors, so called chimeric antigen receptors (CARs). T-cells can be engineered to express different generations of antigen-specific, transgenic receptors that have evolved over time which differ in terms of costimulatory domains, T-cell signalling domains, and the presence of additional cytokine transgenes (**Fig. 1.2**). CARs are entirely artificial constructs and can recognise any cell surface structure, independent of MHC presentation. This ability greatly broadens the array of antigens that a T-cell can recognise and engage with on the cell surface.

CAR T-cell immunotherapy was reported as the 2018 Advance of the Year by the American Society of Clinical Oncology (ASCO), one year after the two CAR T-cell therapies tisagenlecleucel (Kymriah™) and axicabtagene ciloleucel (Yeskarta™) received FDA approval for the treatment of acute lymphoblastic leukemia (ALL) and diffuse large B-cell lymphoma (DLBCL), respectively [23]. More recently, Tecartus™ (brexucabtagene autoleucel), the first and only CAR T-cell therapy for the treatment of adult patients with relapsed or refractory mantle cell lymphoma (MCL), was granted FDA approval. Cell therapies are emerging with great therapeutic potential and are becoming an integral and vital component of modern medicine. Recent advances have also led to the development of new cell-based therapies for cardiac [24]–[26], neural [27] and pancreatic tissue regeneration [28] amongst others and even COVID-19 [29]. Cell therapies account for

the largest number of agents that are being developed in the field of onco-immunology [30] and the vast majority of all oncological clinical cell therapy trials are focused on CD19 being the most dominant target for CARs [31].

ACT is a highly-personalised cell-based therapy and a ‘living treatment’ due to the proliferation of cells *in vivo* that maintain their anti-tumour behaviour [32]. Unlike small molecules, cells represent a dynamic form of treatment. They can migrate, proliferate, respond to their environment, and replace damaged, dying or diseased cells to a certain extent via cell division. In contrast, biologicals and small molecules undergo a metabolic pathway and are typically degraded shortly after administration and their half-lives can be tuned via chemical modifications. However, T-cell based drugs have been reported to persist for years [33],[34] and our current knowledge of their properties present substantial challenges in engineering such drugs with many unanswered questions that still need to be addressed. Compared to small molecules and biologics as tools in medicine, cells exhibit a much more multifaceted and complex field of action. Only cells can perform complex biological functions and naturally perform therapeutic tasks, e.g. recruit adaptive immune cells or take up important ions or sense molecules like glucose to maintain certain functions in the human body. Small molecules and biologics do not have on or off switches to exert their biological effect, and rely on a specific molecular recognition. In contrast, cells can sense their surroundings and respond in the presence of a specific impetus or signal.

The unique characteristics of cells and their use as therapeutic products in a clinical setting pose important questions to regulators, the medical community and industry alike: for example, are cell therapies considered drugs or not? For regulatory frameworks, this question is very important and also how cell therapies can be reliably and consistently produced. The automation of the manufacturing process is currently of significant interest and advances have been achieved in this area [35], yet there are remaining considerations that need to be taken into account. Compared to traditional biopharmaceutical production (e.g. of therapeutic antibodies) the process is based on using one well characterised strain and can be reproduced relatively well and consistently. However, the cell and gene therapy manufacturing processes require increasingly adaptive process strategies that take the inherent variability of the living

product into account. In addition, the manipulation of these cell products when adding contrast agents for imaging purposes may face different challenges compared to those encountered when labelling conventional small molecule drugs or antibodies with a radionuclide, where the toxicology and biodistribution of the unlabelled molecule can frequently be used to support the use of a labelled molecule. This may not be as straightforward and easy for cell therapy products where labelling can influence cell function and fate.

The next section will introduce an up-to-date overview of the clinical trial landscape and trends in the cancer cell therapy pipeline between 2019 and 2021. Following that, a brief overview of the challenges associated with cell therapies will be given leading to necessary tools that can help in the development of these therapies.

1.2 Clinical landscape of cell-based therapies and its challenges

The clinical cell therapy landscape has evolved tremendously over the past decade. A search on clinicaltrials.gov for 'cell therapies' (March 2021) yielded 10,995 currently active and recruiting studies of which 8,217 (75 %) fall within the field of oncology with the remaining 25 % covering all other areas, such as autoimmune diseases, neurological disorders, infections and inflammations but also COVID-19 amongst others. Another 3970 trials (March 2021) combine cell therapy with other forms of treatment for cancer and non-cancer diseases, which underline the present impetus to investigate combinatorial therapy approaches to optimise clinical utility over monotherapy, especially with immune checkpoint inhibitors. **Fig. 1.3** and **Fig. 1.4** give an overview of the cancer cell therapy trial pipeline covering 2019 to 2021.

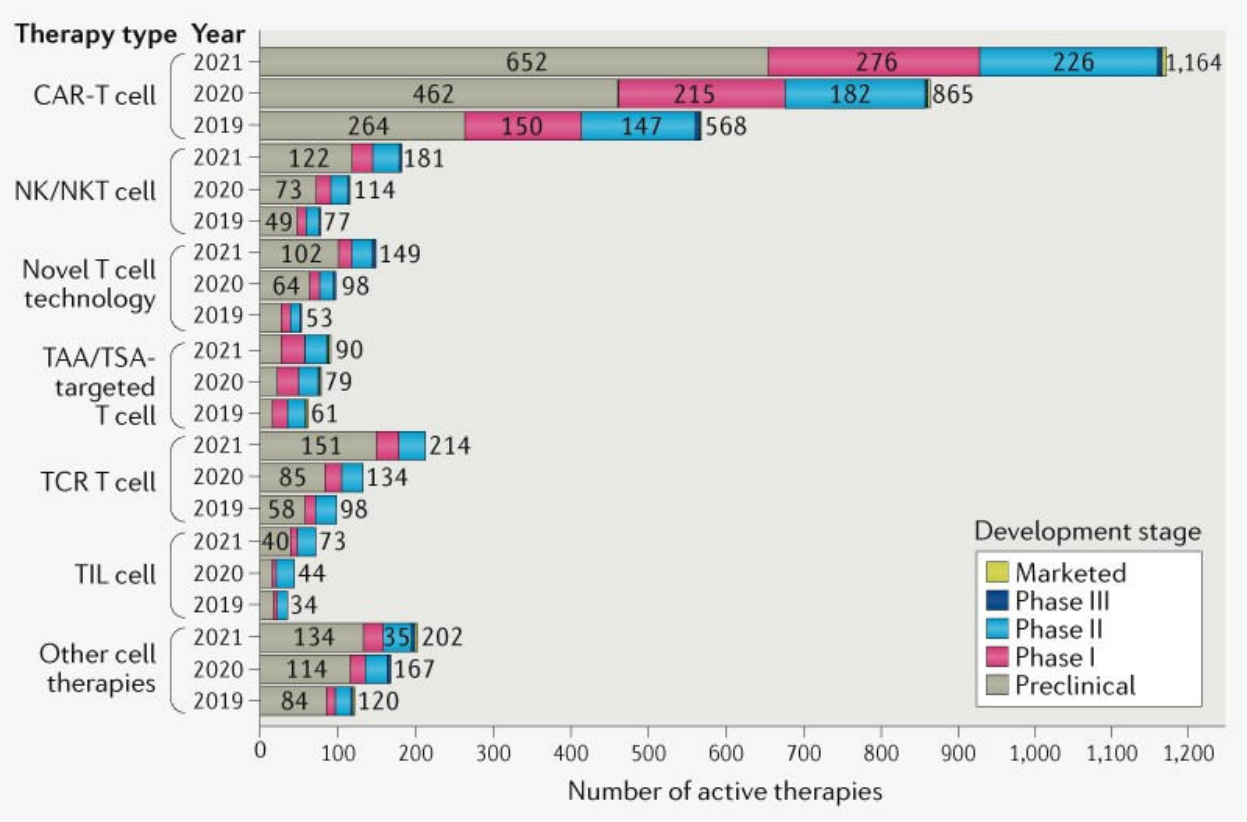

Figure 1.3 Trends in the cancer cell therapy pipeline. Comparison of the pipeline from in 2019 to 2021. TAA, tumour-associated antigen; TCR, T-cell receptor; TIL, tumour-infiltrating lymphocyte; TSA, tumour-specific antigen. Figure copyright [31].

The most promisingly results using CAR T-cells were obtained in B-cell lymphoma targeting CD19 [36],[37]. When infused into patients with acute lymphoblastic leukaemia (ALL), CD19 CAR T-cells were able to induce a remarkable 90% remission [38]. CD19 continues to be the top target for blood cancers (**Fig. 1.4 A**) and top solid tumour targets explored remain largely the same, with undisclosed tumour-associated antigen (TAA) being at the top (**Fig. 1.4 B**). TAAs are exclusively found on cancer cells and not on normal cells, making them attractive for targeted therapy.

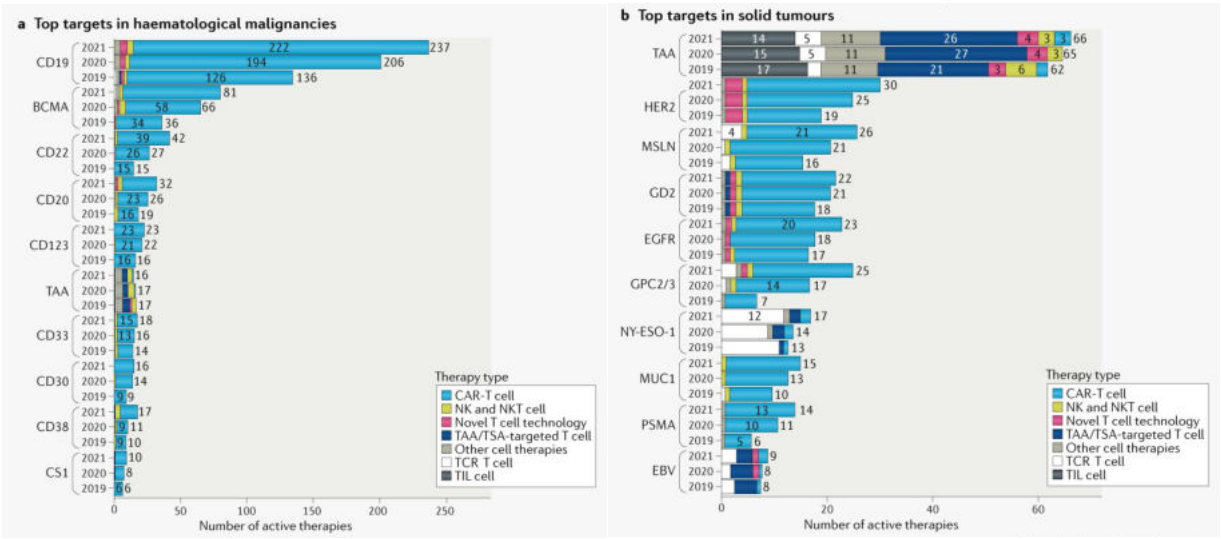

Figure 1.4 Top targets of cell therapies for **(A)** blood and **(B)** solid tumours. Figure copyright from [31].

The number of clinical trials and regulatory approvals for cell and gene therapies are expected to rise over the coming years with an anticipated approval of 10-20 cell and gene therapy products per year by 2025 [39]. Separate estimates suggest that by 2030 half a million patients in the US alone will have been treated with 40-60 approved gene or cell therapy products [40]. Nevertheless, past and predicted developments also pose a flip side of the coin and cell therapies similarly entail several challenges.

Many challenges of cell therapies originate from the manufacturing of the final product. These include a limited shelf-life (i.e. cell viability), limited availability of the starting material, product and test method development, small lot size, limited sample volumes for postprocess testing, patient variability and cell heterogeneity. As with any

pharmaceutical drugs, the safety profile is one major prerequisite that needs to be established during early development and all cell therapies require extensive characterisation to demonstrate safety and compatibility. Some clinical trials using CD19 targeted CAR T-cells have encountered significant setbacks. In some cases off-target activities have led to severe adverse events with fatalities such as neurotoxicity leading to death and other adverse effects such as cytokine release syndrome (CRS) and Immune effector cell-associated Neurotoxicities Syndrome (ICANS) [41]. CRS is a systemic inflammatory response characterized among others by fever, hypotension, hypoxia and potential multiple organ failure whereas ICANS is characterized by various neurologic symptoms ranging from confusion and tremor to aphasia, dysgraphia, seizures or coma. These generally occur in the first weeks after CAR T-cell infusion as a results of high levels of cytokines not only produced by CAR T-cells but also by their activation of myeloid cells [42]. Pyrexia, fatigue, cytopenias and infections are also frequent after CAR T-cell therapy. In addition, cell therapies can also cause an autoimmune reaction known as graft-vs.-host disease whereby transplanted immune cells attack the body's own tissue and cells [43].

Apart from CAR T-cells, already utilised and explored in the clinic, the genetic engineering of other cells such as stem cells have not yet been explored widely which can entail new and additional unknow safety risks which still need to be investigated.

Although treatment successes have been reported for CAR T-cell therapies, not all patients respond in this way, and some effects are only temporary [34],[44]. Additionally, CAR T-cell therapy has generally been disappointing in solid tumours. Nevertheless, a variety of concepts are being investigated to overcome certain barriers and current limitations of CAR T-cell therapy in solid tumours, such as inadequate penetration into the tumour due to the surrounding stroma and infiltrating pro-tumour immune cells as well as the heterogeneity of target antigens on solid tumours [45] which is not the case with blood malignancies and approved CAR T-cell therapies have shown promising results.

Once cells are administered to subjects the distribution, persistence and survival remain unknown. Given the tremendous costs involved with cell therapies, their efficacy and cost-efficiency play a major role in the decision-making progress and whether

patients may benefit from this treatment on an individual level. Currently, approved CAR T-cell therapies cost around $373,000 in the United States and nearly £300,000 in the United Kingdom, although Gilead and Novartis agreed to a discounted undisclosed price for use within the NHS from 2019. Therefore, health economic factors and cost-benefit, as well as the impact of budget is a major topic of interest whereby cost-effectiveness has already been analysed and modelled in one study [46].

Despite many clinical trials that evaluate and investigate the potential of these therapeutic approaches, the translation from benchtop science into the clinic will require several new considerations for cell therapies in the future. Consequently, broad investigations into some of the above factors affecting cell therapy development and clinical translation are needed. The next sub-chapter will focus on the labelling and imaging of cells and how this can help in the development and translation of cellular therapies.

1.3 Cellular labelling and imaging

1.3.1 General introduction

As described in the previous section, there have been significant advances in the development of immune therapies. Immune checkpoint inhibitors and cell-based therapies are rapidly evolving treatment modalities, however only a subgroup of patients respond, and many patients experience side effects associated with these new therapies. Current methods to monitor levels of circulating lymphocytes, cytokines, and immunoglobulins from whole blood samples or from biopsies within a heterogeneous tumour, spleen or lymph node are invasive and do not accurately reflect the dynamic and spatial changes in the immune responses to therapeutic interventions. In order to successfully implement and translate cell therapies into clinical practice, a better understanding of their biodistribution and persistence after administration is required and there is an unmet need for new tools to allow optimisation of cell therapies and the key parameters to tailor therapy for each patient as part of personalized medicine include: cell localisation, cell numbers at the target site, the dynamic distribution and viability of

cells, as well as the precise dosing, timing, and delivery of administered cells to the desired sites in the body.

The concept of labelling a drug, in particular antibodies, and evaluating its pharmacokinetics and pharmacodynamics through imaging is well established and can provide a powerful approach for an optimal stratification of patients at staging and during the evaluation of the response to therapy where traditional assessment criteria, i.e. response evaluation criteria in solid tumours (RECIST), are not reliable in evaluating early tumour response [47]. In this respect, a continuous adaptation of immune-related response criteria (irRC) is required to overcome the problem and the imaging of immune response has become an important tool to assist in this and to predict response to therapy. For instance, labelled antibodies and immune checkpoint inhibitors have shown great potential to reveal crucial *in vivo* information in regards to target expression and engagement at the site of action, disease stage, pharmacokinetic behaviour and tissue drug disposition which can be seen as 'whole body immunohistochemistry' [48].

Imaging has an important role in many different stages of early drug discovery, and also plays an important role during the development within the pharmaceutical industry where this concept increasingly leverages the drug development process itself [49]–[51]. Imaging a drug in a phase one proof-of-concept study could help to reduce late phase attrition and support futility decision making already early in the development stage, e.i. whether a drug shows promising results in terms of pharmacokinetics (PK) and pharmacodynamics (PD) to move into the next trial phase. The burgeoning field of anti-cancer immunotherapy has stimulated the need for imaging to address some of the challenges faced with cell therapies. Labelling and imaging of cells could provide valuable tools in the development of cellular therapies and has the potential to give crucial information for future developments in this field. *In vivo* imaging of labelled cells can provide much needed information on cell location and fate post-administration, cell functionality and viability, as well as providing useful information for improving accuracy and efficacy of cell therapies. In addition, imaging can have utility in the measurement and prediction of the extent of toxicities associated with cell therapies. This can include non-specific tracer for general inflammation such as [^{18}F]FDG [52] but also cell specific

lineage markers that may provide insight into toxicities involving specific organ systems [53].

The next section will focus on the different cell labelling methods and modalities used to image the trafficking of cells *in vivo*, with a special emphasis on different labelling agents used in various settings to date.

1.3.2 Cell labelling methods and requirements for cell tracking and imaging

Cells can be labelled directly or indirectly. In a direct labelling approach, a tracer is added directly to cells *in vitro* prior to them being reinfused into recipients. Labelling can be achieved through the uptake of nanoparticles, antibodies targeting certain antigens, lipophilic and cell permeable tracer (e.g. [^{111}In]In-Oxine, [^{89}Zr]Zr-Oxine, [^{99m}Tc]Tc-HMPAO) or receptor and transporter targeting small molecules (e.g. [^{18}F]FDG amongst others). In comparison, indirect (*in vivo*) labelling makes use of imaging reporter genes that are inserted into cells by transfecting them with a vector. The incorporated reporter gene will be expressed solely in viable cells and live cells can therefore be distinguished from dead cells. Genetically modified cells are administered to subjects prior to the injection of the respective imaging probe specific for the reporter gene. An analogous approach to indirect cell labelling with reporter genes can also be achieved with antibodies. A labelled antibody is injected into subjects that targets an endogenous antigen *in vivo* on the cells of interest that have been reinfused. On the other hand antibodies can also be used to directly label cells *in vitro* before being reinfused.

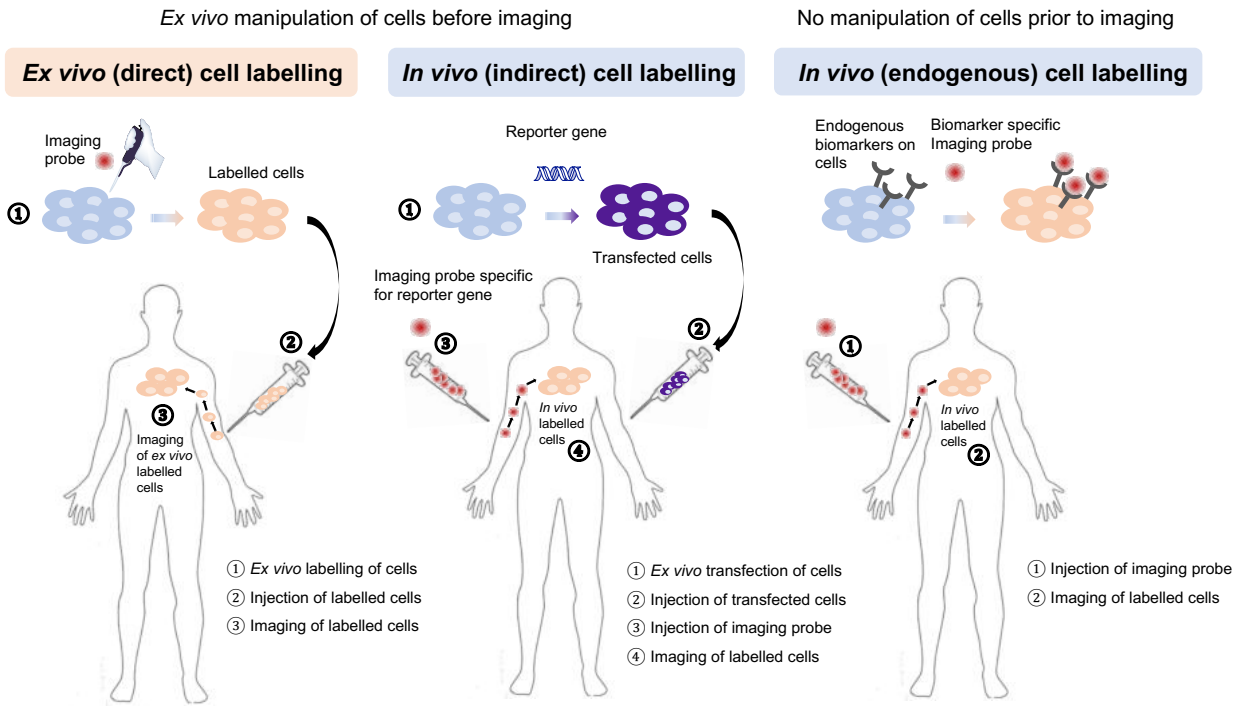

Figure 1.5 Overview of the different cell labelling strategies including their steps from labelling to *in vivo* imaging.

The different approaches to cell labelling provide complementary information: some approaches assess the resident tumour immune populations [54], while others report on the trafficking of cells in and out of the tumour. Although direct *ex vivo* cell labelling specifically shows the distribution of the injected labelled population and how it is taken up into the tumour or organ or interest [55], with little or no background signal to complicate the analysis, although some of the label could be released extracellularly to accumulate in adjacent cellular subpopulations. Antibody or antibody fragment labelling is also highly specific [56], although for a target rather than a cell population so may label more than one resident cell population and will demonstrate some non-specific background accumulation which may reduce the sensitivity for detection. Antibody labelling also has the benefit of providing functional information in addition to spatial localization and can inform on cellular activation status and cell-cell interactions [57].

Reporter genes are the most attractive approach given their potential for a very high level of cellular specificity and because the target is not diluted due to cellular proliferation and tumour metastasis [58]. The choice of reporter gene/target is based on multiple

factors: a) availability of specific tracers, and clinically approved; b) physiological expression in tumours or normal organs, ideally none or as low as possible; c) favourable dosimetry, to minimise concerns over radiation exposure and allow for measurement at multiple time points after administration of the tagged cells; d) limited or no biological effect deriving from expression of the transgene; e) alternatively, a transgene may be chosen due to its biological features and to serve as a therapeutic effector or target for its application. The potential for non-human reporter genes to be immunogenic must also be taken into consideration when addressing ideal system design, since this may affect functionality and survival of transduced cells once injected into humans. The introduction of a transgene into live cells for human administration can raise safety concerns and requires extensive regulatory scrutiny and validation before it can be considered for clinical use to ensure long term stability and safety. In addition, preparation of transduced cells for human injection is significantly more complicated and expensive than the requirements for direct cell labelling procedures. Although gene reporters pose significant challenges before being used routinely in a clinical setting, they present many benefits when this can be achieved.

To ensure the safe administration of *in vitro* labelled cells and to achieve successful *in vivo* imaging and labelling of cells through an indirect approach, certain prerequisites have to be met that can assure this. Various factors must be considered in the development, improvement and optimization of cellular imaging which are summarised in **Table 1.1**.

Table 1.1 Different factors and cell labelling requirements for optimal cellular imaging

Factor	Optimal cellular labelling conditions and requirements for cellular imaging
Cell behaviour post-labelling	• Maintenance of cell functionality (viability, cytotoxicity...) • No additional activation of cells *in vitro* and *in vivo* • Maintenance of cell surface receptor/antigen expression
Label prerequisites	• Efficient and stable uptake of the label • Retention of the label with no cellular efflux (*in vitro* approach) • Stable tracer for *in vivo* targeting and labelling (*in vivo* approach) • Non-toxic to cells • Reproducible tracer synthesis (GMP compliant) and applicability in humans
Physical properties	• Sensitive and quantitative detection (small numbers of cells) • Longitudinal tracking with sufficient signal over time and low background noise

A range of techniques and imaging modalities can be used to label and image cells which will be elaborated and discussed in detail in the following sections of this chapter.

1.3.3 Optical Imaging (OI)

Live-cell imaging has enabled breakthroughs in the characterization and quantification of biological processes at the cellular and subcellular level. The most important imaging modalities for live-cell imaging at single-cell resolution use light sources to excite fluorescent molecules (i.e. fluorophores) that are attached to the cells of interest within the tissue with subsequent detection of the emitted fluorescent light. These modalities include wide-field fluorescence microscopy, confocal fluorescence microscopy and multiphoton fluorescence microscopy. The necessary microscopes are comparatively easy to operate, inexpensive, and are therefore widely available.

Among optical imaging tools, bioluminescence imaging (BLI) is an indirect cell labelling technique that uses the expression of reporter genes, such as light-generating enzymes called luciferases. Bioluminescence imaging of small animals enables observation over long periods without the need for a light source to excite the fluorophores. Luciferases from different organisms are specific for distinct substrates (e.g. luciferin) and which, when oxidised, emit photons of different wavelengths that can be distinguished and therefore allow the simultaneous use of more than one marker [59]. Firefly luciferase (Fluc) is the best-characterised protein capable of generating bioluminescene which is widely used as a tool for reporting gene expression levels within living cells. Despite rather low turnover numbers of luciferase with quite poor thermal stability in solution, luciferase protein is quite stable when expressed in cells and can accumulate at high levels [60].

BLI has been a valuable tool for the longitudinal assessment of the fate of transplanted stem cells both *in vitro* and *in vivo* and several groups have investigated the biodistribution of these cells for the treatment of myocardial ischemia using BLI. It can provide a significant amount of data, such as the real-time and long-term visualization of transplanted stem cells where the *in vivo* dynamics, migration, proliferation, cell death, and even cell differentiation of stem cells can be monitored noninvasively [61]. BLI can also be used to track immune cells, e.g. migration to sites of inflammation and measure the life span of adoptively transferred T-cells for tumour immunotherapy [62]. More recently, Iwano et al. performed directed evolution on firefly luciferase using a red-shifted

and highly deliverable luciferin analogue to establish AkaBLI, an all-engineered bioluminescence *in vivo* imaging system that can produce emissions *in vivo* that are brighter by a factor of 100 to 1000 than conventional systems, allowing non-invasive visualization of single cells deep inside freely moving animals [63].

Alternatively, fluorescence imaging can be used for the long-term and whole-body cell tracking in animals. The instrumentation for this is equipped with a laser, fluorescence filter sets, and a sensitive camera detecting the blue to near-infrared (NIR) wavelength region which can be summarised as intravital microscopy (IVM). The laser can excite fluorescent dyes, nanoparticles, or transgenic-labelled fluorescence proteins in cells. Various fluorescent proteins, such as green fluorescent protein (GFP), enhanced green fluorescent protein (EGFP), mCherry, yellow fluorescent protein, red fluorescent protein and cyan fluorescent protein have been widely used to label cells to study various aspects of innate and adaptive immune responses to cancer, infection and inflammatory disorders [64],[65] but have also been applied for the imaging of resident T-cells on human *ex vivo* tumour slices [66]. The two most frequently used imaging approaches used with IVM are confocal fluorescence microscopy and two-photon fluorescence microscopy. Compared with BLI, fluorescence-based imaging has higher signal intensities, and the emission wavelength can reach the NIR, where deeper imaging depth can be achieved. BLI, however, is the most sensitive and specific imaging method to track cells *in vivo* and is also well suited to study tumour growth, anti-tumour treatments and metastasis spread. At the same time, BLI affords a high signal-to-noise ratio and therefore low background signal.

Additionally, dual modality cell imaging approaches have been employed to build on the strengths of different imaging modalities in combination with microscopy which allow cross-correlation studies and can allow to overcome sensitivity issues encountered with one imaging modality. Most commonly used examples include the combination of BLI with MRI [67]. Another example is radioluminescence microscopy (RLM), an imaging technique that allows quantitative analysis of clinical radiolabelled drugs and probes in single cells. In RLM, a scintillator crystal is placed directly under or above the radiolabelled cells to observe optical flashes resulting from the decay of single radioactive molecules. By capturing a series of image frames and individually counting the scintillation flashes

within each frame, RLM can quantify how many radioactive molecules are present within individual cell with high sensitivity, i.e. down to fewer than 1,000 molecules per cell, and has the potential to measure and show heterogenous radiotracer uptake in cells [68]–[70] (e.g. **Fig 1.6**).

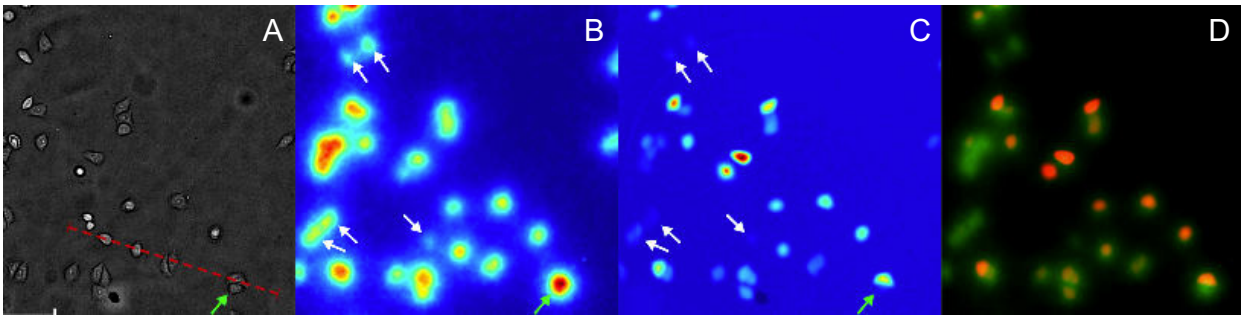

Figure 1.6 HeLa cells transfected with a fusion PET/fluorescence reporter gene and incubated with [^{18}F]FHBG: (**A**) Brightfield (scale bar, 50 μm), (**B**) radioluminescence ([^{18}F]FHBG), (**C**) fluorescence (RFP), (**D**) overlay of radioluminescence and fluorescence. The green arrow points to a cell with no RFP expression but ambiguous radioluminescence intensity. Figure reproduced from [70].

The clinical translation of bioluminescence imaging and fluorescent-based cell tracking into humans is significantly restricted owning to the physical constraints of light scatter and poor tissue penetration. However, similar to fluorescence-guided surgery (FGS), these studies can provide high throughput screening on a microscopic and preclinical level of potential cell types that are most beneficial or elucidate certain mechanisms and therefore can help in guiding drug discovery [71]–[73]. Cerenkov luminescence imaging (CLI), the use of inherent light emission of radionuclides for optical *in vivo* imaging is a newly emerging imaging tool [74]. Cerenkov light is generated when a charged β particle (β^+ or β^-) exceeds the speed of light in a dielectric medium [75]. The emitted short wavelength light is easily scattered and absorbed by a few millimeters of overlying tissue and therefore the detected CLI signal originates predominately from the surface of the tissue. This provides higher spatial resolution, at the expense of poor depth penetration, thus making it suited to detection in the surgical environment [76]. CLI was

first demonstrated in humans for thyroid imaging using iodine-131 [77] and later also for the detection and imaging of [18F]FDG [78].

1.3.4 Single-Photon Emission Computed Tomography (SPECT)

Single-photon emission computed tomography (SPECT) was first introduced in the 1960s [79] and has become a clinical routine tool in most nuclear medicine departments. The principles of SPECT are very similar to the ones applied for planar scintigraphy which include the detection of gamma rays emitted by radiotracer that can be detected using a gamma camera. Unlike scintigraphy, SPECT imaging is performed by rotating the gamma camera around the patient acquiring multiple 2D images (projections) from multiple angles and a computer is used to apply a tomographic reconstruction algorithm to the multiple projections, thus yielding a 3D data set. Therefore, the nature of the SPECT image differs from planar imaging with significant improvement of image contrast [80]. Narrow collimators are used to determine the origin of the emitted photons (**Fig. 1.7**) which on one side allows high spatial resolution SPECT imaging but on the other side compromises sensitivity since the process of collimation excludes a significant amount of diagonally incident photons. The balance between collimator aperture and associated spatial resolution often determines the needed amount of radioactivity and required scanning time for different SPECT imaging applications.

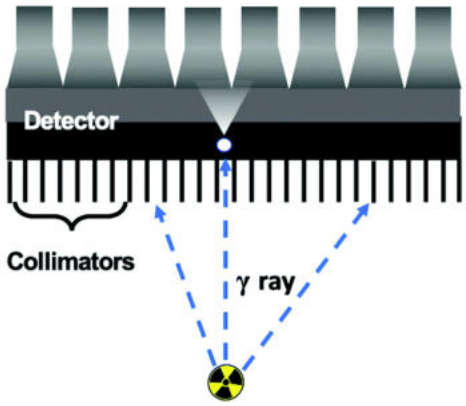

Figure 1.7 Schematic representation of SPECT and the principles of detection via collimators. Figure reproduced from [81].

SPECT has found extensive application in- and outside of the field of oncology [82] and is widely used for cell labelling and imaging. The two SPECT tracers [^{111}In]In-Oxine ($t_{1/2}$ = 67.2 h) and [^{99m}Tc]Tc-Hexamethylpropyleneamine oxime ([^{99m}Tc]Tc-HMPAO, $t_{1/2}$ = 6.06 h) were the first agents that were used to label leukocytes in the 1980s and 1990s, respectively, to image sites of infection or inflammation [83],[84] (**Fig. 1.8**). Together with [^{111}In]In-Tropolone, they are the only cell labelling agents that have been applied in clinical routine for cellular imaging.

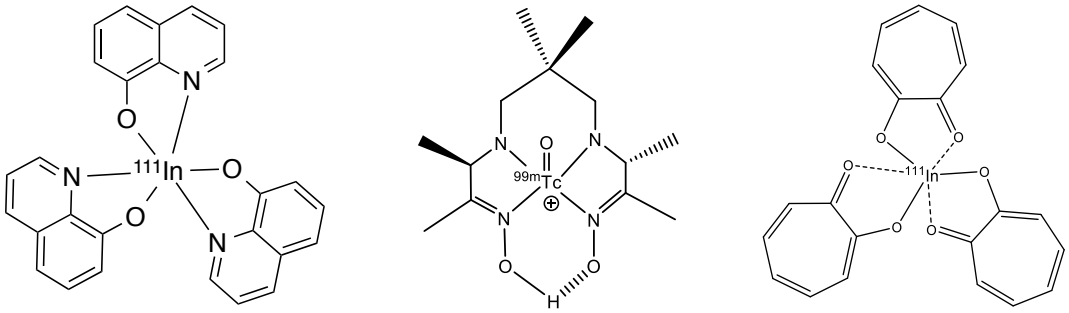

Figure 1.8 Chemical structure of [^{111}In]In-Oxine, [^{99m}Tc]Tc-HMPAO and [^{111}In]In-Tropolone

Leukocytes are harvested from patient blood, radiolabelled, and then reinjected intravenously. In the early 1990s, lymphokine-activated killer cells were activated *in vitro,* labelled with ^{111}In-Oxine and subsequently reinfused into patients with malignant melanoma for diagnostic imaging [85]. Guidelines for the use of [^{111}In]In-Oxine and [^{99m}Tc]Tc-HMPAO) for cell labelling have been published [86],[87] and accepted protocols for diagnostic imaging have been established. In comparison, no standard clinically approved imaging technique or protocol exists for the longitudinal imaging of transferred therapeutic cells, either for *in vivo* or *ex vivo* cell labelling approaches (see schematic depiction in **Fig. 1.9**).

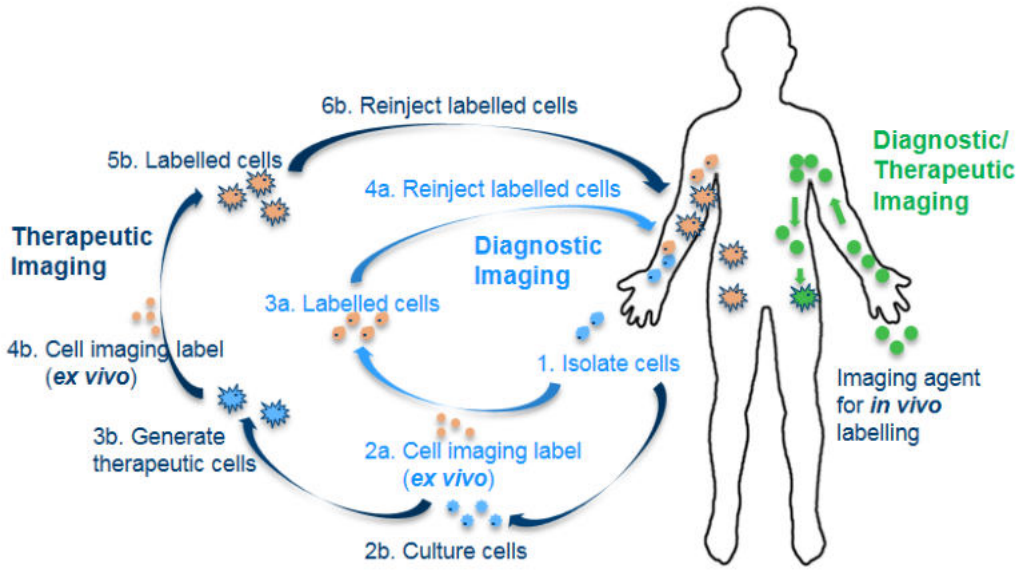

Figure 1.9 Schematic overview of the different cell imaging approaches. Generation of therapeutic cells can include expansion and transfection. Figure modified from Srinivas et al. [88].

[^{111}In]In-(oxinate)$_3$, known as '[^{111}In]In-Oxine', was withdrawn from the EU market a few years ago [89] due to economic reasons. More recently, [^{111}In]In-Oxine has regained attention to label and image a variety of immune cells in patients. [^{111}In]In-Oxine-labelled DCs as an anticancer vaccine were used in trials to track the migration of cells in breast, lung and colon cancer in humans [90],[91]. Patients with metastatic melanoma were injected with [^{111}In]In-Oxine-labelled TILs to evaluate the efficiency of adoptively transferred cells [92],[93]. In addition, [^{111}In]In-Oxine was also used to label HER2/neu-specific T-cells in a breast cancer patient [94] which demonstrated evidence of T-cell homing to all disease sites and together with concurrent [^{18}F]FDG PET/CT a tumour metabolism flare response could be observed. In another human study, CAR T-cells targeting tumour-associated glycoprotein 72 (TAG-72) were labelled with [^{111}In]In-Oxine to monitor the trafficking to sites of disease in patients with metastatic colorectal cancer [95] and acute myeloid leukaemia [96] .

Given its well established clinical application, it does not come as a surprise that direct cell labelling and imaging with ^{111}In-SPECT is rather dominated by clinical studies and preclinical work is relatively scarce [97]–[99]. However, indirect cell labelling and imaging via reporter genes using SPECT has only found application in pre-clinical settings rather

recently. Instead of indium-111, technetium-99m in the form of pertechnetate ([^{99m}Tc]TcO^{4-}) can be taken up by cells receptor-mediated via the Sodium Iodide Symporter (NIS). NIS is the thyroidal sodium iodide symporter, which can take up radioiodine and related radioactive anions of the same ionic radius (e.g. [^{99m}Tc]TcO^{4-}, [^{18}F]BF$_4^-$) into NIS-expressing cells [100]. In one study [^{99m}Tc]TcO^{4-} was added directly to regulatory T-cells (Tregs) transduced with the human NIS as well as with the fluorescent protein mCherry and incubated *in vitro* to label cells to be imaged in healthy mice at 24 hours post-injection in conjunction with organ biodistribution and flow cytometry analysis [101]. [^{99m}Tc]TcO^{4-} was also used to study and image the trafficking behaviour of Tregs in mice with human skin transplants for up to 40 days [102]. In the same study the detection sensitivity of [^{99m}Tc]TcO^{4-}-labelled NIS-positive Tregs in a cell pellet of 10^6 untransduced Tregs was found to be 10,000 cells. Concurrent [^{99m}Tc]TcO^{4-}-SPECT and PET was used in another study to track CAR T-cells expressing the human NIS which showed that both PET and SPECT radiotracers were feasible options for longitudinal CAR T-cell imaging with minimal damage to CAR T-cells through radionuclide imaging [103]. This imaging approach via reporter genes will be further highlighted in chapter 2 with the focus on imaging cells using PET.

Although many preclinical studies using indium-111 to directly label cells have successfully monitored the fate of transplanted cells *in vivo*, these have not been used for quantitative cell tracking. Jin *et al*. used [^{111}In]In-Tropolone to determine the minimum number of labelled stem cells that could be detected on a clinical SPECT system considering background noise, Compton scatter and attenuation may impact on the detectable number of cells [104]. The detection limit of [^{111}In]In-Tropolone labelled cells was derived from the maximum activity per cell that did not affect viability and proliferation and the minimum detectable activity of indium-111 on SPECT images. The minimum detectable activities for 16, 32 and 64 min scans with background correction were observed to be 1.4 kBq, 700 Bq and 400 Bq, respectively which was estimated to be equal to 10,000, 5000 and 2900 cells, respectively.

SPECT is widely available, cheaper compared to PET and MRI and has a high translational potential from animals to humans given the already approved and available clinical probes. Compared to MRI nanoparticles, SPECT tracers have a relatively short

incubation time and can be rapidly taken up with a higher sensitivity (SPECT: 10^{-9} to 10^{-11} mol/L vs MRI: 10^{-3} to 10^{-5} mol/L) [105]. Nevertheless, SPECT is hampered by a low-resolution, semiquantitative acquisition of 2D images that are prone to artefacts and severe attenuation. However, SPECT has been a rapidly changing field and the past two decades have seen new developments in both hardware technology and image-processing algorithms that can allow absolute quantification in terms of activity concentration [106],[107]. New clinical devices include high-count sensitivity cardiac SPECT systems and the introduction of diagnostic-quality hybrid SPECT/CT systems. Another unique advantage of SPECT is the ability to collect photons of different energies form separate images. Two radiotracers with different energy photons can be administered to a single subject, and SPECT imaging can be used to image each radiotracer independently at a single time point which is not possible with PET.

1.3.5 Magnetic Resonance Imaging (MRI)

The use of magnetic resonance imaging (MRI) for cell tracking dates back to the late 1980s and early 1990s when superparamagnetic iron oxide nanoparticles (SPIOs) were first utilised to label and track transplanted cells in the brain of rats [108],[109], as a contrast agent for MR imaging of the liver [110], and as an intravenous contrast agent for assessing lymph nodes [111]. MRI uses strong magnetic fields (clinical MRI up to 10.5T; preclinical MRI up to 18T) that align the magnetic moments of protons or other NMR-active nuclei in a sample, e.g. fluorine-19, creating an equilibrium magnetization along the z-axis (M_z) with a magnitude of M_0. T_1 describes the time constant of the exponential recovery process of M_0 along the z-axis after a radiofrequency pulse whereas T_2 is the time constant of the exponential decay of transverse magnetization (M_{xy}) after a radiofrequency pulse. MRI contrast agents affect both T_1 and T_2 with SPIONs primarily altering T_2 values of water protons surrounding the particle. The presence of SPIONs in cells causes a distortion in the magnetic field that leads to abnormal signal that appear as regions of low intensity (hypointensities) on images, and therefore create a negative contrast. The degree of contrast on MRI depends on the relaxivity effects of the agent

used, contrast agent concentration, and imaging parameters such as magnetic field strength, pulse sequence, resolution and signal-to-noise ratio (SNR).

In 1996 the SPIO formulation ferumoxides (Feridex I.V.®, Bayer Healthcare, USA; sold as Endorem in Europe) gained FDA approval. Originally, ferumoxides was first developed as a liver MRI contrast agent and is the only pharmaceutical-grade compound that has been used in clinical studies for cell tracking [112]–[114].Ferumoxytol (Feraheme®), an FDA approved intravenous iron preparation for the treatment of anaemia was also approved as an Investigational New Drug (IND) for a first-in-human study to label neural stem cells (NSCs) before transplant into patients with brain tumours [115]. Ferumoxytol has also been recently applied as an MRI contrast agent for the indirect labelling of macrophages *in vivo* to highlight areas of inflammation after myocardial infarction [116]. In one clinical cell tracking study, both SPECT and MRI were used to assess the success of intranodal injection of dendritic cells (DCs) consisting of a 1:1 mixture of SPIONs- and ^{111}In-labelled DCs [114]. In contrast to SPECT, MRI allowed the accurate assessment of DC delivery and of inter- and intranodal cell migration. Despite the ultrasound guided cell injection, MRI revealed that cells in three patients were not injected into the target lymph node but in the perinodal fat (**Fig. 1.9 A** and **B**) and that no detectable cell migration could be observed. In two other patients DCs were injected only partly in the target lymph node. This study clearly showed that monitoring the delivery of administered cells to the target lymph nodes is pivotal to evaluate the outcome of cell therapy.

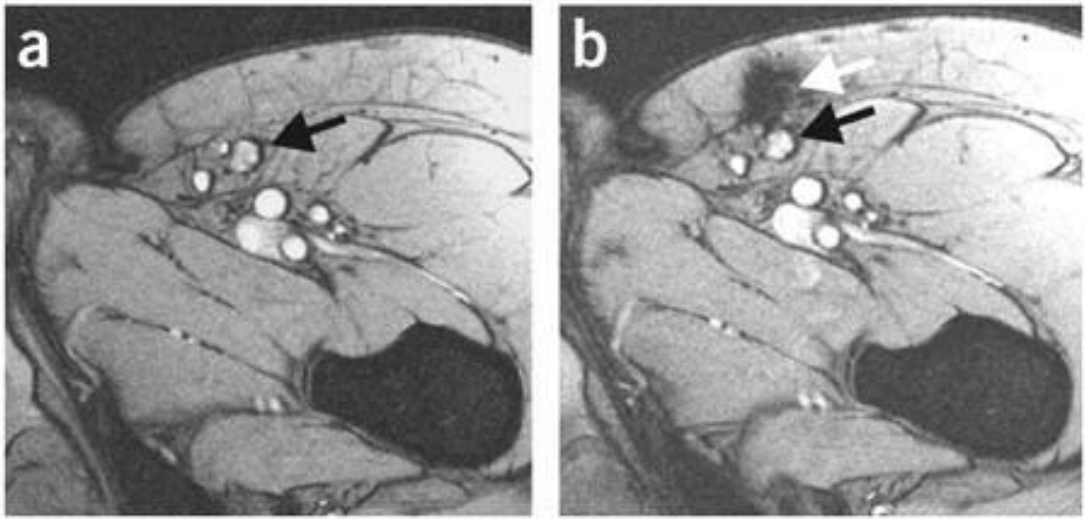

Figure 1.9 (**A**) T2*-weighted MRI (3T) before cell administration; the inguinal lymph node to be injected is indicated with a black arrow and (**B**) after injection showing that the dendritic cells were not accurately delivered into the inguinal lymph node (black arrow) but in the vicinity, i.e. the subcutaneous fat (white arrow). Acquisition parameters: average echo time of 15 ms (flip angle 36°, repetition time (TR) 1,060 ms, total acquisition time ~9 min, 30 slices, resolution 0.50 × 0.50 × 3.50 mm). Figure was copied from de Vries et al. [114].

Overall, a detection limit of 15,000 cells was found on MRI in the same study that are equal to ~2 × 10^3 cells/voxel assuming that the distribution of SPIO-positive cells in the lymph node was homogeneous. The above mentioned landmark study set the stage for subsequent clinical studies. In addition, autologous $CD34^+$ bone marrow stem cells were injected into the spinal cord by means of a lumbar puncture in patients with spinal cord injury (SCI) [117]. In another study that involved 20 patients, the systemic delivery of no less than 1 × 10^9 SPIO-labelled PBMCs was found to be safe [118]. No changes in cellular cytokine release profiles, cell migration, and the homing to induced inflammation could be observed which are very important prerequisites for the administration of cells. As for the recipients, no significant changes in cardiovascular physiology, blood chemistry, and white blood cell counts were noticed. In order to test the sensitivity of detecting cells with MRI, Verdijk et al. investigated the minimum amount of label and the number of cells required for MR imaging [119]. Dendritic cells were labelled with different concentrations of SPIONs (Endorem®) and imaged on a clinical 3T and 7T MR scanner. Results showed

that when cells were loaded with ~30 pg Fe/cell, cell numbers as low as 1,000 cells/mm^3 at 3 T and 500 cells/mm^3 at 7 T could be readily detected.

However, it is important to note that first-generation iron oxide nanoparticles such as ferumoxide (Feridex/Endorem®) and ferucarbotran (Resovist) have been discontinued in 2008 and 2009, respectively and are no longer available for clinical use in Europe or the United States. Ferucarbotran, known as VivoTrax (Magnetic Insight, Alameda, Calif), is still marketed specifically for magnetic particle imaging (MPI) cell tracking (see section 1.3.6 below) and is available in Japan and supplied as a preclinical agent in the United States. Therefore, ferumoxytol remains the most commonly used iron oxide nanoparticle formulation for cell labelling next to other second-generation nanoparticles such as ferumoxtran-10.

As a consequence, ferumoxytol has been widely used over the last decade in pre-clinical studies for the labelling and imaging of stem cells [120]–[122] to a great extend but also to label bone marrow stromal cells, monocytes, T-cells and hematopoietic stem cells [123] or to monitor islet transplantation [124]. In addition, many pre-clinical MRI cell tracking studies have made use of multimodality approaches, i.e. the combination of MRI with another modality such as BLI [125] or SPECT [126] to glean complementary information from a single experiment and also to make use of the strength of each modality. An *in vivo* detection limit of 500 cells labelled with ultrasmall SPIONs (USPIONs) in rats using a 7 T small animal MRI [127] was initially demonstrated before Stroh et al. established an *in vivo* detection limit of 100 SPION-labelled embryonic stem cells in striatum in rats at 17.6 T [128]. Single cell detection has been demonstrated *in vitro* by several groups but has later been reported also *in vivo* in mouse liver [129] and mouse brain [130].

The *in vitro* cell labelling approach using iron oxide-based MRI agents is simple, it does not involve radiation, and has the advantage of high spatial resolution, particularly for the anatomical allocation of the cellular signal. However, there are still some limitations associated with iron-based MRI cell tracking. Generally, the uptake of nanoparticles into cells have shown to be dependent on the cell type [131] and cell division state [132] and a high concentration is needed to obtain sufficient contrast on MRI which may have an

impact on more sensitive and smaller cell types. Like with any other direct cell labelling method, the SPION label gets diluted with cell division which can affect the signal and it is not possible to discriminate live from dead cells which can only be overcome with the use of reporter genes. In addition, quantification of iron-induced signal loss is complicated, as the measure of the signal void volume is not linear with the number of cells. Nanoparticles, depending on the composition, often do not biodegrade and can be deposited in the liver potentially causing toxicities and oxidative stress with potential iron overload amongst others [133].

An alternative approach to cell tracking with SPION-MRI is ^{19}F-MRI which can also overcome some of the limitations associated with SPION-MRI. This technique commonly uses perfluorocarbon (PFC) nano-emulsions added directly to cells that can be detected on a ^{19}F-MRI in a hotspot image (positive contrast) with high specificity since there is little endogenous fluorine-19 within biological tissue. Contrary to the visualisation of SPIONs, the spins of ^{19}F nuclei are directly detected and the positive image contrast is directly linear to the number of ^{19}F nuclei per voxel, which allows for the quantification of ^{19}F labelled cells *in vivo*. Cell numbers can be determined by an *in vitro* measurement of ^{19}F-containing test tube (reference) by NMR spectroscopy. The ^{19}F signal intensity for the cells of interest is compared to the ^{19}F signal intensity of a reference tube containing a known fluorine-19 concentration and the NMR calibration value [134].

^{19}F-MRI was used in colorectal adenocarcinoma patients to detect *ex vivo* PFC-labelled immunotherapeutic dendritic cells (DCs) directly injected into peripheral tissue. Apparent DC numbers could be quantified in two patients on ^{19}F-hot-spot images (**Fig. 1.10**) and decreased to half of the original values by 24 h post-administration as a result of cell migration to nearby lymph nodes, other tissues, or due to cell death and subsequent clearance of PFC material [135]. ^{19}F-MRI was also used various times preclinically in animals to monitor [^{19}F]-PFC-labelled human and mouse MSCs [136], human PBMCs [137], human neural stem cells (hNSCs) [138], human therapeutic DCs [139], as well as progenitor stem cells and macrophages [140] amongst others [141].

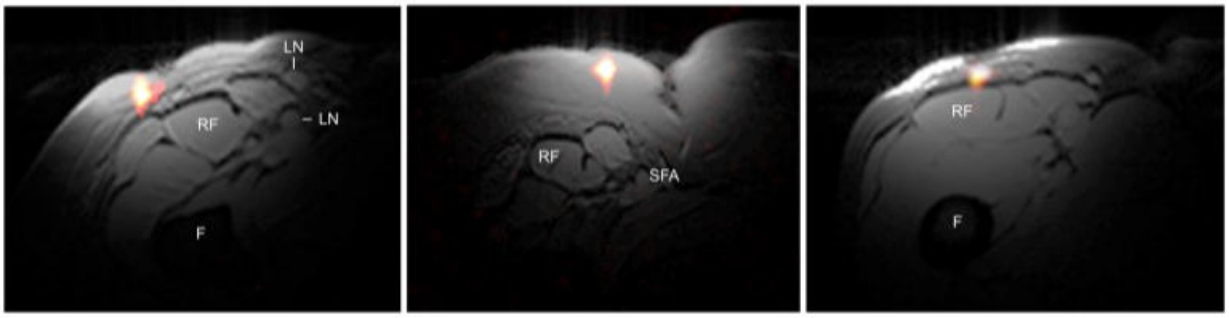

Figure 1.10 Axial composite $^{19}F/^{1}H$ images of the right thigh at 4 h post-inoculation in three different patients (left, middle and right), where the DCs are rendered with a hot-iron pseudo-colour overlay and the ^{1}H anatomy is displayed in grayscale (F = femur, RF = rectus femoris, SFA = superficial femoral artery, LN = inguinal lymph node). Figure copied from Ahrens *et al.* [135]. Imaging parameters: repetition time/echo time (TR/TE) = 100/4.15 ms, NA = 96, flip angle (FA) = 45°, slice thickness 2 cm, number of slices (NS) = 3, field of view (FOV) = $(28.8\ cm)^2$, and matrix size 64 × 64. For anatomical reference, co-registered ^{1}H FLASH images were collected with parameters TR/TE = 115/4.92 ms, NA = 2, FA = 25°, slice thickness 5 mm, NS = 12, FOV = $(28.8\ cm)^2$, and matrix size 192 × 192.

However, one of the key limitations of ^{19}F-MRI probes can be sensitivity which is limited by the total amount and distribution of fluorine atoms in the probe and is much less than iron oxide agents. The gyromagnetic ratios of ^{1}H and ^{19}F differ by only ~6%, and the relative sensitivity is ~0.83 [142]. NMR data has shown that DCs contain ~5.2×10^{12} fluorine spins on average and it was estimated that ~2×10^{5} labelled cells per voxel could be detected [143]. Fluorine sensitivity improves with higher field strengths and the number of detectable spins (i.e. labelled cells) per voxel will be significantly lower. Phantom studies on a 3 T scanner showed a cellular detection limit of ~10^{5} cells/voxel [135].

1.3.6 Magnetic Particle Imaging (MPI)

As described in the previous section, MRI has a long-standing application for *in vivo* cell tracking. Magnetic Particle Imaging (MPI) is an emerging and novel imaging modality that was developed in the early 2000s [144]. Contrary to MR imaging, sonography, x-ray, and CT, MPI is not a structural imaging technique but rather a functional (tracer) imaging technique similar to PET and SPECT. MPI makes use of an inhomogeneous magnetic gradient field (selection field), to saturate all superparamagnetic iron oxide (SPIO) magnetizations outside a central field-free region, known as a field-free point (FFP) or field-free line (FFL). In order to produce an image, the FFL traverses a SPION location via a rapidly varying excitation/drive field. As a result, the SPION's magnetisation changes nonlinearly in response and the time-varying magnetization induces a voltage in the receiver coil, which can be assigned to the instantaneous FFL location to reconstruct an image. The voltages induced are linearly proportional to the number of SPIONs at the instantaneous FFL location, enabling quantification of SPIONs. Therefore, MPI cell tracking has the potential to address many of the limitations presented by MRI-based cell tracking [145] and is able to directly detect SPIONs [146],[147] which endows MPI with a positive ‘hot spot’ contrast that is not affected by the endogenous iron present in the body and is a major advantage for perfusion imaging and cell tracking. The resolution of MPI compares well with clinical nuclear techniques and is in the milimetre range [148]. Its relatively high sensitivity stems from the direct detection of the electronic magnetization that is 10^8 times larger compared to the nuclear magnetization detected in MRI [149]. However, one of the shortcomings of MPI include a relatively low spatial resolution compared to MRI with human-scale magnetic particle imaging system tailored for cerebral imaging being in the range of 6 mm [150]. In addition, MPI requires anatomical images to be acquired separately with a different imaging approach.

First *in vivo* MPI studies using prototype scanners and, more recently, commercial animal scanners have demonstrated applications in vascular imaging [151], lung perfusion imaging [152] oncology [153]–[155] and also cell tracking. In a first initial study it was shown that rat and human adult stem cells can take up SPIONS and that they localise in the cytoplasm [156]. Another proof-of-concept study confirmed that human

MSCs labelled with SPIONs were instantly entrapped in the pulmonary vasculature of mice following intravenous injection and cleared to the liver within one day whereas standard iron oxide particle (Resovist) injections are immediately taken up by the liver and spleen [157]. MPI was also used to evaluate the long-term tracking of neural implants. Neural progenitor cells (NPGs) labelled with SPIONs were implanted into the forebrain of rats and the graft signals monitored using MPI imaging for a period of 87 days post-administration. MPI together with histology and MRI validation revealed the presence of SPIOs adjacent to the lateral ventricle and that tagged cells had migrated posteriorly throughout the ventricle [158]. In a direct comparison with MRI, MPI was used to image and quantify ferumoxytol- and ferucarbotran-labelled MSCs in a mouse model of osteoarthritis and showed that MPI of ferumoxytol-labelled cells was sensitive to changes in the cell number *in vivo* over 14 days, whereas the voids detected in ^{1}H MRI did not detect this change [159]. Sehl *et al*. showed for the first time that iron-based ^{1}H MRI, ^{19}F-MRI, and MPI can be used together to noninvasively monitor MSCs and macrophages in a trimodal imaging approach [160]. MSCs were labelled with ferumoxytol and detected on ^{1}H images as regions of negative signal and on MPI images as regions of positive signal. Macrophages that accumulate at the site of MSC implantation were labelled *in vivo* with a PFC agent and detected with ^{19}F-MRI. This was also the first study to demonstrate the ability to image macrophage infiltration *in vivo* using fluorine-19 on a clinical (3 T) MRI system. The possibility to directly quantify the MPI and ^{19}F MRI signal was used to estimate the relative number of MSCs and macrophages over time. This multimodality imaging approach allowed for the confirmation of MSC delivery, the measurement of MSC number over time and quantification of inflammation (**Fig. 1.11**).

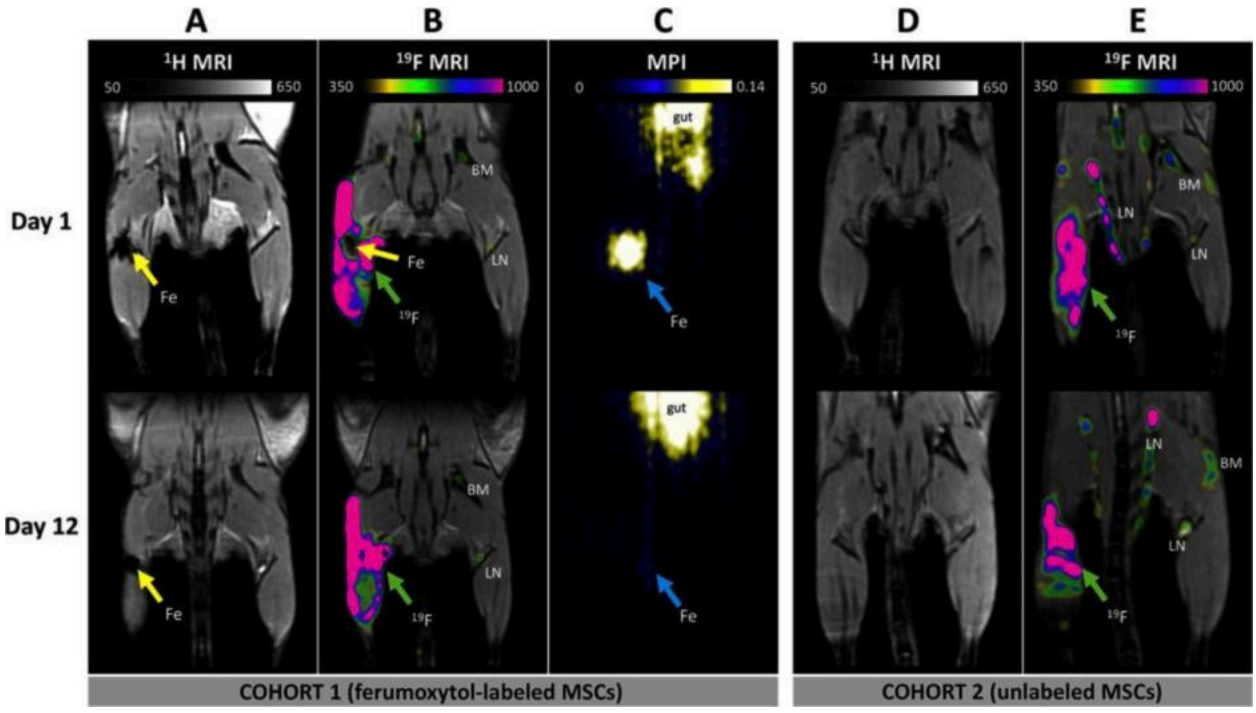

Figure 1.11 ***In vivo*** **^{1}H/^{19}F MRI and MPI**. In ^{1}H images, ferumoxytol-positive MSCs were detected as regions of signal loss 1 and 12 days following MSC implantation (**A**). PFC-positive immune cells are detected in the bone marrow (BM), lymph nodes (LN), and in the muscle surrounding the MSC implant on ^{19}F MRI (**B**). Ferumoxytol-positive MSCs are also detected in MPI images as bright spots (**C**). In these images, iron in the gut of the mice is also detected by MPI. Mice that received unlabelled MSCs (controls) had no signal voids present in ^{1}H MRI (**D**) and ^{19}F-signal persisting (**E**), in response to the implant. Image adopted from Sehl *et al.* [160].

Current MPI systems have detection limits as low as ~200 cells labelled with ferucarbotran in a voxel [158],[161] and theoretically, the MPI detection limit may be as little as 1-10 iron oxide labelled cells in a voxel [158]. As MPI technology matures, cellular sensitivity is likely to improve and considerable work remains to be undertaken to investigate MPI detection limits more closely. Human scanners are being developed and will become available in a few years.

1.3.7 Ultrasound

Ultrasound is a safe, portable and low-cost technology widely used in biomedicine since the 1960s and uses high frequency (megahertz range) sound waves and their echoes to create images. A transducer emits ultrasound waves and detects the sound waves that are reflected back (echoes) by boundaries between tissues in the path of the beam (e.g. boundary between fluid and soft tissue or tissue and bone). Using the speed of sound and the time it takes for each echo to return, a scanner calculates the distance from the transducer to the tissue boundary. These distances are then used to generate two-dimensional images of tissues and organs. Ultrasound can easily penetrate most tissues and enable deep and non-invasive imaging with excellent spatial and temporal resolution (~100 μm (clinical), 30 μm (preclinical) and ~1 ms, respectively) [162],[163].

Despite its advantages, ultrasound has played a relatively small role in cellular imaging. Most early studies focused at the tissue and organ level but with the advent of high-frequency ultrasound, wavelengths approaching the size of the cell allowed studying the backscattering from smaller cell ensembles like spheroids [164],[165] which was also sensitive to structural changes that cells undergo during cell death, such as apoptosis [166],[167]. However, the use of ultrasound for cell imaging is limited by the low contrast of cells above the adjacent tissue. Therefore, nano-size particles that are much smaller than the current generation of ultrasound contrast agents, have found promising applications for labelling and imaging cells in several settings as they can increase the echogenicity of labelled cells. For example, exosome-like silica (ELS) nanoparticles have been used to label stem cells that were subsequently implanted subcutaneously into nude mice and imaged using ultrasound [168] (**Fig. 1.12**). Other types of nanoparticles and also nanobubbles were investigated to track the location of injected stem cells *in vivo* that also included multimodality approaches [169],[170]. One study reported the detection limit to be around 4000 cells *in vitro* [171]. The recently developed super-resolution (below 10 pm) ultrafast ultrasound technique will most likely push current boundaries and open up new possibilities to image cells with ultrasound in the future [172].

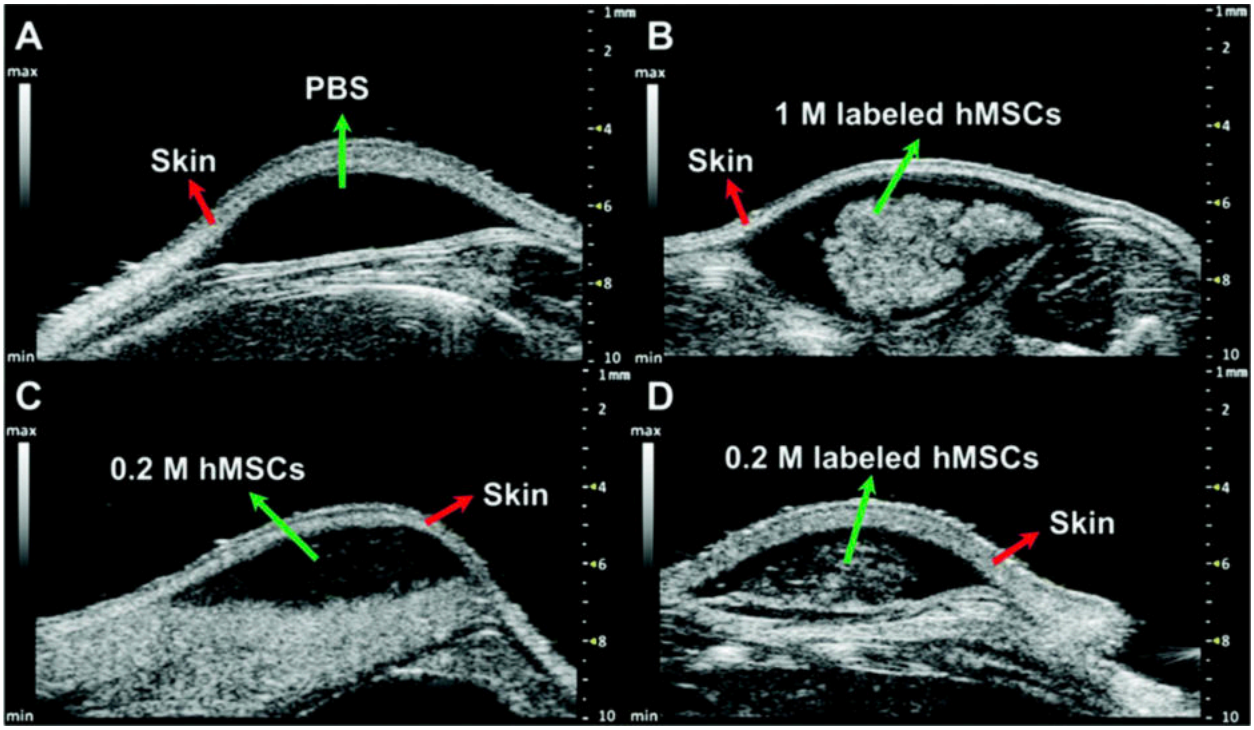

Figure 1.12 Ultrasound images and *in vivo* quantification of cells echogenicity. *In vivo* ultrasound images of (**A**) PBS, (**B**) 1 million ELS-labelled hMSCs, (**C**) 0.2 million unlabelled hMSCs, and (**D**) 0.2 million ELS-labelled hMSCs. Image copyright from Chen *et al.* [168].

The prospect of using ultrasound to image the function of specific cells is limited by the lack of suitable molecular reporters. Conventional micron-sized microbubbles as ultrasound contrast agents are too large for cellular labelling and their long-term instability hampers their use for monitoring the function of specific cells. Very recently, a unique class of gas-filled proteins, so called gas vesicles (GVs), were introduced as the first biomolecular contrast agents for ultrasound. These air-filled protein nanostructures comprise a 2 nm thick protein shell enclosing a hollow interior with dimensions in the order of 250 nm and originally evolved in aquatic photosynthetic microbes as a means to regulate buoyancy for optimal access to sunlight and other nutrients [173]. In 2014, it was shown that GVs can produce ultrasound contrast inside cells and *in vivo*, making GVs the first established acoustic biomolecules [174]. After these initial findings, considerable advances have been made in understanding the acoustic properties of GVs and improving sensitivity and specificity. One key finding was that the acoustic properties of GVs can be engineered at the genetic level. It was further demonstrated that engineered

cells could be imaged *in vivo* in proof-of-concept models of gastrointestinal tumour localization and that acoustically distinct reporters could be developed enabling multiplexed imaging of mammalian cell populations [175],[176]. Cells at concentrations as low as 5×10^7 cells ml^{-1} produced a detectable signal. This equates to approximately 100 cells per voxel based on cubic voxel dimensions of 100 μm.

1.3.8 Photoacoustic Imaging (PAI)

An alternative mechanism by which ultrasound can facilitate the visualization of cells *in vivo* is photoacoustic imaging (PAI), also referred to as photoacoustic tomography (PAT). This type of imaging is based on the photoacoustic effect, i.e. a physical phenomenon that converts absorbed optical energy into acoustic energy which can then be detected by backscatter mode ultrasound (B-mode) [177] and offers certain advantages. PAI is inherently suited for functional, metabolic, and histologic imaging through endogenous contrast and for molecular and cellular imaging through exogenous contrast. It is non-invasive and quantitative and has fast scan times. Its spatial (50-150 *μ*m) and temporal resolution (100 ms) are excellent. PAI provides far greater penetration with a scalable spatial resolution as biological tissue is orders of magnitude more transparent to sound than to light, which is one advantage over optical microscopy. Nevertheless, PAI is complementary to and compatible with other imaging modalities, especially optical imaging and ultrasound imaging. Using Photoacoustic microscopy (PAM), detailed sub-micrometre resolution images of single cells can be produced with contrast dependent primarily on the optical absorption properties of the cell.

Endogenous contrast can be achieved with chromophores such as haemoglobin, lipids, melanin, and genetically engineering chromophores or reporter genes. Photoacoustic cell imaging has been used mainly for stem cell tracking where exogenous contrast agents are often necessary to generate stem-cell-specific signal. For example, MSCs were labelled with silica-coated nanorods [178], gold nanocages [179] and efficient near-infrared (NIR) probes in the form of nanoparticle emulsions [180]. The latter study showed that subcutaneously injected labelled and luciferase-expressing MCS could be clearly visualised up to 11 days post-injection with PAI whereby viability of cells

throughout the experiment could be confirmed in conjunction with BLI. In addition, detection limits encountered with this approach were investigated as shown in **Fig. 1.13** which demonstrated that cells in the magnitude of 10^5 could be detected.

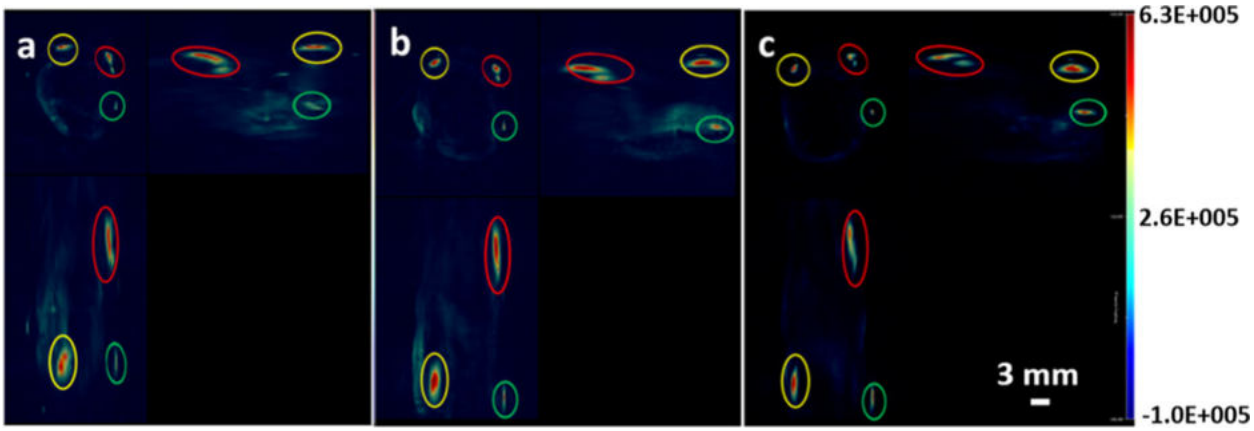

Figure 1.13 3D view of a mouse after injection with MSCs on (A) day 1, (B) day 7 and (C) day 11. Each panel shows the three cross-sectional views: top left, transverse plane; top right, sagittal plane; bottom left, coronal plane. Red circles indicate 1×10^6 cells labelled with perylene diimide derived nanoprobes (PDI), yellow circles indicate 0.5×10^6 PDI-labelled cells, and green circles indicate 0.25×10^6 PDI-labelled cells. Figure reproduced from [180].

Photoacoustic microscopy (PAM) can provide detailed sub-micrometre resolution images of single cells with insight into their anatomical, biomechanical, and functional properties. This information can be used to identify specific cells, or to enhance the understanding of biological processes at the single cell level [181]. The major advantage of photoacoustic imaging compared to pure ultrasound is its ability to leverage existing molecular tools developed for optical imaging, including fluorescent proteins or light-absorbing pigments such as melanin. However, this technique is still difficult to employ at depths beyond one to two centimetres without causing tissue phototoxicity.

1.4 Summary

In summary, various techniques can be used to label cells and several modalities can be employed to track cells. **Table 1.2** presents an overview of clinical imaging modalities used for cell imaging with features of each modality that have also been covered in chapter 1 including the detection limits encountered. The next Chapter will solely focus on the use of positron emission tomography (PET) for cell labelling and imaging and will give a detailed insight into the different cell labelling techniques with various available and emerging radiotracers.

Table 1.2 Comparison of common clinical imaging modalities used for cell imaging.

Adapted from [148],[182] and further added to from various sources and literature.

Modality	Ultrasound	MRI	PET	SPECT	MPI
Form of energy used	High frequency sound waves	Radio frequency waves	Annihilation photons	Gamma rays	Radio frequency waves
Spatial resolution	0.04 – 0.1 mm (small animal US); 0.1 - 1 mm (clinical US)	0.01-0.1 mm (small animal MRI); 0.5 - 1.5 mm (clinical MRI)	1-2 mm (microPET); 6-10 mm (clinical PET)	0.5-2 mm (microSPECT); 7-15 mm (clinical SPECT)	0.2-2.0 mm (small animal MRI); 6 mm (clinical MRI)
Temporal resolution	<1 second	Seconds to hours	Minutes	Minutes	<1 second to minutes
Contrast agents/tracers	Microbubbles	Gadolinium, iron oxide particles, perfluorocarbon nano-emulsions	Radioactive tracers	Radioactive tracers	Iron oxide particles
Required molecular probe	10^3-10^6 ng	10^3-10^6 ng	1-100 ng	1-100 ng	~30 ng
Sensitivity	Low (~ μM)	Low (mM-μM)	High (fM)	High (pM-fM)	High (μM-pM)
Cellular detection limit	10^3 cells *in vitro*; 10^5 cells in mice	Single cell detection *in vitro* and in mice; 10^4 cells *in vivo* in humans	Single cell detection in mice; 10^4 cells *in vitro* on clinical PET	10^5 cells in mice; 10^4 cells *in vitro* on clinical SPECT	10^3 cells *in vitro*
Patient risk	Heating and cavitation	Heating and peripheral nerve stimulation	Radiation	Radiation	Heating and peripheral nerve stimulation
Cost	Low	High	High	Medium	Medium

1.5 References

1. Fischbach MA, Bluestone JA, Lim WA. Cell-Based Therapeutics: The Next Pillar of Medicine. *Sci Transl Med*. 2013;5(179):179ps7-179ps7.
2. Couzin-Frankel J. Cancer immunotherapy. *Science (80-)*. 2013;342(6165):1432-1433.
3. Hoos A. Development of immuno-oncology drugs — from CTLA4 to PD1 to the next generations. *Nat Rev Drug Discov*. 2016;15(4):235-247.
4. Chen DS, Mellman I. Oncology meets immunology: The cancer-immunity cycle. *Immunity*. 2013;39(1):1-10.
5. McCarthy EF. The toxins of William B. Coley and the treatment of bone and soft-tissue sarcomas. *Iowa Orthop J*. 2006;26:154-158.
6. Oiseth SJ, Aziz MS. Cancer immunotherapy: a brief review of the history, possibilities, and challenges ahead. *J Cancer Metastasis Treat*. 2017;3(10):250.
7. Atkins MB, Clark JI, Quinn DI. Immune checkpoint inhibitors in advanced renal cell carcinoma: experience to date and future directions. *Ann Oncol Off J Eur Soc Med Oncol*. 2017;(April):1484-1494.
8. Zang X. 2018 Nobel Prize in medicine awarded to cancer immunotherapy: Immune checkpoint blockade – A personal account. *Genes Dis*. 2018;5(4):302-303.
9. Naran K, Nundalall T, Chetty S, Barth S. Principles of Immunotherapy: Implications for Treatment Strategies in Cancer and Infectious Diseases. *Front Microbiol*. 2018.
10. Rosenberg SA, Lotze MT, Muul LM, et al. Observations on the Systemic Administration of Autologous Lymphokine-Activated Killer Cells and Recombinant Interleukin-2 to Patients with Metastatic Cancer. *N Engl J Med*. 1985;313(23):1485-1492.
11. Dudley ME, Yang JC, Sherry R, et al. Adoptive cell therapy for patients with metastatic melanoma: Evaluation of intensive myeloablative chemoradiation preparative regimens. *J Clin Oncol*. 2008;26(32):5233-5239.
12. Rosenberg SA, Yang JC, Sherry RM, et al. Durable complete responses in heavily pretreated patients with metastatic melanoma using T-cell transfer immunotherapy. *Clin Cancer Res*. 2011;17(13):4550-4557.

13. Stevanović S, Draper LM, Langhan MM, et al. Complete regression of metastatic cervical cancer after treatment with human papillomavirus-targeted tumor-infiltrating T cells. *J Clin Oncol*. 2015;33(14):1543-1550.
14. Andersen R, Westergaard MCW, Kjeldsen JW, et al. T-cell responses in the microenvironment of primary renal cell carcinoma-implications for adoptive cell therapy. *Cancer Immunol Res*. 2018;6(2):222-235.
15. Lee HJ, Kim YA, Sim CK, et al. Expansion of tumor-infiltrating lymphocytes and their potential for application as adoptive cell transfer therapy in human breast cancer. *Oncotarget*. 2017.
16. Ben-Avi R, Farhi R, Ben-Nun A, et al. Establishment of adoptive cell therapy with tumor infiltrating lymphocytes for non-small cell lung cancer patients. *Cancer Immunol Immunother*. 2018.
17. Maetzig T, Galla M, Baum C, Schambach A. Gammaretroviral vectors: Biology, technology and application. *Viruses*. 2011;3(6):677-713.
18. Rohaan MW, Wilgenhof S, Haanen JBAG. Adoptive cellular therapies: the current landscape. *Virchows Arch*. 2019;474(4):449-461.
19. D'angelo SP, Melchiori L, Merchant MS, et al. Antitumor activity associated with prolonged persistence of adoptively transferred NY-ESO-1c259T cells in synovial sarcoma. *Cancer Discov*. 2018;8(8):944-957.
20. Lauss M, Donia M, Harbst K, et al. Mutational and putative neoantigen load predict clinical benefit of adoptive T cell therapy in melanoma. *Nat Commun*. 2017;8(1).
21. Robbins PF, Lu YC, El-Gamil M, et al. Mining exomic sequencing data to identify mutated antigens recognized by adoptively transferred tumor-reactive T cells. *Nat Med*. 2013;19(6):747-752.
22. Garcia-Garijo A, Fajardo CA, Gros A. Determinants for neoantigen identification. *Front Immunol*. 2019;10(JUN).
23. FDA approves CAR-T cell therapy to treat adults with certain types of large B-cell lymphoma. *https://www.fda.gov/NewsEvents/Newsroom/PressAnnouncements/ucm581216.htm*. 2017.

24. Bagno L, Hatzistergos KE, Balkan W, Hare JM. Mesenchymal Stem Cell-Based Therapy for Cardiovascular Disease: Progress and Challenges. *Mol Ther*. 2018;26(7):1610-1623.
25. Young PP, Schäfer R, Su X, et al. Cell-based therapies for cardiac disease: a cellular therapist's perspective. *Transfusion*. 2015;55(2):441-451.
26. Aghajanian H, Kimura T, Rurik JG, et al. Targeting cardiac fibrosis with engineered T cells. *Nature*. 2019.
27. Hu X, Leak RK, Thomson AW, et al. Promises and limitations of immune cell-based therapies in neurological disorders. *Nature Reviews Neurology*. 2018:559-568.
28. Ellis C, Ramzy A, Kieffer TJ. Regenerative medicine and cell-based approaches to restore pancreatic function. *Nat Rev Gastroenterol Hepatol*. 2017;14(10):612-628.
29. Turner L. Preying on Public Fears and Anxieties in a Pandemic: Businesses Selling Unproven and Unlicensed "Stem Cell Treatments" for COVID-19. *Cell Stem Cell*. 2020;26(6):806-810.
30. Xin Yu J, Hubbard-Lucey VM, Tang J. Immuno-oncology drug development goes global. *Nat Rev Drug Discov*. 2019;18(12):899-900.
31. Yu JX, Upadhaya S, Tatake R, Barkalow F, Hubbard-Lucey VM. Cancer cell therapies: the clinical trial landscape. *Nat Rev Drug Discov*. 2020;19(9):583-584.
32. Rosenberg SA, Restifo NP. Adoptive cell transfer as personalized immunotherapy for human cancer. *Science (80-)*. 2015;348(6230):62-68.
33. Kalos M, Levine BL, Porter DL, et al. T cells with chimeric antigen receptors have potent antitumor effects and can establish memory in patients with advanced leukemia. *Sci Transl Med*. 2011;3(95).
34. Maude SL, Laetsch TW, Buechner J, et al. Tisagenlecleucel in Children and Young Adults with B-Cell Lymphoblastic Leukemia. *N Engl J Med*. 2018.
35. Moutsatsou P, Ochs J, Schmitt RH, Hewitt CJ, Hanga MP. Automation in cell and gene therapy manufacturing: from past to future. *Biotechnol Lett*. 2019;41(11):1245-1253.

36. Kochenderfer JN, Dudley ME, Kassim SH, et al. Chemotherapy-refractory diffuse large B-cell lymphoma and indolent B-cell malignancies can be effectively treated with autologous T cells expressing an anti-CD19 chimeric antigen receptor. *J Clin Oncol*. 2015;33(6):540-549.
37. Kalos M, Frey N V, Grupp S a, et al. Randomized, Phase II Dose Optimization Study Of Chimeric Antigen Receptor Modified T Cells Directed Against CD19 (CTL019) In Patients With Relapsed, Refractory CLL. *Blood* . 2013;122:873.
38. Maude SL, Frey N, Shaw PA, et al. Chimeric Antigen Receptor T Cells for Sustained Remissions in Leukemia. *N Engl J Med*. 2014;371(16):1507-1517.
39. US Food and Drug Administration (FDA). Statement from FDA Commissioner Scott Gottlieb, M.D. and Peter Marks, M.D., Ph.D., Director of the Center for Biologics Evaluation and Research on new policies to advance development of safe and effective cell and ge.
40. MIT NEWDIGS. Projections from the existing pipeline of cell and gene therapies: Launches and patient numbers. https://newdigs.mit.edu/sites/default/files/FoCUS Research Brief 2018F210v027.pdf (2018).
41. Saudemont A, Jespers L, Clay T. Current status of gene engineering cell therapeutics. *Front Immunol*. 2018;9(FEB).
42. Yakoub-Agha I, Chabannon C, Bader P, et al. Management of adults and children undergoing chimeric antigen receptor T-cell therapy: Best practice recommendations of the European Society for Blood and Marrow Transplantation (EBMT) and the Joint Accreditation Committee of ISCT and EBMT (JACIE). *Haematologica*. 2020;105(2):297-316.
43. Nassereddine S, Rafei H, Elbahesh E, Tabbara I. Acute graft versus host disease: A comprehensive review. *Anticancer Res*. 2017;37(4):1547-1555.
44. Neelapu SS, Locke FL, Bartlett NL, et al. Axicabtagene Ciloleucel CAR T-Cell Therapy in Refractory Large B-Cell Lymphoma. *N Engl J Med*. 2017.
45. Yong CSM, Dardalhon V, Devaud C, Taylor N, Darcy PK, Kershaw MH. CAR T-cell therapy of solid tumors. *Immunol Cell Biol*. 2017;95(4):356-363.
46. Lin JK, Muffly LS, Spinner MA, Barnes JI, Owens DK, Goldhaber-Fiebert JD. Cost effectiveness of chimeric antigen receptor T-cell therapy in multiply relapsed or

refractory adult large B-cell lymphoma. *J Clin Oncol*. 2019;37(24):2105-2119.

47. Kuhl CK. RECIST needs revision: A wake-up call for radiologists. *Radiology*. 2019;292(1):110-111.
48. Yoon JK, Park BN, Ryu EK, An YS, Lee SJ. Current perspectives on 89Zr-PET imaging. *Int J Mol Sci*. 2020;21(12):1-18.
49. Saleem A, Murphy P, Plisson C, Lahn M. Why are we failing to implement imaging studies with radiolabelled new molecular entities in early oncology drug development? *Sci World J*. 2014;2014.
50. Matthews PM, Rabiner EA, Passchier J, Gunn RN. Positron emission tomography molecular imaging for drug development. *Br J Clin Pharmacol*. 2012;73(2):175-186.
51. Kraeber-Bodere F, Bailly C, ChÃ©rel M, Chatal JF. ImmunoPET to help stratify patients for targeted therapies and to improve drug development. *Eur J Nucl Med Mol Imaging*. 2016;43(12):2166-2168.
52. Iravani A, Hicks RJ. Imaging the cancer immune environment and its response to pharmacologic intervention, Part 1: The role of 18F-FDG PET/CT. *J Nucl Med*. 2020.
53. Horti AG, Naik R, Foss CA, et al. PET imaging of microglia by targeting macrophage colony-stimulating factor 1 receptor (CSF1R). *Proc Natl Acad Sci U S A*. 2019.
54. Pandit-Taskar N, Postow MA, Hellmann MD, et al. First-in-Humans Imaging with 89Zr-Df-IAB22M2C Anti-CD8 Minibody in Patients with Solid Malignancies: Preliminary Pharmacokinetics, Biodistribution, and Lesion Targeting. *J Nucl Med*. 2020;61(4):512-519.
55. Singla R, Wall DM, Anderson S, et al. First in-human study of in vivo imaging of ex vivo labeled CAR T cells with dual PET-MR. *J Clin Oncol*. 2020;38(15_suppl):3557-3557.
56. Dammes N, Peer D. Monoclonal antibody-based molecular imaging strategies and theranostic opportunities. *Theranostics*. 2020.
57. Alam IS, Mayer AT, Sagiv-Barfi I, et al. Imaging activated T cells predicts response to cancer vaccines. *J Clin Invest*. 2018;128(6):2569-2580.
58. Serganova I, Blasberg RG. Molecular imaging with reporter genes: Has its promise been delivered? *J Nucl Med*. 2019;60(12):1665-1681.

59. Wood K V., Lam YA, Seliger HH, McElroy WD. Complementary DNA coding click beetle luciferases can elicit bioluminescence of different colors. *Science (80-)*. 1989;244(4905):700-702.
60. Feeney KA, Putker M, Brancaccio M, O'Neill JS. In-depth Characterization of Firefly Luciferase as a Reporter of Circadian Gene Expression in Mammalian Cells. *J Biol Rhythms*. 2016;31(6):540-550.
61. Kim JE, Kalimuthu S, Ahn BC. In Vivo Cell Tracking with Bioluminescence Imaging. *Nucl Med Mol Imaging (2010)*. 2015.
62. Costa GL, Sandora MR, Nakajima A, et al. Adoptive Immunotherapy of Experimental Autoimmune Encephalomyelitis Via T Cell Delivery of the IL-12 p40 Subunit. *J Immunol*. 2001;167(4):2379-2387.
63. Iwano S, Sugiyama M, Hama H, et al. Single-cell bioluminescence imaging of deep tissue in freely moving animals. *Science (80-)*. 2018;359(6378):935-939.
64. Krekorian M, Fruhwirth GO, Srinivas M, et al. Imaging of T-cells and their responses during anti-cancer immunotherapy. *Theranostics*. 2019.
65. Fruhwirth GO, Kneilling M, de Vries IJM, Weigelin B, Srinivas M, Aarntzen EHJG. The Potential of In Vivo Imaging for Optimization of Molecular and Cellular Anti-cancer Immunotherapies. *Mol Imaging Biol*. 2018.
66. Bougherara H, Mansuet-Lupo A, Alifano M, et al. Real-time imaging of resident T cells in human lung and ovarian carcinomas reveals how different tumor microenvironments control T lymphocyte migration. *Front Immunol*. 2015;6(OCT).
67. Volpe A, Kurtys E, Fruhwirth GO. Cousins at work: How combining medical with optical imaging enhances in vivo cell tracking. *Int J Biochem Cell Biol*. 2018;102:40-50.
68. Kim TJ, Wang Q, Shelor M, Pratx G. Single-cell radioluminescence microscopy with two-fold higher sensitivity using dual scintillator configuration. *PLoS One*. 2020;15(7).
69. Gallina ME, Kim TJ, Vasquez J, Tuerkcan S, Abbyad P, Pratx G. Single-cell analysis of radiotracers' uptake by fluorescence microscopy: direct and droplet approach. In: *Imaging, Manipulation, and Analysis of Biomolecules, Cells, and Tissues XV*. Vol 10068. ; 2017:100680Y.

70. Pratx G, Chen K, Sun C, et al. Radioluminescence Microscopy: Measuring the Heterogeneous Uptake of Radiotracers in Single Living Cells. *PLoS One*. 2012.
71. Wu JC, Chen IY, Sundaresan G, et al. Molecular imaging of cardiac cell transplantation in living animals using optical bioluminescence and positron emission tomography. *Circulation*. 2003;108(11):1302-1305.
72. Sheikh AY, Lin S-A, Cao F, et al. Molecular imaging of bone marrow mononuclear cell homing and engraftment in ischemic myocardium. *Stem Cells*. 2007;25(10):2677-2684.
73. Shah K, Weissleder R. Molecular optical imaging: applications leading to the development of present day therapeutics. *NeuroRx*. 2005;2(April):215-225.
74. Mc Larney B, Skubal M, Grimm J. A Review of Recent and Emerging Approaches for the Clinical Application of Cerenkov Luminescence Imaging. *Front Phys*. 2021;9.
75. Ruggiero A, Holland JP, Lewis JS, Grimm J. Cerenkov Luminescence Imaging of Medical Isotopes. *J Nucl Med*. 2010;51(7):1123-1130.
76. Lewis DY, Mair R, Wright A, et al. [18 F]fluoroethyltyrosine-induced Cerenkov Luminescence Improves Image-Guided Surgical Resection of Glioma. *Theranostics*. 2018;8(14):3991-4002.
77. Spinelli AE, Ferdeghini M, Cavedon C, et al. First human Cerenkography. *J Biomed Opt*. 2013;18(2):020502.
78. Thorek DLJ, Riedl CC, Grimm J. Clinical cerenkov luminescence imaging of 18F-FDG. *J Nucl Med*. 2014;55(1):95-98.
79. Image Separation Radioisotope Scanning. *JAMA J Am Med Assoc*. 1963;184(4):187.
80. Groch MW, Erwin WD. SPECT in the year 2000: Basic principles. *J Nucl Med Technol*. 2000.
81. Pellico J, Gawne PJ, T. M. de Rosales R. Radiolabelling of nanomaterials for medical imaging and therapy. *Chem Soc Rev*. 2021:3355-3423.
82. Mariani G, Bruselli L, Kuwert T, et al. A review on the clinical uses of SPECT/CT. *Eur J Nucl Med Mol Imaging*. 2010;37(10):1959-1985.
83. McAfee JG, Samin A. In-111 labeled leukocytes: A review of problems in image interpretation. *Radiology*. 1985;155(1):221-229.

84. Palestro CJ, Love C, Bhargava KK. Labeled leukocyte imaging: Current status and future directions. *Q J Nucl Med Mol Imaging*. 2009;53(1):105-123.
85. Schäfer E, Dummer R, Eilles C, et al. Imaging pattern of radiolabelled lymphokine-activated killer cells in patients with metastatic malignant melanoma. *Eur J Nucl Med*. 1991;18(2):106-110.
86. De Vries EFJ, Roca M, Jamar F, Israel O, Signore A. Guidelines for the labelling of leucocytes with 99mTc-HMPAO. *Eur J Nucl Med Mol Imaging*. 2010;37(4):842-848.
87. Roca M, De Vries EFJ, Jamar F, Israel O, Signore A. Guidelines for the labelling of leucocytes with 111In-oxine. *Eur J Nucl Med Mol Imaging*. 2010;37(4):835-841.
88. Srinivas M, Aarntzen EHJG, Bulte JWM, et al. Imaging of cellular therapies. *Adv Drug Deliv Rev*. 2010;62(11):1080-1093.
89. Dhawan RT, Peters AM. Withdrawal of indium-111: Implications for white-cell imaging. The nuclear medicine community must act. *Nucl Med Commun*. 2014;35(8):789-791.
90. Aarntzen EHJG, Srinivas M, Bonetto F, et al. Targeting of 111in-labeled dendritic cell human vaccines improved by reducing number of cells. *Clin Cancer Res*. 2013;19(6):1525-1533.
91. Morse MA, Coleman RE, Akabani G, Niehaus N, Coleman D, Lyerly HK. Migration of human dendritic cells after injection in patients with metastatic malignancies. *Cancer Res*. 1999;59(1):56-58.
92. Fisher B, Packard BS, Read EJ, et al. Tumor localization of adoptively transferred indium-111 labeled tumor infiltrating lymphocytes in patients with metastatic melanoma. *J Clin Oncol*. 1989;7(2):250-261.
93. Pockaj BA, Sherry RM, Wei JP, et al. Localization of 111Indium-labeled tumor infiltrating lymphocytes to tumor in patients receiving adoptive immunotherapy. Augmentation with cyclophosphamide and correlation with response. *Cancer*. 1994;73(6):1731-1737.
94. Stanton SE, Eary JF, Marzbani EA, et al. Concurrent SPECT/PET-CT imaging as a method for tracking adoptively transferred T-cells in vivo. *J Immunother Cancer*. 2016;4(1):27.

95. Hege KM, Bergsland EK, Fisher GA, et al. Safety, tumor trafficking and immunogenicity of chimeric antigen receptor (CAR)-T cells specific for TAG-72 in colorectal cancer. *J Immunother Cancer*. 2017;5(1):22.
96. Ritchie DS, Neeson PJ, Khot A, et al. Persistence and efficacy of second generation CAR T Cell against the LeY Antigen in acute myeloid leukemia. *Mol Ther*. 2013;21(11):2122-2129.
97. Aicher A, Brenner W, Zuhayra M, et al. Assessment of the tissue distribution of transplanted human endothelial progenitor cells by radioactive labeling. *Circulation*. 2003;107(16):2134-2139.
98. Chin BB, Nakamoto Y, Bulte JWM, Pittenger MF, Wahl R, Kraitchman DL. In oxine labelled mesenchymal stem cell spect after intravenous administration in myocardial infarction. *Nucl Med Commun*. 2003;24(11):1149-1154.
99. Brenner W, Aicher A, Eckey T, et al. 111In-labeled CD34+ hematopoietic progenitor cells in a rat myocardial infarction model. *J Nucl Med*. 2004;45(3):512-518.
100. Alan R. Penheiter, Stephen J. Russell, Stephanie K. Carlson. The Sodium Iodide Symporter (NIS) as an Imaging Reporter for Gene, Viral, and Cell-based Therapies. *Curr Gene Ther*. 2012;12(1):33-47.
101. Sharif-Paghaleh E, Sunassee K, Tavaré R, et al. In vivo SPECT reporter gene imaging of regulatory T cells. *PLoS One*. 2011.
102. Jacob J, Nadkarni S, Volpe A, et al. Spatiotemporal in vivo tracking of polyclonal human regulatory T cells (Tregs) reveals a role for innate immune cells in Treg transplant recruitment. *Mol Ther - Methods Clin Dev*. 2021;20:324-336.
103. Volpe A, Lang C, Lim L, et al. Spatiotemporal PET Imaging Reveals Differences in CAR-T Tumor Retention in Triple-Negative Breast Cancer Models. *Mol Ther*. 2020;28(10):2271-2285.
104. Jin Y, Kong H, Stodilka RZ, et al. Determining the minimum number of detectable cardiac-transplanted 111In-tropolone-labelled bone-marrow-derived mesenchymal stem cells by SPECT. *Phys Med Biol*. 2005.
105. Li X, Hacker M. Molecular imaging in stem cell-based therapies of cardiac diseases. *Adv Drug Deliv Rev*. 2017;120:71-88.

106. Madsen MT. Recent advances in SPECT imaging. *J Nucl Med*. 2007;48(4):661-673.
107. Dickson J, Ross J, Vöö S. Quantitative SPECT: the time is now. *EJNMMI Phys*. 2019.
108. Hawrylak N, Ghosh P, Broadus J, Schlueter C, Greenough WT, Lauterbur PC. Nuclear Magnetic Resonance (NMR) Imaging of Iron Oxide-Labeled Neural Transplants. *Exp Neurol*. 1993;121(2):181-192.
109. Norman AB, Thomas SR, Pratt RG, Lu SY, Norgren RB. Magnetic resonance imaging of neural transplants in rat brain using a superparamagnetic contrast agent. *Brain Res*. 1992;594(0006-8993 (Print) LA-eng PT-Journal Article RN-0 (Contrast Media) RN-0 (Ferric Compounds) RN-0 (Wheat Germ Agglutinins) RN-1317-54-0 (ferrite) SB-IM):279-283.
110. Stark DD, Weissleder R, Elizondo G, et al. Superparamagnetic iron oxide: clinical application as a contrast agent for MR imaging of the liver. *Radiology*. 1988;168(2):297-301.
111. Weissleder R, Elizondo G, Wittenberg J, Lee AS, Josephson L, Brady TJ. Ultrasmall superparamagnetic iron oxide: An intravenous contrast agent for assessing lymph nodes with MR imaging. *Radiology*. 1990;175(2):494-498.
112. Bulte JWM. In vivo MRI cell tracking: Clinical studies. *Am J Roentgenol*. 2009;193(2):314-325.
113. Zhu J, Zhou L, XingWu F. Tracking Neural Stem Cells in Patients with Brain Trauma. *N Engl J Med*. 2006;355(22):2376-2378.
114. De Vries IJM, Lesterhuis WJ, Barentsz JO, et al. Magnetic resonance tracking of dendritic cells in melanoma patients for monitoring of cellular therapy. *Nat Biotechnol*. 2005;23(11):1407-1413.
115. Gutova M, Frank JA, D'Apuzzo M, et al. Magnetic Resonance Imaging Tracking of Ferumoxytol-Labeled Human Neural Stem Cells: Studies Leading to Clinical Use. *Stem Cells Transl Med*. 2013.
116. Stirrat CG, Alam SR, MacGillivray TJ, et al. Ferumoxytol-enhanced magnetic resonance imaging assessing inflammation after myocardial infarction. *Heart*. 2017;103(19):1528-1535.

117. Callera F, De Melo CMTP. Magnetic resonance tracking of magnetically labeled autologous bone marrow CD34+ cells transplanted into the spinal cord via lumbar puncture technique in patients with chronic spinal cord injury: CD34+ cells' migration into the injured site. *Stem Cells Dev*. 2007;16(3):461-466.
118. Richards JMJ, Shaw CA, Lang NN, et al. In vivo mononuclear cell tracking using superparamagnetic particles of iron oxide feasibility and safety in humans. *Circ Cardiovasc Imaging*. 2012.
119. Verdijk P, Scheenen TWJ, Lesterhuis WJ, et al. Sensitivity of magnetic resonance imaging of dendritic cells for in vivo tracking of cellular cancer vaccines. *Int J Cancer*. 2007.
120. Khurana A, Nejadnik H, Chapelin F, et al. Ferumoxytol: A new, clinically applicable label for stem-cell tracking in arthritic joints with MRI. *Nanomedicine*. 2013;8(12):1969-1983.
121. Yin Y, Zhou X, Guan X, Liu Y, Jiang C Bin, Liu J. In Vivo tracking of human adipose-derived stem cells labeled with ferumoxytol in rats with middle cerebral artery occlusion by magnetic resonance imaging. *Neural Regen Res*. 2015;10(6):909-915.
122. Castaneda RT, Khurana A, Khan R, Daldrup-Link HE. Labeling stem cells with ferumoxytol, an FDA-approved iron oxide nanoparticle. *J Vis Exp*. 2011;(57).
123. Thu MS, Bryant LH, Coppola T, et al. Self-assembling nanocomplexes by combining ferumoxytol, heparin and protamine for cell tracking by magnetic resonance imaging. *Nat Med*. 2012;18(3):463-467.
124. Jin SM, Oh SH, Oh BJ, et al. Feasibility of islet magnetic resonance imaging using ferumoxytol in intraportal islet transplantation. *Biomaterials*. 2015;52(1):272-280.
125. de Vocht N, Reekmans K, Bergwerf I, et al. Multimodal imaging of stem cell implantation in the central nervous system of mice. *J Vis Exp*. 2012;(64).
126. Shen D, Liu D, Cao Z, Acton PD, Zhou R. Coregistration of magnetic resonance and single photon emission computed tomography images for noninvasive localization of stem cells grafted in the infarcted rat myocardium. *Mol Imaging Biol*. 2007.

127. Hoehn M, Küstermann E, Blunk J, et al. Monitoring of implanted stem cell migration in vivo: A highly resolved in vivo magnetic resonance imaging investigation of experimental stroke in rat. *Proc Natl Acad Sci U S A*. 2002.
128. Stroh A, Faber C, Neuberger T, et al. In vivo detection limits of magnetically labeled embryonic stem cells in the rat brain using high-field (17.6 T) magnetic resonance imaging. *Neuroimage*. 2005.
129. Shapiro EM, Sharer K, Skrtic S, Koretsky AP. In vivo detection of single cells by MRI. *Magn Reson Med*. 2006;55(2):242-249.
130. Heyn C, Ronald JA, Mackenzie LT, et al. In vivo magnetic resonance imaging of single cells in mouse brain with optical validation. *Magn Reson Med*. 2006;55(1):23-29.
131. Weissleder R, Nahrendorf M, Pittet MJ. Imaging macrophages with nanoparticles. *Nat Mater*. 2014;13(2):125-138.
132. Kim JA, Åberg C, Salvati A, Dawson KA. Role of cell cycle on the cellular uptake and dilution of nanoparticles in a cell population. *Nat Nanotechnol*. 2011;7(1):62-68.
133. Yao Y, Zang Y, Qu J, Tang M, Zhang T. The toxicity of metallic nanoparticles on liver: The subcellular damages, mechanisms, and outcomes. *Int J Nanomedicine*. 2019;14:8787-8804.
134. Chapelin F, Capitini CM, Ahrens ET. Fluorine-19 MRI for detection and quantification of immune cell therapy for cancer. *J Immunother Cancer*. 2018.
135. Ahrens ET, Helfer BM, O'Hanlon CF, Schirda C. Clinical cell therapy imaging using a perfluorocarbon tracer and fluorine-19 MRI. *Magn Reson Med*. 2014.
136. Gaudet JM, Ribot EJ, Chen Y, Gilbert KM, Foster PJ. Tracking the fate of stem cell implants with fluorine-19 MRI. *PLoS One*. 2015.
137. Fink C, Gaudet JM, Fox MS, et al. 19F-perfluorocarbon-labeled human peripheral blood mononuclear cells can be detected in vivo using clinical MRI parameters in a therapeutic cell setting. *Sci Rep*. 2018;8(1).
138. Boehm-Sturm P, Aswendt M, Minassian A, et al. A multi-modality platform to image stem cell graft survival in the naïve and stroke-damaged mouse brain. *Biomaterials*. 2014;35(7):2218-2226.

139. Koshkina O, Lajoinie G, Baldelli Bombelli F, et al. Multicore Liquid Perfluorocarbon-Loaded Multimodal Nanoparticles for Stable Ultrasound and 19 F MRI Applied to In Vivo Cell Tracking. *Adv Funct Mater*. 2019;29(19).
140. Constantinides C, Maguire M, McNeill E, et al. Fast, quantitative, murine cardiac19F MRI/ MRS of PFCE-labeled progenitor stem cells and macrophages at 9.4T. *PLoS One*. 2018;13(1).
141. Wu L, Liu F, Liu S, Xu X, Liu Z, Sun X. Perfluorocarbons-based19f magnetic resonance imaging in biomedicine. *Int J Nanomedicine*. 2020;15:7377-7395.
142. Bachert P. Pharmacokinetics using fluorine NMR in vivo. *Prog Nucl Magn Reson Spectrosc*. 1998.
143. Ahrens ET, Flores R, Xu H, Morel PA. In vivo imaging platform for tracking immunotherapeutic cells. *Nat Biotechnol*. 2005.
144. Gleich B, Weizenecker J. Tomographic imaging using the nonlinear response of magnetic particles. *Nature*. 2005.
145. Bulte JWM, Walczak P, Gleich B, et al. MPI cell tracking: what can we learn from MRI? In: *Medical Imaging 2011: Biomedical Applications in Molecular, Structural, and Functional Imaging*. ; 2011.
146. Bulte JWM. Superparamagnetic iron oxides as MPI tracers: A primer and review of early applications. *Adv Drug Deliv Rev*. 2019.
147. Zheng B, Yu E, Orendorff R, et al. Seeing SPIOs Directly In Vivo with Magnetic Particle Imaging. *Mol Imaging Biol*. 2017;19(3):385-390.
148. Wu XLC, Zhang XY, Steinberg XG, et al. A review of magnetic particle imaging and perspectives on neuroimaging. *Am J Neuroradiol*. 2019;40(2):206-212.
149. Saritas EU, Goodwill PW, Croft LR, et al. Magnetic particle imaging (MPI) for NMR and MRI researchers. *J Magn Reson*. 2013;229:116-126.
150. Graeser M, Thieben F, Szwargulski P, et al. Human-sized magnetic particle imaging for brain applications. *Nat Commun*. 2019;10(1).
151. Ludewig P, Gdaniec N, Sedlacik J, et al. Magnetic Particle Imaging for Real-Time Perfusion Imaging in Acute Stroke. *ACS Nano*. 2017.
152. Zhou XY, Jeffris KE, Yu EY, et al. First in vivo magnetic particle imaging of lung perfusion in rats. *Phys Med Biol*. 2017;62(9):3510-3522.

153. Arami H, Teeman E, Troksa A, et al. Tomographic magnetic particle imaging of cancer targeted nanoparticles. *Nanoscale*. 2017;9(47):18723-18730.
154. Tomitaka A, Arami H, Gandhi S, Krishnan KM. Lactoferrin conjugated iron oxide nanoparticles for targeting brain glioma cells in magnetic particle imaging. *Nanoscale*. 2015;7(40):16890-16898.
155. Finas D, Baumann K, Sydow L, et al. Lymphatic tissue and superparamagnetic nanoparticles - Magnetic particle imaging for detection and distribution in a breast cancer model. *Biomed Tech*. 2013;58(SUPPL.1).
156. Lüdtke-Buzug K, Rapoport DH, Schneider D. Characterization of iron-oxide loaded adult stem cells for magnetic particle imaging in targeted cancer therapy. In: *AIP Conference Proceedings*. Vol 1311. ; 2010:244-248.
157. Zheng B, Von See MP, Yu E, et al. Quantitative magnetic particle imaging monitors the transplantation, biodistribution, and clearance of stem cells in vivo. *Theranostics*. 2016;6(3):291-301.
158. Zheng B, Vazin T, Goodwill PW, et al. Magnetic particle imaging tracks the long-term fate of in vivo neural cell implants with high image contrast. *Sci Rep*. 2015;5.
159. Nejadnik H, Pandit P, Lenkov O, Lahiji AP, Yerneni K, Daldrup-Link HE. Ferumoxytol Can Be Used for Quantitative Magnetic Particle Imaging of Transplanted Stem Cells. *Mol Imaging Biol*. 2019.
160. Sehl OC, Makela A V., Hamilton AM, Foster PJ. Trimodal Cell Tracking In Vivo: Combining Iron- and Fluorine-Based Magnetic Resonance Imaging with Magnetic Particle Imaging to Monitor the Delivery of Mesenchymal Stem Cells and the Ensuing Inflammation. *Tomogr (Ann Arbor, Mich)*. 2019.
161. Song G, Chen M, Zhang Y, et al. Janus Iron Oxides @ Semiconducting Polymer Nanoparticle Tracer for Cell Tracking by Magnetic Particle Imaging. *Nano Lett*. 2018;18(1):182-189.
162. Piraner DI, Farhadi A, Davis HC, et al. Going Deeper: Biomolecular Tools for Acoustic and Magnetic Imaging and Control of Cellular Function. *Biochemistry*. 2017;56(39):5202-5209.
163. Maresca D, Lakshmanan A, Abedi M, et al. Biomolecular ultrasound and sonogenetics. *Annu Rev Chem Biomol Eng*. 2018;9:229-252.

164. Sherar MD, Noss MB, Foster FS. Ultrasound backscatter microscopy images the internal structure of living tumour spheroids. *Nature*. 1987;330(6147):493-495.
165. Bérubé LR, Harasiewicz K, Foster FS, Dobrowsky E, Sherar MD, Rauth AM. Use of a high frequency ultrasound microscope to image the action of 2-nitroimidazoles in multicellular spheroids. *Br J Cancer*. 1992;65(5):633-640.
166. Czarnota GJ, Kolios MC, Vaziri H, et al. Ultrasonic biomicroscopy of viable, dead and apoptotic cells. *Ultrasound Med Biol*. 1997;23(6):961-965.
167. Tunis AS, Czarnota GJ, Giles A, Sherar MD, Hunt JW, Kolios MC. Monitoring structural changes in cells with high-frequency ultrasound signal statistics. *Ultrasound Med Biol*. 2005;31(8):1041-1049.
168. Chen F, Ma M, Wang J, et al. Exosome-like silica nanoparticles: A novel ultrasound contrast agent for stem cell imaging. *Nanoscale*. 2017.
169. Lemaster JE, Chen F, Kim T, Hariri A, Jokerst J V. Development of a Trimodal Contrast Agent for Acoustic and Magnetic Particle Imaging of Stem Cells. *ACS Appl Nano Mater*. 2018.
170. Jokerst J V., Khademi C, Gambhir SS. Intracellular aggregation of multimodal silica nanoparticles for ultrasound-guided stem cell implantation. *Sci Transl Med*. 2013.
171. Foroutan F, Jokerst J V., Gambhir SS, Vermesh O, Kim HW, Knowles JC. Sol-gel synthesis and electrospraying of biodegradable (P2O5)55-(CaO)30-(Na2O)15glass nanospheres as a transient contrast agent for ultrasound stem cell imaging. *ACS Nano*. 2015.
172. Errico C, Pierre J, Pezet S, et al. Ultrafast ultrasound localization microscopy for deep super-resolution vascular imaging. *Nature*. 2015;527(7579):499-502.
173. Pfeifer F. Distribution, formation and regulation of gas vesicles. *Nat Rev Microbiol*. 2012;10(10):705-715.
174. Shapiro MG, Goodwill PW, Neogy A, et al. Biogenic gas nanostructures as ultrasonic molecular reporters. *Nat Nanotechnol*. 2014;9(4):311-316.
175. Bourdeau RW, Lee-Gosselin A, Lakshmanan A, et al. Acoustic reporter genes for noninvasive imaging of microorganisms in mammalian hosts. *Nature*. 2018;553(7686):86-90.

176. Farhadi A, Ho GH, Sawyer DP, Bourdeau RW, Shapiro MG. Ultrasound imaging of gene expression in mammalian cells. *Science (80-)*. 2019;365(6460):1469-1475.
177. Wang L V., Yao J. A practical guide to photoacoustic tomography in the life sciences. *Nat Methods*. 2016.
178. Jokerst J V., Thangaraj M, Kempen PJ, Sinclair R, Gambhir SS. Photoacoustic imaging of mesenchymal stem cells in living mice via silica-coated gold nanorods. *ACS Nano*. 2012;6(7):5920-5930.
179. Zhang YS, Wang Y, Wang L, et al. Labeling human mesenchymal stem cells with gold nanocages for in vitro and in vivo tracking by two-photon microscopy and photoacoustic microscopy. *Theranostics*. 2013.
180. Yang Y, Fryer C, Sharkey J, et al. Perylene Diimide Nanoprobes for in Vivo Tracking of Mesenchymal Stromal Cells Using Photoacoustic Imaging. *ACS Appl Mater Interfaces*. 2020.
181. Strohm EM, Moore MJ, Kolios MC. Single Cell Photoacoustic Microscopy: A Review. *IEEE J Sel Top Quantum Electron*. 2016.
182. Xing Y, Zhao J, Conti PS, Chen K. Radiolabeled nanoparticles for multimodality tumor imaging. *Theranostics*. 2014;4(3):290-306.

Chapter 2

Positron Emission Tomography – A powerful tool for *in vivo* cell tracking

This chapter contains material that has been written up as a review and was accepted for publication:

Lecherman LM, Lau D, Attili B, Aloj L and Gallagher FA. *In Vivo* Cell Tracking in Oncology using PET: Opportunities and Challenges for Clinical Translation. *Cancers*. 2021;13(16):4042

2.1 Authorship and contributions

This chapter contains material from a review article in submission. I confirm that I am the first author for the publication having undertaken all of the literature review, outline and structure of the manuscript including figure and table design unless specified otherwise in the text and figure caption. Sections 2.5 and 2.6 contain contributions to the writing done by Dr Doreen Lau, Dr Bala Attili and Dr Luigi Aloj with editing and additions from my side.

2.2 Introduction

As mentioned in the previous chapter, *in vivo* tracking and imaging of cells can provide much needed information and help improving the accuracy and efficacy of cell therapies. The ideal monitoring tool is an imaging modality that allows whole-body, non-invasive, quantitative and longitudinal visualization of processes on a molecular level.

Positron Emission Tomography (PET) is a powerful non-invasive imaging technique that can also be utilised for spatial and longitudinal tracking of different (therapeutic) cell types and has become increasingly available. PET presents a quantitative method with limitless depth of penetration and despite the fact that it implies ionizing radiation PET offers superior sensitivity for cell tracking compared to other imaging modalities [1],[2]. PET provides the most promising pathway towards cell tracking *in vivo* and at the whole-body level [3],[4], allows the administration and detection of picomolar tracer concentrations and is particularly amenable to clinical translation. The development of the dual-modality imaging PET/MRI system helped to improve spatial resolution issues associated with PET [5]. Although PET has been utilised clinically for over 30 years, the developments of new PET radiotracers have vastly expanded the use of PET to detect and longitudinally track therapeutic cells *in vivo*. Additionally, recent developments in the total-body PET scanner technology offer the potential of sensitivity to increase by up to 40-fold for the whole body and up to 4-5 fold for a single organ [6] and thus offer a promising and highly sensitive approach to image labelled cells. The potential for single cell tracking using PET was recently demonstrated by Jung et al who showed that PET can function as a ‘cellular global positioning system’ that can detect a single cell over time in a mouse [7]. The authors used cells labelled with mesoporous silica nanoparticles (MSNs) bearing a large concentration of gallium-68 (58 Bq per cell) and were able to show that cells travelled at an average velocity of 50 $mm\,s^{-1}$ and reached the lungs 2-3 seconds after tail-vein injection into the mice.

The different and detailed cell labelling approaches were previously depicted in Chapter 1 (**Fig. 1.5**). This chapter briefly explains the PET technology and focuses on the three above mentioned cell labelling techniques using PET radiotracers for cell imaging in preclinical models as well as in first clinical settings. The different cell labelling approaches will be further elaborated in each section in the text. One of the beauties of PET is the plethora of available metabolic tracers and the possibility to image immune cells based on their metabolic activity which will, however, not be covered here**.**

2.3 Principles of Positron Emission Tomography (PET)

Positron emission tomography (PET) is a non-invasive imaging technique which traces physiological and pathophysiological processes at a molecular level. PET is based on the detection of two annihilation photons that are produced after the positron emission from a decaying radionuclide. Once an emitted positron interacts with a nearby electron it undergoes annihilation, releasing energy in the form of two gamma ray photons emitted in opposite directions with an approximate angle of ~ 180° to each other and a distinct energy of 511 keV (**Fig. 2.1 A**). Before undergoing annihilation the emitted positron travels a finite distance within a tissue medium which is defined by the positron range, which varies with positron energy and is isotope-specific e.g. 0.6 mm for fluorine-18, 1.2 mm for zirconium-89, and 2.9 mm for gallium-68 [8].

PET provides molecular imaging of biological functions instead of anatomy whereby the detection of both annihilation photons in coincidence yields increased sensitivity over other forms of medical imaging. A PET scanner is constructed as a cylindrical assembly of block detectors in a ring structure for the detection of the annihilation 511 keV gamma rays, also known as coincidence detection (**Fig. 2.1 B**).

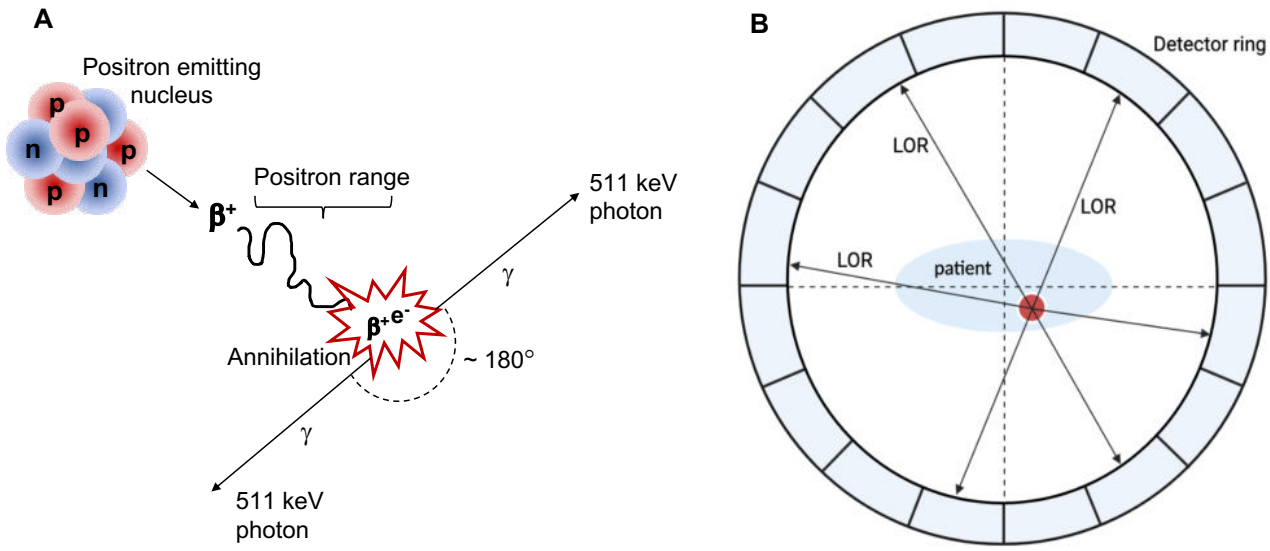

Figure 2.1 Schematic overview of (**A**) positron emission and subsequent annihilation; (**B**) Detector ring and scanner set-up with a possible line of response (LOR).

The sensitive volume inside the detector cylinder that a patient can occupy is called the field-of-view (FOV). The precise origin of the annihilation event can be localised along a so-called 'line of response' (LOR), however multiple coincidences generated by activation of more than two detectors within the same interval are not allowed as assigning LOR and would not be possible. The approximate location of the PET radionuclide can be determined with a spatial resolution in the millimetre range, which is heavily influenced by the respective positron range and energy of the positron typical for each radioisotope. To obtain clinically useful images and accurate quantitative information, effects like random and scattered coincidence and the interaction of photons within tissue in the body need to be corrected for in a process called attenuation correction.

PET/CT systems are combinations of stand-alone CT and PET scanners in one gantry with a shared patient bed. The x-ray CT scan provides anatomical images that, after some processing, can also be used for attenuation correction in PET. CT-based attenuation correction offers the significant advantage that the CT data has much lower statistical noise and can be acquired in a shorter time than a standard PET transmission scan. Similarly combined PET/MRI offers combining structural information with functional image from PET and better soft tissue contrast over CT, yet it has many technical challenges due to the interference between the modalities. An additional advantage of MRI is that it offers motion correction in reconstruction of the anatomical information, however one of the most challenging issues of hybrid PET/MRI systems is attenuation correction which is an ongoing

research topic. MR based attenuation correction (MRAC) have been extensively pursued, especially for brain imaging over the past years but remains challenging. MR imaging provides information on proton density and MR relaxation rates. It does not provide direct information on electron density needed by PET attenuation correction. Bone has near-zero signal in conventional MR images due to low spin density and a rapid T2 relaxation rate while it causes the most photon attenuation per unit volume. On the other hand, air space appears similarly as the bone in conventional MR images, while it does not cause photon attenuation. Therefore, the most difficult tasks of MRAC are to separate bone from other tissue and air, and assign correct linear attenuation coefficients accordingly. It has been demonstrated that improperly accounting for bone leads to large underestimation of PET signal, particularly in tissue near bone [9].

Over the past years, several approaches have been proposed for the attenuation correction of PET/MRI. There are two major categories of methods there are two major categories of methods to generate CT like images for PET/MRI attenuation correction. The first category consists of an atlas-based approach[10]. This typically relies on a precompiled atlas of paired MR and CT images and an algorithm to generate a pseudo-CT image from patient MR images. These pseudo-CTs are subsequently converted to PET attenuation maps through the same scaling operation used in PET/CT attenuation correction. The second category of MRAC consists of direct MR imaging using Dixon, ultra-short echo (UTE) or zero echo time (ZTE) without using complex image registration and processing procedures [11].

PET is still suboptimal from a physics point of view: only a small amount of the emitted radiation from the patient is detected by the imaging system, even the best commercial systems have about 1% sensitivity. The idea of total-body PET has already been proposed 30 years ago. The concept is to surround the patient with much more detectors in the axial direction to increase the sensitivity with a large factor which also entails certain challenges vastly related to engineering development amongst others and is the subject of several ongoing research studies. First in human studies have been performed on the EXPLORER total-body PET scanner with the possibility to image [^{18}F]-FDG distribution for up to 10 h post-injection [12]. The first total-body PET scanner was approved for clinical use by the FDA in early 2019.

2.4 Cell imaging with *ex vivo* labelled cells

In a direct cell labelling approach the tracer is directly added to cells *ex vivo* followed by incubation for cellular uptake of the label before labelled cells are injected into recipients for subsequent imaging. Different strategies for cell labelling using this approach have been explored using PET (**Fig. 2.2**).

In a first in human study [^{18}F]FDG ([^{18}F], $t_{1/2}$ = 109.7 min), the most frequently used PET tracer for clinical routine work, has been used to follow the intracoronary delivery of bone marrow cells in patients after myocardial infarction [13] and with acute pancreatitis [14] and is deemed to be more sensitive than standalone [^{18}F]FDG in this setting given the high levels of [^{18}F]FDG uptake in some organs [15]. [^{18}F]FDG is taken up into the cell by endothelial glucose transporter and is converted to [^{18}F]FDG-6-phosphate. Unlike glucose, which is metabolized further, the phosphorylated [^{18}F]FDG cannot undergo further metabolism and is then trapped in the cell.

[^{18}F]FDG-labelled macrophage activated killer (MAK) cells were injected into ten patients with peritoneal relapse of epithelial ovarian carcinoma and have shown a reproducible pattern of *in vivo* biodistribution and trafficking to tumour sites up to 4 h post-injection whereby MAK cells initially accumulated in the lungs whereby clearance could be observed as early as one hour after injection [16]. In another notable preclinical study, parental NK-92 and genetically engineered NK-92-scFv(FRP5)-zeta cells labelled with [^{18}F]FDG demonstrated differential tumour uptake within a 2-h time frame whereby NK-92-scFv(FRP5)-zeta cells showed an increased uptake of radioactivity in HER2/neu-positive tumours contrary to NK-92 cells as confirmed by autoradiography and histopathology [17]. The theoretical detection limit of [^{18}F]FDG-labelled cancer cells was investigated by Fischer *et al.* and was found to be around 10^5 cells using clinical PET/CT [18].

Several other groups have labelled mesenchymal stem cells [19], hematopoietic stem cells [20], multipotent adult progenitor cells and neural stem cells [21] with [^{18}F]FDG to monitor their biodistribution in mice. Olasz *et al*. demonstrated the cell surface labelling of mouse bone marrow-derived dendritic cells (BMDC) with Fluorine-18 using N-succinimidyl-4-[^{18}F]fluorobenzoate ([^{18}F]SFB) which, commonly used as a prosthetic group, covalently binds to the lysine residues of cell surface proteins and was used to monitor the migration of BMDCs at four hours post injection [22]. Ma *et al*. developed hexadecyl-4-[^{18}F]-fluorobenzoate ([^{18}F]HFB), a long chain fluorinated benzoic acid ester that is absorbed into the lipophilic cell membrane and was used to label rat mesenchymal stem cells [23]. In

another study, [^{18}F]HFB was used in direct comparison to [^{18}F]FDG to label human circulating progenitor cells (hCPCs) and showed superior retention in cells over four hours compared to [^{18}F]FDG and seemed more reliable in assessing the distribution of HCPCs [24]. Simultaneous *in vivo* PET/MRI was used in a study where mouse mesenchymal stem cells (mMSCs) were labelled with iron oxide-based nanoparticles (Fe_3O_4@$Al(OH)_3$) that can bind [^{18}F]F^- ions and thus allow visualization and quantification with both PET and MRI [25]. While liver uptake of radiolabelled nanoparticles could be detected on both PET and MRI, the uptake of labelled mMSCs in lungs could only be observed with PET.

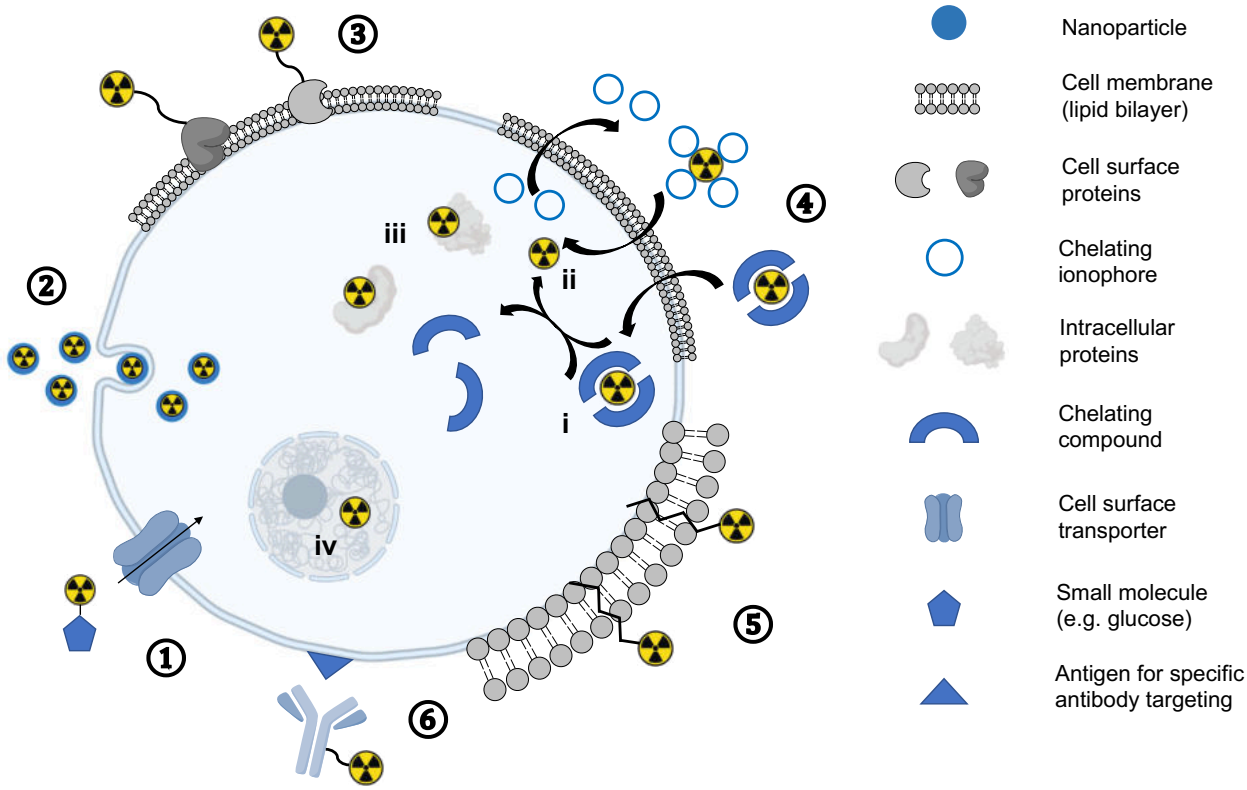

Figure 2.2. **Overview of different direct cell labelling methods**: ① Transporter mediated uptake (e.g. small molecules), ② endocytosis mediated uptake of nanoparticles, ③ cell surface protein labelling, ④ passive diffusion through the lipophilic cell membrane either as intact chelate inside the cell (**i**) or dissociating in the cytosol (**ii**) and association with intracellular proteins (**iii**) or cell organelles (**iv**), ⑤ insertion of ligands into the lipophilic membrane and ⑥ specific antigen targeting and subsequent internalization of labelled antibodies.

The more short-lived [^{11}C]-methyl iodide ([^{11}C], $t_{1/2}$ = 20.3 min) has been used to label murine natural killer (NK) cells to measure the short-term kinetics of cell delivery to the tumour and systemic distribution up to one hour post-injection in a fibrosarcoma model [26]. Differences in the tumour accumulation between ^{11}C-labelled activated and non-activated

cells as well the cellular retention in the tumour up to one hour post-injection were observed. Despite promising initial imaging results, the short half-lives of Carbon-11 and Fluorine-18 do not meet the requirements for longitudinal tracking of directly labelled cells over several days, given the usual timescale for cellular migration. A general disadvantage of metabolic tracers, is that they are taken up into cells by an active transporter and cellular retention and the labelling efficiency are heavily dependent on these functional processes which may vary between cells or within cells over time.

In an approach to use longer-lived PET isotopes, the conjugation of copper-64 ([^{64}Cu], $t_{1/2}$ = 12.7 h) to nanoparticles for subsequent cell labelling was investigated for the labelling of CD19-specific CAR T-cells using SPIONs [27] and also gold nanoparticles [28]. In a first in human study, CAR T-cells specific for the carbohydrate Lewis Y antigen were labelled *ex vivo* with novel ^{64}Cu-labeled SPIONs, facilitated with a transfecting agent, and reinfused into patients with solid tumours to investigate the distribution of labelled cells to various body organs and lesions within the first 3-5 days using a clinical hybrid PET/MRI approach [29]. The findings provided valuable insight into individual responses to therapy and the dynamic cell trafficking to tumour sites with extended persistence. Direct and intracellular cell labelling using antibodies was also investigated in conjunction with copper-64. [^{64}Cu]CuDOTA-KJ1-26 mAb was used to label chicken-ovalbumin-TCR transgenic TH1 cells in vitro [30]. This study examined the intracellular accumulation of the mAb-TCR complex which was further evaluated *in vivo* in a mouse model of OVA-induced acute airway delayed-type hypersensitivity reaction (DTHR) to detect cOVA-specific T-cell homing. [^{64}Cu]Cu-pyruvaldehyde-bis(*N*4-methylthiosemicarbazone), [^{64}Cu]Cu-PTSM), a commonly used PET perfusion tracer, has also been used in various settings to study the biodistribution of labelled cells in healthy mice [31]–[33]. The lipophilic [^{64}Cu]Cu-PTSM passively diffuses through the cell membrane and gets trapped upon reduction of copper inside the cell. However the rapid cellular efflux of copper-64 has shown to be a persistent problem [33]–[35] and imaging is possible for only up to few days maximum.

Since the need for high quality cell tracking is increasing with new applications in cell therapy, longer half-life tracers with more reliable labelling and cellular retention are required. Iodine-124 as a longer lived radioactive halide ([^{124}I], $t_{1/2}$ = 4.2 d) has also been suggested as another direct cell label. Hexadecyl-4-[^{124}I]-iodobenzoate ([^{124}I]-HIB) inserts into the lipophilic cell membrane similarly to [^{18}F]HFB and was used to label transplanted adipose-derived stem cells (ADSCs) whereby tracking to myocardial infarction was possible for 9 days [36]. ^{124}I-2′-fluoro-2′-deoxy-1-β-D-arabinofuranosyl-5-iodouracil ([^{124}I]FIAU), more

commonly used to indirectly label and image herpes simplex virus type 1-thymidine kinase (HSV1-tk) expressing cells, was investigated for *in vitro* labelling and *in vivo* tracking of human chronic myelogenous leukemia cells in direct comparison to [^{64}Cu]Cu-PTSM [32]. Despite of high labelling yields and radiolabel retention of [^{124}I]FIAU *in vitro*, the rapid and significant efflux *in vivo* of [^{124}I]FIAU at 24 hours makes it less suitable for longitudinal cell tracking *in vivo*. In an attempt to anchor iodine-124 to the cell surface for labelling the dual PET and fluorescent labelling reagent [^{124}I]-FIT-$(PhS)_2$Mal was used to label Jurkat cells on the cell surface via thiol bioconjugation which was confirmed by confocal microscopy [37]. Labelled cells showed very good cellular retention of iodine-124 over 7 days with an initial, rapid loss of ~25% of radioactivity that could also be confirmed on PET imaging at 4 hours and 24 hours post-injection of ^{124}I-labelled Jurkat cells into healthy NSG mice as indicated by the accumulation of radioactivity in the bladder followed by a main accumulation in the lungs and liver over 7 days.

Iodine-124 was also used to develop ^{124}I-labelled tannic acid gold core-shell nanoparticles ([^{124}I]-TA-Au@AuNPs) to label dendritic cells (DCs) to monitor their migration behaviour to lymphoid organs in mice [38]. This study also investigated the sensitivity of DC detection *in vivo* whereby different numbers of [^{124}I]-TA-Au@AuNP-labeled cells were subcutaneously injected to the dorsal sites of mice. As low as 1 × 10^2 cells could be detected on PET/CT (**Fig. 2.3**).

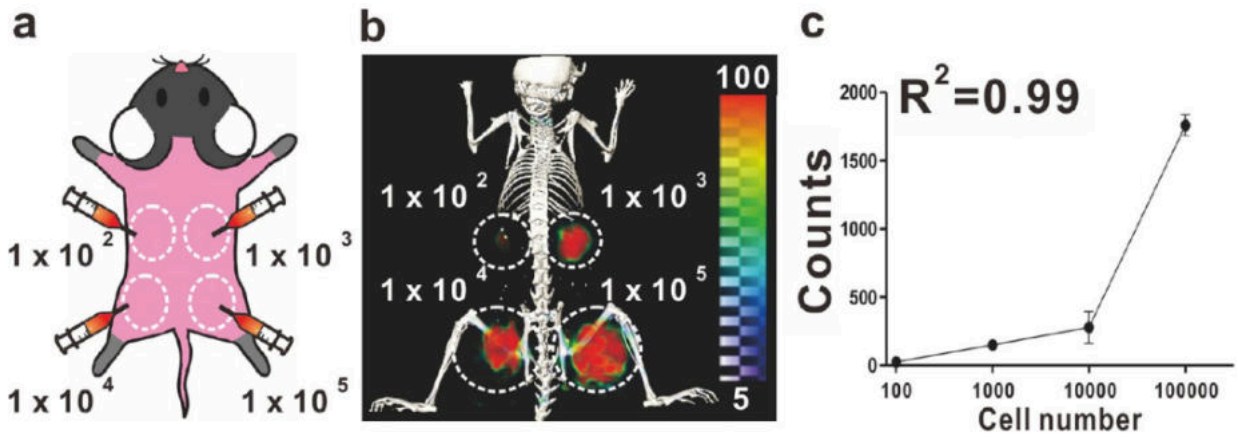

Figure 2.3. (**A, B**) Detection of ^{124}I-TA-Au@AuNP-labeled DCs subcutaneously injected at the indicated concentrations to the dorsal sites of mice; (**C**) Increase in PET signal linearly correlated with the number of injected cells. Figure copied from [38].

Another notable study has shown the labelling of transgenic $CD8^+$ T-cells specific for the ovalbumin peptide SIINFEKL using 5-^{124}I-iodo-2′-deoxyuridine ([^{124}I]IUdR) [39].

[^{124}I]IUdR is an analogue of thymidine, exclusively labels proliferating cells and gets incorporated into the DNA of cells. ^{124}I-labelled T-cells were adoptively transferred into mice carrying subcutaneous tumours of the ovalbumin-expressing malignant melanoma cell line B16-OVA and showed increased iodine-124 accumulation on PET/MRI whereby accumulation of iodine-124 was significantly higher in B16-OVA than in B16 tumours not expressing the OVA antigen after five days. The number of $CD8^+$ cells per gram tumour tissue increased steadily until day 5, when an average number of 3.3×10^6 cells per gram tissue was detected.

Increasing interest to find a more suitable radioisotope for antibody-based imaging has been the driving force behind the extensive use and success of zirconium-89 for Immuno-PET imaging within the last decade [40]–[44]. Zirconium-89 ([^{89}Zr], $t_{1/2} = 78.4$ h) has emerged fairly recently as a promising PET radioisotope for direct cell labelling. Analogous to [^{111}In]In-Oxine, zirconium-89 can form neutral tetrakis complexes with four oxinate (8-hydroxychinolin) ligands bound to Zirconium-89 ([^{89}Zr]Zr(oxinate)$_4$ or [^{89}Zr]Zr-Oxine, **Fig. 2.4**).

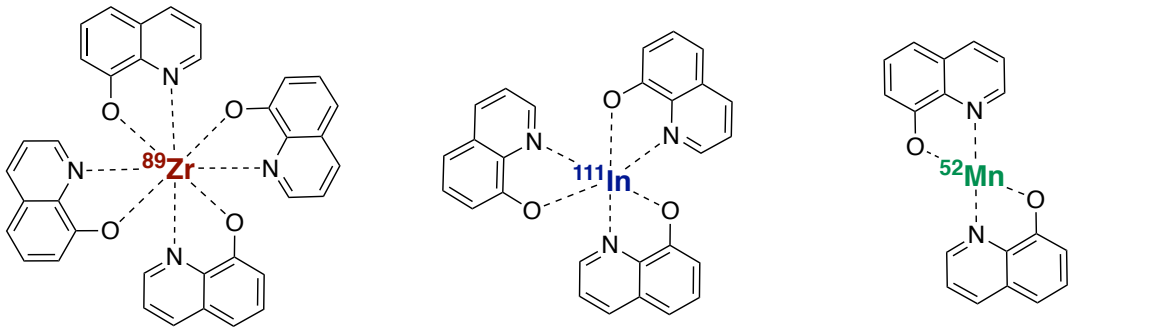

Figure 2.4. Molecular structures of different radio-ionophore complexes using Oxine (8-hydroxychinolin) as ligand.

Oxine acts as an ionophore that can transport radiometals across the cell membrane and dissociate as a meta-stable complex to deposit the radiometal inside the cell [45]. Zirconium does not have any biological role in the cell and body and can bind to nuclear and cytoplasmic proteins (**Fig. 2.2 iii, iv**) within the cell and is ideally suited for longitudinal cell imaging applications with its residualizing properties in cells [42]. In recent years, [^{89}Zr]Zr-Oxine has been evaluated in various preclinical studies *in vitro* and *in vivo* for cellular labelling and tracking of therapeutic cells which is summarised in **Table 2.1**. This approach

allows the imaging of labelled cells for 7 days post-injection given that cells are labelled with an appropriate starting activity that enables detection despite radioactive decay.

Table 2.1 Preclinical cell labelling and imaging studies using [^{89}Zr]Zr-Oxine.

Cell type	Purpose	Imaging [time]	Labelling efficiencies [%]	Reference
Dendritic cells (DCs), activated **cytotoxic T-cells** (CTLs), **natural killer cells** (NKs)	*In vitro* labelling study and *in vivo* tracking of CTLs to B16-OVA melanoma tumours	7 days	43.9 ± 17.4 (DCs) 13.0 ± 1.4 (naïve CTLs)	[46]
Mesenchymal Stem cells (MSCs) transduced to express TNF-related apoptosis inducing ligand (TRAIL)	*In vivo* tracking and biodistribution of MSC-TRAILs to mesothelioma tumours	7 days	43.0 ± 3.6	[47]
Natural killer cells	*In vivo* tracking and biodistribution in healthy rhesus macaques	7 days	n/a	[48], [49]
Vγ9Vδ2 subtype of human **γδ-T-cells**	*In vivo* tracking of γδ-T-cells in a xenograft model of breast cancer	7 days	46.6 ± 3.4	[50]
Bone marrow cells	*In vivo* tracking and quantification in a bone marrow transplantation model	7 days	26-30	[51]
Human CD^{19+} CAR T cells	Trafficking of intraventricular injected IL13Rα2-CAR T-cells to tumour sites	7 days	75 ± 17	[52]

Opposite to the intracellular trapping of zirconium-89 using [^{89}Zr]Zr-Oxine, cell surface labelling with zirconium-89 can also be achieved via chelation with desferrioxamine (DFO) which forms amide bonds with primary amine groups on the cell surface via bifunctional

linkers such as p-isothiocyanatobenzyl-linker (NCS). The stability of the [^{89}Zr]Zr-DFO complex is of pivotal importance since the release of zirconium-89 from the DFO chelator also entails the uptake of zirconium-89 not associated with cells by especially the bone in vivo. ^{89}Zr-labelled *p*-isothiocyanato-benzyl-desferrioxamine ([^{89}Zr]Zr-DFO-Bz-NCS) has been used to randomly label primary cell surface protein amines on human mesenchymal stem cells (hMSCs) and mouse dendritic cells amongst others [53] (**Fig. 2.5**) with very good retention of zirconium-89 over seven days post-labelling. In addition, hMSCs were both myocardically delivered and intravenously administered for biodistribution purposes in a an ischemia/reperfusion model over seven days whereby in both instances a distribution to lung, liver and bones could be observed. [^{89}Zr]Zr-DFO-Bz-NCS has also been used in another study to label CD19 targeting CAR expressing Jurkat cells and human CD19 targeting CAR T-cells that were intravenously injected into mouse xenograft models with bilateral CD19 positive and negative tumours and imaged over seven days. Cells were observed to have gradually migrated from the lung to the liver and spleen by day one, and remained stable in these sites until day seven. No increased radioactivity and cell homing into tumours could be observed over the seven days on imaging whereas immunohistochemical staining revealed some tumour infiltration of the human CD19^{+} CAR T-cells [54] highlighting the importance of existing sensitivity and detection limits encountered with imaging.

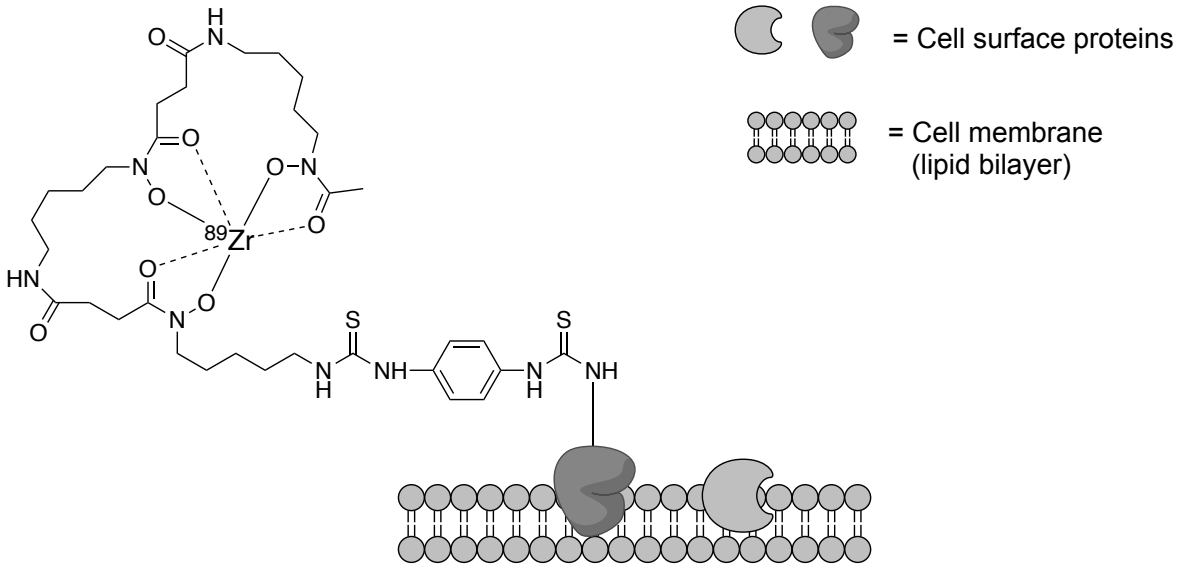

Figure 2.5 Cell surface labelling using [^{89}Zr]Zr-DFO-Bz-NCS via primary amines of cell surface proteins.

More recently, Manganese-52 ([^{52}Mn], $t_{1/2}$ = 5.6 days), was also used to synthesise the radio-ionophore [^{52}Mn]Mn(oxinate)$_2$ (**Fig. 2.4**) and tested for its cell labelling potential directly compared with [^{89}Zr]Zr-Oxine but high cellular efflux of the isotope limits its use for prolonged cell tracking [45]. Manganese just like copper are essential metabolic elements with several key roles in cells where the maintenance of homeostasis can lead to low intracellular retention of the radiometal making them less suitable for cellular labelling and imaging using the two PET isotopes copper-64 and manganese-52 at late time points. Consequently, Zirconium-89 has emerged as one of the most promising and suitable radiometals and isotopes for longitudinal cell imaging at later imaging timepoints using a direct cell labelling approach. In the future more alternative direct cell labelling approaches compared to the existing ones might emerge that build upon the existing knowledge and drawbacks of current approaches.

The use of a direct cell labelling approach requires certain considerations that need to be taken into account which can affect the cells itself and eventually impact on the imaging. It is of paramount importance that *in vitro* labelled cells maintain their function and viability post-labelling and also retain the label over an extended time, ideally throughout the imaging time frame. Efflux of the radiotracer or radioisotope *in vivo* can lead to non-specific signal and retention of free tracer in other tissues, thus decrease detectability of the cells of interest. The sensitivity of this approach is further compromised by the dilution of the signal from labelled cells due to cell proliferation and the detected radioactivity does not equal the number of originally labelled and injected cells. Furthermore, in the case of especially lipophilic compounds that enter the cell via passive diffusion dead cells cannot be differentiated from live cells as both populations are passively labelled, however label retention will heavily depend on viability, i.e. intactness of the cell membrane. Dead cells may release the radioactive label relatively soon after injection *in vivo* which creates non-specific signal and affects detection. In addition, only few of the PET tracer used for direct cell labelling as described in this section can be produced under GMP compliant conditions on an automated synthesis unit (e.g. [^{18}F]FDG) or with a rapid synthesis kit (e.g. [^{64}Cu]Cu-PTSM and more recently [^{89}Zr]Zr-Oxine). However, for tracer like [^{89}Zr]Zr-Oxine, [^{64}Cu]Cu-PTSM and [^{89}Zr]Zr-DFO no purification of the tracer is possible. Although direct cell labelling has been practised clinically for decades and this approach enables easier clinical translation compared to the manipulation of cells with gene reporters, the integration of a direct cell labelling approach into an established, automated manufacturing process of therapeutic cells (e.g. CAR T-cells) may be challenging as it may be regarded as additional

manipulation of cells. Therefore, the effect of the label on cells needs to be carefully investigated with this approach.

2.5 Cell imaging with *in vivo* labelled cells using reporter genes

In comparison to the assessment of cell migration using direct labelling (*ex vivo*), indirect (*in vivo*) cell labelling makes use of reporter genes that are inserted into cells by transfecting them with a vector that induces the expression of reporter genes. Genetically modified cells are administered to subjects prior to injecting the respective imaging probe specific for the reporter gene of interest. The first reporter systems were developed in the 1980s and were originally intended to measure and visualise enzyme activity which was initially dominated by fluorescent and bioluminescent reporter genes. Radionuclide-based reporter imaging blossomed in the mid 1990s. Different reporter genes have been developed since which can be imaged with a plethora of existing and new PET probes (**Fig. 2.6**) and will be discussed in more detail in the following sections of this chapter. Most cell tracking studies employing reporter gene systems have been undertaken in conjunction with the use of engineered CAR T-cells and are summarised in **Table 2.2**.

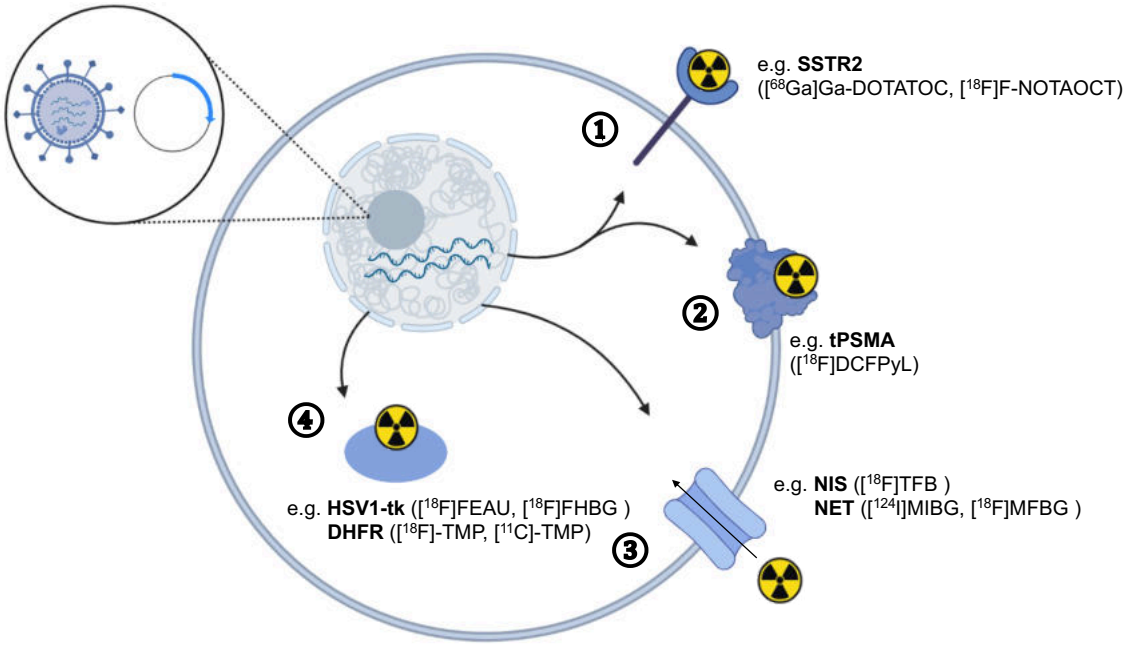

Figure 2.6 Overview of different indirect cell labelling strategies using reporter genes with respective PET tracers. Transfection of cells with vector plasmid leading to the transcription and expression of reporter genes in cells that can be specifically labelled via ① receptors ② cell surface enzymes ③ transporter ④ intracellular enzymes. The respective PET tracer specific for each reporter gene is indicated in brackets. Figure was partly created with BioRender.com

Table 2.2 Summary of the commonly used reporter genes for cell tracking in cancer models using engineered T-cells.

Gene reporter	Tracer	Cell type/model	Detection limit	Reference
NIS	[^{18}F]TFB	T4NT CAR T-cells	3×10^3 cells *in vitro*	[55]
tPSMA^{N9de}	[^{18}F]DCFPyL	CD19-tPSMA$^{(N9del)}$ CAR T-cells	2×10^3 cells *in vitro*	[56]
hSSTr2	[^{68}Ga]Ga-DOTATOC, [^{18}F]F-NOTAOCT	ICAM-1 specific CAR T-cells; Jurkat T-cells	4×10^6 cells/cm^3 *in vivo*	[57], [58]
HSV1-tk	[^{18}F]FEAU, [^{18}F]FHBG	IL-13 zetakine CAR T-cells, CD19 CAR T-cells, hPSMA specific CAR T cells	~3×10^5 cells *in vivo*	[59]–[62]
eDHFR	[^{18}F]-TMP, [^{11}C]-TMP	GD2$^+$ CAR T-cells	4×10^6 cells/cm^3 *in vitro*	[63], [64]
hNET	[^{124}I]MIBG, [^{18}F]MFBG	Comparative study with transduced T-cells	3-4×10^4 cells *in vivo*	[65]

Herpes Simplex Virus Thymidine Kinase (HSV-tk)

The reporter-gene technology was used for the first time in a human to image therapeutic cells in 2009. A patient with grade IV glioblastoma multiforme (GBM) was treated with genetically modified cytolytic T-cells (CTLs) expressing the herpex simplex virus-1-thymidine kinase (HSV1-tk) and imaged with 9-[4-[^{18}F]fluoro-3-(hydroxymethyl)butyl]guanine ([^{18}F]FHBG) [59]. HSV1-tk is an intracellular enzyme and its activity can be measured in mammalian cells using specific radiolabeled substrates of the enzyme, which are relatively poor substrates for mammalian thymidine kinases. Currently, these radiolabeled substrates are nucleoside analogs, which are transported into mammalian cells and are trapped there only if they are phosphorylated (similar to the phosphorylation and subsequent trapping of [^{18}F]FDG by endogenous hexokinase), resulting in a reporter-based, enzymatic amplification of the radioactive signal. Eissenberg *et al*. demonstrated in a first-in-man clinical study the use of T-cells that were transduced with a CD34-Herpex Simplex Virus-1-thymidine kinase retrovirus (CD34-TK75) [66]. Cells were infused into relapsed allogeneic stem cell transplant patients before being

administered [^{18}F]FHBG to specifically track the genetically modified T-cells over time. [^{18}F]FHBG has also been used to longitudinally monitor HSV1-tk reporter gene expression in chimeric antigen receptor (CAR) engineered CTLs in patients with recurrent glioma after infusion of CTLs [60] (**Figure 2.7**) where a significant increase in [^{18}F]FHBG total activity was observed representing the CTL trafficking to tumour. PET has also found successful application in the detection of TK^{+} tumour-specific T-cells in various preclinical studies [67]–[69]. This approach provides the possibility to control the activity of infused therapeutic cells providing a safety switch that can be activated using therapeutic concentrations of ganciclovir analogues when desired to stop the activity of the transferred adoptive cells which has been explored in preclinical models [70],[71]. This may be particularly relevant in the regulation and control of CAR-T cells [72].

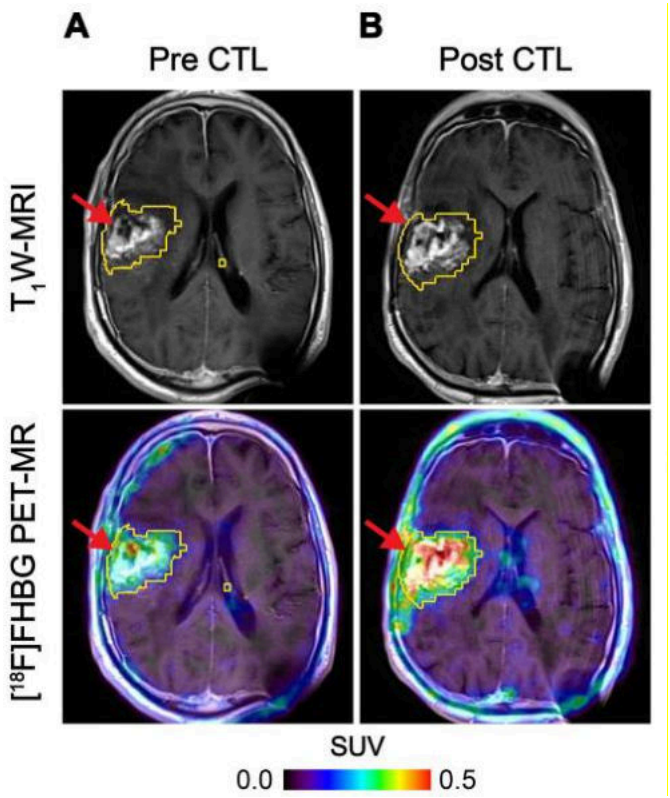

Figure 2.7 Tumour-associated CTL imaging with [^{18}F]FHBG. [^{18}F]FHBG-PET imaging was performed in a 66 year-old male with a recurrent right frontoparietal glioblastoma multiforme tumour (**A**) before and (**B**) one week after CTL infusions. Allogeneic CTLs and IL-2 were injected intratumorally (red arrows). Figure copyright from [60].

The sodium iodide symporter (NIS)

The human sodium iodine symporter (hNIS) is an additional reporter gene system that has been investigated for longitudinal cell tracking. The hNIS is physiologically expressed in thyroid, stomach and salivary glands and drives uptake of diagnostic and therapeutic radioactive isotopes of iodine and ^{99m}Tc-pertechnetate ([^{99m}Tc]TcO^{4-}) into these cells. An experimental hNIS substrate, [^{18}F]Tetrafluorborate ([^{18}F]TFB) [73],[74], has been utilised in humans to image patients with thyroid cancer [75], as well as to image tumours and metastases in preclinical models [76],[77]. hNIS is a good candidate reporter gene for human application as it is non-immunogenic, is not internalized, and is only functional in viable cells [73]. [^{18}F]TFB-PET has been used for quantifying differences in NIS-transduced CAR T-cell tumour retention in different triple-negative breast cancer models in mice with an impressive detection limit of ~ 3000 hNIS expressing cells [55]. Although physiological uptake in normal hNIS expressing tissues is of concern, most background uptake with these tracers will be located in the head and neck region which would allow application in many other parts of the body. Several groups are validating this concept and clinical trials are in preparation.

Somatostatin receptor 2 (SSTR-2)

Somatostatin receptor (SSTR) 2 is a G-protein-coupled cell surface receptor overexpressed in neuroendocrine tumours [78]. Several high affinity analogues of somatostatin have been developed as tracers and are routinely used for imaging SSTR2 overexpressing cancers in the clinical setting [79]. The most commonly utilised radiopharmaceutical for this purpose is the high affinity ligand [^{68}Ga]Ga-DOTATOC [80] that has been explored in combination with SSTR2 for reporter gene imaging [81] and has been used to visualise the biodistribution and tumour infiltration of SSTR2-expressing human T-cells in a Jurkat cell murine tumour model [57]. The uptake of [^{68}Ga]Ga-DOTATOC was shown to correlate with tumour size and percentage of SSTR2-expressing T-cells. The very high binding affinity, rapid diffusion and clearance of SSTR2 targeting PET tracers following injection in addition to the location of the target on the cell surface allows rapid high level target to background binding. Clinical imaging is usually performed 1 hour after injection which provides optimal targeting [82], as opposed to the 2-3 hours for HSV1-tk-based systems [59],[83]. The ^{18}F-labelled somatostatin analogue ^{18}F-NOTA-octreotide (NOTAOCT) has been used to image SSTR-expressing neuroendocrine tumours in a

clinical research study [84]. It has been successfully applied in mice to track Intracellular Adhesion Molecule 1 (ICAM-1) targeting CAR T-cells transduced with SSTR2 with PET/CT [85]. ^{18}F-NOTA-octreotide-PET showed specific uptake by SSTR2-transduced CAR T-cells. Peak CAR-T cell signal was seen approximately 4 days following the peak tumour burden and gradually decreased to background levels thereafter.

Prostate specific membrane antigen (PSMA)

PSMA is a cell-surface membrane glycoprotein that has been widely exploited for prostate cancer imaging. Novel ^{68}Ga- and ^{18}F-labelled small molecule PET ligands have been developed that can bind to PSMA with high selectivity and many of these are now in routine clinical application including the very recently FDA approved, radiofluorinated inhibitor of PSMA, 2-(3-{1-carboxy-5-[(6-[^{18}F]fluoro-pyridine-3-carbonyl)-amino]-pentyl}-ureido)-pentanedioic acid ([^{18}F]DCFPyL) [86]. Given the favourable pharmacokinetics and the very low expression in non-target organs, this system lends itself to applications for cell tracking. Anti-CD19 CAR T-cells expressing a N-terminal modified (N9del) PSMA, engineered to prevent internalisation and intracellular signalling which may affect cell physiology, have been tracked in a model of acute lymphoblastic leukaemia using [^{18}F]DCFPyL [56]. PET imaging of CD19-tPSMA$^{(N9del)}$ CAR T-cells showed very high sensitivity with a detection limit of ~2000 injected cells. Given the high sensitivity of this approach and the availability of therapeutic ligands of PSMA as safety switches, further development of this approach is appealing.

Norepinephrine transporter (NET)

The human NET (hNET) is a transmembrane protein is expressed in the central nervous system as well as in tumours derived from the neural crests and mediates the transport of norepinephrine, dopamine, and epinephrine across the cell membrane [87]. Radiolabelled derivatives of norepinephrine have been clinically available for many years to image phaeochromocytoma, paraganglioma and neuroblastoma. Metaiodobenzyl-guanidine (MIBG) labelled with iodine-131 or iodine-123 are routinely used for imaging and therapy of disease. The development of ^{18}F-labelled metafluorobenzyl-guanidine ([^{18}F]MFBG) as well as the use of ^{124}I-metaiodobenzylguanidine ([^{124}I]MIBG) have opened up the use of PET for this approach. hNET has also been used as a reporter gene to image transduced T-cells in mice with [^{124}I]MIBG and [^{18}F]MFBG with the latter offering the highest

sensitivity in the range of 3-4×10^4 T-cells at the site of injection [88]. However, little work has been undertaken to further develop this concept for clinical translation which can be ascribed to the fact that the endogenous NET expression in organs with sympathetic innervation with significant background signals generally obtained by NET imaging are not favourable for cell tracking [89].

E Coli dihydrofolate reductase (eDHFR)

More recently an approach making use of the bacterial enzyme dihydrofolate reductase derived from *E Coli* (eDHFR) as a reporter gene system for cell imaging has been described. The ligand is a derivative of the antibiotic trimethoprim (TMP) and is a highly specific small molecule inhibitor of the bacterial enzyme. TMP has previously been labelled with carbon-11 ([^{11}C]TMP) [63] and more recently with fluorine-18 ([^{18}F]TMP) [64] to study the trafficking of anti-GD2 CAR T cells in NSG mice bearing GD2$^+$ human osteosarcoma xenografts. Radiolabelled TMP has the potential to achieve low background in unmodified mammalian tissues and high retention in eDHFR engineered cells, providing high contrast imaging. A high sensitivity of detection for identifying tumour-infiltrating CD8 CAR T-cells with [^{18}F]TMP was found to be ~11,000 cells per mm^3. Little work has been undertaken on the additional validation and clinical translation of this concept. The eDHFR system does not provide a readily available safety switch and requires stable expression of a bacterial protein which is less desirable than the expression of a human protein.

In summary, cell tracking using reporter genes have shown great potential and can answer some questions that direct cell labelling and subsequent imaging can't provide, such as the viability of cells and multiple injections with short lived tracer are possible over an extended period of time without the compromise of signal dilution or radioactive decay over several days. The choice of reporter gene/target is based on multiple factors: a) availability of specific tracers, ideally suitable for PET and clinically approved; b) physiological expression in tumours or normal organs, ideally none or as low as possible; c) favourable dosimetry, to minimise concerns over radiation exposure and allow for measurement at multiple time points after administration of the tagged cells; d) limited or no biological effect deriving from expression of the transgene; e) alternatively, a transgene may be chosen due to its biological features and to serve as a therapeutic effector or target for its application. The potential for non-human reporter genes to be immunogenic must also be taken into consideration when addressing ideal system design since this may affect functionality and

survival of transduced cells once injected into humans. Due to safety concerns reporter gene systems are not easily translatable into routine clinical settings and require extensive regulatory scrutiny and validation. In addition, preparation of transduced cells for human injection comes with significant costs related to materials and dedicated facilities which significantly exceed those required for direct cell labelling procedures. However given the fact that CAR T-cells are transduced cells already this provides a compatible platform for the application of *in vivo* cell labelling via gene reporter. Nevertheless, quantification of cell numbers and determination of sensitivity is not straightforward as it cannot be specified how much activity/tracer is taken up *in vivo* into cells. In addition, reporter expression levels are cell type-dependent and their sensitivities need to be determined individually on existing instrumentation.

Another way of indirect cell imaging via non-reporter gene models can be achieved via the injection of imaging agents specific for metabolic targets or endogenous activation marker on cells *in vivo* such as 1-(2'-deoxy-2'-[^{18}F]fluoroarabinofuranosyl) cytosine ([^{18}F]FAC) [90], 2′-deoxy-2′-[^{18}F]fluoro-9-β-D-arabinofuranosylguanine ([^{18}F]F-AraG) to map and visualise immune cell activation but also 3'-deoxy-3'-[^{18}F]fluorothymidine ([^{18}F]FLT) and [^{18}F]FDG to image and analyse changes DNA synthesis and glycolysis, respectively. This will not be discussed here in further detail .

2.6 Cell imaging with labelled antibodies (Immuno-PET)

With the recent clinical successes of immunotherapies that alter the tumour immune microenvironment, the ability to noninvasively monitor the tumour immune response to therapy has become increasingly important. CD4 and CD8 expressing T-cells participate in the inflammation and cytotoxic attack within tumours and have shown to be important predictive indicators within the tumour microenvironment for the response to immune therapy [91]. Radiolabelled antibodies and antibody fragments can also be used to image therapeutic cells *in vivo*. This form of indirect labelling of cells has the advantage of high affinity and specificity of antibodies for their targets and established conjugation strategies and radiolabelling approaches for synthesis of antibody-based imaging probes [92]. The presence and density or number of therapeutic cells at the tumour sites after administration can be longitudinally tracked using repeated injection overcoming the problems with signal dilution following a single injection [93]. Cell surface markers such as CD3, CD4 and CD8, as well as activation or exhaustion markers such as OX40, ICOS and PD-1 can be detected non-invasively using radiolabelled antibodies to determine the functional status of the administered cells which is summarized in **Table 2.3.**

When using antibodies to target a specific cell population, it is important to validate their potential antagonistic or agonistic effects on cell function, viability and proliferation *in vivo* [22]. The presence of an intact Fc region in certain clones of antibodies has been shown to deplete target cells which can be overcome by engineering antibodies with cleaved Fc region or antibody fragments without the Fc receptor [92],[94]. Full-length, unmodified antibodies (~150 kDa) can exhibit slow clearance due to interaction with the neonatal Fc receptor and a prolonged serum half-life: imaging at earlier time points can therefore be problematic due to high background signal and non-specific tissue accumulation. To circumvent this, technologies based on enzymatic or genetic modifications of antibodies have been used to engineer smaller antibody derivatives (~25-100 kDa) such as monovalent F(ab') and divalent $F(ab')^2$ with just the antigen-binding regions linked by disulfide bonds and no Fc portion, single-chain variable fragments (scFv), minibodies, diabodies, and even smaller therapeutic proteins (< 6 KDa) such as affibodies and nanobodies (**Fig. 2.8**). Each of these antibody derivatives exhibit different pharmacokinetics and clearance properties. Smaller fragments with sizes below the renal filtration threshold (< 60 kDa) are generally excreted through the kidneys and have a rapid blood clearance with minimal background signal, whilst full-length and larger antibody derivatives are

cleared through the hepatobiliary route. However, there is often a trade-off between maximum target accumulation and minimal background signal. Larger molecules may accumulate non-specifically in solid tumours due to the enhanced permeability and retention (EPR) effects as tumours tend to have irregular blood vasculature and inefficient lymphatic drainage [95]. When designing antibody-based radiopharmaceuticals, it is thus very important to be able to distinguish non-specific tumour uptake from true target engagement.

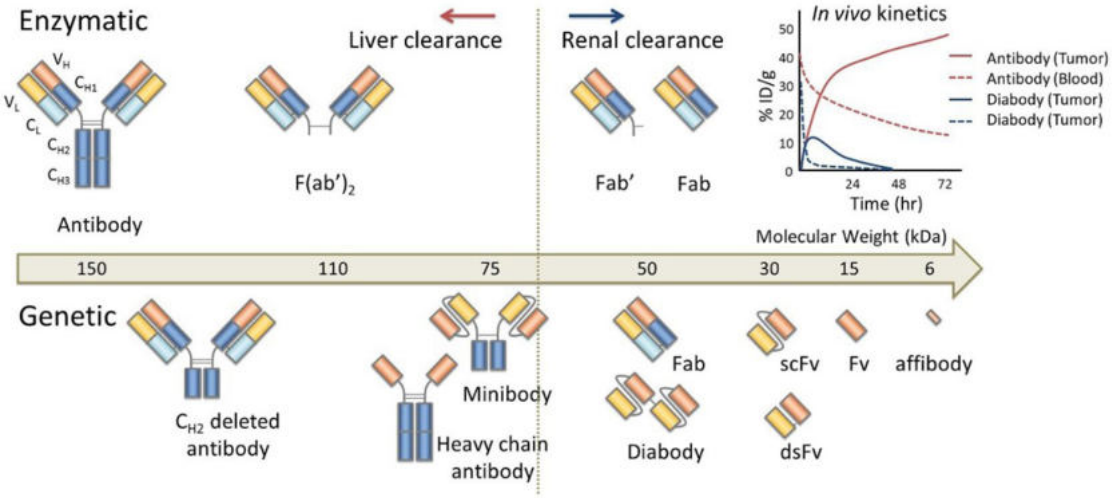

Figure 2.8 Different types of enzymatically (upper) and genetically (lower) produced antibody fragments. Small fragments that are smaller than 60 kD are generally excreted through the kidneys, resulting in rapid blood clearance. The tumour uptake is generally higher in long circulating antibodies and their fragments due to a superior input function. Figure copied from [94].

The choice of antibody conjugation strategy is equally as important when designing radiopharmaceuticals to detect therapeutic cells [96]. Ideally, all chemical modifications should not compromise the functionality and binding affinity of an antibody to its target, and the reactions should occur under mild conditions to minimize protein denaturation. Bifunctional chelators are often employed as a link between the antibody and a metal-based radionuclide [97]. A wide range of bifunctional chelators are available for conjugation to antibodies. Examples include diethylenetriamine pentaacetate (DTPA), tris(hydroxypyridinone) (THP) and DFO that can be radiolabelled under ambient temperature and mild acidic to neutral pH. The choice of radionuclide should ideally match the biological half-life ($t_{1/2}$) of the molecules. Short-lived radionuclides such as Gallium-68 are suitable for scFv and diabodies with rapid blood clearance whilst a long-lived positron emitter like zirconium-89 is more suitable for detecting therapeutic cells with full-length antibodies [98].

Table 2.3 Tracking therapeutic cell location and functional status using radiolabelled antibodies.

Target	Tracer and stage of development	Imaging	Reference
Cell Surface Markers			
CD3	[^{89}Zr]Zr-DFO-CD3 (preclinical)	CD3 cell infiltration (after anti-CTLA-4 treatment)	[99], [100]
CD4	[^{89}Zr]Zr-DFO-CD4 (preclinical)	Whole body assessment of CD4 status to predict response to checkpoint inhibition	[101]
CD8	[^{89}Zr]Zr-malDFO-169 cDb [^{89}Zr]Zr-Df-IAB22M2C [^{64}Cu]Cu-NOTA-anti-CD8 (Preclinical and Clinical *NCT03802123)*	CD8 T-cell distribution/infiltration and changes in response to immunotherapy	[102]–[104]
TCR	[^{89}Zr]Zr-Df-aTCRmu-F(ab')$_2$ (preclinical)	T-cell receptor (detection limit: 1.0 x 10^4 T-cells)	[105]
Activation Markers			
OX40	[^{64}Cu]Cu-DOTA-AbOX40 (preclinical)	Detection of T-cell activation to predict tumour response to vaccine	[106]
ICOS	[^{89}Zr]Zr-DFO-ICOS (preclinical)	Non-invasive tracking of murine CD19-28z CAR T-cells in B-cell lymphoma	[107]
NKp30	[^{64}Cu]Cu-NKp30Ab (preclinical)	Tumour-infiltrating NK cells and adoptive transfer of NK cells for therapy	[108]
Exhaustion Markers			
CTLA-4	[^{64}Cu]Cu-NOTA-ipilimumab-F(ab')$_2$ (preclinical)	Expression of CTLA-4 on tumour-infiltrating lymphocytes	[109]
PD-1	[^{89}Zr]Zr-nivolumab (Clinical: *NCT03843515*)	Expression of PD-1 on tumour-infiltrating lymphocytes	[110], [111]
PD-L1	[^{89}Zr]Zr-atezolizumab [^{18}F]F-BMS-986192 (Clinical: *NCT04222426, NCT03843515*)	Expression of PD-L1 in tumour microenvironment	[110],[112]
LAG-3	[^{89}Zr]Zr-DFO-REGN3767 (Clinical: *NCT04706715*)	Expression of LAG-3 on tumour-infiltrating lymphocytes	[113]

Imaging and detecting the presence of therapeutic T-cells in tumours has been demonstrated using CD8 antibody fragments [102],[103],[114]. A notable example is the use of CD8 cys-diabodies ([^{89}Zr]Zr-malDFO-169 cDb) engineered from rat hybridoma cell lines for the non-invasive tracking of cytotoxic T-cells in murine models of cancer immunotherapy [102]. Higher uptake of the tracer was detected in ovalbumin-expressing tumours following adoptive transfer of CD8$^+$ T-cells expressing the MHC Class I-restricted TCR specific for ovalbumin (Ova). Transverse images showed distribution of the tracer throughout the Ova$^+$ tumours, whilst the Ova$^-$ tumours demonstrated only diffuse uptake. Preliminary data from a first-in-human study on 6 patients using [^{89}Zr]Zr-IAB22M2C, a radiolabelled minibody targeting CD8 demonstrated favourable pharmacokinetics and good safety profile [103]. Tracer uptake in CD8$^+$ T-cell-rich tissues such as the lymph nodes was seen as early as 2 h post-injection. Tumour uptake was noted in 2 patients receiving immunotherapy (metastatic melanoma and hepatocellular carcinoma, **Fig. 2.9**) but not in the remaining 4 patients with lung metastases. Tumour uptake of [^{89}Zr]Zr-IAB22M2C was also histologically confirmed as CD8$^+$ T-cell infiltration at the periphery of a deltoid muscle metastatic lesion in the melanoma patient.

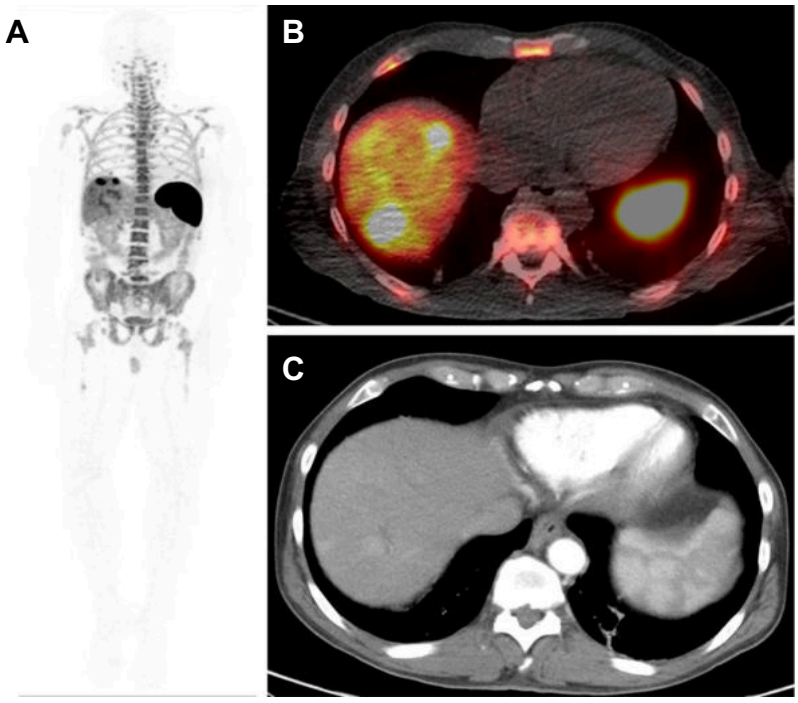

Figure 2.9 (A) 24 hour whole-body (MIP) image, (B) fused PET/CT image and (C) contrast enhanced CT of a patient with hepatocellular carcinoma injected with 0.5 mg [^{89}Zr]Zr-IAB22M2C. [^{89}Zr]-IAB22M2C-positive lesions are seen in 2 liver metastases and additional uptake is seen in 3 abdominal lymph node metastases. Figure copyright from [103].

Mall and colleagues developed [^{89}Zr]Zr-Df-aTCRmu-F(ab')$_2$ specific for the murine T-cell receptor (TCR) beta domain to track transgenic human T-cells engineered with murine sequences in the TCR [115]. *In vivo* imaging with ^{89}Zr-aTCRmu-F(ab')$_2$ was able to map the differential distribution of T-cell infiltrations within the tumour and could classify different tumour rejection phases that reflected the dynamics of T-cell response of T-cell receptor (TCR) transduced T-cells without any impact on the function of targeted T cells. The sensitivity and clinical applicability of the method was further evaluated in a separate study [105], whereby a detection limit of 1×10^4 T cells was observed when imaging was performed on tumour-bearing NSG mice injected with different numbers of transgenic T cells. This observation at the preclinical level is promising, as human CAR T-cells are usually tested with a doses ranging from 10^4 to 10^8 per kilogram body weight in clinical trials [116].

Radiolabelled antibodies can also be used for the monitoring the efficacy of NK cell therapies. A recent example is the use of radiolabelled IgG1 antibodies specific for the human NK cell activation receptor NKp30 i.e. [^{64}Cu]Cu-NKp30Ab to detect NK cell trafficking in an adoptive cell transfer model [108]. High specific uptake of the tracer was demonstrated *in vitro* on human NK cell line NK92MI and human NK cells isolated from buffy coats and *in vivo* on NKp30-expressing xenografts. The specific detection of human NK cells residing in the liver and spleen of NSG mice following adoptive cell transfer further demonstrated the clinical feasibility of this approach.

Determining the functional status of therapeutic cells over the course of treatment is important to ensure treatment efficacy. Radiolabelled antibodies targeting activation and exhaustion markers on therapeutic cells have been developed for oncological applications. Expression of the T-cell activation marker, inducible T-cell costimulatory receptor (ICOS) was evaluated using a full-length ICOS antibody [^{89}Zr]Zr-DFO-ICOS 5 days after CD19-specific T-cell administration in a murine model of B-cell lymphoma [107]. Although specific uptake of the tracer seen in the bones correlated with the presence of CAR T-cells infiltrating B-cell lymphoma in the bone marrow, using a full-length antibody for imaging ICOS was limited as a substantial amount of non-specific uptake was observed in highly vascularized organs such as the heart, liver and spleen. Therefore, further modification of the ICOS antibody into more miniaturized forms may be needed to improve the pharmacokinetics of this tracer and for clinical translation.

On the other hand, the expression of immune checkpoint proteins on tumour-infiltrating lymphocytes and CAR T-cells is a strong indication of immune tolerance and exhaustion, and a hallmark of treatment failure [117]. Monitoring the expression of immune checkpoint

proteins on therapeutic T-cells and in the tumour microenvironment is important for determining long-term treatment efficacy. Notable examples of radiopharmaceuticals that are now at the stage of clinical testing include radiolabelled antibodies targeting the programmed cell death 1 receptor (PD-1) [^{89}Zr]Zr-nivolumab, its ligand PD-L1 [^{89}Zr]Zr-atezolizumab and [^{18}F]F-BMS-986192, as well as the lymphocyte-activation gene 3 (LAG-3) specific [^{89}Zr]Zr-DFO-REGN3767 [110],[112],[113]. [^{89}Zr]Zr-nivolumab has been investigated both in a humanized mouse model of lung cancer [111], as well as in patients with non-small cell lung carcinoma [110]. The tracer showed high specific binding to PD-1 expressing T-cells both *in vitro* and *in vivo*, and was associated with T-cell infiltration in the tumours, salivary and lacrimal glands of NSG mice engrafted with human peripheral blood mononuclear cells [111]. In patient studies, high tracer accumulation was observed in the spleen, likely to be due to interactions with PD-1 expressed on lymphocytes and dendritic cells [110]. [^{89}Zr]Zr-nivolumab uptake in tumours was histologically confirmed as PD-1^{+} T-cells and was predictive of response to nivolumab treatment (**Fig. 2.10**).

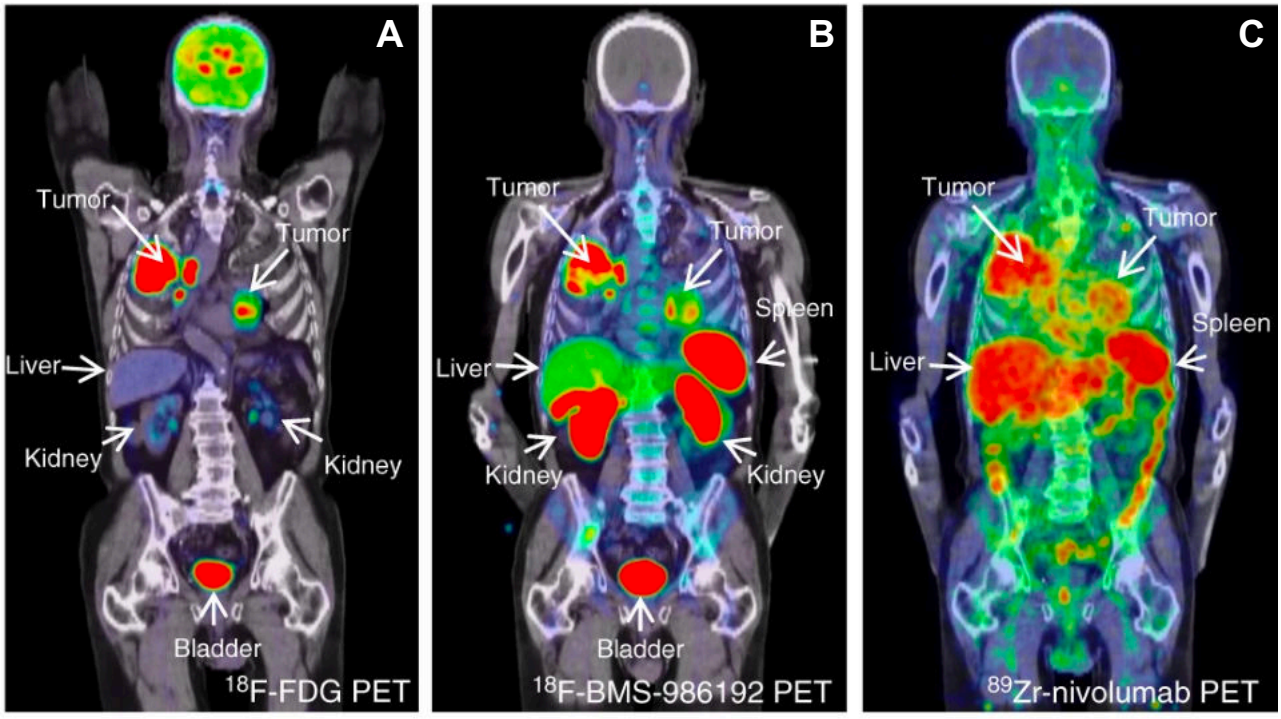

Figure 2.10 PET/CT fusion images of a patient with PD-1/PD-L1 positive tumour. (**A**) [^{18}F]-FDG PET (225 MBq) demonstrates high glucose metabolism of tumours in both lungs and mediastinal lymph nodes, (**B**) [^{18}F]-BMS-986192 PET (145.7 MBq, imaging time point 1 h post-injection (p.i.)) and (**C**) ^{89}Zr-labeled Nivolumab PET (37.09 MBq, 162 h p.i.) demonstrate heterogeneous tracer uptake within and between tumours. Figure copyright from [110].

2.7 Thesis aims and objectives

This thesis describes the set-up of the first use of zirconium-89 in Cambridge with all its prerequisites. As described in this chapter, up to today there are only two preclinically evaluated ^{89}Zr-tracers applied for direct cell labelling, namely [^{89}Zr]Zr-DFO-NCS for cell surface labelling and [^{89}Zr]Zr-Oxine for intracellular labelling. These two compounds have been first used for cell labelling around 2015 and have only been evaluated preclinically up to today. The translation into a clinical setting, in particular for [^{89}Zr]Zr-Oxine, is planned but this has been hindered by the nature of the tracer itself. Both [^{89}Zr]Zr-Oxine and [^{89}Zr]Zr-DFO-NCS cannot be purified, e.g. via a cartridge. Up until very recently, the [^{89}Zr]Zr-Oxine synthesis was cumbersome and due to its lipophilicity most of the tracer sticks to the vial, pipette tip and other equipment. This will be further explained and highlighted in chapter 3.

The purpose and objectives of this thesis were the following:

i. Firstly, to investigate the sensitivity and detection limits associated with the tracking of cells directly labelled with [^{89}Zr]Zr-Oxine as a function of cell number, radioactivity exposure per cell and the influence on detection using clinical PET

ii. Secondly, to investigate an alternative, clinically translatable tracer concept compared to [^{89}Zr]Zr-Oxine for direct cell labelling using zirconium-89

iii. Lastly, to test and evaluate alternative cell labelling compounds on cells in direct comparison to [^{89}Zr]Zr-Oxine

The results of preliminary experiments for the project set-up are summarised in chapter 3, followed by chapter 4, 5 and 6 summarising the experimental results obtained during this project. Concluding remarks, future work and plans are outlined in chapter 7.

2.8 References

1. Rahmim A, Zaidi H. Pet versus spect: Strengths, limitations and challenges. *Nucl Med Commun*. 2008;29(3):193-207.
2. Rodriguez-Porcel M. In vivo imaging and monitoring of transplanted stem cells: Clinical applications. *Curr Cardiol Rep*. 2010;12(1):51-58.
3. Langford ST, Wiggins CS, Santos R, Hauser M, Becker JM, Ruggles AE. Three-dimensional spatiotemporal tracking of fluorine-18 radiolabeled yeast cells via positron emission particle tracking. *PLoS One*. 2017;12(7).
4. Ouyang Y, Kim TJ, Pratx G. Evaluation of a BGO-Based PET System for Single-Cell Tracking Performance by Simulation and Phantom Studies. *Mol Imaging*. 2016;15.
5. Lahooti A, Sarkar S, Laurent S, Shanehsazzadeh S. Dual nano-sized contrast agents in PET/MRI: a systematic review. *Contrast Media Mol Imaging*. 2016;11(6):428-447.
6. Cherry SR, Jones T, Karp JS, Qi J, Moses WW, Badawi RD. Total-body PET: Maximizing sensitivity to create new opportunities for clinical research and patient care. *J Nucl Med*. 2018;59(1):3-12.
7. Jung KO, Kim TJ, Yu JH, et al. Whole-body tracking of single cells via positron emission tomography. *Nat Biomed Eng*. 2020;4(8):835-844.
8. Partridge M, Spinelli A, Ryder W, Hindorf C. The effect of β+ energy on performance of a small animal PET camera. *Nucl Instruments Methods Phys Res Sect A Accel Spectrometers, Detect Assoc Equip*. 2006;568(2):933-936.
9. Andersen FL, Ladefoged CN, Beyer T, et al. Combined PET/MR imaging in neurology: MR-based attenuation correction implies a strong spatial bias when ignoring bone. *Neuroimage*. 2014;84:206-216.
10. Sekine T, Buck A, Delso G, et al. Evaluation of atlas-based attenuation correction for integrated PET/MR in human brain: Application of a head atlas and comparison to true ct-based attenuation correction. *J Nucl Med*. 2016;57(2):215-220.
11. Keereman V, Fierens Y, Broux T, De Deene Y, Lonneux M, Vandenberghe S. MRI-based attenuation correction for PET/MRI using ultrashort echo time sequences. *J Nucl Med*. 2010;51(5):812-818.
12. Badawi RD, Shi H, Hu P, et al. First human imaging studies with the explorer total-body PET scanner. *J Nucl Med*. 2019.
13. Hofmann M, Wollert KC, Meyer GP, et al. Monitoring of bone marrow cell homing into the infarcted human myocardium. *Circulation*. 2005;111(17):2198-2202.

14. Bhattacharya A, Kochhar R, Sharma S, et al. PET/CT with 18F-FDG-labeled autologous leukocytes for the diagnosis of infected fluid collections in acute pancreatitis. *J Nucl Med*. 2014;55(8):1267-1272.
15. Wu C, Ma G, Li J, et al. In vivo cell tracking via 18F-fluorodeoxyglucose labeling: A review of the preclinical and clinical applications in cell-based diagnosis and therapy. *Clin Imaging*. 2013;37(1):28-36.
16. Ritchie D, Mileshkin L, Wall D, et al. In vivo tracking of macrophage activated killer cells to sites of metastatic ovarian carcinoma. *Cancer Immunol Immunother*. 2007.
17. Meier R, Piert M, Piontek G, et al. Tracking of [18F]FDG-labeled natural killer cells to HER2/neu-positive tumors. *Nucl Med Biol*. 2008;35(5):579-588.
18. Fischer BM, Olsen MWB, Ley CD, et al. How few cancer cells can be detected by positron emission tomography? A frequent question addressed by an in vitro study. *Eur J Nucl Med Mol Imaging*. 2006;33(6):697-702.
19. Wolfs E, Struys T, Notelaers T, et al. 18F-FDG labeling of mesenchymal stem cells and multipotent adult progenitor cells for PET imaging: Effects on ultrastructure and differentiation capacity. *J Nucl Med*. 2013;54(3):447-454.
20. Faivre L, Chaussard M, Vercellino L, et al. 18F-FDG labelling of hematopoietic stem cells: Dynamic study of bone marrow homing by PET–CT imaging and impact on cell functionality. *Curr Res Transl Med*. 2016;64(3):141-148.
21. Stojanov K, De Vries EFJ, Hoekstra D, Van Waarde A, Dierckx RAJO, Zuhorn IS. [18F]FDG labeling of neural stem cells for in vivo cell tracking with positron emission tomography: Inhibition of tracer release by phloretin. *Mol Imaging*. 2012;11(1):1-12.
22. Olasz EB, Lang L, Seidel J, Green M V., Eckelman WC, Katz SI. Fluorine-18 labeled mouse bone marrow-derived dendritic cells can be detected in vivo by high resolution projection imaging. *J Immunol Methods*. 2002;260(1-2):137-148.
23. Ma B, Hankenson KD, Dennis JE, Caplan AI, Goldstein SA, Kilbourn MR. A simple method for stem cell labeling with fluorine 18. *Nucl Med Biol*. 2005.
24. Zhang Y, da Silva JN, Hadizad T, et al. 18F-FDG cell labeling may underestimate transplanted cell homing: More accurate, efficient, and stable cell labeling with hexadecyl-4-[18F]fluorobenzoate for in vivo tracking of transplanted human progenitor cells by positron emission tomography. *Cell Transplant*. 2012;21(9):1821-1835.
25. Belderbos S, González-Gómez MA, Cleeren F, et al. Simultaneous in vivo PET/MRI using fluorine-18 labeled Fe3O4@Al(OH)3 nanoparticles: comparison of nanoparticle and nanoparticle-labeled stem cell distribution. *EJNMMI Res*. 2020;10(1).

26. Brownell AL, Jain RK, Shoup TM, Brownell GL. Imaging of Activated Natural Killer Cells in Mice by Positron Emission Tomography: Preferential Uptake in Tumors. *Cancer Res*. 1993;53(24):5867-5871.
27. Bhatnagar P, Alauddin M, Bankson JA, et al. Tumor lysing genetically engineered t cells loaded with multi-modal imaging agents. *Sci Rep*. 2014;4.
28. Bhatnagar P, Li Z, Choi Y, et al. Imaging of genetically engineered T cells by PET using gold nanoparticles complexed to Copper-64. *Integr Biol*. 2013;5(1):231-238.
29. Singla R, Wall DM, Anderson S, et al. First in-human study of in vivo imaging of ex vivo labeled CAR T cells with dual PET-MR. *J Clin Oncol*. 2020;38(15_suppl):3557-3557.
30. Griessinger CM, Maurer A, Kesenheimer C, et al. 64Cu antibody-targeting of the T-cell receptor and subsequent internalization enables in vivo tracking of lymphocytes by PET. *Proc Natl Acad Sci U S A*. 2015;112(4):1161-1166.
31. Griessinger CM, Kehlbach R, Bukala D, et al. In vivo tracking of th1 cells by PET reveals quantitative and temporal distribution and specific homing in lymphatic tissue. *J Nucl Med*. 2014;55(2):301-307.
32. Park JJ, Lee TS, Son JJ, et al. Comparison of cell-labeling methods with 124I-FIAU and 64Cu-PTSM for cell tracking using chronic myelogenous leukemia cells expressing HSV1-tk and firefly luciferase. *Cancer Biother Radiopharm*. 2012;27(10):719-728.
33. Li Z-B, Chen K, Wu Z, Wang H, Niu G, Chen X. 64Cu-Labeled PEGylated Polyethylenimine for Cell Trafficking and Tumor Imaging. *Mol Imaging Biol*. 2009;11(6):415.
34. Bhargava KK, Gupta RK, Nichols KJ, Palestro CJ. In vitro human leukocyte labeling with 64Cu: an intraindividual comparison with 111In-oxine and 18F-FDG. *Nucl Med Biol*. 2009;36(5):545-549.
35. Adonai N, Adonai N, Nguyen KN, et al. Ex vivo cell labeling with 64Cu-pyruvaldehyde-bis(N4-methylthiosemicarbazone) for imaging cell trafficking in mice with positron-emission tomography. *Proc Natl Acad Sci U S A*. 2002;99(5):3030-3035.
36. Kim MH, Woo SK, Lee KC, et al. Longitudinal monitoring adipose-derived stem cell survival by PET imaging hexadecyl-4-124I-iodobenzoate in rat myocardial infarction model. *Biochem Biophys Res Commun*. 2015.
37. Pham TT, Lu Z, Davis C, et al. Iodine-124 Based Dual Positron Emission Tomography and Fluorescent Labeling Reagents for in Vivo Cell Tracking. *Bioconjug Chem*. 2020;31(4):1107-1116.

38. Lee SB, Lee SW, Jeong SY, et al. Engineering of Radioiodine-Labeled Gold Core-Shell Nanoparticles As Efficient Nuclear Medicine Imaging Agents for Trafficking of Dendritic Cells. *ACS Appl Mater Interfaces*. 2017;9(10):8480-8489.
39. Agger R, Petersen MS, Petersen CC, et al. T cell homing to tumors detected by 3D-coordinated positron emission tomography and magnetic resonance imaging. *J Immunother*. 2007;30(1):29-39.
40. Perk LR, Visser GWM, Vosjan MJWD, et al. (89)Zr as a PET surrogate radioisotope for scouting biodistribution of the therapeutic radiometals (90)Y and (177)Lu in tumor-bearing nude mice after coupling to the internalizing antibody cetuximab. *J Nucl Med*. 2005;46(11):1898-1906.
41. Perk LR, Visser OJ, Stigter-Van Walsum M, et al. Preparation and evaluation of 89Zr-Zevalin for monitoring of 90Y-Zevalin biodistribution with positron emission tomography. *Eur J Nucl Med Mol Imaging*. 2006;33(11):1337-1345.
42. Deri MA, Zeglis BM, Francesconi LC, Lewis JS. PET imaging with 89Zr: From radiochemistry to the clinic. *Nucl Med Biol*. 2013;40(1):3-14.
43. Perk LR, Vosjan MJWD, Visser GWM, et al. P-Isothiocyanatobenzyl-desferrioxamine: A new bifunctional chelate for facile radiolabeling of monoclonal antibodies with zirconium-89 for immuno-PET imaging. *Eur J Nucl Med Mol Imaging*. 2010;37(2):250-259.
44. Vosjan MJWD, Perk LR, Visser GWM, et al. Conjugation and radiolabeling of monoclonal antibodies with zirconium-89 for PET imaging using the bifunctional chelate p-isothiocyanatobenzyl-desferrioxamine. *Nat Protoc*. 2010;5(4):739-743.
45. Gawne P, Man F, Fonslet J, et al. Manganese-52: applications in cell radiolabelling and liposomal nanomedicine PET imaging using oxine (8-hydroxyquinoline) as an ionophore. *Dalt Trans*. 2018;47(28):9283-9293.
46. Sato N, Wu H, Asiedu KO, Szajek LP, Griffiths GL, Choyke PL. 89Zr-oxine complex PET cell imaging in monitoring cell-based therapies. *Radiology*. 2015;275(2):490-500.
47. Patrick PS, Kolluri KK, Zaw Thin M, et al. Lung delivery of MSCs expressing anti-cancer protein TRAIL visualised with 89Zr-oxine PET-CT. *Stem Cell Res Ther*. 2020;11(1):256.
48. Davidson-Moncada J, Sato N, Hoyt RF, et al. A Novel Method to Study the in Vivo Trafficking and Homing of Adoptively Transferred NK Cells in Rhesus Macaques and Humans. *Blood*. 2014;124(21):659-659.

49. Sato N, Stringaris K, Davidson-Moncada JK, et al. In Vivo Tracking of Adoptively Transferred Natural Killer Cells in Rhesus Macaques Using 89Zirconium-Oxine Cell Labeling and PET Imaging. *Clin Cancer Res*. 2020;26(11):2573-2581.
50. Man F, Lim L, Volpe A, et al. In Vivo PET Tracking of 89 Zr-Labeled Vγ9Vδ2 T Cells to Mouse Xenograft Breast Tumors Activated with Liposomal Alendronate. *Mol Ther*. 2019;27(1):219-229.
51. Asiedu KO, Koyasu S, Szajek LP, Choyke PL, Sato N. Bone marrow cell trafficking analyzed by 89Zr-oxine positron emission tomography in a murine transplantation model. *Clin Cancer Res*. 2017;23(11):2759-2768.
52. Weist MR, Starr R, Aguilar B, et al. PET of adoptively transferred chimeric antigen receptor T Cells with 89Zr-Oxine. *J Nucl Med*. 2018;59(10):1531-1537.
53. Bansal A, Pandey MK, Demirhan YE, et al. Novel 89Zr cell labeling approach for PET-based cell trafficking studies. *EJNMMI Res*. 2015;5(1):19.
54. Lee SH, Soh H, Chung JH, et al. Feasibility of real-time in vivo 89Zr-DFO-labeled CAR T-cell trafficking using PET imaging. *PLoS One*. 2020;15(1).
55. Volpe A, Lang C, Lim L, et al. Spatiotemporal PET Imaging Reveals Differences in CAR-T Tumor Retention in Triple-Negative Breast Cancer Models. *Mol Ther*. 2020;28(10):2271-2285.
56. Minn I, Huss DJ, Ahn HH, et al. Imaging CAR T cell therapy with PSMA-targeted positron emission tomography. *Sci Adv*. 2019;5(7).
57. Vedvyas Y, Shevlin E, Zaman M, et al. Longitudinal PET imaging demonstrates biphasic CAR T cell responses in survivors. *JCI Insight*. 2016;1(19).
58. Park S, Shevlin E, Vedvyas Y, et al. Micromolar affinity CAR T cells to ICAM-1 achieves rapid tumor elimination while avoiding systemic toxicity. *Sci Rep*. 2017;7(1).
59. Yaghoubi SS, Jensen MC, Satyamurthy N, et al. Noninvasive detection of therapeutic cytolytic T cells with 18F–FHBG PET in a patient with glioma. *Nat Clin Pract Oncol*. 2009;6(1):53-58.
60. Keu KV, Witney TH, Yaghoubi S, et al. Reporter gene imaging of targeted T cell immunotherapy in recurrent glioma. *Sci Transl Med*. 2017;9(373):eaag2196.
61. Najjar AM, Manuri PR, Olivares S, et al. Imaging of Sleeping Beauty-Modified CD19-Specific T Cells Expressing HSV1-Thymidine Kinase by Positron Emission Tomography. *Mol Imaging Biol*. 2016;18(6):838-848.
62. Dobrenkov K, Olszewska M, Likar Y, et al. Monitoring the efficacy of adoptively transferred prostate cancer-targeted human T lymphocytes with PET and bioluminescence imaging. *J Nucl Med*. 2008;49(7):1162-1170.

63. Sellmyer MA, Lee I, Hou C, et al. Quantitative PET Reporter Gene Imaging with [11C]Trimethoprim. *Mol Ther*. 2017;25(1):120-126.
64. Sellmyer MA, Richman SA, Lohith K, et al. Imaging CAR T Cell Trafficking with eDFHR as a PET Reporter Gene. *Mol Ther*. 2019.
65. Moroz MA, Zhang H, Lee J, et al. Comparative analysis of T cell imaging with human nuclear reporter genes. *J Nucl Med*. 2015;56(7):1055-1060.
66. Eissenberg LG, Rettig MP, Ritchey JK, et al. FHBG PET/CT imaging of CD34-TK75 transduced donor T cells in relapsed allogeneic stem cell transplant patients: Safety and feasibility. *Mol Ther*. 2015;23(6):1110-1122.
67. Ponomarev V, Doubrovin M, Serganova I, et al. Cytoplasmically retargeted HSV1-tk/GFP reporter gene mutants for optimization of noninvasive molecular-genetic imaging. *Neoplasia*. 2003;5(3):245-254.
68. Dubey P, Su H, Adonai N, et al. Quantitative imaging of the T cell antitumor response by positron-emission tomography. *Proc Natl Acad Sci U S A*. 2003;100(3):1232-1237.
69. Koehne G, Doubrovin M, Doubrovina E, et al. Serial in vivo imaging of the targeted migration of human HSV-TK-transduced antigen-specific lymphocytes. *Nat Biotechnol*. 2003;21(4):405-413.
70. Casucci M, Perna SK, Falcone L, et al. Graft-versus-leukemia effect of HLA-haploidentical central-memory t-cells expanded with leukemic APCs and modified with a suicide gene. *Mol Ther*. 2013;21(2):466-475.
71. Eissenberg LG, Rettig M, Dehdashti F, Piwnica-Worms D, DiPersio JF. Suicide genes: Monitoring cells in patients with a safety switch. *Front Pharmacol*. 2014;5(Nov).
72. Brandt LJB, Barnkob MB, Michaels YS, Heiselberg J, Barington T. Emerging Approaches for Regulation and Control of CAR T Cells: A Mini Review. *Front Immunol*. 2020;11.
73. Alan R. Penheiter, Stephen J. Russell, Stephanie K. Carlson. The Sodium Iodide Symporter (NIS) as an Imaging Reporter for Gene, Viral, and Cell-based Therapies. *Curr Gene Ther*. 2012;12(1):33-47.
74. Ravera S, Reyna-Neyra A, Ferrandino G, Amzel LM, Carrasco N. The Sodium/Iodide Symporter (NIS): Molecular Physiology and Preclinical and Clinical Applications. *Annu Rev Physiol*. 2017;79:261-289.

75. O'Doherty J, Jauregui-Osoro M, Brothwood T, et al. 18F-tetrafluoroborate, a PET probe for imaging sodium/iodide symporter expression: Whole-body biodistribution, safety, and radiation dosimetry in thyroid cancer patients. *J Nucl Med*. 2017;58(10):1666-1671.
76. DIocou S, Volpe A, Jauregui-Osoro M, et al. [18F]tetrafluoroborate-PET/CT enables sensitive tumor and metastasis in vivo imaging in a sodium iodide symporter-expressing tumor model. *Sci Rep*. 2017;7(1).
77. Vandergaast R, Khongwichit S, Jiang H, et al. Enhanced noninvasive imaging of oncology models using the NIS reporter gene and bioluminescence imaging. *Cancer Gene Ther*. 2020;27(3-4):179-188.
78. Reubi JC. Peptide receptors as molecular targets for cancer diagnosis and therapy. *Endocr Rev*. 2003;24(4):389-427.
79. Virgolini I, Ambrosini V, Bomanji JB, et al. Procedure guidelines for PET/CT tumour imaging with 68Ga-DOTA- conjugated peptides: 68Ga-DOTA-TOC, 68Ga-DOTA-NOC, 68Ga-DOTA-TATE. *Eur J Nucl Med Mol Imaging*. 2010;37(10):2004-2010.
80. Graham MM, Gu X, Ginader T, Breheny P, Sunderland JJ. 68Ga-DOTATOC imaging of neuroendocrine tumors: A systematic review and metaanalysis. *J Nucl Med*. 2017;58(9):1452-1458.
81. Zhang H, Moroz MA, Serganova I, et al. Imaging expression of the human somatostatin receptor subtype-2 reporter gene with 68Ga-DOTATOC. *J Nucl Med*. 2011;52(1):123-131.
82. Velikyan I, Sundin A, Sörensen J, et al. Quantitative and qualitative intrapatient comparison of 68Ga-DOTATOC and 68Ga-DOTATATE: Net uptake rate for accurate quantification. *J Nucl Med*. 2014;55(2):204-210.
83. Yaghoubi SS, Gambhir SS. PET imaging of herpes simplex virus type 1 thymidine kinase (HSV1-tk) or mutant HSV1-sr39tk reporter gene expression in mice and humans using [18F]FHBG. *Nat Protoc*. 2007;1(6):3069-3075.
84. Pauwels E, Cleeren F, Tshibangu T, et al. [18F]AlF-NOTA-octreotide PET imaging: biodistribution, dosimetry and first comparison with [68Ga]Ga-DOTATATE in neuroendocrine tumour patients. *Eur J Nucl Med Mol Imaging*. 2020.
85. Park S, Shevlin E, Vedvyas Y, et al. Micromolar affinity CAR T cells to ICAM-1 achieves rapid tumor elimination while avoiding systemic toxicity. *Sci Rep*. 2017;7(1):14366.
86. Schwarzenboeck SM, Rauscher I, Bluemel C, et al. PSMA ligands for PET imaging of prostate cancer. *J Nucl Med*. 2017;58(10):1545-1552.

87. Pacholczyk T, Blakely RD, Amara SG. Expression cloning of a cocaine-and antidepressant-sensitive human noradrenaline transporter. *Nature*. 1991;350(6316):350-354.
88. Moroz MA, Zhang H, Lee J, et al. Comparative analysis of T cell imaging with human nuclear reporter genes. *J Nucl Med*. 2015;56(7):1055-1060.
89. Ashmore-Harris C, Iafrate M, Saleem A, Fruhwirth GO. Non-invasive Reporter Gene Imaging of Cell Therapies, including T Cells and Stem Cells. *Mol Ther*. 2020;28(6):1392-1416.
90. Radu CG, Shu CJ, Nair-Gill E, et al. Molecular imaging of lymphoid organs and immune activation by positron emission tomography with a new [18F]-labeled 2′-deoxycytidine analog. *Nat Med*. 2008;14(7):783-788.
91. Juergens RA, Zukotynski KA, Singnurkar A, Snider DP, Valliant JF, Gulenchyn KY. Imaging Biomarkers in Immunotherapy. *Biomark Cancer*. 2016;8(Suppl 2):1-13.
92. Dammes N, Peer D. Monoclonal antibody-based molecular imaging strategies and theranostic opportunities. *Theranostics*. 2020.
93. Liu Z, Li Z. Molecular imaging in tracking tumor-specific Cytotoxic T Lymphocytes (CTLs). *Theranostics*. 2014;4(10):990-1001.
94. Kobayashi H, Choyke PL, Ogawa M. Monoclonal antibody-based optical molecular imaging probes; considerations and caveats in chemistry, biology and pharmacology. *Curr Opin Chem Biol*. 2016;33:32-38.
95. Bolkestein M, De Blois E, Koelewijn SJ, et al. Investigation of factors determining the enhanced permeability and retention effect in subcutaneous xenografts. *J Nucl Med*. 2016;57(4):601-607.
96. Fay R, Holland JP. The impact of emerging bioconjugation chemistries on radiopharmaceuticals. *J Nucl Med*. 2019;60(5):587-591.
97. Sarko D, Eisenhut M, Haberkorn U, Mier W. Bifunctional Chelators in the Design and Application of Radiopharmaceuticals for Oncological Diseases. *Curr Med Chem*. 2012;19(17):2667-2688.
98. van Dongen GAMS, Visser GWM, Lub-de Hooge MN, de Vries EG, Perk LR. Immuno-PET: A Navigator in Monoclonal Antibody Development and Applications. *Oncologist*. 2007;12(12):1379-1389.
99. Larimer BM, Wehrenberg-Klee E, Caraballo A, Mahmood U. Quantitative CD3 PET imaging predicts tumor growth response to anti-CTLA-4 therapy. *J Nucl Med*. 2016;57(10):1607-1611.

100. Beckford Vera DR, Smith CC, Bixby LM, et al. Immuno-PET imaging of tumor-infiltrating lymphocytes using zirconium-89 radiolabeled anti-CD3 antibody in immune-competent mice bearing syngeneic tumors. *PLoS One*. 2018;13(3).
101. Kristensen LK, Fröhlich C, Christensen C, et al. CD4+ and CD8a+ PET imaging predicts response to novel PD-1 checkpoint inhibitor: Studies of Sym021 in syngeneic mouse cancer models. *Theranostics*. 2019;9(26):8221-8238.
102. Tavaré R, Escuin-Ordinas H, Mok S, et al. An effective immuno-PET imaging method to monitor CD8-dependent responses to immunotherapy. *Cancer Res*. 2016;76(1):73-82.
103. Pandit-Taskar N, Postow MA, Hellmann MD, et al. First-in-Humans Imaging with 89Zr-Df-IAB22M2C Anti-CD8 Minibody in Patients with Solid Malignancies: Preliminary Pharmacokinetics, Biodistribution, and Lesion Targeting. *J Nucl Med*. 2020;61(4):512-519.
104. Nagle VL, Henry KE, Hertz CAJ, et al. Imaging tumor-infiltrating lymphocytes in brain tumors with [64 Cu]Cu-NOTA-anti-CD8 PET. *Clin Cancer Res*. 2021;27(7):1958-1966.
105. Yusufi N, Mall S, Bianchi H de O, et al. In-depth characterization of a TCR-specific tracer for sensitive detection of tumor-directed transgenic T cells by immuno-PET. *Theranostics*. 2017;7(9):2402-2416.
106. Alam IS, Mayer AT, Sagiv-Barfi I, et al. Imaging activated T cells predicts response to cancer vaccines. *J Clin Invest*. 2018;128(6):2569-2580.
107. Simonetta F, Alam IS, Lohmeyer JK, et al. Molecular Imaging of Chimeric Antigen Receptor T Cells by ICOS-ImmunoPET. *Clin Cancer Res*. 2021;27(4):1058-1068.
108. Shaffer TM, Aalipour A, Schürch CM, Gambhir SS. PET Imaging of the Natural Killer Cell Activation Receptor NKp30. *J Nucl Med*. 2020;61(9):1348-1354.
109. Ehlerding EB, Lee HJ, Jiang D, et al. Antibody and fragment-based PET imaging of CTLA-4+ T-cells in humanized mouse models. *Am J Cancer Res*. 2019.
110. Niemeijer AN, Leung D, Huisman MC, et al. Whole body PD-1 and PD-L1 positron emission tomography in patients with non-small-cell lung cancer. *Nat Commun*. 2018;9(1).
111. England CG, Jiang D, Ehlerding EB, et al. 89Zr-labeled nivolumab for imaging of T-cell infiltration in a humanized murine model of lung cancer. *Eur J Nucl Med Mol Imaging*. 2018;45(1):110-120.

112. Bensch F, van der Veen EL, Lub-de Hooge MN, et al. 89Zr-atezolizumab imaging as a non-invasive approach to assess clinical response to PD-L1 blockade in cancer. *Nat Med*. 2018;24(12):1852-1858.
113. Kelly MP, Tavare R, Giurleo JT, et al. Abstract 3033: Immuno-PET detection of LAG-3 expressing intratumoral lymphocytes using the zirconium-89 radiolabeled fully human anti-LAG-3 antibody REGN3767. In: ; 2018:3033-3033.
114. Parisi G, Saco JD, Salazar FB, et al. Persistence of adoptively transferred T cells with a kinetically engineered IL-2 receptor agonist. *Nat Commun*. 2020;11(1).
115. Mall S, Yusufi N, Wagner R, et al. Immuno-PET imaging of engineered human T cells in tumors. *Cancer Res*. 2016;76(14):4113-4123.
116. Davey AS, Call ME, Call MJ. The influence of chimeric antigen receptor structural domains on clinical outcomes and associated toxicities. *Cancers (Basel)*. 2021;13(1):1-16.
117. Sharma P, Allison JP. Immune checkpoint targeting in cancer therapy: Toward combination strategies with curative potential. *Cell*. 2015;161(2):205-214.

Chapter 3

Zirconium-89 for cellular labelling and imaging using positron emission tomography (PET)

3.1 Contributions and collaborators

Part of the initial training and work for the project set-up was done in collaboration with the VUMC Amsterdam where I was a visitor for a short period of time as part of my training. Apart from this, I undertook all work described below which includes the writing of several radiation safety and ethics documents that were filled out and revised on a regular basis by myself. I undertook the lab set-up alone, including the set-up of instruments. Initial cell work was carried out in collaboration with Dr Lorna Jarvis in Dr Joanne Jones' lab who taught me cell culture and assisted with flow cytometry experiments and analysis. I carried out the flow cytometry analysis as described below.

3.2 Introduction

3.2.1 General introduction

During the atomic testing period of the 1950's and 1960's, zirconium-93 and zirconium-95 emerged as important fission products [1]. The early interests in fission/fallout lead to animal studies to investigate the biological distribution of Zirconium-93 and zirconium-95 in the 1950's and 1960's which included the toxicity [2] and the biodistribution of zirconium-95 in rats and mice [3],[4]. These early studies demonstrated low toxicity in rats but showed a high affinity of zirconium for bones using autoradiography. One of the earliest studies describing the use of zirconium-89 in the human body was performed in 1957. John Mealey studied the excretion dynamics of zirconium-89 from the bloodstream and its distribution between plasma proteins [5] as well as the application of zirconium-89 for the possible "external localization of human brain tumours" [6]. It was not until the mid 2000s that there has been a renewed interest in the use of zirconium-89 as a potential PET isotope for the labelling of monoclonal antibody for *in vivo* cancer imaging [7]. In addition, Zirconium-89 has emerged recently as a very promising PET isotope for direct cell labelling [8], as described in detail in the previous chapter, but also for the labelling and tracking of nanoparticles and liposomes [9],[10].

3.2.2 Zirconium isotopes and zirconium-89 decay

There are several radioactive zirconium isotopes that include zirconium-86, zirconium-87, zirconium-88, zirconium-89, zirconium-93 and zirconium-95, zirconium-96 and zirconium-97. Among these radioisotopes zirconium-89 is the only positron emitting isotope that can be used for imaging. Zirconium-89 decays into a metastable-state yttrium-89m with a half-life of 78.4 hours, via both positron emission (22.7 %) and electron capture (76.6 %) which in turn decays to stable ^{89}Y via a gamma ray emission (909 keV) with a half-life of 15.7 s (**Fig. 3.1**). The relatively low emitted positron energy of $E_{mean} = 0.396$ MeV ($E_{max} = 0.902$ MeV) with a positron range of $R_{mean} = 1.3$ mm ($R_{max} = 3.8$ mm) allows for images with high resolution [11], however higher level of corrupt events (scatter and random coincidences) can potentially increase image noise.

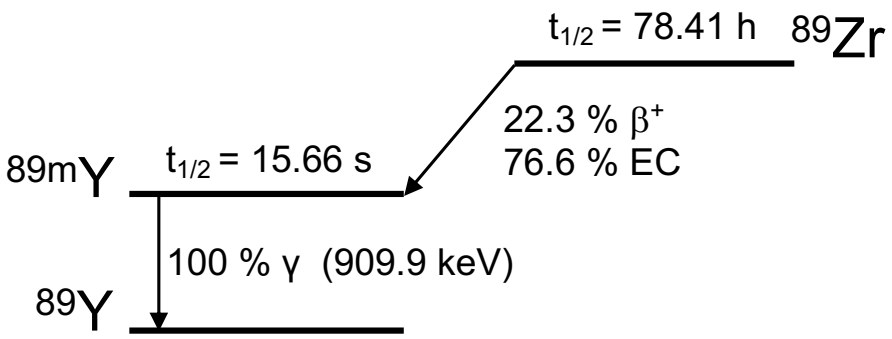

Figure 3.1 Simplified decay scheme of zirconium-89. Data based on [12].

Based on the decay scheme of zirconium-89, the cascade gamma rays are emitted ~ 15 s later than the positron, which is many orders of magnitude greater than the coincidence window of the PET camera (~5×10^{-9} s) [13]. Compared to other non-pure positron emitting isotopes, such as iodine-124, the so-called prompt gamma emission that often co-occurs with positrons is not the case with zirconium-89 due to the ~15 s long half-life of the metastable yttrium-89m and therefore normal random coincidence correction schemes can be used in this case.

Despite some favourable physical properties overall, the abundant, high-energy and highly penetrating 909 keV gamma-ray necessitates more shielding for transport and safe handling than is generally considered adequate for fluorine-18 for example. This also limits the amount of activity that can be injected in terms of patient dose. A typical effective dose for the whole body in case of ^{89}Zr-labelled antibodies ranges from 0.26-0.54 mSv/MBq [14]–

[16] which is much higher compared to a standard [^{18}F]FDG scan resulting in ~0.019 mSv/MBq [17].

3.2.3 Zirconium-89 production

Zirconium-89 can be obtained by the irradiation of natural yttrium via the most commonly applied ^{89}Y(p,n)^{89}Zr reaction in a cyclotron. In the early studies by Mealey zirconium-89 was prepared and administered in the form of [^{89}Zr]Zr-citrate (formulated in 1% sodium citrate, pH 6-7) [5]. The findings by Baroncelli and Grossi that hydroxamic acids have high specific affinity for zirconium and can form very stable complexes paved the way to more efficient production and specific separation processes of zirconium-89 from the yttrium target material [18]. Meijs et al. were the first to described the separation of zirconium-89 from the yttrium target with an in house prepared hydroxamate resin by eluting the no carrier added zirconium-89 with 1.0 M oxalic acid [19]. Oxalic acid can keep zirconium-89 in solution very stably as [^{89}Zr][Zr(oxalate)$_4$]$^{4-}$, given that oxalate as a ligand needs to have a stronger affinity to zirconium-89 than to the hydroxamate resin itself. Holland *et al.* showed that the concentration of oxalic acid in the solution with zirconium-89 did not impact on the formation of complexes with the desferrioxamine (DFO) chelator [20]. Zirconium-89 can also be produced as [^{89}Zr]ZrCl$_4$ or be converted to [^{89}Zr]ZrCl$_4$ from [^{89}Zr][Zr(oxalate)$_4$]$^{4-}$ in a 2-step procedure via a QMA cartridge [21]. Although [^{89}Zr]ZrCl$_4$ is very reactive, hygroscopic and prone to form oxychloride hydrates that are hard to chelate [22],[23], it has shown to be the favourable starting material to label tetraazamacrocyclic ligands such as the 1,4,7,10-tetraazacyclododecane *N*,*N*′,*N*″,*N*‴-tetraacetic acid (DOTA) chelator compared to [^{89}Zr][Zr(oxalate)$_4$]$^{4-}$ yielding complexes with “extraordinary stability” [24]. Therefore, the chemical form of the isotope is very important and often decisive for the subsequent radiochemistry but also for applications where oxalic acid can be a major problem due to its toxicity and where it can’t be removed from the tracer solution. Both [^{89}Zr]Zr(oxalate)$_4$ and [^{89}Zr]ZrCl$_4$ offer the possibility to be able to choose the better starting compound depending on the chelation chemistry and application.

The vast majority of hydroxamate resins currently used by different institutions and described in the literature are prepared in-house, hence minor differences in the experimental data are normal and expected. The material and methods section at the end of this chapter describes in more detail the production of zirconium-89 that was used during the time of this work. One of the main advantages of the cyclotron production of zirconium-89 is that there is no need to use an isotopically enriched target material, since yttrium as

the starting material is a monoisotopic element [25] which is also cheap and makes the production process affordable and efficient.

3.2.4 Zirconium-89 chemistry and chelator design for PET imaging

Zirconium primarily exists as an ion with the oxidation state of +4 in aqueous solution. This Zr^{4+} cation is a relatively large ion which typically forms coordination complexes with high coordination numbers and a preference for anionic oxygen donor [26]. The hexaaqua ion $Zr(H_20)_6^{+4}$ only exists in very low zirconium concentrations and in highly acidic aqueous solutions. In neutral solutions, i.e. in the absence of any complexing agents, zirconium is mostly found in polynuclear and polymeric form [27] which hinders the complex formation with a chelator. As with any radiometal, special care and attention needs to be paid to appropriate and optimal labelling conditions to reach high radiochemical yields and efficient chelation.

Several chelators have been evaluated for efficient and stable ^{89}Zr-chelation over the years, such as diethylenetriaminepentaacetic acid (DTPA) and ethylenediaminetetraacetic acid (EDTA), however with rather limited success due to low stability [28]. The most prominent chelator that has emerged for the chelation of zirconium-89 is DFO which has become the most frequently employed chelator for antibody labelling. [^{89}Zr]Zr-DFO-mAb conjugates have been used in a number of clinical trials for *in vivo* tracking and quantification of monoclonal antibodies (mAbs) by PET with good imaging quality. However, there have been concerns about the stability of the complexes *in vivo*, not only in relation to image quality, but also in regard to radiation dose. Several preclinical studies have reported noticeable bone accumulation of dissociated zirconium-89 from the labelled antibody [29],[30]. Unchelated zirconium-89, in the form of [^{89}Zr]Zr-chloride and [^{89}Zr]Zr-$(oxalate)_4$, results in bone uptake of ~15% ID/g and ~20% ID/g respectively at 8 h post-injection *in vivo*. Zirconium has a high affinity for phosphates and it is very likely that zirconium-89 is chelated by hydroxyapatite, which forms the matrix of bones [31]. Despite the apparent instability of the [^{89}Zr]Zr-DFO complex observed in mice, human immuno-PET imaging studies using zirconium-89 do not appear to suffer from the same degree of dechelation *in vivo* and subsequent bone uptake [32],[33].The observed instability of some [^{89}Zr]Zr-DFO-mAb conjugates *in vivo* has led to the development and investigation of more stable octadentate ligands compared to DFO as a hexadentate ligand (**Fig. 3.2**) and work on predicting the thermodynamic stability of ^{89}Zr-tracer has been undertaken in addition [34].

However, the design of the chelator and ligand used for cell labelling applications differs with the respective cell labelling approach, e.g. direct versus indirect cell labelling, as elaborated in detail in the previous chapter 2 and metastable complexes like [^{89}Zr]Zr-Oxine are well suited to intracellularly label cells.

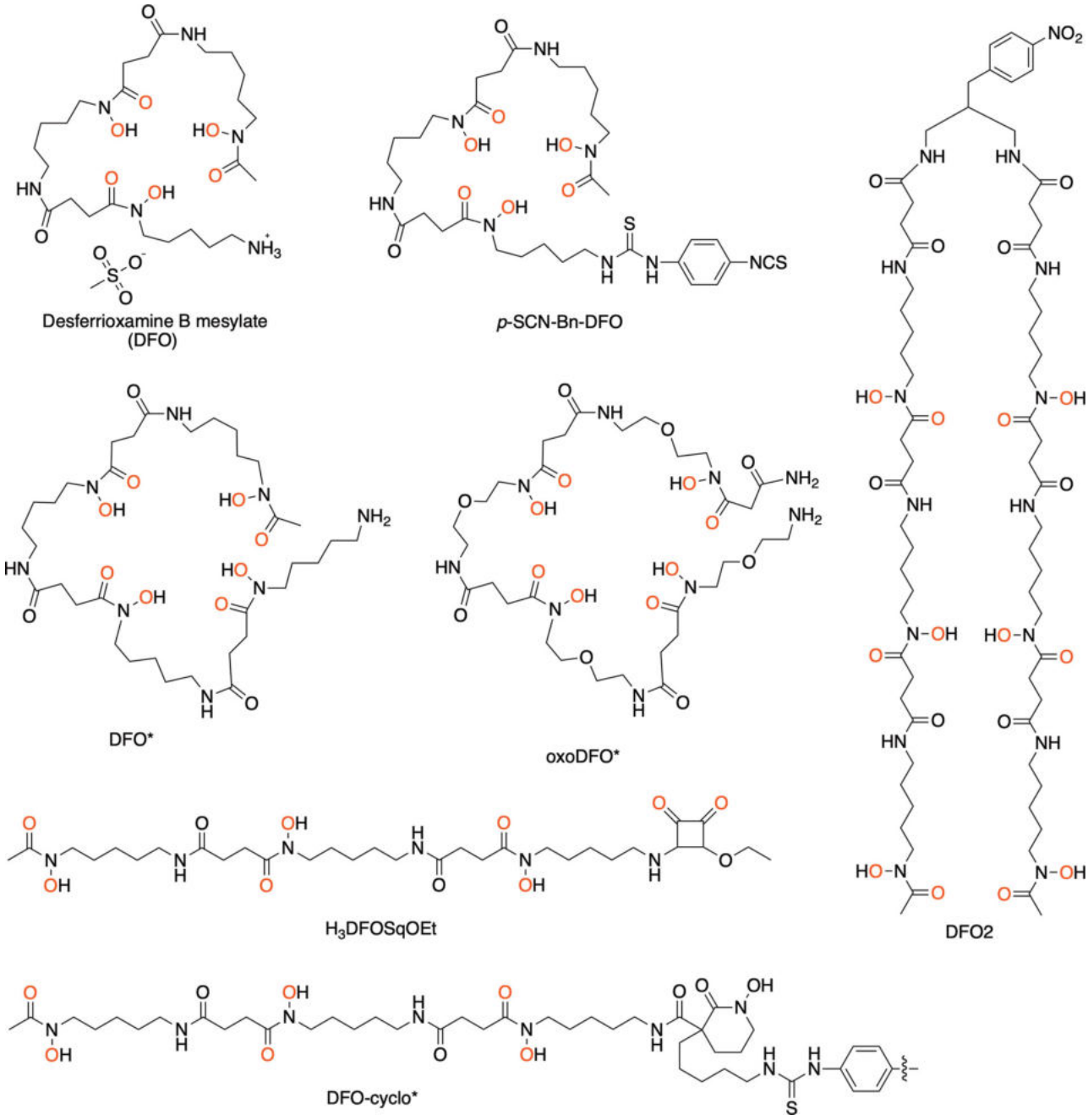

Figure 3.2 Chemical structures of selected and recently reported bifunctional chelators for zirconium-89. Oxygen donors for ^{89}Zr-chelation are highlighted in red. Figure copied from [35].

3.2.5 Zirconium-89 for cellular labelling

[^{89}Zr]Zr-Oxine has emerged as the PET analogue to [^{111}In]In-Oxine that has been used for white blood scintigraphy. Up to today, several different synthesis methods of [^{89}Zr]Zr-Oxine that are summarised briefly in **Table 3.1**.

Table 3.1 Different synthesis methods for [^{89}Zr]Zr-Oxine described in the literature.

Method	Chemical form of zirconium-89	Reference
Chloroform method	[^{89}Zr]Zr(oxalate)$_4$	[36]
HEPES method	[^{89}Zr]Zr(oxalate)$_4$	[37]
Chloride method	[^{89}Zr]ZrCl$_4$	[38]
Kit formulation	[^{89}Zr]Zr(oxalate)$_4$/[^{89}Zr]ZrCl$_4$	[39]

The first method described for the synthesis of [^{89}Zr]Zr-Oxine included a two-phase system where zirconium-89 was added in an aqueous solution to oxine (8-hydroxychinolin) in a chloroform phase ('chloroform method') [36]. Phase mixing and subsequent separation can yield [^{89}Zr]Zr-Oxine in the chloroform phase after evaporation and [^{89}Zr]Zr-Oxine can be formulated in DMSO for further use. This procedure includes many time-consuming phase separation steps and pipetting steps with increased exposure and hand dose. In comparison, the HEPES method uses oxine dissolved only in HEPES buffer where the zirconium-89 in the form of [^{89}Zr]Zr(oxalate)$_4$ is added to. According to the literature, was not required using this method [37]. In order to prevent the use and application of oxalic acid on cells the 'chloride method' uses [^{89}Zr]ZrCl$_4$, either converted to from [^{89}Zr]Zr(oxalate)$_4$ or as synthesised in some cyclotrons at other sites. Only recently did the development of a 'kit formulation' emerge for more translatable and easier cell labelling. Either [^{89}Zr]Zr(oxalate)$_4$ or [^{89}Zr]ZrCl$_4$ can be added to a premixed formulation containing oxine as a ligand and also a surfactant which at the same time minimises tracer loss while avoiding the use of DMSO for better solubility of [^{89}Zr]Zr-Oxine.

All of the above methods for the synthesis of [^{89}Zr]Zr-Oxine and their subsequent application for cell labelling differ from the methods used for white blood scintigraphy with indium-111 which uses different radiometal chemistry as described in section 3.2.3. However, the established and patented kit formulation method is the first that comes close the ^{111}In-method [40].

Before working with zirconium-89 and labelling cells, several prerequisites had to be established which included the necessary documentation and paper work regarding safety, lab space, equipment, and also logistics that are significantly for long-lived, high energy isotopes compared to the requirements for short-lived isotopes. Long-lived isotopes like zirconium-89 require a higher safety and risk awareness which needs to be implemented and respected in the work flow, such as dedicated equipment. In preparation for future cell work and to analyse the functional effect of radiotracer on cells using flow cytometry, the staining and subsequent storage for up to two weeks (in order for radioactivity to decay) before analysis at a later point was assessed. Two weeks is ~4 half-lives of zirconium-89 and can significantly reduce the radioactivity in the sample so that it can be safely analysed on a shared instrument where radioactivity is not commonly used. This essential work will be elaborated briefly in this chapter together with some preliminary work in preparation for the cell labelling work.

3.3 Materials and Methods

All starting reagents and solvents were obtained from commercial sources and used without further purification unless otherwise stated. Rituximab (10 mg/mL stock solution), directed against CD20 and Nivolumab (10 mg/mL stock solution), directed against PD-1, were obtained from VU Medical Center Amsterdam. ^{89}Zr (>0.15 GBq/nmol in 1 mol/L oxalic acid) was obtained from BV Cyclotron VU and was produced by the ^{89}Y(p,n)^{89}Zr reaction as publishes previously [41]. Briefly, an ^{89}Y-target was bombarded with 14 MeV protons for 2-3 h (65-80 A) while the target support was cooled with water (AVF cyclotron; Philips). ^{89}Y targets were prepared by sputtering an ^{89}Y layer (35 m; Highways International) on a copper support (Mallinckrodt Medical) as described by Meijs *et al.* [19]. Hydroxamate column material for purification of zirconium-89 was prepared from Accell Plus CM cation exchange medium (300 Å, 0.35 mmol/g ligand density; Waters). In the second reaction step, hydroxamate groups were introduced on the resin via the reaction of the ester groups with an excess of hydroxylamine hydrochloride (Aldrich). After loading of the ^{89}Zr-target solution onto the column, the column was rinsed with 6 mL of 2 mol/L HCl and 6 mL of sterile water for injection, respectively. Under these conditions, zirconium-89 and the trace amount of zirconium-88 remained bound to the resin, whereas yttrium-89 and radionuclide metal impurities were eluted. The zirconium isotopes were eluted with 5 successive portions of 0.5 mL of 1 mol/L oxalic acid (Aldrich).

Ethical approval for all cell studies was sought from an independent UK National Research Ethics Committee. Blood from healthy donors was collected for isolation of peripheral blood mononuclear cells (PBMC) and all human biological samples were sourced ethically and their research use was in accord with the terms of the informed consents under an Institutional Review Board/Ethics Committee (IRB/EC) approved protocol (REC reference: 17/NE/0168, IRAS project ID: 222704). All donors provided written, informed consent.

Cell work

PBMC's from heparinised blood were processed and extracted via Ficoll-Paque gradient centrifugation. Freshly taken blood was allowed to remain in heparin tubes for at least 20 min at RT before use. Blood samples were transferred into an Erlenmeyer flask and diluted 1 in 4 with PBS (Fisher Scientific). The diluted blood was carefully layered over 10 mL of Ficoll-Paque PLUS (VWR) into 50 mL tubes up to 45 mL total volume and spun for 25 min at 400 x g at RT. The PBMC's were carefully removed from the interface between the Ficoll and plasma using a sterile plastic pipette and then transferred into a fresh 50 mL falcon tube. An excess of PBS (at RT) was added to the isolated PBMC's up to a volume of 40 mL. The falcon tube was gently inverted and the cells were spun down at 350 x g for 5 min at RT. The supernatant was decanted off, the remaining cell pallet was flicked, and 15 mL PBS was added. All PBMC-PBS suspensions were combined in one falcon tube and spun again at 350 x g for 5 min. All supernatants were poured off by holding the tube inverted for 10 seconds and the remaining PBS droplet was flicked off. The remaining cell pellet was flicked as well and resuspended in 5 mL PBS. The cell suspension was filtered through a Partec 0.3 µm filter and the original tube was rinsed with 1 mL PBS and added to the filter as well. Cells were then counted using a haemocytomer using 0.4 % trypan blue solution. The cells were then either frozen for stock or used immediately for further experiments at a later point.

Lab set-up, equipment and logistics

For the set-up of a dedicated working area, lead bricks were collected from the radiation safety office to construct a lead castle as a shielded working area for radiosynthesis (**Fig. 3.3**). A Capintec CRC-55t dose calibrator was purchased and installed to measure activities used for synthesis. In addition, a dedicated incubator for radioactive cell culture was

purchased and installed in the radio-lab together with CO_2 supply and monitoring. A micro-centrifuge for spinning down radioactive cell samples was also purchased and installed. A laminar flow cabinet (LFC) was acquired and set-up for sterile culture of radioactive cells (**Fig. 3.3**).

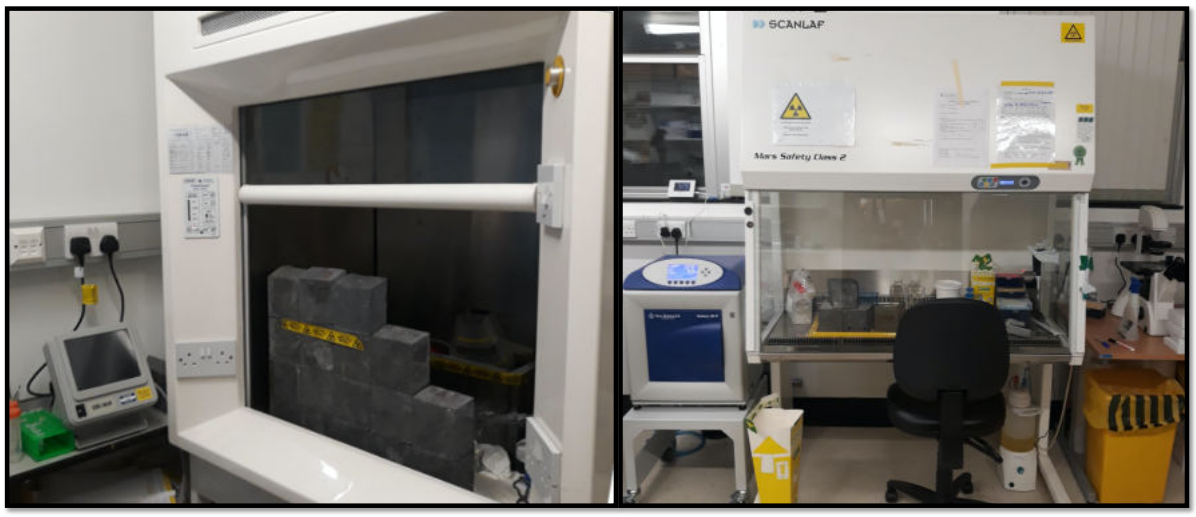

Figure 3.3 Laboratory set-up in the hot lab for radiosynthesis (left photo) and for radioactive cell culture (right photo).

As the cell culture area is outside of the hot lab, rules and risk assessments for the movement of radioactivity with the according safety measurements had to be established. A system for both the purchase and the delivery of zirconium-89 had to be set up from scratch. The involved parties had to be trained for the process and the necessary paperwork beforehand and upon arrival had to be taken care of. In addition, a ledger for the arrival of the isotope had to be created that documents the arrival and holding of all ^{89}Zr-stocks in the goods in department. Stock and sub-stock sheets for the handling in the lab also had to be drawn up that include the documentation of every aliquot taken from the ^{89}Zr-stock and its waste route. Finally, the waste disposal route and the logistics around it had to be established, all approved and audited by the safety office similarly to the local rules that had to be written and established for this particular work. A list of all necessary documentation and risk assessments that needed to be established is provided in the next section. **Figure 3.4** gives a graphical overview of all required steps that need to be taken care of for each delivered zirconium-89 batch starting from the ordering and delivery of the isotope to the final disposal after decay storage.

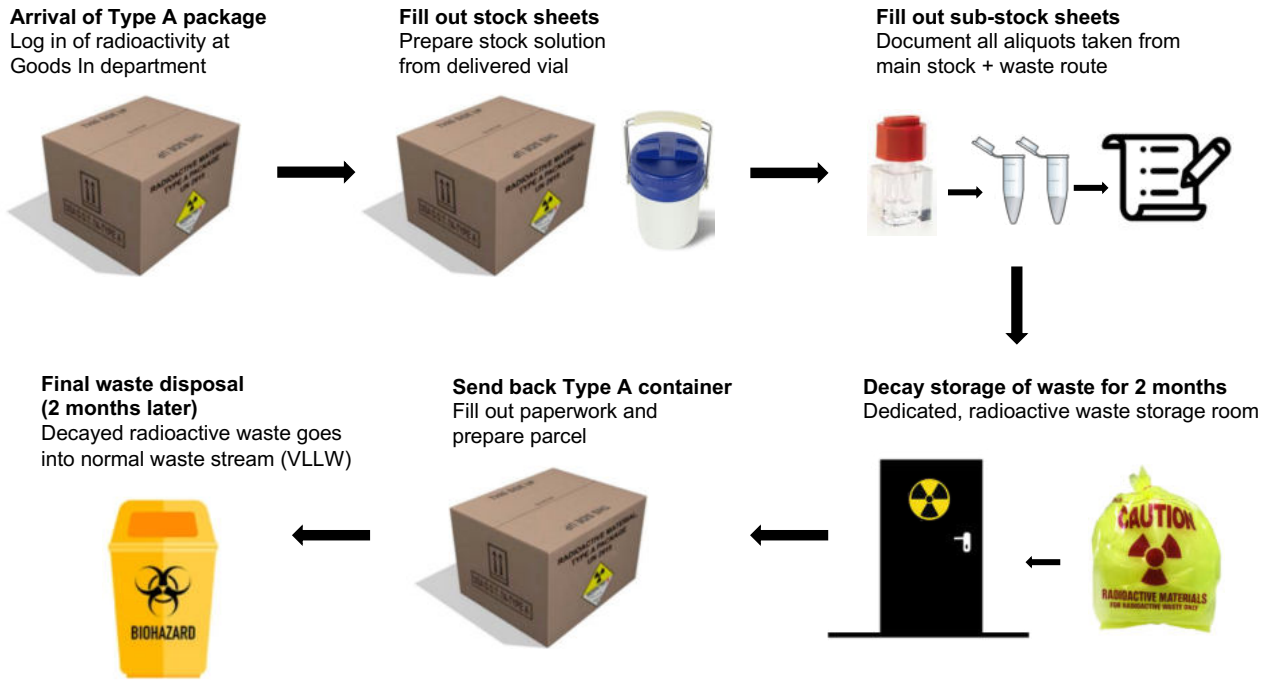

Figure 3.4 Overview of all necessary steps for each delivered zirconium-89 batch from delivery to final disposal.

Ethical approval and safety documents

For this project a new study was set-up and new ethics were written and submitted for approval. The approved study allows the recruitment of healthy volunteers for taking blood to extract cells from whole blood for radiolabelling experiments. To be able to receive zirconium-89, the Addenbrooke's site permit had to be amended and a local sub-permit for the use of zirconium-89 had to be obtained based on the radiation safety documents that were written and approved (**Table 3.2**). These documents can be found in the **Special Appendix** to this thesis.

Table 3.2 Different types of documents that needed to be written and put in place before work with zirconium-89 could commence.

Type of document	Specification and purpose
Ethics application	Set-up of new IRAS project and ethics application to gain HRA approval for cell labelling study
Local rules	Establishment of local rules for the procedures carried out in the hot lab including purchase, disposal of zirconium-89 and action plan in case of spills and emergencies
Risk assessment	Risk assessment of radiochemical synthesis and all necessary steps
Risk assessment	Risk assessment of radioactive cell culture
Risk assessment	Risk assessment of movement and transport of radioactive samples to other facilities for experiments or analysis
Stock sheets	Establishment of stock sheets that record the incoming radioactivity and its sub-stocks used for synthesis including the waste route
Waste sheets	Waste record sheets for the disposal of every ^{89}Zr-delivery including record for decay storage

Flow cytometry

Cells were stained using a range of antibodies (BD, eBioscience, Biolegend; see **Table 3.3**) and blocked using 2% mouse serum (or 1% FCS for murine cells) in FACS buffer and/or Tru block monocyte blocker (Biolegend) as required. Briefly, cells were first resuspended in PBS and then stained with 100 µL fixable viability dye (Zombie NIR, Biolegend used at 1:200) for 15 min at room temperature in the dark. Next, the cells were washed twice in FACS buffer with a spin at 600 g for 5 min and then labelled with 100 µL of lymphocyte phenotyping panel antibody cocktail containing TruBlock (Biolegend) in FACS buffer for an additional 15 min at 4 ^{o}C. Cells were then kept on ice and washed twice with FACS buffer, pelleted at 600 g for 5 minutes before finally being resuspended in fixative (either 0.25% or 1% PFA or BD Facs Fix buffer, BD biosciences). Single colour and FMO controls were prepared for each channel using cells and/or compbeads (Invitrogen). Flow acquisition for phenotyping was performed on the FACSCanto™ II or LSR-Fortessa™ (BD Biosciences)

and analysed using FlowJo v7.6.5-v10.0 (Tree Star Inc). The detailed gating strategy is shown in **Figure 3.9**. An average of 100000 events were recorded per sample.

Table 3.3 Antibodies used for staining and subsequent flow cytometry analysis.

Channel	Marker: Canto Panel	Marker: Fortessa Panel	Antibody/clone/manufacturer	Amount/test
FITC	CD14	CD14	BD # 555397	20
PE	CD19	CD19	BD #555413	20
PEcy5	CD4		BD #555348	10
PEcy7	CD3		BD clone SK7 #557851	4
V450	CD69		BD Horizon: clone FN50 #560740	5
		CD4	BD clone RPA-T4: #560345	4
BV510	CD56	CD56	BD clone NCAM16.2 #563041	5
APC	CD8	CD8	BD #555369	20
APCcy7	Z.NIR*	z.NIR	Biolegend #423105	1:100 in PBS
UV395		CD3	BD horizon clone SK7: #564001	5
UV737		CD69	BD horizon clone FN50: #564439	5

* Zombie NIR™ is an amine reactive fluorescent dye that is non-permeant to live cells, but permeant to the cells with compromised membranes. Thus, it can be used to assess live vs. dead status of mammalian cells. Zombie NIR™ is a polar water soluble dye, providing red fluorescence, making it suitable for multi-color detection.

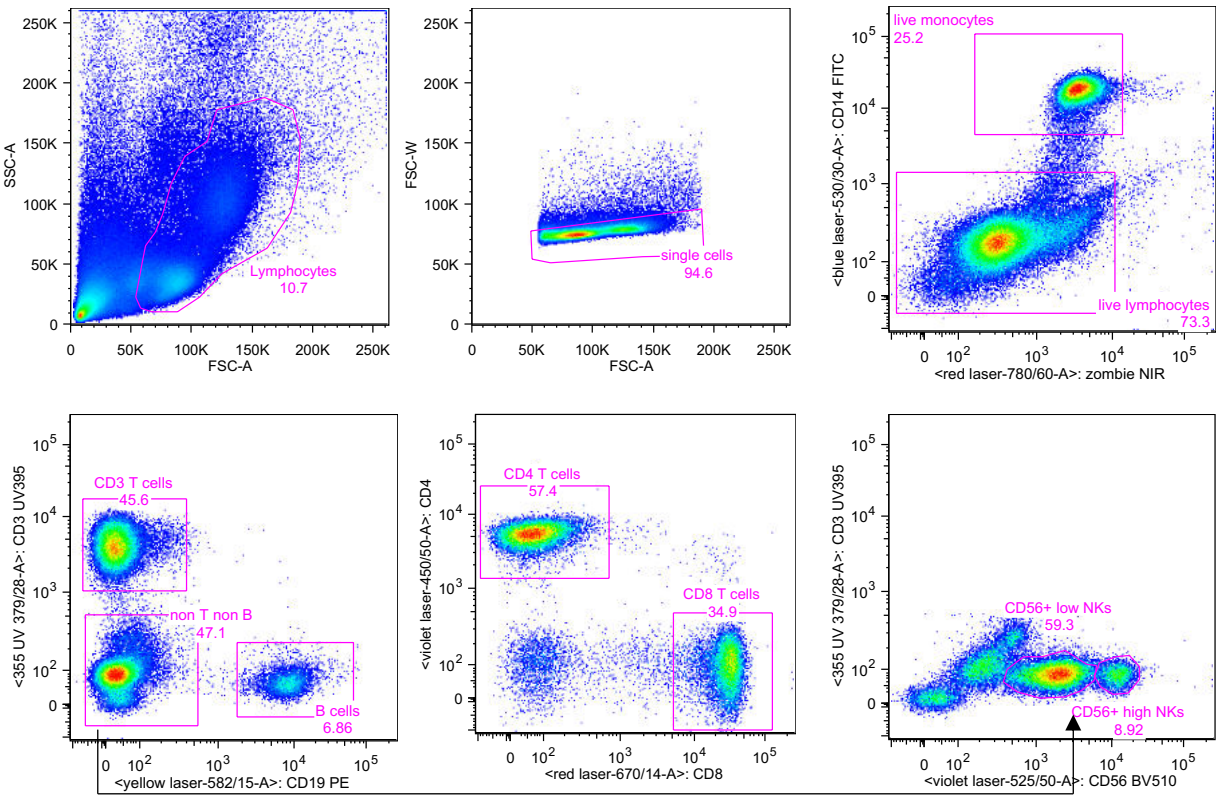

Figure 3.5 Gating strategy used for the analysis of stained PBMCs. Cells were gated based on size and granularity using FSC-A vs SSC-A to eliminate debris and clumped cells. Single cells were sub-gated using fixable viability dye zombie NIR™ and monocytes discriminated by the expression of CD14 (top row from left to right). Subsequently, lymphocytes were sub-gated and and T-cells and B cells discriminated by the expression of CD3 and CD19 respectively, with further sub-gating of the CD3 population into CD4 and CD8 T-cells. Finally, non T- and B-cells were sub-gated and NK cell populations discriminated by the expression of high and low CD56 (bottom row from left to right). SSC-A: side scatter area, FSC-A: forward scatter.

Synthesis of ^{nat}Zr-(oxalate)$_4$

^{nat}Zr-(oxalate)$_4$ was prepared according to an in house developed method at the VUMC. Prior to the preparation of the hydroxamate column, 1 M oxalic acid (pH acceptance 0.5-0.9, Sigma Aldrich 24-753-7), 4 M HCl and 2 M HCl (from 37 % HCl, Fluka 84415) were freshly prepared. 100 mg hydroxamate column material (BV cyclotron VU Amsterdam) was weighed into a sterile glass vial. 4 mL of sterile 0.9 % NaCl for injection (hospital pharmacy) was added to the vial and the column material was resuspended. An Alltec, extra-clean tube (volume: 1.5 mL), and a frit plus adapter were attached to a 20 mL syringe without a luer lock. The 1.5 mL extract-clean tube was placed into a 50 mL sterile plastic tube with a punctured cap. The tube functions as a holder and waste container. The hydroxamate

column material suspension was pipetted into the extract-clean tube and the glass vial with column material was rinsed two times with 2 ml 0.9 % NaCl. The syringe plunger was used for washing the column with 20 mL MeCN. The 50 mL tube with MeCN was used as waste container and a new 50 mL tube was attached to the extract-clean tube. Subsequently, the column was washed with 30 mL 0.9 % NaCl and 12 mL 2 M HCl afterwards. To dry the column, air was pushed through the column with the plunger. 11 vacutainer blood collection tubes (no additives) were taken from a sterile store cupboard and labelled with:

1. 5 mL 2 M HCl
2. 5 mL 2 M HCl
3. 3 mL Water
4. 3 mL Water
5. 0.5 mL 1 M Oxalic acid
6. 0.5 mL 1 M Oxalic acid
7. 0.5 mL 1 M Oxalic acid
8. 0.5 mL 1 M Oxalic acid
9. 0.5 mL 1 M Oxalic acid
10. 0.5 mL 1 M Oxalic acid

A 15 ml solution of 4 M HCl solution containing $ZrCl_4$ and a trace of [^{89}Zr]Zr-(oxalate)$_4$ was prepared (3.8 mg $ZrCl_4$; 16.31 µmol + ^{89}Zr: 88583 cpm for the first run; 10.2 mg $ZrCl_4$; 43.77 µmol + ^{89}Zr: 92815 cpm for the second run) and transferred into the syringe that is connected to the hydroxamate column. The solution was pushed slowly over the hydroxamate column. The syringe was washed with 15 mL 4 M HCl and the waste was collected.

The ^{89}Zr/Zr mixture was eluted from the hydroxamate column in the order as the labelled vacutainers with the required volumes of mobile phase, followed by puncturing the container until the solvent is passed over the column. 1 ml sample of the waste (whole waste 30 ml) in a blood tube (weighed before and after) is taken for gamma counting. The activity of all fractions was measured in the gamma counter to be able to calculate the concentration of ^{nat}zirconium in oxalic acid based on the amount of ^{89}Zr-oxalate eluted from the hydroxamate column.

Synthesis of [^{89}Zr]Zr-Oxine

Chloroform method: [^{89}Zr]Zr-Oxine was synthesized in an aqueous solution according to a published literature procedure [36]. [^{89}Zr]Zr-oxalate stock was diluted to 500 µL water and neutralised with 1 M NaOH. 20 µL of a 10-mg/mL solution of 8-hydroxyquinoline in chloroform, in a screw-top round-bottomed tube and held onto a vortex mixer for 5 min using. Chloroform was added (480 µL) before vortexing for 25 min. After brief centrifugation, the chloroform phase containing [^{89}Zr]Zr-Oxine was removed and evaporated at 80 °C in a conical bottom vial before resuspension in 15 µL of DMSO.

HEPES method: The [^{89}Zr]Zr-Oxine complex was synthesized in an aqueous solution according to a published literature procedure [37]. 250 µL (1.8 µmol) of a 1 mg/mL 8-hydroxychinoline (oxine) solution in 0.1 M HEPES was added to 6.4-7.5 MBq of neutralized [^{89}Zr]Zr-Oxalate (pH 7). The solution was incubated for 30 min at room temperature.

Chloride method: [^{89}Zr]$ZrCl_4$ was obtained by loading commercial [^{89}Zr]Zr-oxalate onto a Sep-Pak Light Plus QMA cartridge (Waters), washing the cartridge with 10 mL H_2O, and eluting with 500 µL of 1 M HCl according another published literature procedure [42]. Oxine in 0.04 N HCl (102 µL, 20 mmol/L) and $^{89}ZrCl_4$ were mixed in the presence of Tween 80 (4 µL, 20%) (Sigma-Aldrich, St Louis, Mo). $NaHCO_3$ (500 mmol/L) was slowly added to this solution while it was spun in a vortex, thereby allowing chelation of ^{89}Zr by oxine to take place while neutral oxine was released from its acidic forms.

Kit formulation: Briefly, a solution containing 8-hydroxyquinoline (oxine; final concentration 0.5 mg/mL), 1 M HEPES and polysorbate 80 (1 mg/mL) in ultrapure H_2O was adjusted to pH 7.9–8.0 with aqueous NaOH (10 M). The resulting solution was dispensed in 100 µL aliquots into Eppendorf tubes and stored at RT. This solution is referred to as ‘kit formulation’. 0.5-2.8 MBq [^{89}Zr]Zr-oxalate in 1 M oxalic acid was added to the kit formulation and left at RT for 5 min before quality control via TLC and further use. Alternatively, [^{89}Zr]$ZrCl_4$ can be used instead of [^{89}Zr]Zr-oxalate.

3.4 Results

Preliminary work

Firstly, the preliminary work included training undertaken at the VUMC Amsterdam in the Radionuclide Centre where I learned about the handling, precautions and arrangements required for a lab when working with zirconium-89. This included ^{89}Zr-labelling of antibodies but also the synthesis of cold ^{nat}Zr(oxalate)$_4$ and their respective analytical methods. Secondly, cell labelling with zirconium-89 was set-up and established using the methods described in section 3.2.5 and below. Finally, flow cytometry work was undertaken to test whether samples could be stored for longer and still be analysed in preparation for potential radioactive work at a later stage.

^{89}Zr-labelling of monoclonal antibodies (VUMC)

Two monoclonal antibodies (mAbs), Rituximab and Nivolumab, were labelled with [^{89}Zr]Zr-(oxalate)$_4$ solution, produced at the BV Cyclotron in Amsterdam. The labelling work was carried out over several days using different linker strategies to conjugate the DFO chelator to the respective antibody for subsequent labelling, purification via PD-10 cartridge and quality control of the ^{89}Zr-labelled antibodies. These included radio-thin layer chromatography (TLC), radio-high performance liquid chromatography (HPLC), sodium dodecyl-sulfate polyacrylamide gel electrophoresis (SDS PAGE) and binding assays (Lindmo assay). This work will not be further elaborated here but was a very important part of the training and set-up of the cell labelling project in Cambridge.

Synthesis of ^{nat}Zr-(oxalate)$_4$ (VUMC)

^{nat}Zr-(oxalate)$_4$ solution was synthesised similar to the production of [^{89}Zr]Zr-(oxalate)$_4$ for radioactive labelling procedures. The aim of this synthesis was to generate the cold equivalent of [^{89}Zr]Zr-(oxalate)$_4$ solution.

First, the hydroxamate column was prepared where ^{nat}zirconium is trapped and subsequently eluted with oxalic acid to give ^{nat}Zr-(oxalate)$_4$ solution as a product. The cold zirconium in the form of $ZrCl_4$ was spiked with [^{89}Zr]Zr-(oxalate)$_4$ solution to determine the final concentration of ^{nat}Zr-(oxalate)$_4$ by assessing the radioactive fraction that is trapped and eluted from the hydroxamate column. The concentration can therefore be inferred from

the radioactive [^{89}Zr]Zr-(oxalate)$_4$ yield. The synthesis was undertaken following a standard procedure developed internally by researchers at the VUMC Amsterdam. Detailed procedures are described in the methods section of this chapter. The ^{nat}Zr-(oxalate)$_4$ was shipped to Cambridge for cold labelling at a later point.

Setup of [^{89}Zr]Zr-Oxine synthesis for cell labelling

A cell labelling methodology was set up using [^{89}Zr]Zr-Oxine, and three of the synthesis methods for [^{89}Zr]Zr-Oxine mentioned above were investigated and tested to enable use of [^{89}Zr]Zr-Oxine as a comparator in subsequent experiments. Whereas the chloroform method was very cumbersome and did not yield much [^{89}Zr]Zr-Oxine, the HEPES method consistently resulted in significant tracer loss in the vial and pipette tips without the use of DMSO, in contrast to what has been previously published [37]. The chloride method was used prior to the publication of the kit formulation [39] which was mostly used for the work described in **chapter 5 and 6**.

Flow cytometry work

Freshly harvested peripheral blood mononuclear cells (PBMCs) were stained with several dyes specific for cell surface markers, i.e. CD14, CD19, CD3, CD4, CD8, CD56, CD69 and Zombie NIR™ to assess viability. The same experiment evaluated 3 different fixatives, namely 0.25 % PFA, 1 % PFA and FacsFix, to potentially optimise the fixation for future staining experiments as both the cells and the analysis can be affected by the fixation process of cell. FacsFix is a commercial product recommended to be better for maintaining flurochrome stability on fixed cells, 1% PFA is a lab standard protocol for fixing cells whereas there is a questions as to whether lower concentration of PFA can be used and are sufficient to fix cells without compromising fluorochrome stability, especially when keeping cells for a long time before running them on the cytometer. This work therefor also integrated the comparison of different fixatives in combination with long-term storage of fixed cells and also investigated the lower end of PFA concentration, in this case 0.25 % PFA, for fixing cells. The gating strategy that was used is shown in the methods section 3.4. Flow cytometry analysis was originally undertaken on both the BD LSR-Fortessa™ and BD FACSCanto™ II instruments, however the Canto II was not functioning to compare the use of tandem dyes and whether these would also be suitable to use in such an experimental set-up in terms of stability. Therefore, the following results reflect the analysis undertaken

on the Fortessa instrument only. **Fig. 3.6**, **Fig. 3.7** and **Fig 3.8** show the analysis over 14 days using 0.25 % PFA, 1 % PFA and FacsFix as a fixative, respectively.

The results show that 0.25 % PFA is sufficient to be able to clearly visualise and differentiate the stained cell populations over 14 days. Compared to 1 % PFA and FacsFix, 0.25 % showed the best results at day 14 in terms of visualisation of the data. The percentage of the different cell populations after gating as shown in **Fig. 3.9** changed only slightly and less than 10 % throughout all experiments and over 14 days. Similarly, the mean fluorescent intensity (MFI) values did not change noticeably over 14 days with only minor differences (**Fig. 3.10**) indicating a stable staining and intactness of the respective antibody. If the antibody-dye conjugates were unstable over time, a drop in MFI over time would be noticed over time which is not the case here. The reason for very low MFI values for CD4 and CD8 goes back to the fact that CD4 and CD8 T-cells have a bimodal distribution with half the cells being positive and half negative. In this case the MFI is not necessarily very informative.

A disadvantage of this approach is that fixation can cause auto-fluorescence from the fixative and can impact on the fluorescence lifetime of the dye. It is therefore important to optimise the fixation method. Flow cytometry analysis is commonly undertaken shortly after the fixation or on live cells, but in some cases samples may need to be stored for a few days until analysis is possible. As a rule of thumb, 4-5 half-lives need to pass for radioactivity to reach an acceptably low level close to background radiation. This would be ~2-2.5 weeks for zirconium-89 and stained samples would need to be stored safely during this time. The results, as depicted in **Fig. 3.6**, **Fig. 3.7** and **Fig. 3.8**. show that it is possible to store stained and fixed cells using different fixative approaches up to day 14, and that this could be a viable option when using ^{89}Zr-labelled cells for analysis. This work has evaluated several commonly used dyes used, and the use of other, more specific dyes would need to be evaluated for this approach to be shown to be widely applicable. In addition, this experiment was undertaken with only one sample per time point and fixative. Therefore, replicate measurements and statistics were not possible due to a limited number of cells that were available for staining.

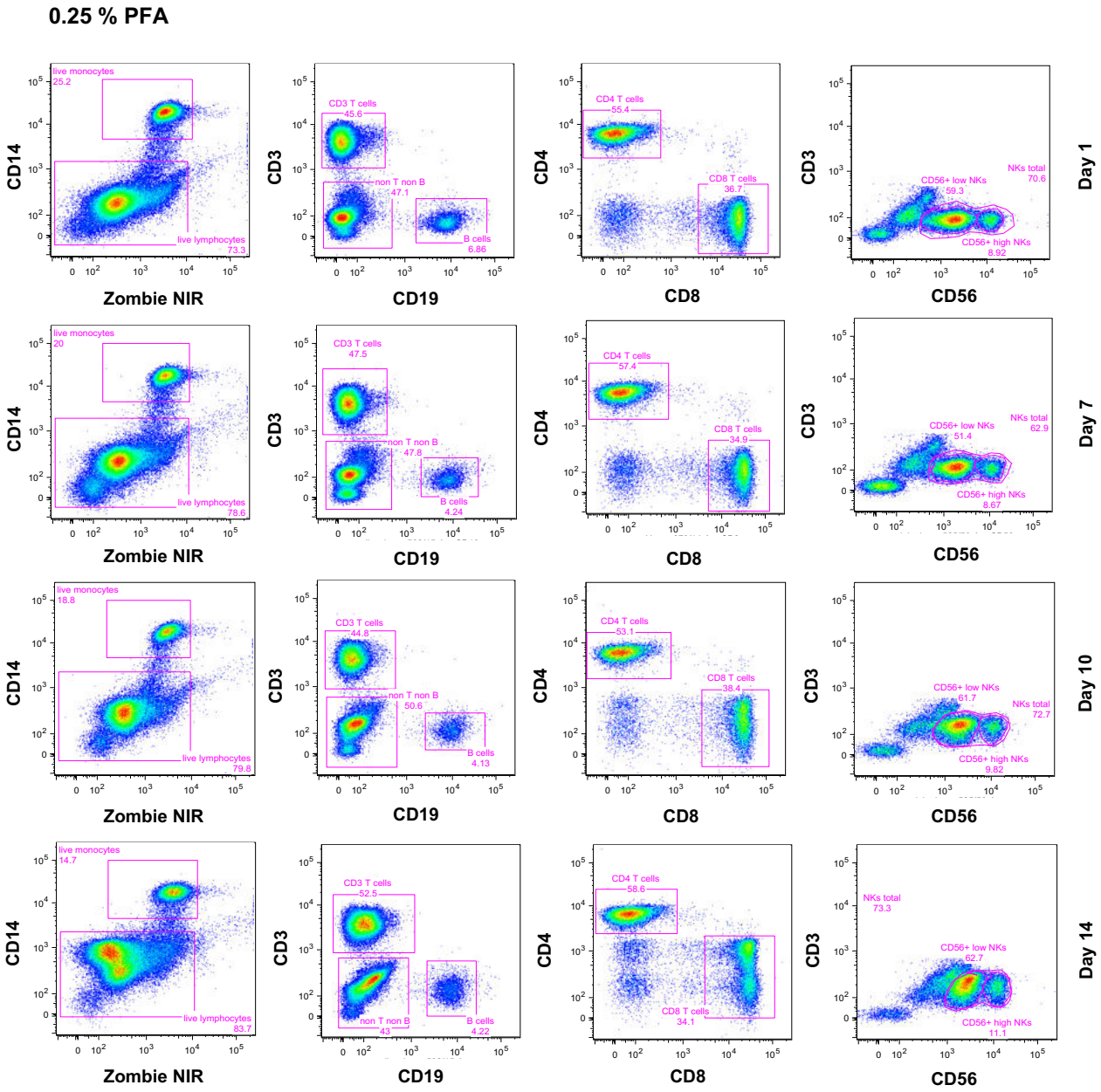

Figure 3.6 Flow cytometry analysis of stained PBMCs using 0.25 % PFA as fixative over 14 days. Gating was undertaken at day 1, 7, 10 and 14 (top row to bottom row) to analyse different cell subpopulations (gating: from left to right in each row). See **Fig. 3.5** in the material and methods section for detailed gating.

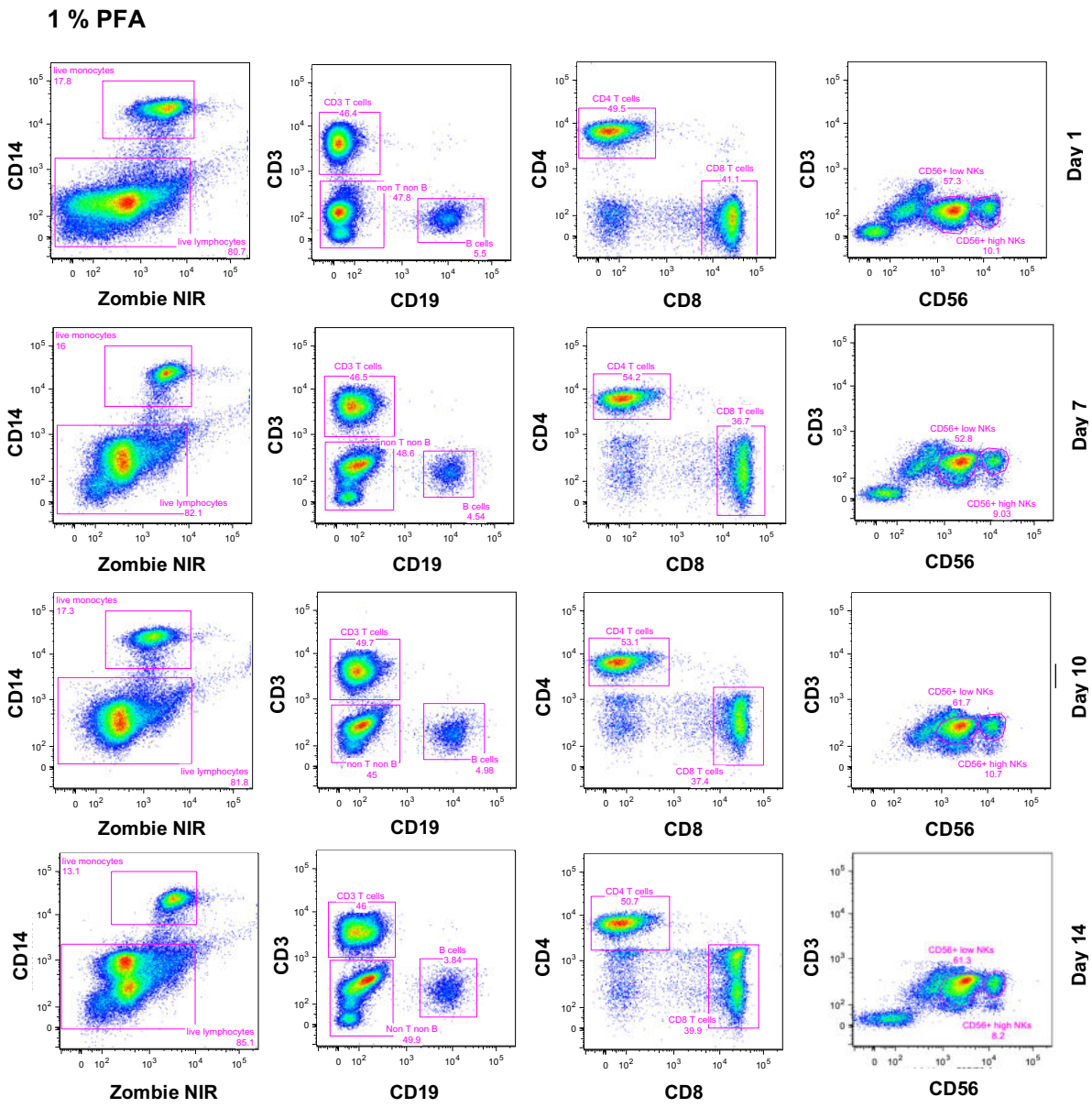

Figure 3.7 Flow cytometry analysis of stained PBMCs using 1 % PFA as fixative over 14 days. Gating was undertaken at day 1, 7, 10 and 14 (top row to bottom row) to analyse different cell subpopulations (gating: from left to right in each row). See **Fig. 3.5** in the material and methods section for detailed gating.

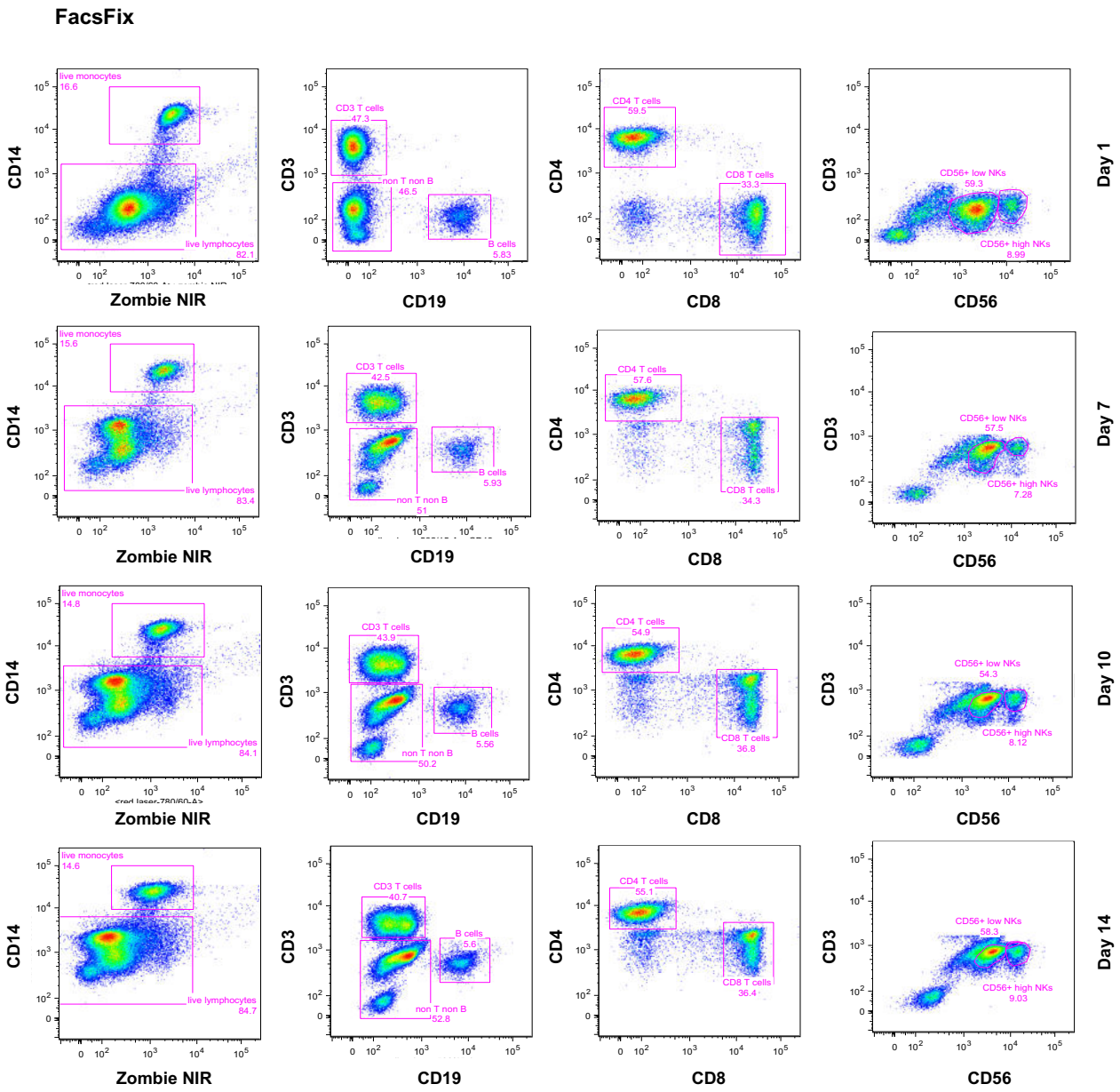

Figure 3.8 Flow cytometry analysis of stained PBMCs using FacsFix as fixative over 14 days. Gating was undertaken at day 1, 7, 10 and 14 (top row to bottom row) to analyse different cell subpopulations (gating: from left to right in each row). See **Fig. 3.5** in the material and methods section for detailed gating.

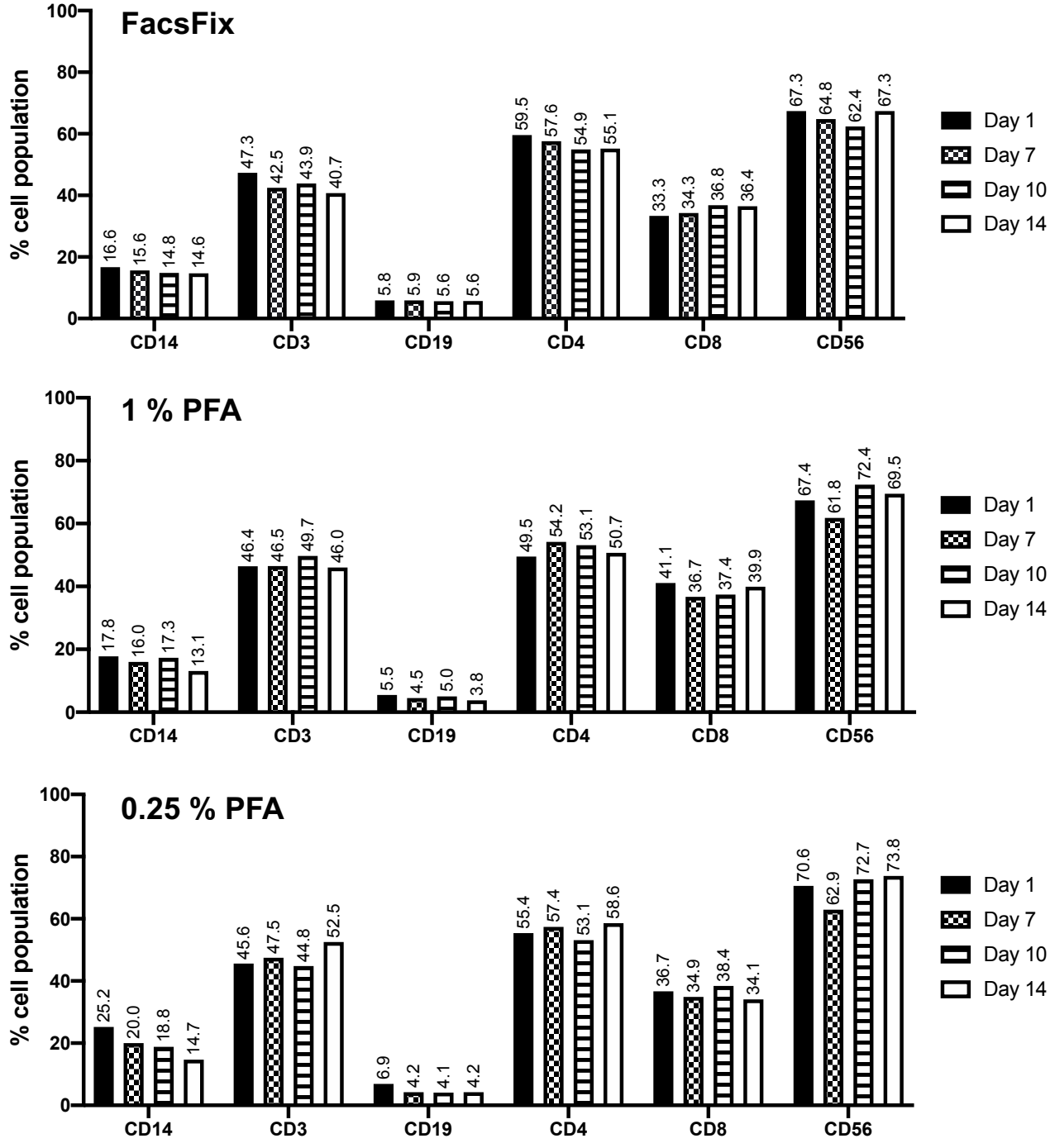

Figure 3.9 Summary of flow cytometry analysis of stained PBMCs and change of percentage of cell population using FacsFix, 1 % PFA, 0.25 % PFA, 1 % PFA over 14 days.

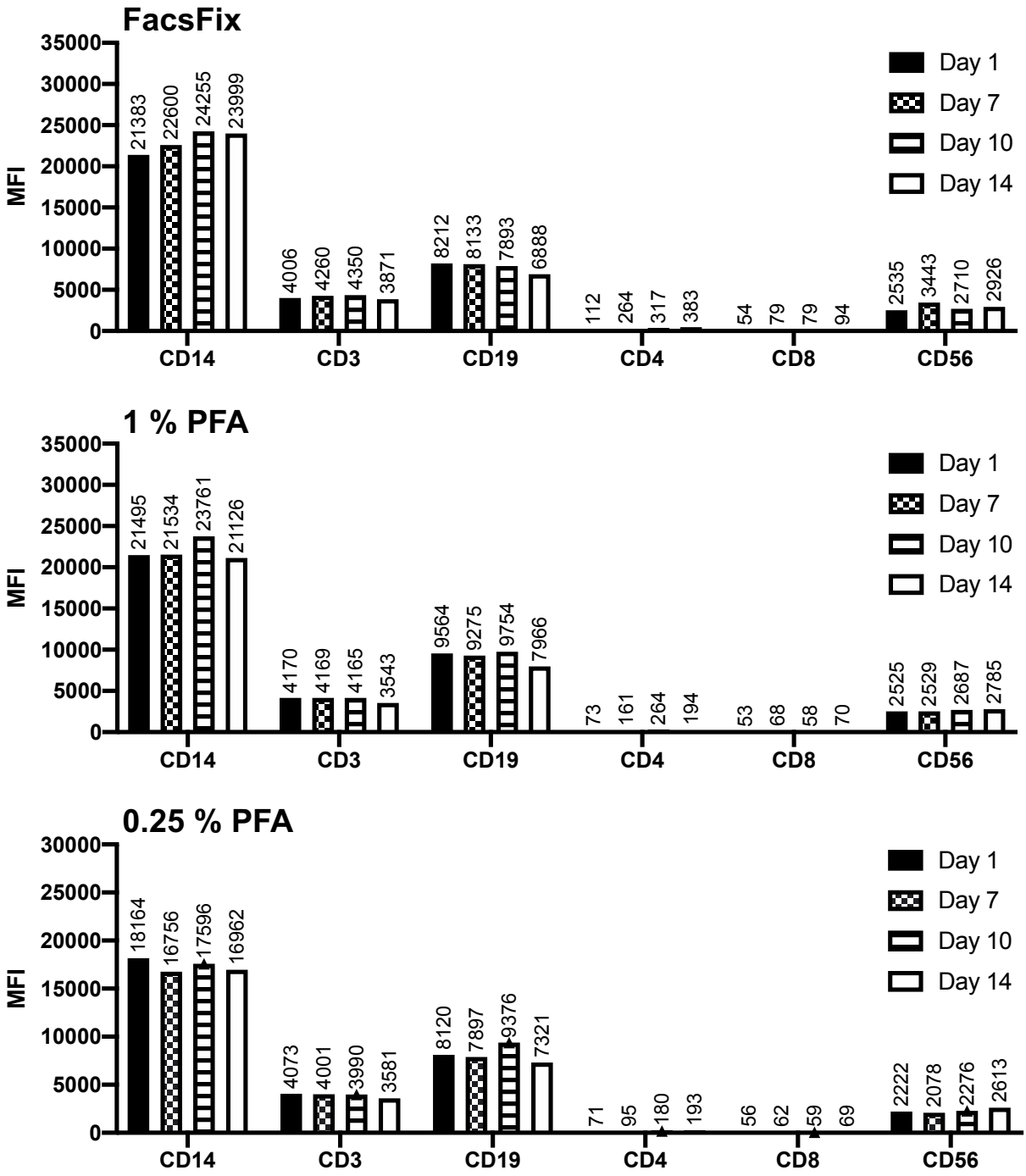

Figure 3.10 Summary of flow cytometry analysis of stained PBMCs and change of the MFI using FacsFix, 1 % PFA, 0.25 % PFA, 1 % PFA over 14 days

3.5 References

1. Cork JM, LeBlanc JM, Martin DW, Nester WH, Brice MK. Nuclear levels associated with zirconium 95 and niobium 95. *Phys Rev*. 1953;90(4):579-581.
2. McCLINTON LT, SCHUBERT J. The toxicity of some zirconium and thorium salts in rats. *J Pharmacol Exp Ther*. 1948;94(1):1-6.
3. Rama Sastry B V., Owens LK, Ball COT. Differences in the distribution of zirconium-95 and niobium-95 in the rat [33]. *Nature*. 1964;201(4917):410-411.
4. Bäckström J, Hammarström L, Nelson A. Distribution of zirconium and niobium in mice: Autoradiographic study. *Acta radiol*. 1967;6(2):122-128.
5. Mealey J. Turn-over of carrier-free zirconium-89 in man. *Nature*. 1957;179(4561):673-674.
6. MEALEY J. Application of positron-emitting zirconium-89 for potential use in brain tumor localization. *Surg Forum*. 1958;9:718-721.
7. McKnight BN, Viola-Villegas NT. 89Zr-ImmunoPET companion diagnostics and their impact in clinical drug development. *J Label Compd Radiopharm*. 2018;61(9):727-738.
8. Kurebayashi Y, Choyke PL, Sato N. Imaging of cell-based therapy using89 zr-oxine ex vivo cell labeling for positron emission tomography. *Nanotheranostics*. 2021;5(1):27-35.
9. Li N, Yu Z, Pham TT, Blower PJ, Yan R. A generic 89Zr labeling method to quantify the in vivo pharmacokinetics of liposomal nanoparticles with positron emission tomography. *Int J Nanomedicine*. 2017;12:3281-3294.
10. Gawne PJ, Clarke F, Turjeman K, et al. PET imaging of liposomal glucocorticoids using 89Zr-oxine: Theranostic applications in inflammatory arthritis. *Theranostics*. 2020;10(9):3867-3879.
11. Conti M, Eriksson L. Physics of pure and non-pure positron emitters for PET: A review and a discussion. *EJNMMI Phys*. 2016;3(1).
12. Table of Radioactive Isotopes. In: *Handbook of Radioactivity Analysis*. ; 1998:719-755.
13. Lubberink M, Herzog H. Quantitative imaging of 124I and 86Y with PET. *Eur J Nucl Med Mol Imaging*. 2011;38(SUPPL. 1).
14. Lindenberg L, Adler S, Turkbey IB, et al. Dosimetry and first human experience with 89Zr-panitumumab. *Am J Nucl Med Mol Imaging*. 2017;7(4):195-203.

15. Pandit-Taskar N, O'Donoghue JA, Ruan S, et al. First-in-human imaging with 89Zr-Df-IAB2M Anti-PSMA minibody in patients with metastatic prostate cancer: Pharmacokinetics, biodistribution, dosimetry, and lesion uptake. *J Nucl Med*. 2016;57(12):1858-1864.
16. Ulaner GA, Lyashchenko SK, Riedl C, et al. First-in-human human epidermal growth factor receptor 2–targeted imaging using 89 Zr-Pertuzumab PET/CT: Dosimetry and clinical application in patients with breast cancer. *J Nucl Med*. 2018;59(6):900-906.
17. Martí-Climent JM, Prieto E, Morán V, et al. Effective dose estimation for oncological and neurological PET/CT procedures. *EJNMMI Res*. 2017;7(1).
18. Fadeeva VI, Tikhomirova TI, Yuferova IB, Kudryavtsev G V. Preparation, properties and analytical application of silica with chemically grafted hydroxamic acid groups. *Anal Chim Acta*. 1989;219(C):201-212.
19. Meijs WE, Herscheid JDM, Haisma HJ, et al. Production of highly pure no-carrier added 89Zr for the labelling of antibodies with a positron emitter. *Appl Radiat Isot*. 1994;45(12):1143-1147.
20. Holland JP, Sheh Y, Lewis JS. Standardized methods for the production of high specific-activity zirconium-89. *Nucl Med Biol*. 2009;36(7):729-739.
21. Graves SA, Kutyreff C, Barrett KE, et al. Evaluation of a chloride-based 89Zr isolation strategy using a tributyl phosphate (TBP)-functionalized extraction resin. *Nucl Med Biol*. 2018;64-65:1-7.
22. Singhal A, Toth LM, Lin JS, Affholter K. Zirconium(IV) tetramer/octamer hydrolysis equilibrium in aqueous hydrochloric acid solution. *J Am Chem Soc*. 1996;118(46):11529-11534.
23. Borjas Nevarez R, Balasekaran SM, Kim E, Weck P, Poineau F. Zirconium tetrachloride revisited. *Acta Crystallogr Sect C Struct Chem*. 2018;74(3):307-311.
24. Pandya DN, Bhatt N, Yuan H, et al. Zirconium tetraazamacrocycle complexes display extraordinary stability and provide a new strategy for zirconium-89-based radiopharmaceutical development. *Chem Sci*. 2017;8(3):2309-2314.
25. De Laeter JR, Böhlke JK, De Bièvre P, et al. Atomic weights of the elements: Review 2000 (IUPAC Technical Report). *Pure Appl Chem*. 2003;75(6):683-800.
26. *Multi-Agency Radiological Laboratory Analytical Protocols Manual (NUREG-1576, Initial Report). 2004, p. 14-191*.
27. Sasaki T, Kobayashi T, Takagi I, Moriyama H. Hydrolysis constant and coordination geometry of Zirconium(IV). *J Nucl Sci Technol*. 2008;45(8):735-739.

28. Deri MA, Zeglis BM, Francesconi LC, Lewis JS. PET imaging with 89Zr: From radiochemistry to the clinic. *Nucl Med Biol*. 2013;40(1):3-14.
29. Perk LR, Visser GWM, Vosjan MJWD, et al. 89Zr as a PET surrogate radioisotope for scouting biodistribution of the therapeutic radiometals 90Y and 177Lu in tumor-bearing nude mice after coupling to the internalizing antibody cetuximab. *J Nucl Med*. 2005;46(11):1898-1906.
30. Chang AJ, DeSilva R, Jain S, Lears K, Rogers B, Lapi S. 89Zr-radiolabeled trastuzumab imaging in orthotopic and metastatic breast tumors. *Pharmaceuticals*. 2012;5(1):79-93.
31. Khurana JS. *Bone Pathology*.; 2009.
32. Ulaner GA, Hyman DM, Lyashchenko SK, Lewis JS, Carrasquillo JA. 89Zr-Trastuzumab PET/CT for detection of human epidermal growth factor receptor 2-positive metastases in patients with human epidermal growth factor receptor 2-negative primary breast cancer. *Clin Nucl Med*. 2017;42(12):912-917.
33. Jauw YWS, Menke-van der Houven van Oordt CW, Hoekstra OS, et al. Immuno-positron emission tomography with zirconium-89-labeled monoclonal antibodies in oncology: What can we learn from initial clinical trials? *Front Pharmacol*. 2016;7(MAY).
34. Holland JP. Predicting the Thermodynamic Stability of Zirconium Radiotracers. *Inorg Chem*. 2020;59(3):2070-2082.
35. Sarbisheh EK, Salih AK, Raheem SJ, Lewis JS, Price EW. A High-Denticity Chelator Based on Desferrioxamine for Enhanced Coordination of Zirconium-89. *Inorg Chem*. 2020;59(16):11715-11727.
36. Patrick PS, Kolluri KK, Zaw Thin M, et al. Lung delivery of MSCs expressing anti-cancer protein TRAIL visualised with 89Zr-oxine PET-CT. *Stem Cell Res Ther*. 2020;11(1):256.
37. Weist MR, Starr R, Aguilar B, et al. PET of adoptively transferred chimeric antigen receptor T Cells with 89Zr-Oxine. *J Nucl Med*. 2018;59(10):1531-1537.
38. Sato N, Wu H, Asiedu KO, Szajek LP, Griffiths GL, Choyke PL. 89Zr-oxine complex PET cell imaging in monitoring cell-based therapies. *Radiology*. 2015;275(2):490-500.
39. Man F, Khan AA, Carrascal-Miniño A, Blower PJ, T.M. de Rosales R. A kit formulation for the preparation of [89Zr]Zr(oxinate)4 for PET cell tracking: White blood cell labelling and comparison with [111In]In(oxinate)3. *Nucl Med Biol*. 2020;90-91:31-40.

40. Roca M, De Vries EFJ, Jamar F, Israel O, Signore A. Guidelines for the labelling of leucocytes with 111In-oxine. *Eur J Nucl Med Mol Imaging*. 2010;37(4):835-841.
41. Verel I, Visser GWM, Boellaard R, Walsum MS Van, Snow GB, Van Dongen GAMS. 89Zr immuno-PET: Comprehensive procedures for the production of 89Zr-labeled monoclonal antibodies. *J Nucl Med*. 2003;44(8):1271-1281.
42. Pandya DN, Bhatt NB, Almaguel F, et al. 89Zr-chloride can be used for immuno-PET radiochemistry without loss of antigen reactivity in vivo. *J Nucl Med*. 2019;60(5):696-701.

Chapter 4

Detection limit and quantification of ^{89}Zr-labelled cells for cellular tracking using clinical PET/CT and PET/MRI

This chapter contains material that was accepted for publication in the European Journal of Nuclear Medicine and Molecular Imaging Research:

Lechermann LM, Manavaki R, Attili B, Lau D, Jarvis LB, Fryer TD, Bird N, Aloj L, Patel N, Basu B, Cleveland M, Aigbirhio FI, Jones JL, Gallagher FA. Detection limit of ^{89}Zr-labeled T cells for cellular tracking: an in vitro imaging approach using clinical PET/CT and PET/MRI. EJNMMI Res. 2020 Jul 14;10(1):82. doi: 10.1186/s13550-020-00667-5

4.1 Authorship, contributions and main collaborators

I confirm that I am the first author for the publication, having undertaken study design, data collection, analysis and manuscript preparation and the final submission. I also confirm that I have undertaken cell culture, radiotracer synthesis and cell labelling including sample preparation for all PET scans. Quality control was assisted by Dr Bala Attili. PET/CT scanning and acquisition was kindly assisted by Dr Nick Bird alongside Dr Roie Manavaki who undertook the main PET acquisition. PET/MR imaging was undertaken by Dr Roie Manavaki and Dr Tim Fryer. PET image processing was done by Dr Roie Manavaki. Image analysis was performed by Dr Roie Manavaki and myself. Overall data analysis was assisted by Dr Roie Manavaki.

4.2 Introduction

As mentioned and elaborated in detail in **chapter 2**, PET holds great potential for cell labelling and tracking with an exquisite repertoire of different available tracer for the direct (i.e. *in vitro*) and indirect (i.e. *in vivo*) cell labelling approach.

With its long half-life and residualizing properties in cells, zirconium-89 lends itself to longitudinal cell tracking applications requiring extended *in vivo* circulation times [1]. [^{89}Zr]Zr-Oxine has been proposed as a direct cell labelling agent that, as a lipophilic compound, can enter the cell by passive transport across the cell membrane, exploiting a similar mechanism to that used to label autologous leukocytes with indium-111 for clinical cell imaging [2],[3]. ^{89}Zr-PET holds promise to improve upon the sensitivity limits encountered with indium-111 SPECT and clinical imaging trials of this approach are intended [4],[5]. Up to today, only preclinical studies have employed [^{89}Zr]Zr-Oxine in several settings as described in detail in **chapter 2**.

Cell imaging and detection using PET is inherently limited by physical factors related to the PET technique as well as biological and pharmacological factors of the cell itself. A key issue for cell tracking is sensitivity, i.e. the need to achieve sufficient radioactivity density of labelled cells in the target region for detection. This is a particular problem for radiosensitive cells, such as T-cells, whose survival is compromised by high density radio-labelling. Estimating the radioactivity density of labelled cells required for detection will be

useful in determining the radiolabelling requirements that provide the best compromise between cell survival and *in vivo* detection.

Only few studies have investigated the limits of detecting directly labelled cells using PET [6],[7]. This work is the first aimed to address the sensitivity issue for cell tracking of radiosensitive T-cells directly labelled with [^{89}Zr]Zr-Oxine. This work had the following objectives:

I. To label Jurkat T-cells as a model cell line with different amounts of activities to generate different cell specific activities on cells (kBq/10^6 cells)

II. To assess the *in vitro* detection limit of ^{89}Zr-labelled cells on clinical PET scanners as a function of cell number, cell specific activities and the impact on detectability as measured by the contrast-to-noise ratio

III. To calculate the expected lowest limit of detection based on the generated data and to model the detection probability with certain background activities also taking into account cell densities

4.3 Materials and Methods

All chemicals, unless otherwise noted, were acquired from Sigma-Aldrich and used without further purification. Human serum was purchased frozen from Sigma-Aldrich. Geltrex™ LDEV-free reduced growth factor basement membrane matrix was purchased from ThermoFisher. All water used was ultrapure (>18.2 MΩcm^{-1}). Zirconium-89 was supplied as Zr^{4+} in a 1 M oxalic acid (PerkinElmer) and was produced at the BV cyclotron Amsterdam via the ^{89}Y(p,n)^{89}Zr reaction in a cyclotron on natural ^{89}Y-targets. Activity measurements were made using a CRC-55t dose calibrator (Capintec Inc. Florham Park, NJ) with a calibration factor of 493 for Zirconium-89. 3D printing of the cubic-well structure was performed at GlaxoSmithKline (Stevenage, UK) on a 3D Systems Viper printer using stereolithography technology.

Cell culture

Jurkat cells, a human lymphoblast cell line (ATCC, TIB-152TM, LGC), were cultured in Roswell Park Memorial Institute medium (RPMI, Gibco), supplemented with 10 % (v/v) FBS (ThermoFischer), 200 U/l penicillin, 0.1 g/l streptomycin, 10 mM 4-(2-hydroxyethyl)-1-piperazineethanesulfonic acid HEPES and 2 mM L-glutamate. Jurkat cells were maintained in suspension using T-25 cm^2 and T-75 cm^2 flasks (Corning) in a standard humidified CO_2 incubator (5 % CO_2 v/v).

[^{89}Zr]Zr-Oxine synthesis

Zirconium-89 as Zr^{4+} in 1 M oxalic acid was buffered to pH 7 with 1 M Na_2CO_3 and diluted to 500 µL with water. This neutralized [^{89}Zr]Zr-oxalate stock solution was used for radiotracer synthesis and also as the control for the *in vitro* cell labelling experiments.
The [^{89}Zr]Zr-Oxine complex was synthesized in an aqueous solution according to a published literature procedure [8]. In order to minimize the exposure and uptake of free oxine, the amount of ligand (oxine) for the synthesis of [^{89}Zr]Zr-Oxine was optimized for the amount of activity used in this experimental procedure. 250 µL (1.8 µmol) of a 1 mg/mL 8-hydroxychinoline (oxine) solution in 0.1 M HEPES was added to 6.4-7.5 MBq of neutralized [^{89}Zr]Zr-Oxalate (pH 7). The solution was incubated for 30 min at room temperature.
The radiochemical purity and yield of [^{89}Zr]Zr-Oxine was monitored using silica gel impregnated instant thin-layer chromatography paper (ITLC-SG; Agilent Technologies) in ethyl acetate and analysed on a Lablogic radio-TLC plate reader equipped with a PET detector using Laura software (Lablogic, UK) (See Appendix Section 4.6).

Labelling of Jurkat T-cells with [^{89}Zr]Zr-Oxine and determination of viability

3-5×10^6 Jurkat cells were washed with phosphate buffered saline (PBS) and re-suspended in 1.5 mL PBS or complete RPMI medium at room temperature. 154-430 kBq of [^{89}Zr]Zr-Oxine solution was incubated with the respective cell solutions for 30 min at room temperature in a scintillation vial. After incubation, cells were centrifuged (5 min, 500 g) and washed twice with PBS. The pellet and corresponding supernatants were

measured in the well counter and dose calibrator to calculate the uptake efficacy [%]. Cells were suspended in complete RPMI medium subsequently for further experiments. In addition, 150-300 kBq of free, neutralized [^{89}Zr]Zr-oxalate solution was added to Jurkat cells in either PBS or RPMI medium and incubated for 30 and 60 min as the control for *in vitro* cell labelling experiments.
Cell viability was determined by trypan blue exclusion. Unlabelled Jurkat cells were used as a control to examine the change of cell viability after each scan.

Detection limit experiment

6-well plate experiment

In order to explore the detection limit and quantification of ^{89}Zr-labeled cells on a human PET scanner, ^{89}Zr-labelled Jurkat cells with different specific activities were seeded in 2 mL RPMI medium at different concentrations into 6-well plates ranging from 10^4-10^6 cells per well. The experimental set-up is depicted in **Fig 4.1** and was as follows:

After Jurkat cells were harvested from 75 cm^3 flasks and counted, 3-5 x 10^6 Jurkat cells in 1.5 mL PBS or complete RPMI medium were labelled with [^{89}Zr]Zr-Oxine at room temperature for 30 min in a scintillation vial ①. ^{89}Zr-labeled cells were centrifuged (5 min, 500 g) and washed twice with PBS. The pellet was resuspended in 0.5 mL complete RPMI medium measured in Triathler well counter (HIDEX, Turku, Finland) to calculate the uptake efficacy [%] and cell bound radioactivity ②. This cell suspension was used to distribute ^{89}Zr-labeled cells into 3 wells of a 6-well plate at different cell concentrations ③. A total volume of 2mL per well was reached by adding completed RPMI medium to the well containing ^{89}Zr-labelled cells. For PET imaging, two 6-well plates containing ^{89}Zr-labeled cell suspensions were placed next to each other on a 1 cm thick polystyrene sheet to be scanned first on a clinical PET/CT (Discovery 690) scanner for 30 min ④ and subsequently on a clinical PET/MRI (GE SIGNA, GE Healthcare, Waukesha, USA) scanner for 30 min ⑤. Directly after the PET/CT and PET/MR imaging, the cell suspension in each well was transferred to a 2 mL Eppendorf tube, centrifuged (5 min,

500 x g) to form a pellet, resuspended in 0.5 mL complete RPMI medium and counted in the well counter for cellular activity retention ⑥. Cells were counted in a hemocytometer and cell viability was quantified as a last step for each cell suspension per well ⑦. The specific activity (SA) per 10^6 cells (kBq/10^6 cells) was calculated for each well containing labelled cells, based on the well counter measurements divided by the total number of cells in each well, normalized to 10^6 cells.

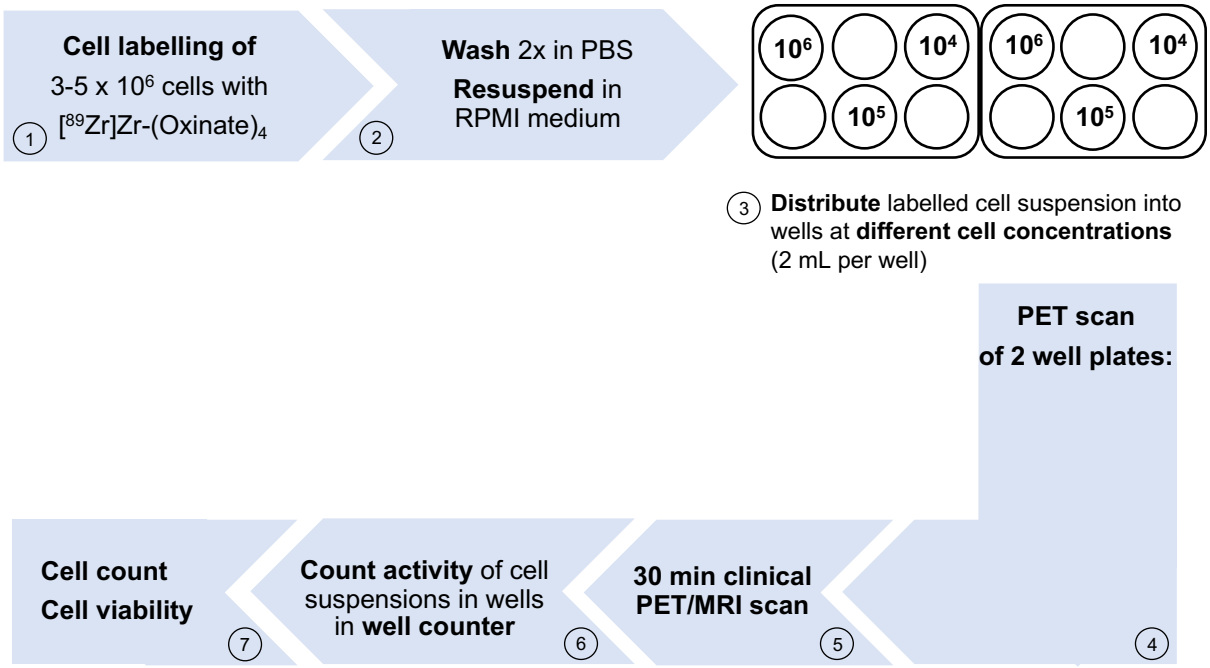

Figure 4.1 Schematic overview of the experimental set-up for one 6-well plate experiment/scan.

3×3 cubic-well plate experiment

In addition to the 6-well plate experiment, ^{89}Zr-labelled Jurkat cells with different specific activities were suspended in Geltrex™ matrix[1] transferred into the 1 cm^3 cubes of a 3D printed 3×3 cubic-well plate in order to better mimic a 3D lesion with labelled cells (**Fig 4.2**).

[1] Geltrex™ matrix is a soluble form of basement membrane extracted from murine Engelbreth-Holm-Swarm (EHS) tumors and is free of viruses, including lactose dehydrogenase elevating virus (LDEV), sometimes found in this type of preparation. The major components of Geltrex™ matrix include laminin, collagen IV, entactin, and heparin sulfate proteoglycans. It is ideal for the promotion and maintenance of differentiated phenotypes in a variety of cell culture.

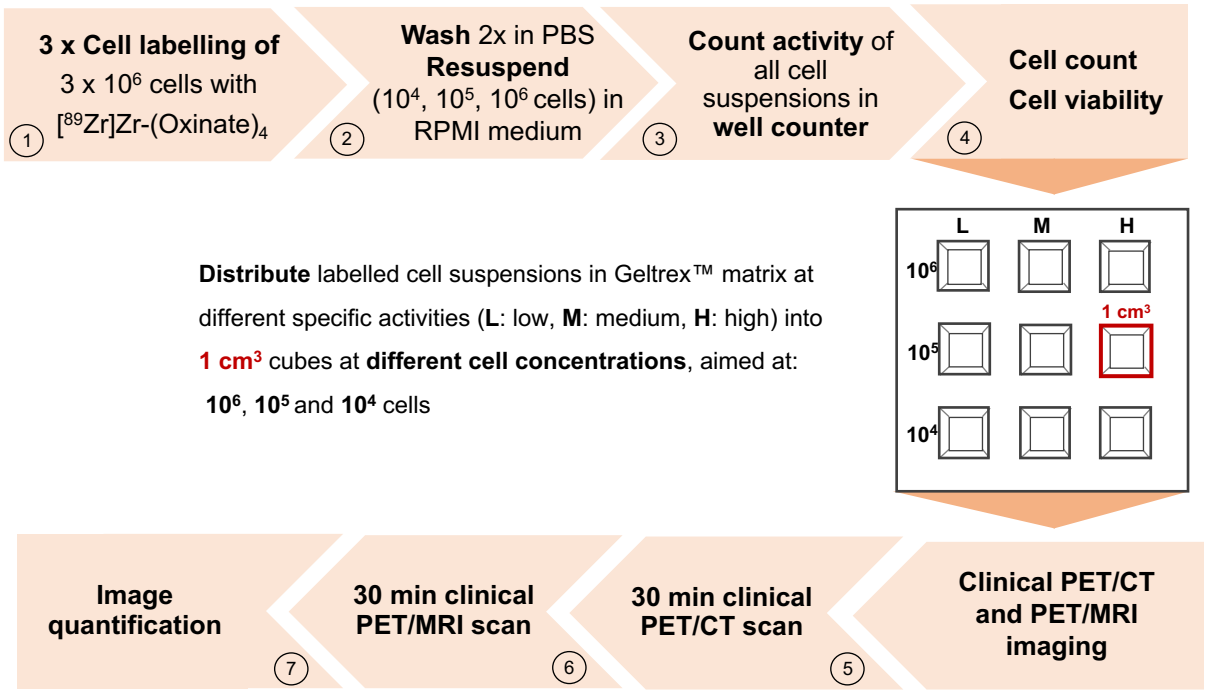

Figure 4.2 Schematic overview of the experimental set-up for one 3D structure experiment/scan.

After Jurkat cells were harvested from 75 cm^3 flasks and counted, three times 3 x 10^6 Jurkat cells in 1.5 mL PBS or complete RPMI medium were prepared to be labelled separately with [^{89}Zr]Zr-Oxine at room temperature for 30 min in a scintillation vial ① to generate cell suspensions with low (L), medium (M) and high (H) specific activities. ^{89}Zr-labelled cells were centrifuged (5 min, 500 g) and washed twice with PBS. The labelled cell suspension in each vial was transferred to a 2 mL Eppendorf tube, centrifuged (5 min, 500 g) to form a pellet, resuspended in 0.5 mL complete RPMI medium and counted in the well counter for cellular uptake efficacy [%] and total cellular activity retention. From each of the labelled cell suspensions different fractions (cell numbers ranging from 10^4 - 10^6) were taken and put into separate 1.5 mL Eppendorf vials ②, filled up to 0.5 mL with complete RPMI medium and counted again in the well counter for total cell associated activity ③. Cells were counted in a hemocytometer and cell viability was quantified for each cell suspension ④ before being mixed with 0.5 mL Geltrex™ matrix in the same vial which was kept on ice (ca. 4 °C). The ice cold ^{89}Zr-labelled cell suspensions mixed with

Geltrex™ were transferred into the 1 cm^3 cubes of the 3D printed structure ⑤ which was immediately put into an incubator at 37 ºC for 30 min with a petri dish lid loosely covering the top of the structure so that the Geltrex™-cell suspension mixture could solidify. For PET imaging, the 3D printed 3×3 cubic-well plate was put into a petri dish, covered with a lid and placed on a 1 cm thick polystyrene sheet and scanned first on a clinical PET/CT scanner for 30 min ⑥ and subsequently on a clinical PET/MRI scanner for 30 min ⑦.

^{89}Zr-labelled cell PET imaging on clinical PET/CT and PET/MRI

Two 6-well plates were scanned next to each other on a 1 cm thick polystyrene sheet containing 0.6 mm diameter spherical oil capsules visible on both the CT and MR images (**Fig. 4.3 A**). The 3D printed structure was additionally placed in a petri dish (**Fig. 4.3 B**). The oil capsules were placed at the four corners of each well-plate to enable co-registration between PET/CT and PET/MR, facilitating CT-based attenuation correction of the PET data acquired on the PET/MR,

PET/CT imaging was performed with the well-plates and 3D printed structure placed centrally in the field-of-view (FOV). Following a CT for attenuation correction, a 30 minutes PET acquisition was performed. Emission data were reconstructed into a 256×256×47 matrix with 1.2×1.2×3.27 mm voxels, using time-of-flight ordered-subsets expectation-maximization (TOF-OSEM) with 4 iterations and 24 subsets. Corrections for normalization, dead-time, random events, scatter, attenuation, decay and sensitivity were applied as implemented on the scanner, together with an isotropic 2 mm full-width-at-half-maximum (FWHM) Gaussian filter post reconstruction. The CT acquisition parameters were as follows: tube voltage: 120 kV; tube current: 50 mA; rotation time: 0.8 s; spiral pitch factor: 1.375, matrix: 512×512; pixel size: 0.5×0.5 mm; slice thickness: 3.75 mm (reconstructed to 3.27 mm).

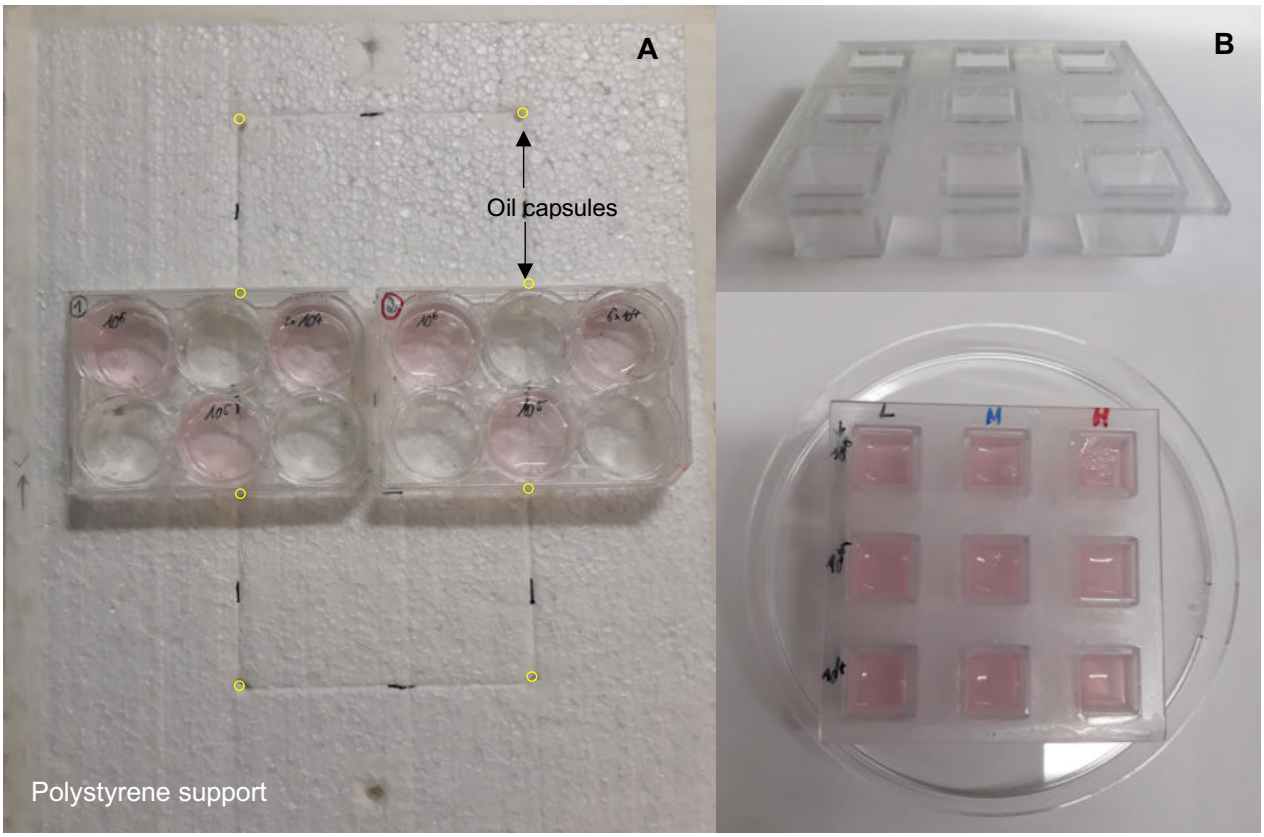

Figure 4.3 Set up for PET scanning: (**A**) **Two 6-well plates** were placed next to each other on a 1-cm thick polystyrene sheet containing 0.6-mm diameter spherical oil capsules visible on both the CT and MR images to enable CT-based attenuation correction of the PET data acquired on PET/MRI, (**B**) **3×3 cubic-well plate** (5×5 cm, material: ClearVue™) containing nine 1 cm^3 cubic wells with ^{89}Zr-labeled Jurkat cells suspended in Geltrex™ matrix. The 3D structure was placed into a petri dish before being supported on the 1 cm thick polystyrene sheet containing 0.6-mm diameter spherical oil capsules.

After the PET/CT scan, the polystyrene support carrying well-plates and the 3D printed structure were transferred for imaging on the PET/MR scanner. MR acquisition involved the manufacturer's 2-point Dixon sequence. To ensure an accurate comparison against PET/CT, emission data were acquired for 30 minutes divided by the radioactive decay factor between PET/CT and PET/MR acquisitions (i.e. >30 mins). Images were reconstructed using TOF-OSEM with 6 iterations and 16 subsets, and an isotropic 2 mm FWHM Gaussian post-reconstruction filter. To approximately match the voxel size used for reconstruction of the PET data on PET/CT, a 256×256×89 matrix with 1.4×1.4×2.78

mm voxels was utilized. Corrections for normalization, deadtime, random events, scatter, decay and sensitivity were applied as implemented on the scanner.

Attenuation correction of the PET data from the PET/MRI acquisitions used the CT images from the corresponding PET/CT acquisition for each experiment to generate attenuation maps for the well-plates. In a first step and for each of the nine experiments, the CT component of the PET/CT acquisition was rigidly registered to the corresponding water or fat images automatically generated by the Dixon sequence, utilizing the oil capsules embedded in the polystyrene support as reference for co-registration. Image registration was performed manually in Analyze 12.0 (AnalyzeDirect Inc., Overland Park, KS, USA), and the quality of registrations was visually inspected.

Thresholding and manual editing were applied to the original CT image from the PET/CT scan to define a binary mask of the 6-well plates (i.e. excluding the scanner bed). This mask was subsequently multiplied with the CT to produce an image encompassing the well-plates only. The edited CT image of the well-plates was converted to a 511-keV attenuation map utilizing bilinear transformation [9] and transformed into the space of water/fat images using the rigid transformation parameters calculated in Analyze 12.0. To produce a complete attenuation map for attenuation correction on the PET/MR scanner, the attenuation maps of the well plates were combined with attenuation templates of the objects present in the FOV of PET/MR scanner during acquisition (bed cradle, plastic gap filler and posterior array) and smoothed with a 5-mm FWHM Gaussian filter. Well-plate attenuation map generation was performed using in-house software implemented in Matlab 2016b (Mathworks Inc, Nattick, NA, USA).

PET image analysis

For each 6-well plate experiment, the PET image from the PET/MRI scan was rigidly registered to its PET/CT counterpart, and both were resampled to the space of the CT image (1×1×1 mm^3 voxels). Volumes of interest (VOI) for each of the wells containing ^{89}Zr-labeled cell suspensions were defined by manually placing circular regions (3.4-cm diameter) on all contiguous coronal slices encompassing the activity distribution on PET

images, utilizing the corresponding CT as guidance. Corresponding background VOIs were generated by placing similarly sized regions within the three empty wells in each plate. The total activity (kBq) in each well was calculated by taking the average of the radioactivity concentration (kBq/mL) within the defined VOI for each well and multiplying by the VOI volume (mL). For data analysis, the specific activities for each well were classified into three categories, defined with the following intervals: 0-5 (low), 5-15 (medium) and 15-35 (high) kBq/10^6 cells.

In a similar manner, cubic VOIs (1 cm^3) were defined for each well of the 3×3 cubic-well plate, with three identically sized background VOIs defined in the area between the 3×3 cubic-well plate and the outer plastic case (**Fig. 4.3**).

As a measure of detectability, the contrast-to-noise ratio (CNR) for each of the wells containing ^{89}Zr-labelled cells was calculated according to Equation 1:

$$CNR_{well} = \frac{\mu_{well} - \mu_{background}}{\sigma_{background}} \quad (1)$$

Where μ_{well} and $\mu_{background}$ refer to the mean radioactivity concentrations in each ^{89}Zr-containing well VOI and for the three background VOIs respectively. Noise was expressed as the standard deviation of voxel values in the background VOIs ($\sigma_{background}$). CNR was chosen as a measure of detectability over signal-to-noise ratio (SNR), because the former takes into account the contrast (i.e. the contrast of the VOI that can be visualised above the background noise) of the lesion and compares it to the level of the background whereby detectability can be related to contrast. On the other hand, SNR compares the level of the desired signal to the level of background noise.

Image analysis was performed in Analyze 12.0 (AnalyzeDirect Inc., Overland Park, USA).

Calculation of the lower limit of detection (LLD), defined as the minimum number of cells required for detection on imaging, was performed by regressing specific activity vs. CNR for all wells across all experiments to obtain the 95% upper confidence limit on CNR, and subsequently substituting this number into the linear regression equation of CNR vs. cell number per well.

The detection probability of ^{89}Zr-labelled cell suspensions on PET/CT and PET/MRI as a function of cell number or specific activity [kBq/10^6 cells] was estimated through binomial logistic regression using Eq. 2:

$$Detection\ Probability = \frac{1}{1+e^{-(\beta_0+\beta_1 x)}} \quad (2)$$

where β_0 and β_1 refer to the logistic regression coefficients and x denotes the cell number or specific activity [6].

Prior to logistic regression, binary classification of PET/CT and PET/MR image CNR was performed using the Rose criterion (i.e. classification using a threshold of CNR=5). To investigate the effect of surrounding background radioactivity on the detection probability of ^{89}Zr-labelled cells, eight different background levels corresponding to 10-80% of the radioactivity concentrations in each ^{89}Zr-containing well were simulated, with $\sigma_{background}$ estimated assuming a Poisson noise model. Simulations were performed in Matlab 2016b (Mathworks Inc, Nattick, NA, USA) and resulted in 248 synthetic datasets.

Estimation of cell densities

For the 1 cm^3 cubic wells, cell density (10^6 cells/mL) was calculated as the number of cells contained in the 1 mL well volume.
Due to the heterogeneity of cell distributions in the 6-well plates, cell density in each well was estimated by fitting the following polynomial equation to the PET image data:

$$A_{ij} = a_{ij}CN_j + b_{ij}SA_j + c_{ij}(CN \cdot SA)_j + d_{ij} + \varepsilon_{ij} \quad (S1)$$

where for the j^{th} well when using scanner i=1 (PET/CT) or 2 (PET/MR), A_{ij} is the well activity as measured on the PET images (kBq), CN_j the cell number (×10^6 cells), and SA_j the specific activity (kBq/10^6 cells). The model parameters are denoted by a_{ij}, b_{ij}, c_{ij} and d_{ij} and ε_{ij} are within-group (i.e. scanner) errors. Fitting was performed using a mixed

effects model implemented in Matlab 2016b with fixed effects for the cell number and specific activity, and random effects accounting for differences between the two scanners. The cell density in each voxel was calculated by substituting the voxel radioactivity concentration (kBq/mL) into equation S1 (term A_{ij}) and solving for cell number per mL. The cell density in each well was subsequently determined by taking the median voxel cell number per mL.

Statistical analysis

Statistical analysis was performed using GraphPad Prism 8.0; (GraphPad Software Inc, La Jolla, USA). Results are presented as mean ± standard deviation (SD) or median [range] as appropriate; the Anderson-Darling test was used to test for distribution normality. Means between two groups were compared using Student's two-tailed t test, whereas the Kruskal-Wallis *H* test was used for comparison between two groups. Correlations between continuous variables were assessed using the Pearson correlation coefficient (r). Bland-Altman analysis was used to evaluate differences in well activity and CNR values between PET/CT and PET/MRI. P-values <0.05 were considered statistically significant.

4.4 Results

Eight independent labelling experiments were performed with different zirconium-89 batches for [^{89}Zr]Zr-Oxine tracer synthesis, using Jurkat cells with the same passage number for each 6-well plate experiment. Overall, 11 and 12 plates with 33 and 36 wells containing ^{89}Zr-labelled cells were scanned using PET/CT and PET/MRI, respectively. Results from 5 wells were excluded for both PET/CT and PET/MRI owing to pipetting error (3 wells) and inability to quantify the cell number (2 wells). In addition, three independent cell labelling experiments were performed with one Zirconium-89 batch for [^{89}Zr]Zr-Oxine tracer synthesis, using Jurkat cells with the same passage number as was used for the 6-well plate experiments in order to create 1 cm^3 gel cubes containing ^{89}Zr-labelled cell suspensions in a 3D printed structure (3×3 cubic-well plate). In this case, the 3D printed structure containing nine 1 cm^3 cubes with ^{89}Zr-labelled cell gels was imaged once using both clinical PET/CT and PET/MRI. The overview of the experimental set-up is shown in **Figure 4.4**.

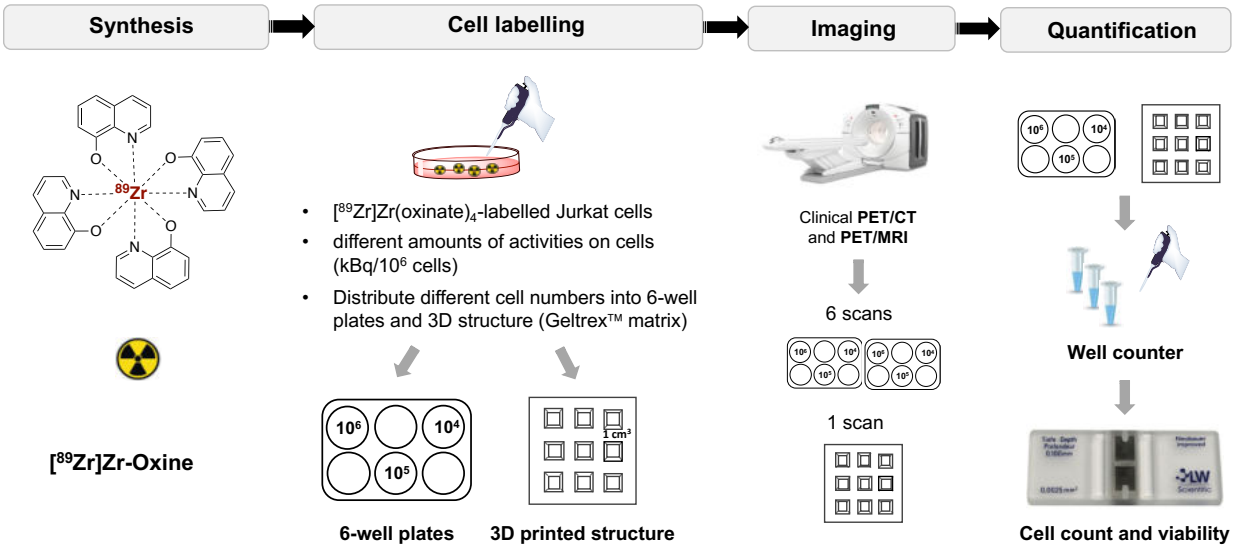

Figure 4.4 Overview of experimental set-up.

[^{89}Zr]Zr-Oxine synthesis and labelling of Jurkat T-cells

The [^{89}Zr]Zr-Oxine complex was synthesized in an aqueous solution at a mean radiochemical yield of 93.5 % ± 3.1 (SD, n = 9) as indicated by thin layer chromatography and was used for cell labelling without further purification (**Fig. 4.5**).

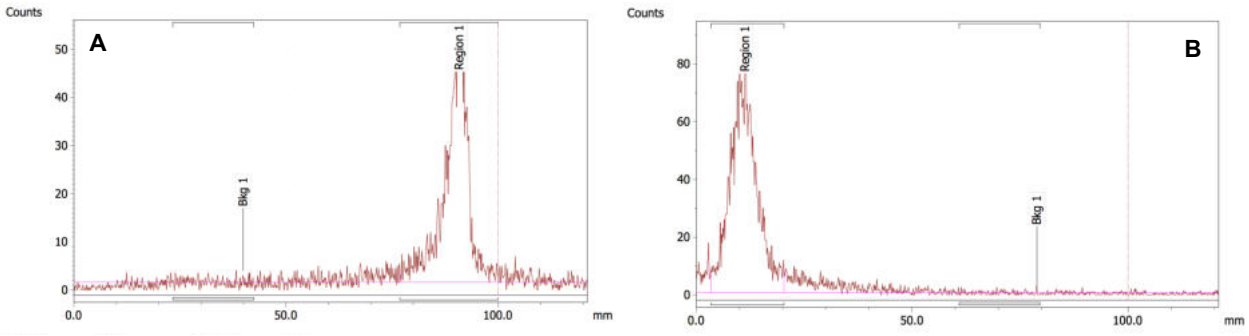

Figure 4.5 Representative radio iTLC chromatogram of [^{89}Zr]Zr-Oxine (R_f ~ 0.9) and [^{89}Zr]Zr-Oxalate (R_f ~ 0). [^{89}Zr]Zr-Oxine or [^{89}Zr]Zr-Oxalate was spotted onto a ca. 9 cm long iTLC plate at 1 cm from the bottom of the plate (starting line) and developed in 100% EtOAc as mobile phase. (**A**) [^{89}Zr]Zr-Oxine moves with the EtOAc whereas free $^{89}Zr^{4+}$ in 1 M oxalic acid stays at the origin. (**B**) Free $^{89}Zr^{4+}$ in 1 M oxalic stays at the origin and does not move with EtOAc.

In order to minimize the exposure and uptake of free oxine, the amount of ligand (oxine) for the synthesis of [^{89}Zr]Zr-Oxine was optimized for the amount of activity used in this experimental procedure (**Table 4.1**).

Table 4.1 Radiochemical yield for the formation of [^{89}Zr]Zr-Oxine using 6.4-7.5 MBq [^{89}Zr]Zr-Oxalate with increasing amount of oxine (8-hydroxycholin) as ligand to optimize the content of oxine in the reaction solution (n=3). Radiochemical yield was measured by TLC.

Amount of Oxine [μg]	Radiochemical yield [%]
10 (69.9 nmol)	< 1 %
100 (0.7 μmol)	56.6 ± 0.2
200 (1.4 μmol)	83.2 ± 4.5
250 (1.8 μmol)	94.5 ± 2.9

The cell labelling efficiency after a 30-minute incubation period ranged from 5.1 - 35.3 % of the added activity. [^{89}Zr]Zr-oxalate showed significantly lower uptake into Jurkat T-cells (< 1% of the added activity, p<0.0001, **Fig. 4.6 A and B**) compared to [^{89}Zr]Zr-Oxine. Labelling and imaging did not significantly affect the cell viability (**Fig. 4.7 A**) throughout the 6-well plate experiments. Given the fact that once the ^{89}Zr-labelled cell suspension in the Geltrex™ matrix gelified, a post labelling analysis was not possible and therefore the cell associated activity, cell count and viability was solely quantifiable before each scan directly post-labelling (**Fig. 4.7 B**).

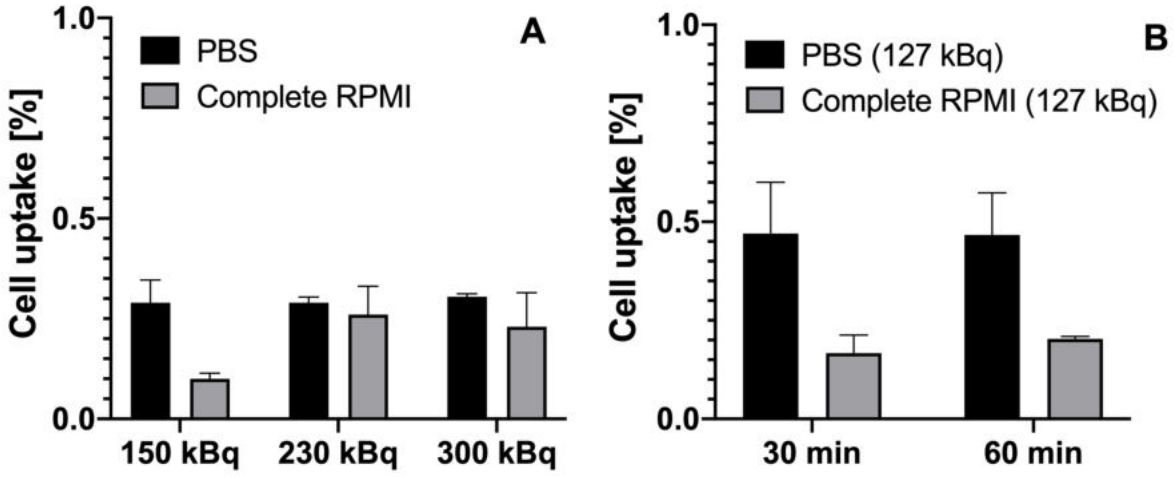

Figure 4.6 Cellular uptake of unchelated [^{89}Zr]Zr-Oxalate into Jurkat cells at different incubation conditions. (A) 30 min incubation with increasing amount of activity added to Jurkat cells (n=3) and **(B)** constant (average) activity added with increasing incubation time (n=3)**.**

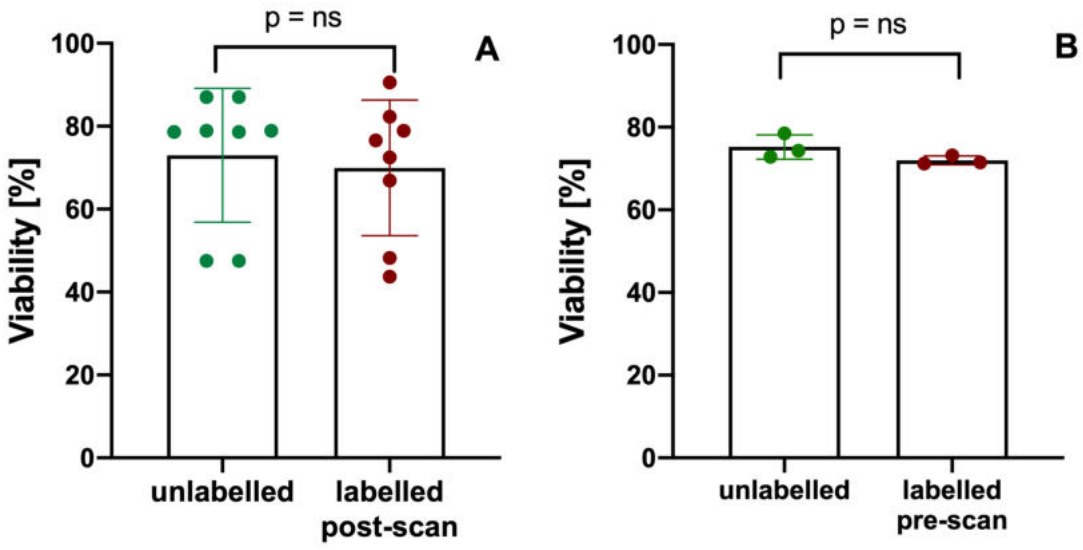

Figure 4.7 Mean viability of unlabelled cells as control compared to the mean viability of cells after labelling with [^{89}Zr]Zr-Oxine. (A) 6-well plate experiment: non-significant (p = 0.16) difference between the mean viability of unlabelled cells (73.0 % ± 16.1 %) and labelled cells (69.2 % ± 18.0 %) after the end of all PET scans performed for the 6-well plates. In two occasions, cells had to be used soon after thawing the cells which is reflected in the low viability (~50 %). **(B) 3×3 cubic-well plate experiment:** non-significant (p = 0.10) difference between the mean viability of unlabelled cells (75.2 % ± 3.0 %) and labelled cells (72.0 % ± 1.1 %) before the labelled cells were prepared in Geltrex™ matrix for subsequent imaging. Error bars indicate the standard deviation (SD) from the mean value; ns = not significant

Imaging and detection limit of ^{89}Zr-labelled cells – 6-well plate experiment

The total activity on cells per well ranged from 0.02-15.57 kBq and 0.01-24.47 kBq (**Fig. 4.8 A, B**), as measured by the gamma counter and PET imaging, respectively. The median cell number in the 10^6, 10^5 and 10^4 wells was 1.08×10^6, 1.45 x 10^5 and 8.5×10^4 respectively (**Fig. 4.8 C**). Jurkat T-cells labelled with different amounts of [^{89}Zr]Zr-Oxine at room temperature in complete RPMI medium or PBS yielded specific activities ranging from 0.4 kBq/10^6 cells to 41.2 kBq/10^6 cells. The median specific activity in the 10^6, 10^5 and 10^4 wells was 7.8 [1.85-31.91], 8.2 [0.43-27.77] and 5.5 [0.63-21.96] kBq/10^6 cells respectively (**Fig. 4.8 D**). No statistically significant difference was observed between the median specific activities in different wells (p = 0.71; Kruskal-Wallis *H*).

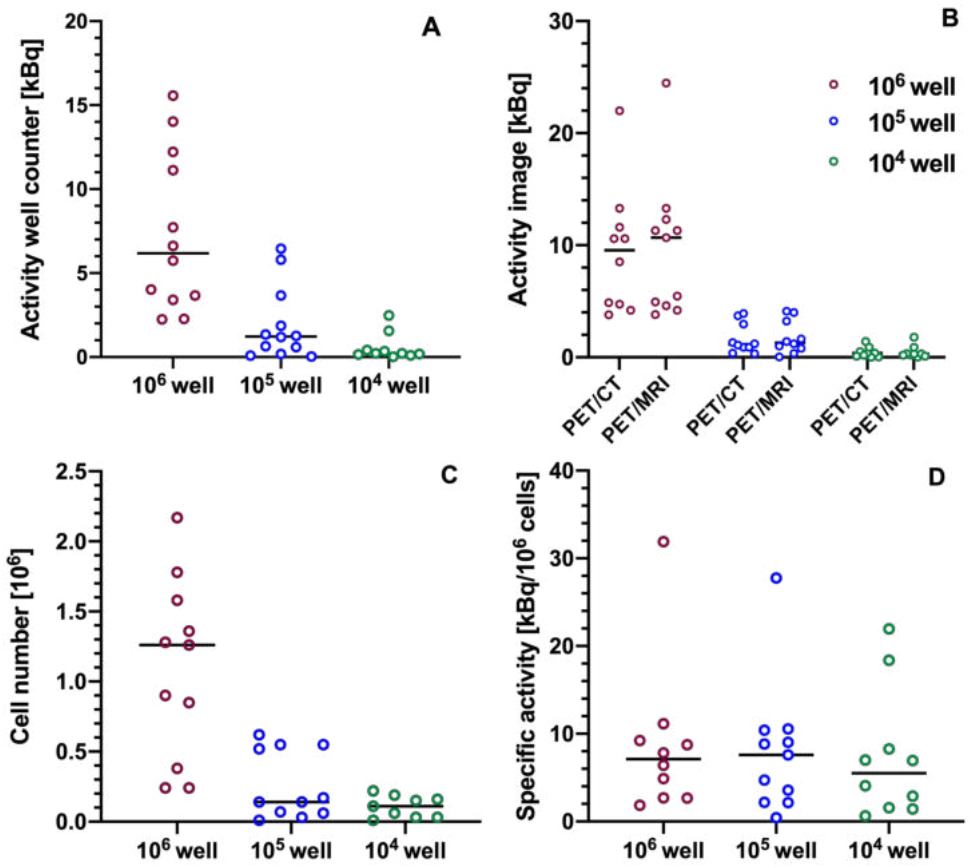

Figure 4.8 Individual value plots and median of: **(A)** total activity [kBq] in 10^6, 10^5 and 10^4 wells as measured in the well counter; **(B)** total activity [kBq] in 10^6, 10^5 and 10^4 wells as obtained from PET images acquired using PET/CT and PET/MRI; **(C)** cell number in 10^6, 10^5 and 10^4 wells; **(D)** specific activity [kBq/10^6 cells] in different wells.

The total activity in each well as determined from PET/CT and PET/MR images showed a strong correlation with the total cell-associated activity in cell suspensions as measured in the well counter (PET/CT: r = 0.84, p<0.0001; PET/MRI: r = 0.85, p<0.0001; **Fig. 4.9 A**). The CNR obtained for all wells from both PET/CT and PET/MRI ranged from 0 - 2106 (**Fig. 4.9 B**) and demonstrated an overall significant positive correlation with the total cell-associated activity (PET/CT: r = 0.82, p<0.0001; PET/MR: r = 0.83, p<0.0001; **Fig. 4.9 C**). Furthermore, a significant positive correlation between the CNR in each well and the corresponding cell number could be observed within each specific activity group for both scanners (**Fig. 4.9 D**). For PET/CT, correlation coefficients for each specific activity category group were: 0-5 kBq/10^6 cells: r = 0.81 (p = 0.003); 5-15 kBq/10^6 cells: r

= 0.80 (p = 0.001); 15-35 kBq/10^6 cells: r = 0.98 (p = 0.02), whereas for PET/MRI these were: 0-5 kBq/10^6 cells: r = 0.79, p = 0.0008; 5-15 kBq/10^6 cells: r = 0.83, p = 0.0005; 15-35 kBq/10^6 cells: r = 0.98, p = 0.02.

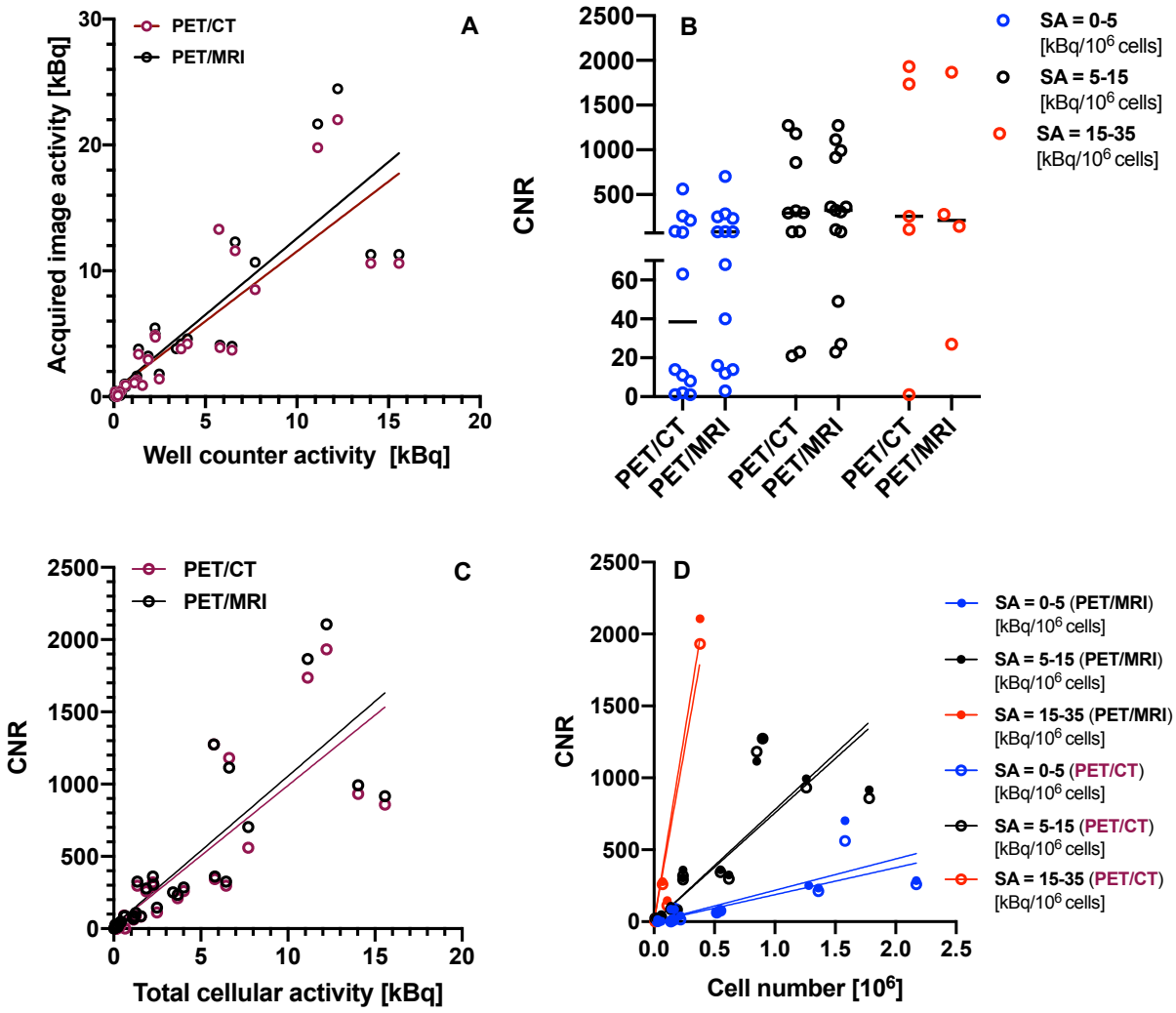

Figure 4.9 (A) Pearson correlation between the total cell-associated activity [kBq] measured in the well counter and total activity obtained from PET/CT and PET/MR images; **(B)** individual value plot and median of CNR per specific activity category for both PET/CT and PET/MRI; **(C)** Pearson correlation of PET/CT and PET/MRI CNR vs. total cellular activity [kBq] as measured in the well counter; **(D)** Scatter plot of PET/CT and PET/MRI well CNR vs. cell number per specific activity category. CNR: contrast-to-noise ratio

In addition, an overall significant positive correlation was found between the corresponding CNR obtained on both PET/CT (r = 0.41, p = 0.03) and PET/MRI (r = 0.42, p = 0.02) and the cell number per well (**Fig. 4.10 A**), as well as with the corresponding specific activity of cells (**Fig. 4.10 B**; PET/CT: r = 0.44, p = 0.02; PET/MR: r = 0.49; p = 0.006).

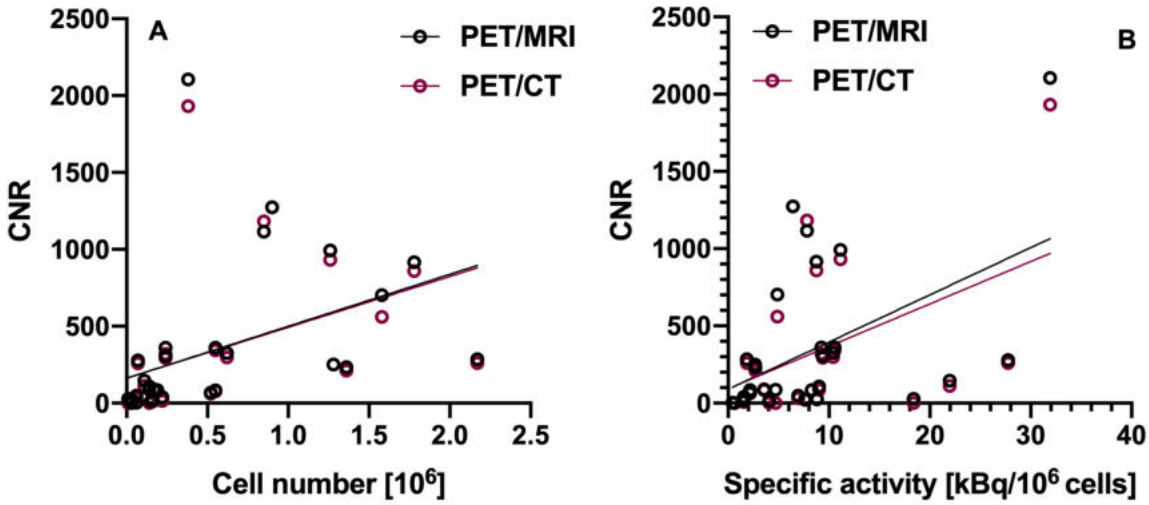

Figure 4.10 (A) Pearson correlation between the cell number [10^6 cells] and the respective contrast-to-noise ratio (CNR) per well acquired using PET/CT and PET/MR (PET/CT: r = 0.41; p = 0.03; PET/MR: r = 0 .42, p = 0.02), (**B**) Pearson correlation between contrast-to-noise ratio (CNR) and specific activity [kBq/10^6 cells] per well as obtained from PET/CT and PET/MR images **(**PET/CT: r = 0.44, p = 0.02; PET/MR: r = 0.49; p = 0.006).

PET/CT and PET/MRI results strongly correlated for both total well activity and CNR (total well activity: r = 0.998, p<0.0001; CNR: r = 0.98, p<0.0001; **Fig. 4.11 A and 4.11 C**. Bland-Altman analysis indicated good agreement between PET/CT and PET/MRI indices of total well activity and CNR (**Fig. 4.11 B** and **4.11 D**).

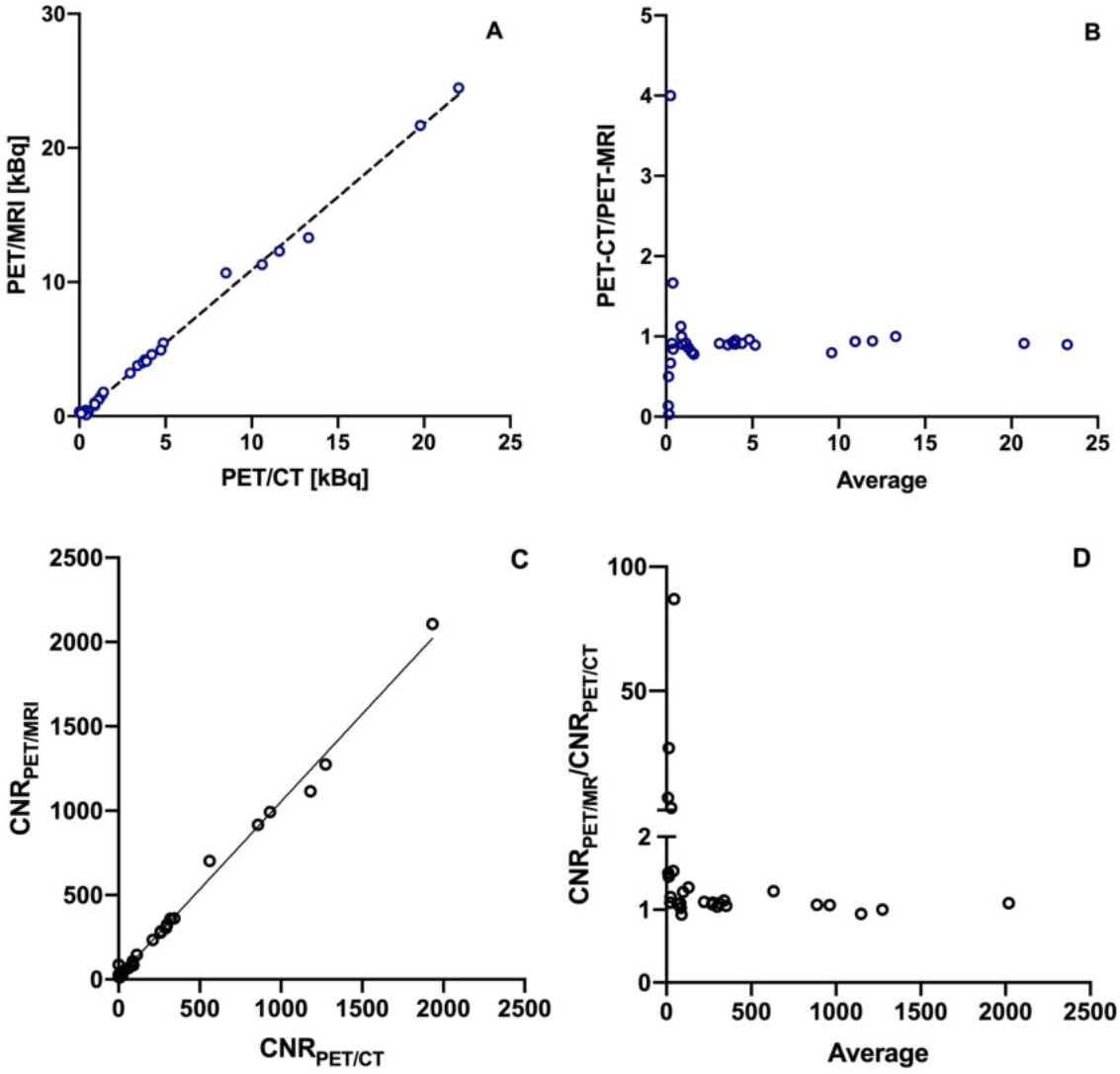

Figure 4.11 (**A**) Correlation and (**B**) Bland-Altman plot of cellular activities [kBq] obtained by PET/CT imaging versus PET/MRI (r=0.998, p<0.0001; Bland-Altman analysis: 0.93 bias (SD: 0.65), 95 % limit of agreement: -0.34-2.20) and (**C**) correlation and (**D**) Bland-Altman plot of CNRs obtained by PET/CT imaging versus PET/MRI (p < 0.0001, r = 0.98, Bland-Altman analysis: 0.19 bias: (SD:0.52), 95 % limits of agreement: 0.83-1.22).

Fig. 4.12 illustrates representative coronal PET images of 6-well plates with different numbers of ^{89}Zr-labelled cells and specific activities per well. In general, lower cell numbers with a higher specific activity could be detected with a higher contrast-to-noise ratio compared to wells with a higher cell number and a lower specific activity. In the example images shown, 5.2×10^5 cells with a specific activity of 2.2 kBq/10^6 cells could be

clearly visualized (**Fig. 4.12**, **A2**), whereas the lowest cell number that could be detected was 6.8×10^4, when the specific activity was 27.8 kBq/10^6 cells (**Fig. 4.12, B2**).

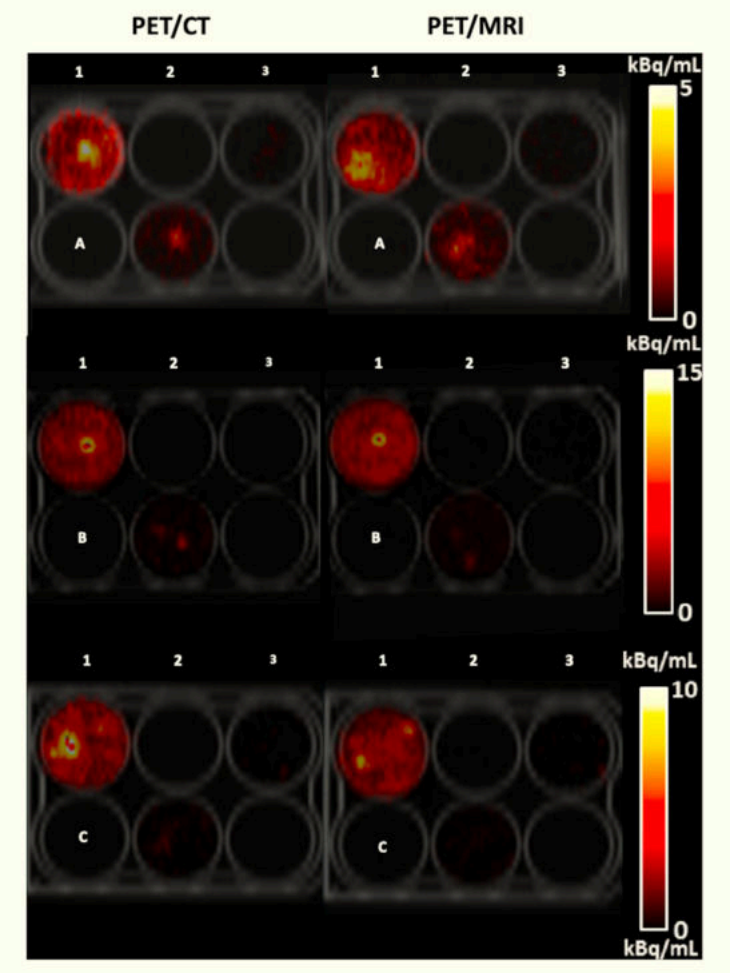

Figure 4.12 PET images of 6-well plates containing ^{89}Zr-labelled Jurkat cells acquired using PET/CT and PET/MRI together with their corresponding co-registered CT image. Cell numbers and specific activities per well (kBq/10^6 cells; indicated parenthetically) were as follows:

(A1) 1.36×10^6 cells (2.70)
(**A2**) 5.20×10^5 cells (2.18)
(**A3**) 1.45×10^5 cells (1.57)
(**B1**) 3.83×10^5 cells (31.91)
(**B2**) 6.75×10^4 cells (27.77)
(**B3**) 1.00×10^4 cells (18.37)
(**C1**) 8.45×10^5 cells (7.83)
(**C2**) 1.65×10^5 cells (3.57)
(**C3**) 6.10×10^4 cells (6.93)

The theoretical lower limit of detection (LLD) for PET/CT and PET/MRI, together with the specific activity at this LLD are given in **Table 4.2**. Detailed calculations for obtaining LLDs are illustrated in **Fig. 4.13** with more details in regards to calculations indicated in the methods section 3.2. The calculations yielded a slightly lower LLD for PET/MR compared to PET/CT, where both values were in the order of 10^5 cells. In the absence of background activity, the CNR required to achieve this LLD was 249 and 276 for PET/CT and PET/MRI respectively. In addition, LLDs were investigated using the Rose criterion for detection and inserting a CNR=5 into the equation for the calculation of LLDs. Using

the Rose criterion, the LLDs for both PET/CT and PET/MRI were a magnitude lower than the LLDs using the CNR obtained from images during this work.

Table 4.2 Theoretical lower limit of detection (LLD) for PET/CT and PET/MRI with respect to cell number and specific activity [kBq/10^6 cells].

	$LLD_{PET/MRI}$	$LLD_{PET/CT}$
Cell number	5.24×10^5 (1.05×10^4)*	5.88×10^5 (1.07×10^4)*
Specific activity [kBq/10^6 cells]	3.26 (0.07)*	3.72 (0.07)*

***** Values in parentheses indicate the theoretical LLD values according the Rose criterion (CNR=5) as a threshold for detectability.

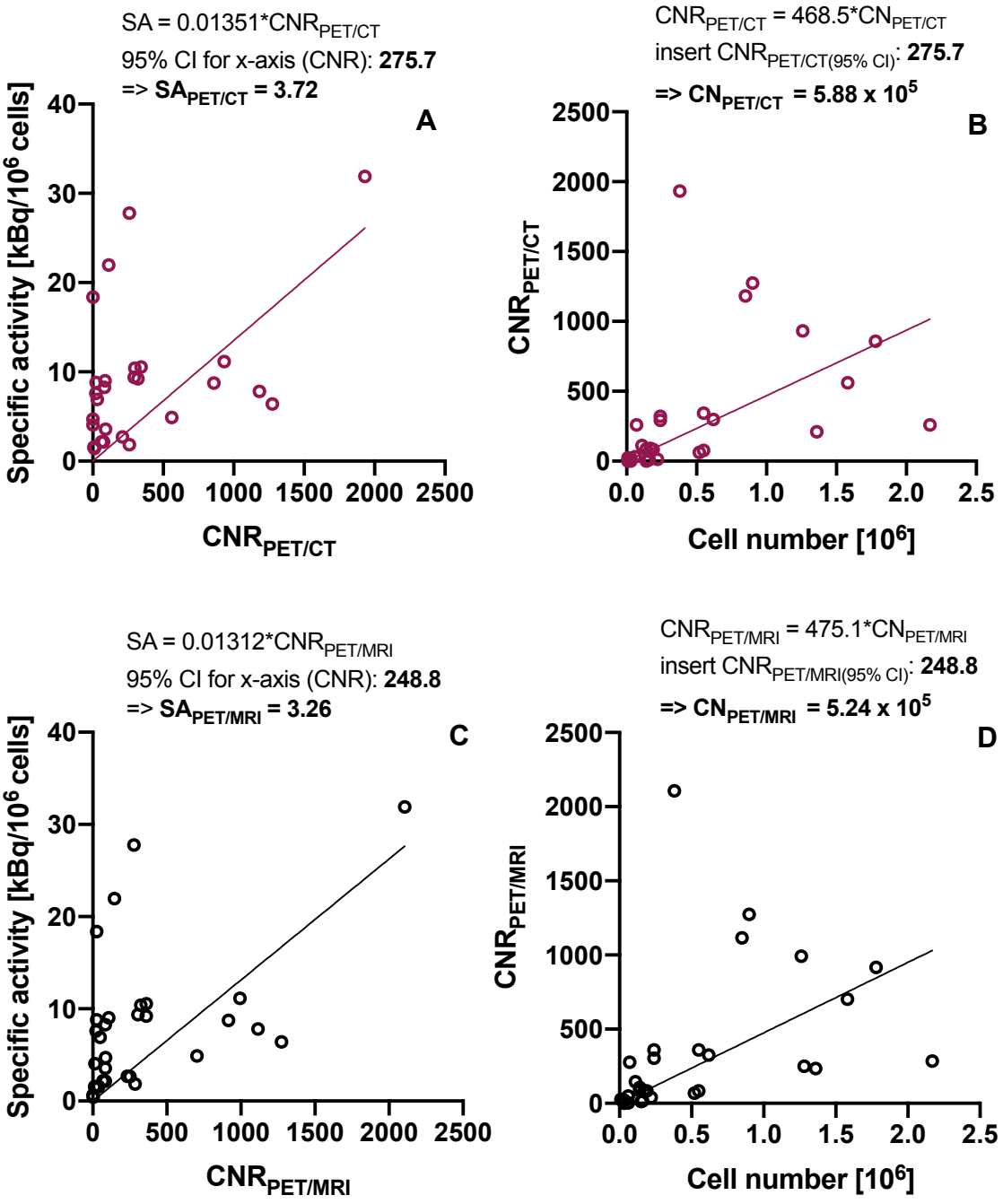

Figure 4.13 Linear regressions of (A, C) contrast-to-noise ratio (CNR) versus specific activity and (B, D) cell number versus CNR for both PET/CT (A, B) and PET/MRI (C, D). Linear regression of specific activity vs. CNR used the upper 95% confidence interval (CI) of the x-intercept (=CNR). This value was subsequently inserted into the linear regression equation for CNR vs. cell number to derive the theoretical lower limit of detection (LLD).

Fig. 4.14 shows the simulated data obtained for the detection probability versus cell number for both PET/CT and PET/MRI using the data set of ^{89}Zr-labelled cells in 6-well plates from the work described above and applying different levels of background corresponding to 20, 40, 60, 80% of the radioactivity concentration in wells. At the LLD (**Table 4.2**), ^{89}Zr-labelled cells could be detected with >90% probability. As expected, a decrease in the detection probability of ^{89}Zr-labelled cell suspensions was observed for increasing background levels and decreasing cell numbers/well.

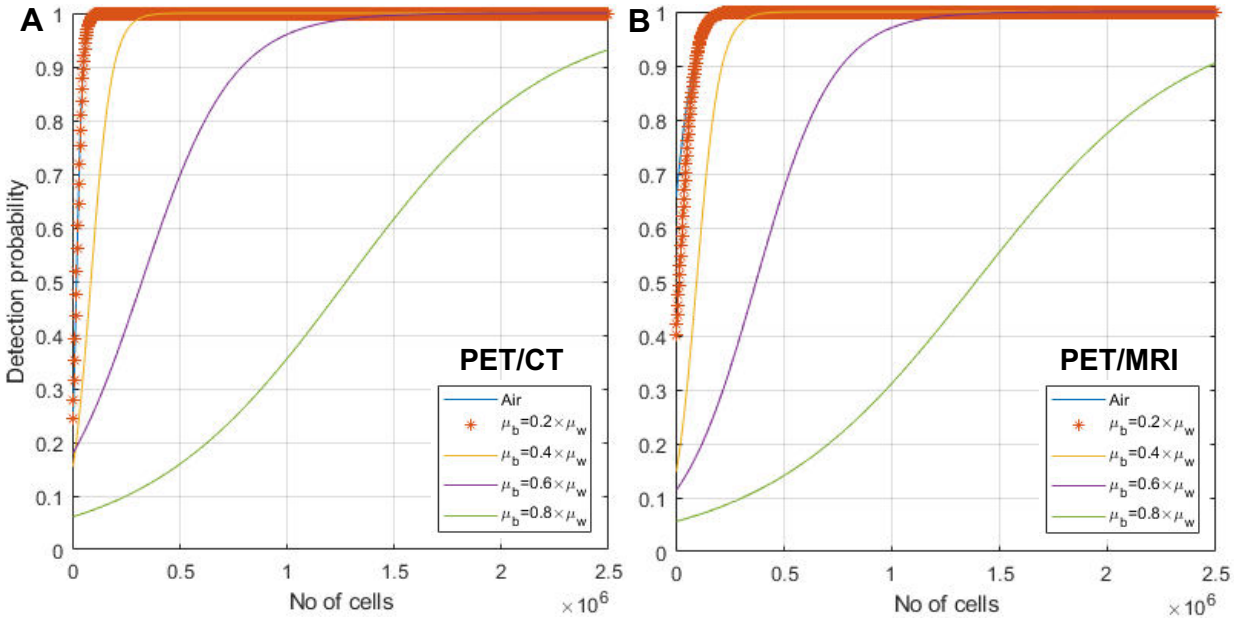

Figure 4.14 Detection probability of ^{89}Zr-labelled cell suspensions at different background levels in regards to cell number. (**A**) PET/CT and (**B**) PET/MRI. μ_w, μ_b: mean radioactivity concentration in ^{89}Zr-containing wells and the background respectively.

Table 4.3 shows the minimum number of ^{89}Zr-labelled cells that would be detected on PET/CT and PET/MRI in the presence of background levels corresponding to 20, 40, 60, 80% of the radioactivity concentration in wells with a detection probability of 50% and ≥90%. For a given detection probability and depending on the level of background activity, differences of two orders of magnitude could be observed in the minimum number of detectable ^{89}Zr-labelled cells.

Table 4.3 Detection probability calculations for the 6-well plate experiment in regards to cell number. Background levels corresponding to 20, 40, 60, 80% of the radioactivity concentration in wells with a detection probability of 50% and ≥90% for both PET/CT and PET/MRI.

Background levels	Cell numbers (Detection probability: 50%)		Cell numbers (Detection probability: 90%)	
6-well plates	**PET/CT**	**PET/MRI**	**PET/CT**	**PET/MRI**
20%	1.64×10^4	1.64×10^4	4.84×10^4	8.79×10^4
40%	8.36×10^4	9.41×10^4	1.91×10^5	2.12×10^5
60%	3.22×10^5	3.70×10^5	7.89×10^5	7.66×10^5
80%	1.28×10^6	1.39×10^6	2.31×10^6	2.47×10^6

In addition, the simulated data obtained for the detection probability versus specific activity for both PET/CT and PET/MRI with different background levels corresponding to 20, 40, 60, 80% of the radioactivity concentration in wells is shown in **Fig. 4.15**. As expected, a decrease in the detection probability of ^{89}Zr-labelled cell suspensions was observed for increasing background levels and decreasing specific activity. For a detection probability of ≥90% at these background levels, the cell suspensions with specific activities of 26.1 vs. 24.7 kBq/10^6 cells and 68.3 vs. 60.9 kBq/10^6 cells were detectable for PET/CT and PET/MR, respectively. For background levels ≤40% of the radioactivity concentration in wells, a specific activity of <1 kBq/10^6 cells was required for detection (**Table 4.4**).

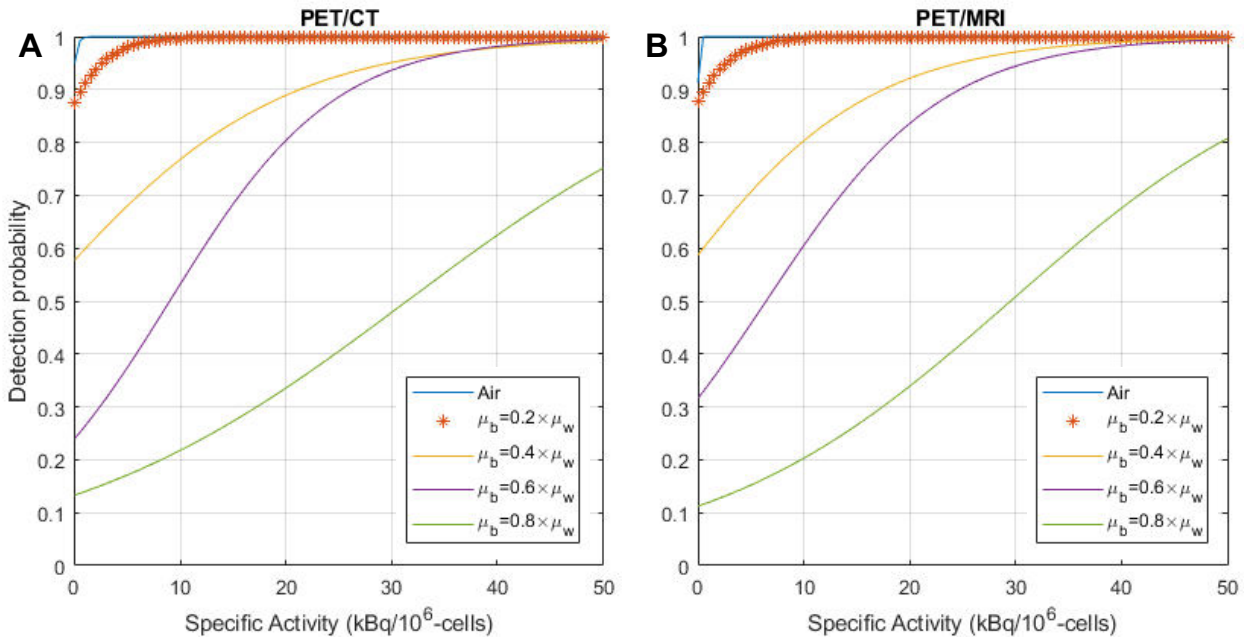

Figure 4.15 Detection probability of ^{89}Zr-labelled cell suspensions at different background levels in regards to cell specific activity. (**A**) PET/CT and (**B**) PET/MRI. μ_w, μ_b: mean radioactivity concentration in ^{89}Zr-containing wells and the background respectively.

Table 4.4 Detection probability calculations for the 6-well plate experiment in regards to cell specific activity. Background levels corresponding to 20, 40, 60, 80% of the radioactivity concentration in wells with a detection probability of 50% and ≥90% for both PET/CT and PET/MRI.

Background levels	Specific activity [kBq/10^6 cells] (Detection probability: 50%)		Specific activity [kBq/10^6 cells] (Detection probability: 90%)	
6-well plates	**PET/CT**	**PET/MRI**	**PET/CT**	**PET/MRI**
20%	~0	~0	0.66	0.62
40%	~0	~0	21.32	17.51
60%	9.00	6.44	26.14	24.74
80%	31.45	29.52	68.32	60.88

Imaging and detection limit of ^{89}Zr-labelled cells – 3×3 cubic-well plate experiment

For the 3×3 cubic-well plate, the total activity per 1 cm^3 well ranged between 0.01-12.22 kBq on PET imaging, and 0.00-9.95 kBq as measured by the gamma counter. Specific activities ranged between 0.14-30.63 kBq/10^6 cells.

The total activity in each 1 cm^3 cubic well as determined from PET/CT and PET/MR images also showed a strong correlation with the total cell-associated activity as measured by the well counter (PET/CT: r = 0.995, p<0.0001; PET/MRI: r = 0.999, p<0.0001, **Fig. 4.16 A)**. Likewise, a significant positive correlation was observed between CNR and the total cell-associated activity (PET/CT: r = 0.994, p<0.0001; PET/MRI: r = 0.999, p<0.0001, **Fig. 4.16 B**). These results are in line with the results obtained from the 6-well plates.

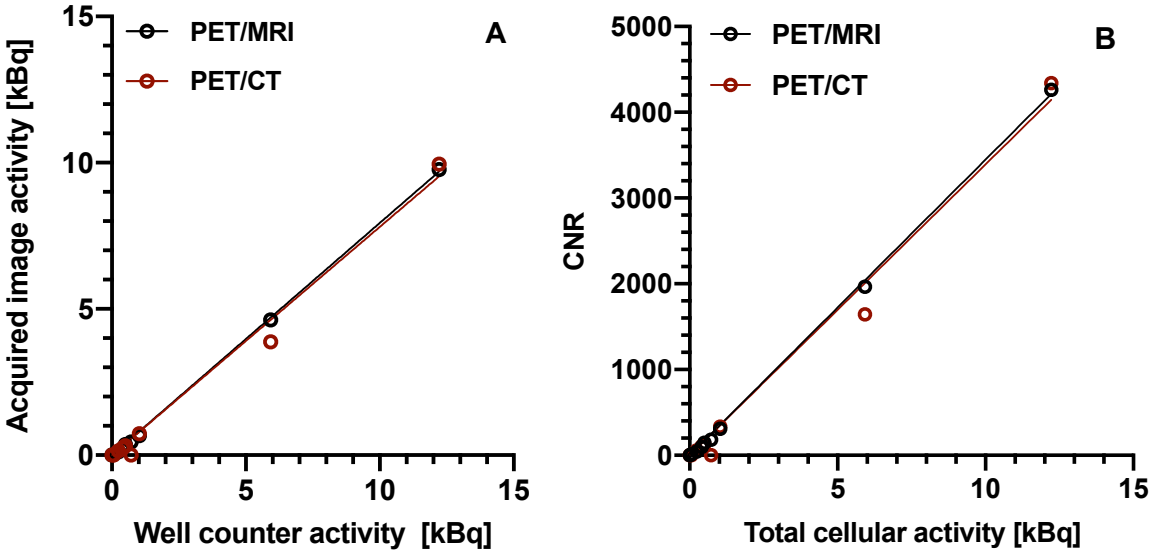

Figure 4.16 (A) Pearson correlation between the total cell-associated activity [kBq] measured in the well counter and on PET images and **(B)** Pearson correlation of CNRs obtained by PET/CT and PET/MRI vs. total cellular activity [kBq] for the 3×3 cubic-well plate.

No overall significant correlation between the CNR and cell number for each 1 cm^3 cubic well could be observed for both PET/CT (r = 0.79, p = 0.52) and PET/MRI (r = 0.32, p = 0.41) (**Fig. 4.17 A**) which is in contrast to the results obtained from the 6-well plates.

There was however a significant positive correlation between the CNR in each 1 cm^3 cubic well and the corresponding specific activity of cells (**Fig. 4.17 B**; PET/CT: r = 0.85, p = 0.004; PET/MRI: r = 0.82; p = 0.007) as could also be observed for the 6-well experiment.

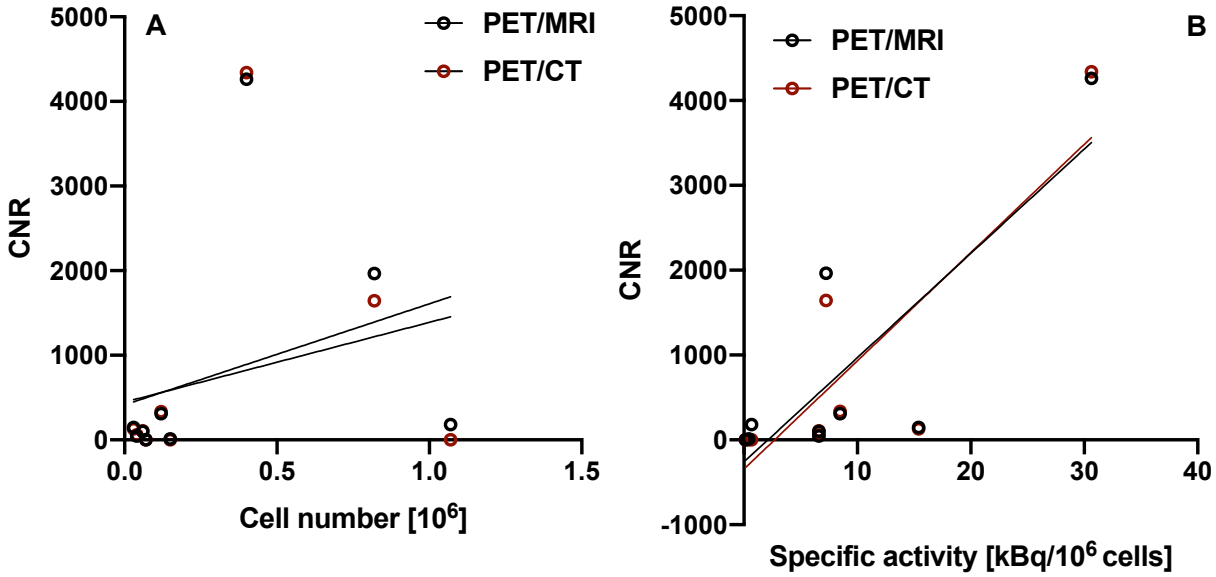

Figure 4.17 (A) Pearson correlation between the cell number [10^6 cells] and the respective contrast-to-noise ratio (CNR) per 1 cm^3 cubic well acquired using PET/CT and PET/MR **(**PET/CT: r = 0.79, p = 0.52; PET/MRI: r = 0.32, p = 0.41), (**B**) Pearson correlation between contrast-to-noise ratio (CNR) and specific activity [kBq/10^6 cells] per 1 cm^3 cubic well as obtained from PET/CT and PET/MR images **(**PET/CT: r = 0.85, p = 0.004; PET/MRI: r = 0.82; p = 0.007).

PET/CT and PET/MRI results strongly correlated for both the total activity in each well and the corresponding CNRs (**Fig. 4.18 A**, **C)**. Bland-Altman analysis indicated good agreement between PET/CT and PET/MRI indices of the total activity in each well and the corresponding CNRs (**Fig. 4.18 B**, **D**).

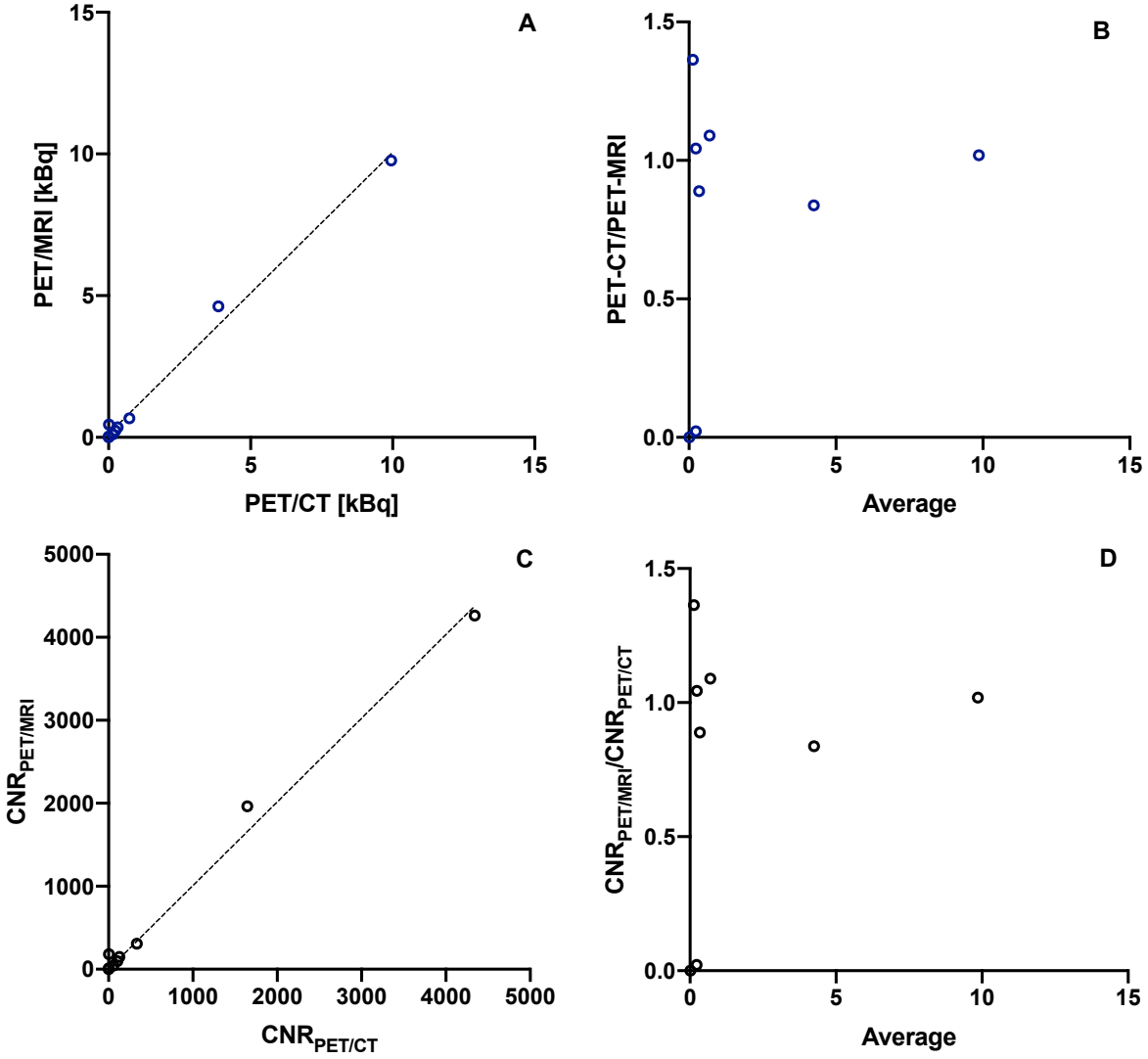

Figure 4.18 (**A**) Correlation and (**B**) Bland-Altman plot of cellular activities [kBq] obtained by PET/CT imaging versus PET/MRI for the 3×3 cubic-well plate (r = 0.992, p<0.0001; Bland-Altman analysis: 0.78 bias (SD = 0.50), 95 % limit of agreement: -0.20-1.77); (**C**) correlation and (**D**) Bland-Altman plot of CNRs obtained by PET/CT imaging versus PET/MRI for the 3×3 cubic-well plate (p<0.0001, r = 0.996, Bland-Altman analysis: 0.78 bias (SD = 0.50), 95 % limits of agreement: -0.20-1.76).

Figure 4.19 shows coronal PET images of the 3×3 cubic-well plate, acquired on both PET/CT and PET/MRI. A similar trend as observed on PET images of 6-well plates was also noticed for the 3×3 cubic-well plate with respect to detection. 1.1×10^6 cells with a specific activity of 0.7 kBq/10^6 cells could not be clearly visualized on PET images of the

3×3 cubic well plate (**Fig. 4.19**, **L1**) while 3.3×10^4 cells could be detected when the specific activity was 15.4 kBq/10^6 cells (**Fig. 4.19**, **M2**).

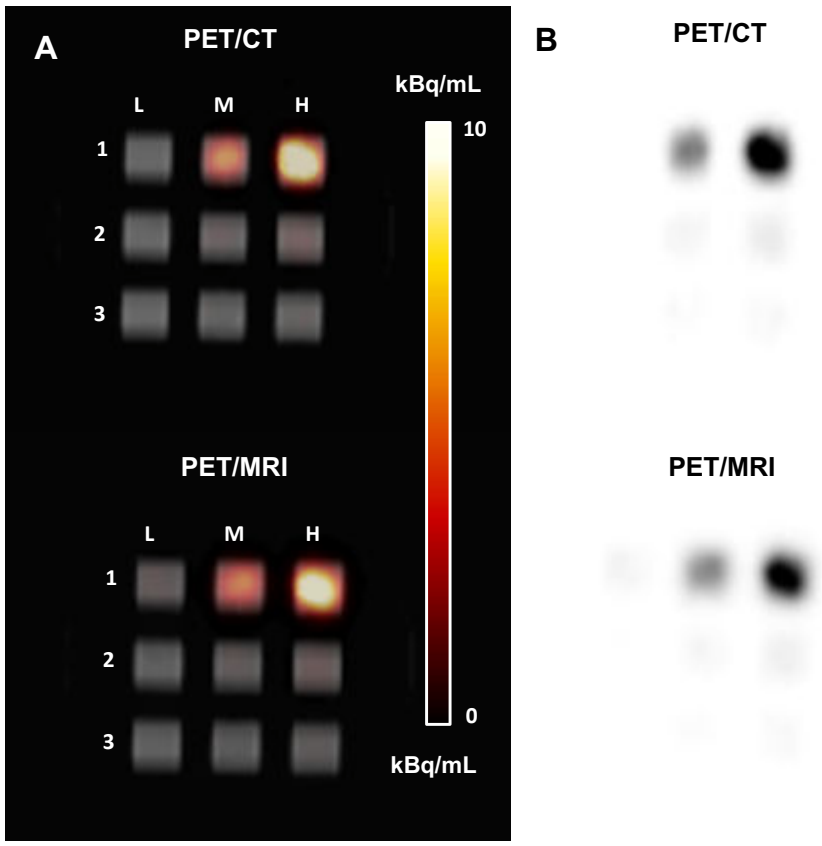

Fig. 4.19 PET images of 3×3 cubic-well plate containing ^{89}Zr-labelled Jurkat cells suspended in Geltrex™ matrix in a 1 cm^3 cube acquired using (**A**) PET/CT and PET/MRI fusion images and (**B**) PET images in grey-scale. Cell numbers and specific activities per well (kBq/10^6 cells; indicated in parenthesis) were as follows:

L1: 1.07×10^6 (0.67), **L2**: 1.50×10^5 (0.42), **L3**: 6.70×10^4 (0.14);
M1: 8.20×10^5 (7.23), **M2**: 3.25×10^4 (15.41), **M3**: 3.61×10^4 (6.61);
H1: 3.99×10^5 (30.63), **H2**: 1.21×10^5 (8.47), **H3**: 6.20×10^4 (6.60);

Figure 4.20 shows the detailed calculations for obtaining the theoretical lower limit of detection (LLD) for the for 3×3 cubic-well plate as it was calculated for the 6-well plate experiment. The calculations yielded a slightly lower LLD for PET/MRI compared to PET/CT where values were in the order of 10^5 cells. The LLD values obtained for the 3×3

cubic-well plate were slightly lower than those obtained for the 6-well experiment (**Table 4.5**), which can be explained by the higher density in the 1-cm^3 wells (**Table 4.6**). Nevertheless, the LLD results of both sets of independently conducted experiments, 6-well plate and 3×3 cubic-well plate experiment, are well in line with each other.

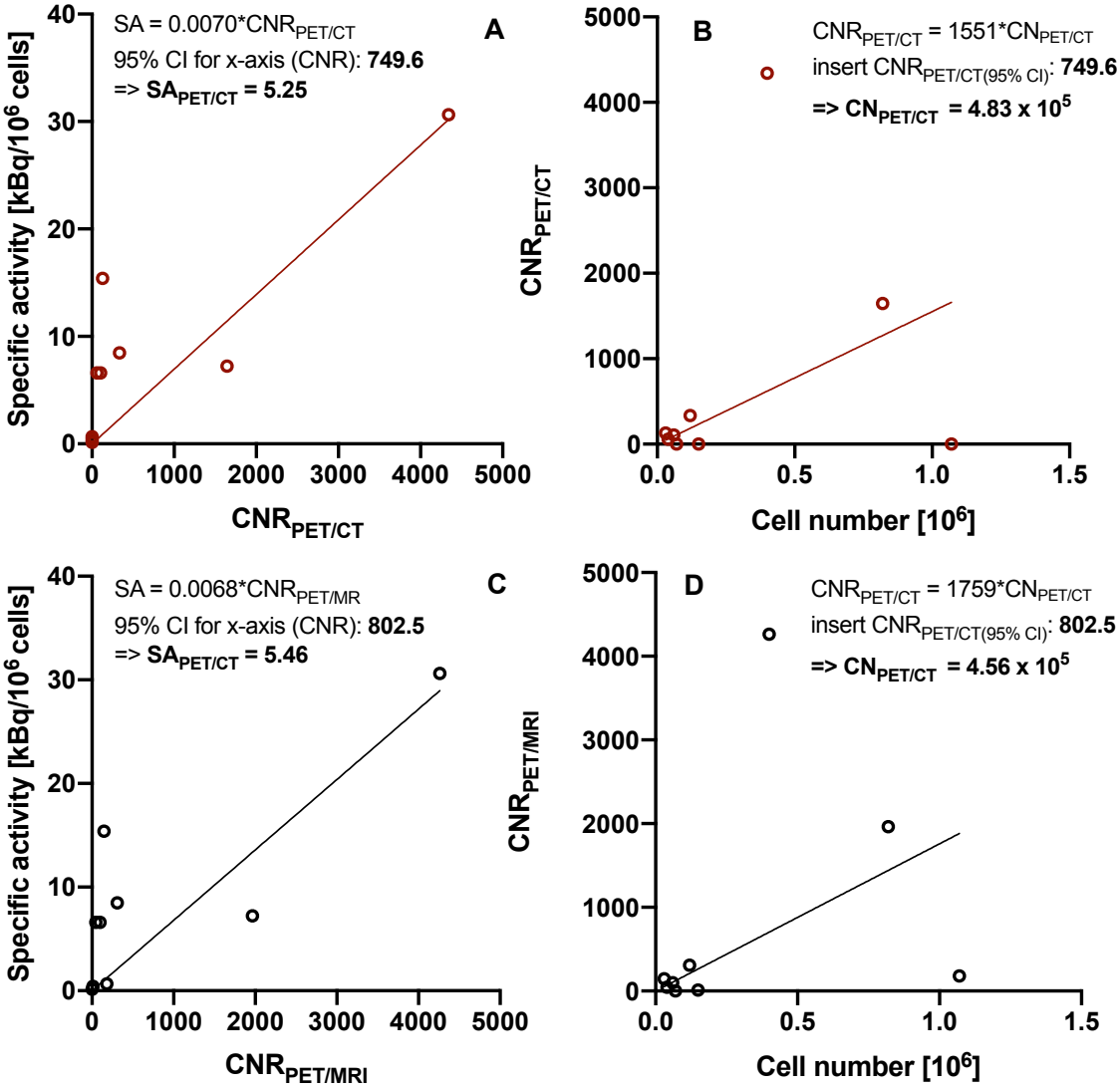

Figure 4.20 Linear regressions of (A, C) contrast-to-noise ratio (CNR) versus specific activity and (B, D) cell number versus CNR for both PET/CT (A, B) and PET/MRI (C, D) for the 3×3 cubic-well plate. Linear regression of specific activity vs. CNR used the upper 95% confidence interval (CI) of the x-intercept (=CNR). This value was subsequently inserted into the linear regression equation for CNR vs. cell number to derive the theoretical lower limit of detection (LLD). The obtained CNR, in the absence of background, was required to achieve the LLD.

Table 4.5 Theoretical lower limit of detection (LLD) for PET/CT and PET/MRI with respect to cell number and specific activity for both the 6-well plate and 3×3 cubic-well plate experiment.

	6-well plates		3×3 cubic-well plate	
LLD	**$LLD_{PET/MRI}$**	**$LLD_{PET/CT}$**	**$LLD_{PET/MRI}$**	**$LLD_{PET/CT}$**
Cell number	5.24×10^5 (1.05×10^4)*	5.88×10^5 (1.07×10^4)*	4.56×10^5 (2.84×10^3)*	4.83×10^5 (3.22×10^3)*
Specific activity [kBq/10^6 cells]	3.26 (0.07)*	3.72 (0.07)*	5.46 (0.03)*	5.25 (0.04)*

***** Values in parentheses indicate the theoretical LLD values according the Rose criterion (CNR=5) as a threshold for detectability.

Table 4.6 Well cell density (10^6 cells/mL) in wells for 6-well plates and the 3×3 cubic-well plate. Data are presented as median [range]. [a] Mann-Whitney *U* test

	6-well plates	3×3 cubic-well plate	p-value
Cell density [10^6 cells/mL]	0.04 [0-0.16]	0.12 [0.03-1.07]	<0.0001[a]

Figure 4.21 presents the image recovery coefficient as a function of cell density and specific activity for the 3×3 cubic-well plate. In general, an improvement in contrast recovery can be observed with increasing specific activity and cell density, indicating that the distribution of cells within a defined volume is an additional factor affecting detection. For the 3×3 cubic-well plate, convergence to a recovery coefficient of 1 for the specific activity obtained at LLD (~5.3 kBq/10^6 cells for both scanners), would require ~8.8×10^6 cells/mL.

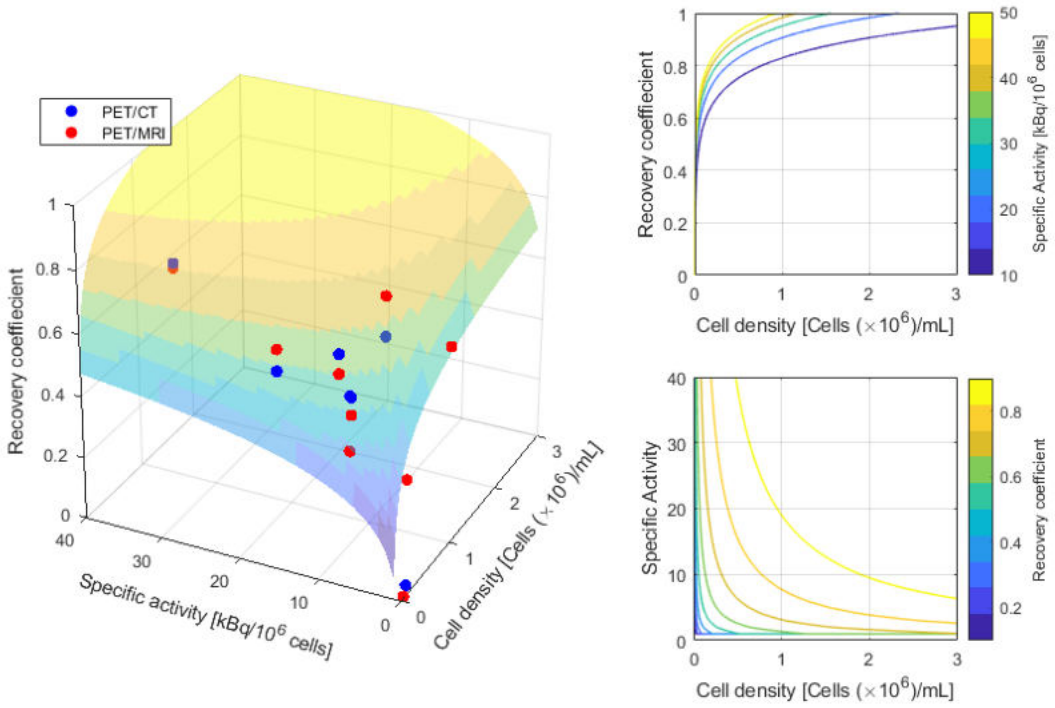

Figure 4.21 Recovery coefficient as a function of cell density (10^6 cells/mL) and specific activity (kBq/10^6 cells) for the 3×3 cubic-well plate. (**A**) Scatter plot of recovery coefficient vs. cell density and specific activity values and corresponding fit surface obtained through a logarithmic model function: y=0.11*log(CD*SA) + 0.57; CD = cell density; SA = specific activity (**B**) Contour plot of specific activity as a function of recovery coefficient and cell density. The contours correspond to specific activities ranging from 10-50 kBq/mL (**C**) Contour plot of recovery coefficient as a function of specific activity and cell density. Contour lines indicate recovery coefficients ranging from 0.1-1.0.

4.5 Discussion

Cell labelling and tracking is a rapidly growing area of clinical interest, particularly in the context of monitoring and evaluating novel cellular therapies (such as CAR-T cells). The sensitivity and quantification of cell labelling approaches are important for the successful clinical translation of this technology but little work has been undertaken to establish this on a clinical scanner. [^{89}Zr]Zr-Oxine has been used as a direct cell labelling method for cellular tracking in mice and holds great promise for clinical imaging due to its superior sensitivity compared to the conventional SPECT tracer [^{111}In]In-Oxine.

This is the first study to examine the theoretical detection limit and quantification of ^{89}Zr-labelled cells on a human PET system with respect to therapeutic cell tracking. Using an *in vitro* approach, cell numbers in the magnitude of 10^5 and 10^4 with an activity concentration of as low as 565 Bq/mL and 935 Bq/mL per well, respectively, could be detected during a 30 min scan. This detection limit is in line with the *in vitro* detection limit of [^{18}F]-FDG labelled cells on a clinical PET/CT whereby activity concentrations as low as 50 Bq/mL could be visualized during a 5 min acquisition [10]. PET sensitivity is influenced by the branching ratio for positron decay, which is more favourable for fluorine-18 (96.9%) compared to zirconium-89 (22.7%). Importantly, the longer half-life of 78.4 hours for zirconium-89 compared to fluorine-18 ($t_{1/2}$ = 109 min) is a requirement for longitudinal cell tracking over several days and lower branching ratios can be compensated for by an increase in scanning time. Furthermore, zirconium-89 is a residualizing isotope with intracellular binding to nuclear and cytoplasmic proteins ensuring retention of zirconium-89 inside the cell and provides better imaging contrast.

During a typical clinical white blood scintigraphy procedure 10-18.5 MBq of ^{111}In-labelled leucocytes are injected into patients to track cells and image sites of inflammation and infection [11]. Tumour infiltrating lymphocytes and peripheral blood mononuclear cells could be tracked and imaged in patients with maximum 1.3-3.7 kBq/10^6 cells with the corresponding range of injected number of cells being 1.5-9.2×10^9 [3, 6]. This specific activity corresponds to the lowest specific activity of ^{89}Zr-labelled cells in this study, where cells in the magnitude of 10^5 could still be detected. With its superior sensitivity over SPECT, PET has the potential to detect cells labelled with less activity or alternatively a

smaller number of cells. Preclinically, ^{89}Zr-labelled cells have been tracked with PET at approximately 10 times lower activities compared to those labelled with Indium-111 [14]. Recent developments in the whole body PET scanner technology will allow sensitivity to increase by a further 40-fold for the whole body and 4-5 fold for a single organ [15], which would allow to reduce scan times, the use of lower cellular activities or even fewer cells could be detected with PET imaging.

Given the radiosensitivity of lymphocytes and their subsets, the lower end of the radioactivity spectrum associated with cells was examined for imaging purposes that, according to literature, has not been shown to cause significant cell damage. Therefore, the focus in this study was to quantify the lower limits of cell detection with specific activities of up to ~35 kBq/10^6 cells. In preclinical animal models, the damage to γδ-T cells was minimal at specific activities up to 20 kBq/10^6 cells [16] whereas CAR-T cells maintained their functionality and viability up to 70 kBq/10^6 cells [8] and ^{89}Zr-labelled bone marrow cells were not altered at 16.6 kBq/10^6 cells and could be imaged up to 7 days after injection *in vivo* [17]. The data obtained from the work presented in this chapter suggests that cells with as low as 2 kBq/10^6 cells can still be visualized on a human PET scanner which is promising for the potential use of ^{89}Zr-labelled cells *in vivo*.

The specific activity per cell is one of the major limiting factors for cellular imaging using radioactive labelling approaches, given that labelling and tracking must not significantly alter the phenotype, viability, and functionality of labelled cells. Ideally, the radioactivity per cell should not affect any of these characteristics but at the same time should be sufficient to enable the visualization of labelled cells on imaging. These characteristics are pivotal prerequisites that need to be incorporated into all *in vivo* cell tracking and especially clinical imaging scenarios.

This work shows that detectability, as measured by the contrast-to-noise ratio, is dependent on the total cellular activity as well as the actual cell number and the specific activity of cells. **Fig. 4.12** demonstrates the strong interplay between the cell number and specific activity for cell detection. Whereas 6.1×10^4 cells with a specific activity of 6.9 kBq/10^6 cells (C3) were not visible on imaging, a similar number of cells (6.8×10^4) could be detected with a 4-times higher specific activity (B2). Likewise, 1.7×10^5 cells could not

be detected (C2) compared to 5.2×10^5 cells (A2) with a similar specific activity. A similar trend was observed for the 3×3 cubic-well plate experiment (**Fig. 4.19**) which demonstrates the overall significant role that both specific activity on cells and the cell number itself play in the detection of labelled cells and which needs to be carefully considered for *in vivo* experiments. Although two different and independent sets of experiments, both the 6-well plate and the 3×3 cubic-well plate experiment are complementing each other. Whereas the 6-well plate experiment yielded detection limits with respect to cell number and cellular specific activities, the 3×3 cubic-well plate experiment further expanded this concept of detectability as a function of cell concentration (density) within a limited volume of distribution (1 cm^3 cube). In fact, cell density is another factor that needs to be accounted for in the detection of labelled cells due to for example T-cell expansion and contraction in response to target elimination at the tumour site resulting in a variation of cell density [18]. Jurkat T-cells have a doubling rate of 48 hours and expand very fast. However, this work has only investigated the imaging of these cells directly after labelling and the effect of proliferation on the detection limit was not investigated. The significantly different cell densities of cell suspensions in 6-well plates compared to the 3D printed cubic well plate were reflected in both slightly lower theoretical limits of detection (LLDs) but also in slightly lower detection limits observed on images for the cubic well plate owing to a higher cell density.

The calculated values obtained for the theoretical lowest limit of detection (LLD) by linear regression were an order of magnitude higher than the Rose criterion (CNR = 5); the lowest CNRs whereby cells could be visualized in this study were 63 and 68 for PET/CT and PET/MRI, respectively. Due to the interplay between cell number, specific activity and CNR described above, these theoretical numbers can vary. Given the very low amount of activity on cells and the uncertainty of how densely cells will travel *in vivo* it is very likely that cell imaging will require higher CNRs to visualize cells than described by the Rose criterion and the application of this criterion for cell tracking is uncertain.

The limitations of this work include that the imaged cell suspensions in each well are not a true representation of an *in vivo* cellular infiltration, where cells probably distribute in a more 3-dimensional manner and less planar way as was seen in well conditions. Images revealed that cells tended to accumulate at the bottom of the 6-wells plates in hot

spots whereas dispersal circulation and infiltration *in vivo* may result in less dense accumulation, a feature which will influence detectability. The advantage of this hot spot-like coalescence of cells is that it more closely represents that the total cell number as counted after the scan. In reality cells will not coalesce in a rather planar way *in vivo*. The 3D printed structure and cells immersed in a 1 cm^3 gel were supposed to mimic a more realistic and 3D-like dispersal of cells in a lesion in a defined volume. In this case a semi-homogenous distribution within the cubic well was assumed. Although the viability of cells and also the release of potential free zirconium-89 from cells after the scan could not be analysed similar to the 6-well plates, this experiment also provided better consistency in terms of the experiment set-up. Cells immersed in gels will not move during a transfer between two scanners and the cells imaged on PET/CT will be in the same position within the gel on the subsequent PET/MRI. The movement of the 6-well plates may have caused the cells to move within the 6-well plate and to be distributed differently even to a small extent within the well which may affect the cell density and eventually the detection. However, the amount of data points obtained for the 6-well plate experiment compared to the 3D printed structure were unequal and correlations including statistics for the cubic 3D printed structure only had few data points. Nevertheless, there was a good agreement between both experiments.

Similarly, this work has not accounted for dilution of the radioactive signal over time due to cell proliferation as the plates were imaged only directly after labelling. Signal dilution could significantly affect *in vivo* detection at later time points. An appropriate starting dose and specific activity on cells needs to be carefully considered for *in vivo* tracking with a direct cell labelling approach. The imaging of ^{89}Zr-labelled cells 7 days post-injection results in an approximately 75% decrease of total cellular activity due to radioactive decay which does not include the effects of label dilution due to cellular proliferation as described above that needs to be considered additionally. Given that cells can still be visualized at 2 kBq/10^6 cells at day 7 following labelling, this would mean a starting dose of at least 10 kBq/10^6 cells would be required. This dose would need to be tolerated by cells without causing cellular damage or impairing their function.

The measured data also did not account for non-specific radioactivity, which will decrease the contrast-to-noise ratio and therefore the detectability. The detection limit of

^{89}Zr-labelled cells is expected to be higher for *in vivo* cell tracking, not only because of non-specific signal but also higher photon attenuation increasing noise, and a higher level of corrupt events (scatter and random coincidences) potentially reducing contrast and increasing image noise. As a consequence, our measured data shows unusually high CNRs that would normally not be observed on patient images. In an attempt to model the effect of non-specific radioactivity on detection, simulations for non-specific signal were performed for the 6-well plate experiment given that a bigger data set with many different specific activities was available for modelling. This theoretical experiment could predict a realistic trend as could be found *in vivo* with natural and increased background activity present and showed that the number of cells that can be detected in the presence of background decreases in the order of magnitudes with increasing background. In reality, the detection limit is most likely one or two magnitudes higher as was shown here. The interplay between cell number, density and cell specific activity is unique in every *in vivo* imaging scenario with different tumours and can't be predicted accurately with *in vitro* data. However, a rough guideline and trends in the detection of radiolabelled cells could be given with this data. Eventually, it will also vastly depend on what type of cells are labelled and imaged but also how much radioactivity cells tolerate for imaging which is one very important factor for cell imaging.

Furthermore, using a direct cell labelling approach with [^{89}Zr]Zr-Oxine, live cells cannot be distinguished from dead cells and the leakage of activity from dead cells is likely to account for non-specific activity in neighbouring tissues and bone over time due to the bone seeking properties of Zirconium-89 and thereby decreases the detectability and quantification of actual labelled cells. [^{89}Zr]Zr-Oxine passively diffuses through the cell membrane of even dead cells but is likely to efflux from a dead or dying cell without being retained over a long period of time due to the disrupted cell membrane.

The images of all well plates and the 3D structure were reconstructed using reference CT-based attenuation maps for both PET/CT and PET/MRI which circumvented the attenuation correction issues associated with PET/MRI and can notably improve the visual quality of the PET images by reducing noise [19]. MRI guided attenuation correction methods have shown promising results in brain PET attenuation correction but are challenging for the whole body. In a clinical scenario, it is unlikely that a patient would

have both PET/CT and PET/MRI scans and MR-based attenuation correction methods would be employed. In regards to detection limit, this work has shown that there was no noticeable difference between PET/CT and PET/MRI. In a realistic, clinical imaging scenario there may be differences between the two modalities given their different operation, acquisition, image processing and other factors, e.g. MR-guided vs CT-guided attenuation amongst others that can influence the detection and quantification.

4.6 Appendix

Table 4.7 Cellular conditions for the 6-well plate experiment: cell number, total cellular activity as measured by the well counter, cellular activities and background noise per well obtained on PET/CT and PET/MRI.

Plate	Well	Cell number [10^6 cells]	Cellular activity (well counter) [kBq]	Cellular activity (PET/CT) [kBq]	Back-ground noise (PET/CT) [kBq]	Cellular activity (PET/MRI) [kBq]	Back-ground noise (PET/MRI) [kBq]
1	10^6	1.58	7.72	8.51	0.001	10.68	0.004
	10^5	0.14	1.26	1.32		1.64	
	10^4	0.03	0.10	0.03		0.22	
2	10^6	1.28	3.41	**n/a**	**n/a**	3.81	0.005
	10^5	0.06	0.03	**n/a**		0.04	
	10^4	0.03	0.02	**n/a**		0.01	
3	10^6	0.24	2.25	4.87	0.004	5.46	0.005
	10^5	0.03	0.19	0.32		0.35	
	10^4	**n/a**	**n/a**	**n/a**	**n/a**	**n/a**	**n/a**
4	10^6	0.24	2.27	4.73	0.005	4.93	0.005
	10^5	0.01	0.09	0.37		0.44	
	10^4	**n/a**	**n/a**	**n/a**	**n/a**	**n/a**	
5	10^6	0.38	12.22	22.00	0.006	24.47	0.013
	10^5	0.07	1.87	2.95		3.23	
	10^4	0.01	0.18	0.01		0.32	

6	10^6	0.27	**n/a**	19.78	0.005	21.67	0.005
	10^5	0.15	**n/a**	3.38		3.78	
	10^4	0.05	**n/a**	0.01		0.34	
7	10^6	0.85	6.62	11.60	0.008	12.30	0.012
	10^5	0.17	0.59	0.90		1.00	
	10^4	0.06	0.42	0.50		0.30	
8	10^6	0.90	5.74	13.30	0.003	13.30	0.009
	10^5	0.14	0.65	0.90		0.80	
	10^4	0.22	0.35	0.40		0.10	
9	10^6	2.17	4.02	4.20	0.003	4.60	0.002
	10^5	0.55	1.19	1.20		1.40	
	10^4	0.16	0.23	0.20		0.30	
10	10^6	1.36	3.67	3.80	0.002	4.20	0.004
	10^5	0.52	1.13	1.10		1.20	
	10^4	0.15	0.23	0.10		0.20	
11	10^6	1.78	15.57	10.60	0.001	11.30	0.006
	10^5	0.62	6.45	3.70		4.00	
	10^4	0.11	2.48	1.40		1.80	
12	10^6	1.26	14.03	10.60	0.002	11.30	0.003
	10^5	0.55	5.80	3.90		4.10	
	10^4	0.19	1.56	0.90		0.90	

Table 4.8 Cellular conditions for the 3D structure experiment: Cell number, total cellular activity as measured by the well counter, cellular activities and background noise per 1 cm^3 cube obtained on PET/CT and PET/MRI.

Cube	Cell number [10^6 cells]	Cellular activity (well counter) [kBq]	Cellular activity (PET/CT) [kBq]	Back-ground noise (PET/CT) [kBq]	Cellular activity (PET/MRI) [kBq]	Back-ground noise (PET/MRI) [kBq]
L-10^6	1.07	0.72	0.01		0.45	
L-10^5	0.15	0.06	0.00		0.03	
L-10^4	0.07	0.01	0.00		0.00	
M-10^6	0.82	5.93	3.87		4.62	
M-10^5	0.03	0.50	0.32	0.002	0.36	0.006
M-10^4	0.04	0.24	0.15		0.11	
H-10^6	0.40	12.22	9.95		9.77	
H-10^5	0.12	1.03	0.73		0.67	
H-10^4	0.06	0.41	0.24		0.23	

4.7 References

1. Holland JP, Sheh Y, Lewis JS. Standardized methods for the production of high specific-activity zirconium-89. *Nucl Med Biol*. 2009;36(7):729-739.
2. McAfee JG, Samin A. In-111 labeled leukocytes: A review of problems in image interpretation. *Radiology*. 1985;155(1):221-229.
3. Palestro CJ, Love C, Bhargava KK. Labeled leukocyte imaging: Current status and future directions. *Q J Nucl Med Mol Imaging*. 2009;53(1):105-123.
4. Rahmim A, Zaidi H. Pet versus spect: Strengths, limitations and challenges. *Nucl Med Commun*. 2008;29(3):193-207.
5. Bhargava KK, Gupta RK, Nichols KJ, Palestro CJ. In vitro human leukocyte labeling with 64Cu: an intraindividual comparison with 111In-oxine and 18F-FDG. *Nucl Med Biol*. 2009;36(5):545-549.
6. Sanchez-Crespo A, Jussing E, Björklund AC, Pokrovskaja Tamm K. Hallmarks in prostate cancer imaging with Ga68-PSMA-11-PET/CT with reference to detection limits and quantitative properties. *EJNMMI Res*. 2018;8.
7. Fischer BM, Olsen MWB, Ley CD, et al. How few cancer cells can be detected by positron emission tomography? A frequent question addressed by an in vitro study. *Eur J Nucl Med Mol Imaging*. 2006;33(6):697-702.
8. Weist MR, Starr R, Aguilar B, et al. PET of adoptively transferred chimeric antigen receptor T Cells with 89Zr-Oxine. *J Nucl Med*. 2018;59(10):1531-1537.
9. Carney JPJ, Townsend DW, Rappoport V, Bendriem B. Method for transforming CT images for attenuation correction in PET/CT imaging. *Med Phys*. 2006;33(4):976-983.
10. Fischer BM, Olsen MWB, Ley CD, et al. How few cancer cells can be detected by positron emission tomography? A frequent question addressed by an in vitro study. *Eur J Nucl Med Mol Imaging*. 2006;33(6):697-702.
11. Roca M, De Vries EFJ, Jamar F, Israel O, Signore A. Guidelines for the labelling of leucocytes with 111In-oxine. *Eur J Nucl Med Mol Imaging*. 2010;37(4):835-841.

12. Muller C, Zielinski CC, Linkesch W, Ludwig H, Sinzinger H. In vivo tracing of indium-111 oxine-labeled human peripheral blood mononuclear cells in patients with lymphatic malignancies. *J Nucl Med*. 1989;30(6):1005-1011.
13. Griffith KD, Read EJ, Carrasquillo JA, et al. In vivo distribution of adoptively transferred indium- 111- labeled tumor infiltrating lymphocytes and peripheral blood lymphocytes in patients with metastatic melanoma. *J Natl Cancer Inst*. 1989;81(22):1709-1717.
14. Noriko Sato, Haitao Wu, Gary Griffiths and PC. Generation and use of long-lasting cell labeling agent for positron emission tomography (PET) imaging. *J Nucl Med*. 2014;55(supplement 1).
15. Cherry SR, Jones T, Karp JS, Qi J, Moses WW, Badawi RD. Total-body PET: Maximizing sensitivity to create new opportunities for clinical research and patient care. *J Nucl Med*. 2018;59(1):3-12.
16. Man F, Lim L, Volpe A, et al. In Vivo PET Tracking of 89 Zr-Labeled Vγ9Vδ2 T Cells to Mouse Xenograft Breast Tumors Activated with Liposomal Alendronate. *Mol Ther*. 2019;27(1):219-229.
17. Asiedu KO, Koyasu S, Szajek LP, Choyke PL, Sato N. Bone marrow cell trafficking analyzed by 89Zr-oxine positron emission tomography in a murine transplantation model. *Clin Cancer Res*. 2017;23(11):2759-2768.
18. Vedvyas Y, Shevlin E, Zaman M, et al. Longitudinal PET imaging demonstrates biphasic CAR T cell responses in survivors. *JCI Insight*. 2016;1(19).
19. Mehranian A, Zaidi H, Reader AJ. MR-guided joint reconstruction of activity and attenuation in brain PET-MR. *Neuroimage*. 2017;162:276-288.

Chapter 5

Cell penetrating peptides – trojan horses for direct cell labelling applications?

5.1 Contributions and collaborators

All radiotracer synthesis, procedures and post-synthesis analysis and characterisation were undertaken by myself except where mentioned in the materials and method section when the source of the starting material was purchased by one of our collaborators. I was also vastly involved in the design of peptides and linker strategy including chelator choice. Peptide synthesis itself was carried out in collaboration.

5.2 General introduction

The use of biologically active molecules such as proteins, peptides and oligonucleotides has opened up and expanded therapeutic approaches in a number of diseases. Biologic agents are generally highly specific, well tolerated, and have shown potential to be transferrable to clinical development. However, the hydrophilic nature of bioactive molecules often limits their therapeutic value because of low membrane permeability which prevents their access to intracellular targets. In comparison, membrane permeability is much higher for lipophilic agents such as [^{89}Zr]Zr-Oxine, [^{111}In]In-Oxine, [^{99m}Tc]Tc-HMPAO and [^{64}Cu]Cu-PTSM as mentioned in the previous chapters and many compounds that need to cross the blood-brain barrier (BBB), which is hampered for hydrophilic molecules.

In 1988, a new class of peptides were introduced by both Frankel et al. [1] and Green et al. [2] who observed that the HIV-trans-activator of transcription (TAT) protein could enter tissue-cultured cells, translocate into the cell nucleus, resulting in target gene expression. In 1991, Joliot et al. revealed that the homeodomain of Antennapedia (pAntp), a synthetic, 60 amino acid long peptide could be internalized by nerve cells [3]. Derossi et al. found that a short peptide sequence with 16 amino acids from the third helix of the antennapedia homeodomain (RQIKIYFQNRRMKWKK), named penetratin, was also able to penetrate the plasma membrane [4]. This new class of peptides that is able to traverse the cell membrane was termed cell-penetrating peptides (CPPs), also known as protein transduction domains (PTDs) or trojan horse peptides.

Generally, CPPs are defined as short, water-soluble and partly hydrophobic, and/or polybasic peptides carrying at most 30-35 amino acids residues with a net positive charge at physiological pH [1]. The main feature of CPPs is that they are able to penetrate the cell membrane at low micromolar concentrations *in vivo* and *in vitro* without using any chiral receptors or causing significant membrane damage. Most importantly, CPPs are capable of internalizing electrostatically or covalently bound cargoes such as therapeutic drugs, DNA, RNA but also nanoparticles and liposomes with high efficiency and low cytotoxicity [5],[6]. Today, various CPPs have been characterised from natural sources and synthetic sources [7] and the fact that CPPs can shuttle cargo into cells together with the possibility to add diverse modifications to the peptide backbone make these trojan horse peptides an excellent candidate for future drug delivery platforms.

CPPs have different biological origins and sequences and thus exhibit a variety of physicochemical properties. The following section will introduce an overview of the different classes of CPPs followed by a section about different cellular uptake mechanisms that also depend on the sequence and properties of each CPP.

5.3 CPP classification

Although several different criteria have been proposed for the classification of CPPs, no unified taxonomy of these peptides presently exists. Based on their physicochemical properties, CPPs can be classified into different subgroups.

(1) CPPs can be categorized based on their origin. This includes protein-derived peptides such as TAT and penetratin, but also chimeric peptides that contain two or more motives from other peptides, e.g. transportan and its shorter analogue TP10. The third group of this category comprises synthetic peptides such as polyarginines [8].

(2) CPPs can be classified into three subgroups based on their physicochemical characters: A) cationic CPPs, B) amphipathic CPPs and C) hydrophobic CPPs. Cationic CPPs comprise peptides with highly positive net charges at physiological pH that primarily originate from the basic short strands of arginines and lysines. Cationic peptides include TAT-derived peptides, penetratin and polyarginines. Amphipathic CPPs are the most

common, accounting for more than 40% of all CPPs. Amphiphathic CPPs contain polar and non-polar amino acid regions, and the non-polar regions are rich in hydrophobic amino acids (e.g. alanine, valine, leucine, and isoleucine). Many amphipathic CPPs are chimeric peptides obtained by covalently binding a hydrophobic domain, which is essential for efficient targeting to cell membranes, to a nuclear localization signal (NLS). The latter is a short cationic peptide based on lysine-, arginine-, or proline-rich motifs that targets the peptide and cargo into the cell nucleus through the nuclear pore complex. Amphipathic CPPs includes peptides such as MPG and Pep-1, amongst others [9].
Hydrophobic CPPs mainly contain nonpolar residues, resulting in a low net charge. Due to their hydrophobic motifs they exhibit a high affinity for the hydrophobic domains of cellular membranes which is crucial for the process of cellular internalization. Only a limited number of hydrophobic peptides has been discovered and explored up to today and their internalization mechanisms have been rarely studied compared with the cationic and amphipathic classes.

(3) Lastly, CPPs can be divided according to their conformation, into either being linear or cyclic CPPs.

Since the first discovery of CPPs, more than 1700 CPPs have been characterized and are listed in the CPPsite 2.0 database[1]. **Table 5.1** summarizes well-known and frequently used CPPs including some of their characteristics. The chemical and structural diversity of peptide sequences results in a range of interactions with the cell membrane and different mechanisms and rates of uptake.

Table 5.1 Overview and summary of different CPPs and their sequence, type and origin. Table copied from [10].

Peptide	Sequence	Type	Lenght	Origin
Antennapedia Penetratin (43–58)	RQIKIWFQNRRMKWKK	Cationic and amphipatic	16	Protein-derived
HIV-1 TAT protein (48–60)	GRKKRRQRRRPPQ	Cationic	13	Protein-derived
pVEC Cadherin (615–632)	LLIILRRRIRKQAHAHSK	Amphipatic	18	Protein-derived
Transportan Galanine/Mastoparan	GWTLNSAGYLLGKINLKAL AALAKKIL	Amphipatic	27	Chimeric
MPG HIV-gp41/SV40 T-antigen	GALFLGFLGAAGSTMGAWS QPKKKRKV	Amphipatic	27	Chimeric
Pep-1 HIV-reverse transcriptase/SV40 T-antigen	KETWWETWWTEWSQPKKKRKV	Amphipatic	21	Chimeric
Polyarginines	R(n); 6 < n < 12	Cationic	6–12	Synthetic
MAP	KLALKLALKALKAALKLA	Amphipatic	18	Synthetic
R6W3	RRWWRRWRR	Cationic	9	Synthetic
NLS	CGYGPKKKRKVGG	Cationic	13	Protein-derived
8-lysines	KKKKKKKK	Cationic	8	Synthetic
ARF (1–22)	MVRRFLVTLRIRRACGPPRVRV	Amphipatic	22	Protein-derived
Azurin-p28	LSTAADMQGVVTDGMASGLDKD YLKPDD	Anionic	28	Protein-derived

[1] https://webs.iiitd.edu.in/raghava/cppsite/

5.4 Mechanism of cell internalization

The mechanisms for cellular internalization of CPPs have been the subject of intense investigation, however the pathways involved in this process have not been fully elucidated. The difficulties in the comprehension of the cellular uptake of these peptides mostly stem from the differing physicochemical properties, size, and concentration of the diverse CPPs and/or CPP-cargo conjugates. These features have shown to have significant impact on the efficiency of cellular entry [11]. Nevertheless, it could be shown that a single CPP can exploit different routes to enter the cell and that these routes may occasionally operate concomitantly, depending on the experimental conditions. The cellular entry routes are broadly divided into two groups: energy-independent direct penetration of the plasma membrane and energy-dependent endocytosis (**Fig. 5.1**). Direct translocation across the cell membrane seems to occur in some cases, mainly at high concentrations of the peptide [12],[13], however it is generally accepted that most CPPs and CPP-cargo conjugates enter cells by endocytosis [14],[15].

Although direct penetration or translocation was first proposed as the main mechanism of CPP internalization, subsequent re-evaluation of the mechanism of CPP uptake and data obtained from ensuing investigations suggested that endocytosis is the principal internalization route for many CPPs and CPP-cargo complexes [16]. Endocytosis is a natural and energy-dependent process occurring in all cells. It may involve several different pathways that can be classified as macropinocytosis, clathrin- or caveolin-mediated endocytosis, and clathrin/caveolin-independent endocytosis [17]. Whether one or another pathway is predominant mostly depends on the size and physicochemical nature of the cargo molecule [18]. While CPPs can be directly localized into the cytosol after translocation by non-endocytic pathways, there is evidence suggesting that some peptides can remain trapped in endosomes during endocytosis [19]. This plays a major role in the delivery of therapeutic cargo and its availability inside the cell upon entry into the cell and therefore impacts the transduction efficacy of a CPP-cargo complex and its retention.

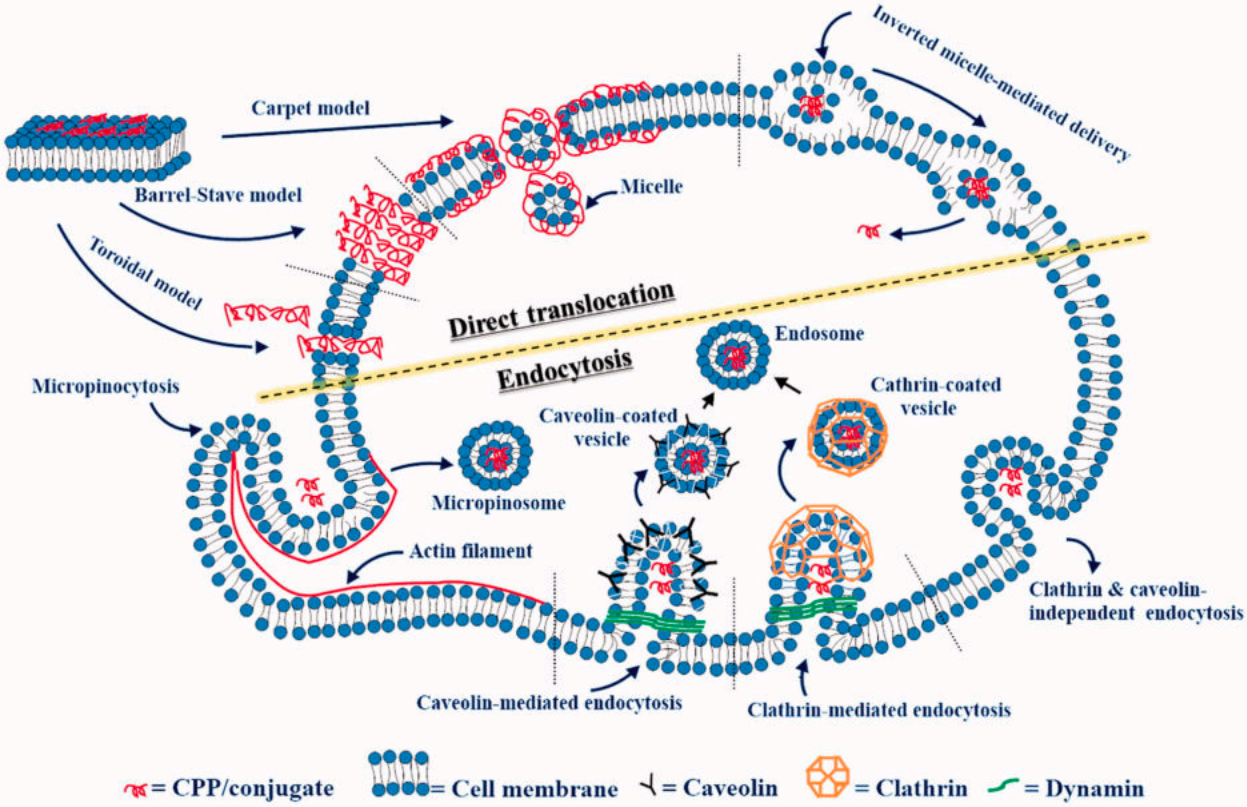

Figure 5.1 Graphical overview of different cellular uptake mechanisms of cell penetrating peptides. Figure reproduced from [20].

Direct translocation involves multiple entry routes that are initially based on the interaction of positively charged CPPs with the negatively charged membrane components and phospholipid bilayer. This interaction is followed by peptide entrance via various mechanisms that have been described as causing transient pore formation or membrane destabilization through either 'toroidal pores' or 'barrel-stave pores' within the plasma membrane. In the former case, CPPs accumulate on the outer leaflet of the phospholipid bilayer which can cause distortion of the membrane and leads to the formation of a transient pore [21]. Once in contact with the lower cytosolic pH, cell membrane fatty acids release CPPs into the cells and the transient pore closes [22]. According to the barrel-stave pore model, peptides adopt an α-helical structure in the membrane with their hydrophilic side chains forming the internal face of the pore which enables the entrance of the CPPs' hydrophilic elements [23]. In addition, the 'carpet-like' model is characterised

by a transient increment in membrane fluidity following the interaction of the positively charged amino acids of CPPs with the negative charges on the membrane surface or the 'inverted-micelle' mechanism, which is based on infolding of the phospholipid bilayer via the formation of inverted micelles encapsulating the peptide [24].

5.5 Applications of CPPs

5.5.1 General overview

The efficiency of CPPs in crossing cell membranes independent of cell type [25] has made them one of the most valuable tools for cellular delivery of cargo molecules but also a major player in medical research. Compared to other translocation techniques, such as electroporation [26], microinjection [27] or using a gene gun [28], CPPs have low cytotoxicity and are capable of safely entering the cells in a noninvasive manner without compromising the integrity of the cellular membranes at high efficiency [29]. CPPs can serve as carriers to transport cargoes such as siRNA [30], nucleic acids [31], proteins [32], small molecule therapeutic agents [33], quantum dots [34], MRI contrast agents [35] as well as metal chelates [36] into cells amongst others. Today, one of the most frequently employed and investigated CPPs is the TAT peptide alongside other peptides that are under clinical investigation for applications ranging from inflammation, pain, cancer, heart diseases and aging [10]. **Table 5.2** gives a short overview of completed phase I to III clinical trials using different CPP-based therapies.

Selective covalent binding between a CPP and a cargo to produce a conjugate involves consideration of their chemically reactive groups and structural properties, selection of a suitable synthetic approach and establishment of conditions. The chemical toolbox can hereby be exploited to create a plethora of constructs. In general, conjugation of CPPs and drug molecules can be either through covalent bonding or non-covalent complex formation via charge interactions. Covalent conjugation is the most common method for producing a well-defined biologically active molecule with a strong bond between the CPP and cargo molecule via a chemical linkage, such as disulfide or thio-ester bonds. Among the chemical linkages, a disulfide linkage has been used most often,

as the bond can be easily cleaved by cytoplasmic degradation enzymes. This concept is also a popular strategy in the design of antibody-drug conjugates where disulfide bond cleavage leads to the release of the drug at the target cell [37].

Table 5.2 Selection of CPP-based therapies under clinical development. Table copied from [10].

CPP	Cargo	Application	Status	Compound	Company	ClinicalTrial.gov ID
R7	Cyclosporine A	Psoriasis	Phase II terminated 2003	PsorBan	CellGate. Inc	N/A
TAT	δPKC inhibitor	Heart attack	Phase II completed 2011	KAI-9803	KAI Pharmaceutical	NCT00785954
PTD4	HSP20 phosphopeptide	Wound healing	Phase II completed 2012	AZX-100	Capstone Therapeutics	NCT00825916
P28	P28	Central Nervous System Tumors	Phase I completed 2013	P28	Pediatric Brain Tumor Consortium	NCT01975116
P28	P28	Solid tumors	Phase I completed 2014	P28	CDG Therapeutics. Inc	NCT00914914
N/A	N/A	Duchenne Muscular Dystrophy (DMD)	Phase II completed 2015	AVI-4658	Sarepta Therapeutics	NCT00844597
TAT	JNK-1	Intraocular inflammation and pain	Phase III completed 2016	XG-102	Xigen SA	NCT02235272
TAT	JNK-1	Acute inner ear hearing loss	Phase III completed 2017	AM-111	Auris Medical	NCT02561091
MTS	Botulinum toxin A	Cervical Dystonia	Phase II completed 2018	R-002	Revance Therapeutics	NCT02706795

Although the number of CPP-based clinical trials has been increasing over the years, there is no CPP or CPP/cargo complexes that has gained FDA approval up to today. Some of the reasons for this include *in vivo* stability issues due to the susceptibility of CPPs to proteolytic degradation and poor efficiency due to the CPP's lack of specificity. This also explains the scarce use of CPPs for imaging purposes which is briefly described in the next section.

5.5.2 CPPs used for imaging

From the vast variety of cargo that can be attached to CPPs only TAT and the polyarginine peptide R_8 have used chemically versatile chelators [36],[38]–[40] that can be attached to CPPs and which can serve as a platform for radiometal conjugates and imaging.

Only few studies have actually employed CPPs in combination with radiometals and molecular imaging in preclinical settings. In 2000, one of the first studies described the use of the TAT peptide modified to accommodate ligands for the chelation of technetium-99m and ruthenium-188 for imaging and radiotherapy [41]. Cytosolic and nucleic localization of TAT conjugates into Jurkat cells could be confirmed with additional fluorescence imaging using fluorescein-5-maleimide. ^{99m}Tc-labelled TAT was also injected into mice in the same study that showed an initial whole-body distribution and a rapid clearance by both renal and hepatobiliary excretion. Another, very similar study confirmed the high liver and kidney uptake of ^{99m}Tc-labelled TAT peptide *in vivo* in mice and high intracellular levels of the complex in various organs was shown by concomitant fluorescence microscopy [42]. Various preclinical studies have investigated fluorescently labelled CPPs for fluorescent guided surgery in tumour bearing mice [43], tumour imaging in conjunction with MRI in mice [44], imaging of atherosclerotic plaques in mice targeting thrombin activity [45], imaging of matrix metalloproteinase-2 (MMP2) secreting tumours [46] and for *ex vivo* and *in vivo* rat retina labelling amongst other applications [47]. Most of these applications have used the TAT peptide. However, it was shown that the fluorochrome can significantly affect cellular uptake, intracellular distribution and cytotoxicity to cells [48],[49]. While anti-γH2AX antibodies are used routinely in *ex vivo* assays to quantify the number of γH2AX foci to detect DNA damage within permeabilised cell populations, the Cornelissen lab was the first to investigate the possibility to image DNA damage *in vivo* by attaching the TAT peptide to the anti-i-γH2AX antibody also conjugated to a chelator for radiometal labelling and imaging with ^{111}In-SPECT [50] and ^{89}Zr-PET [51]–[53]. The TAT peptide facilitates the cellular uptake of the antibody that is retained only if DNA damage occurs in the cell. In a direct comparison, the mean

absorbed dose to the nucleus of cells taking up [^{89}Zr]Zr-DFO-anti-γH2AX-TAT was twofold lower compared to [^{111}In]In-DTPA-anti-γH2AX-TAT [51].

Two groups independently investigated the labelling of the TAT [54] and polyarginine peptide [55] with gadolinium via the DOTA chelator for the subsequent labelling of lymphocytes and mouse fibroblasts, respectively. Despite its potential, both studies never pursued the use of the respective constructs for *in vivo* cell tracking. In another study, quantum dots have been conjugated to the TAT peptide and were used to label mesenchymal stem cells where the distribution of labelled cells was examined in nude mice with fluorescence microscopy [56]. Around the same time, only one study reported the use of TAT for cell labelling and tracking using SPECT: hematopoietic CD34$^+$ and neural progenitor cells were very efficiently tagged with a novel triple-labelled TAT peptide, i.e. magnetic, fluorescent and with the possibility to use ^{111}In-SPECT *in vivo* [35]. Whereas labelled CD34$^+$ cells were clearly detectable within murine bone marrow using MRI, this study actually did not investigate the ^{111}In-labelled TAT peptide for *in vivo* cell tracking but resorted to [^{111}In]In-Oxine instead as a comparison. The use of TAT for cell labelling and *in vivo* imaging was only revisited recently after more than a decade in conjunction with luminescent nanoparticles to track macrophages to inflamed tissue in mice [57]. To date, there is no PET based approach using CPPs for direct cell labelling.

5.6 Chapter objectives and rationale

Given the emerging role and potential of using PET for cell tracking there is a need for clinically translatable probes that fulfil important criteria and prerequisites especially in terms of the applicability directly on cells. As mentioned in detail in chapter 2, only few PET radiotracers have been used for in human cell tracking and yet, after several decades of direct cell labelling and imaging using SPECT in clinical practice, no analogous PET approach using long lived isotopes, such as zirconium-89, have been implemented due to the reasons outlined in **chapter 2 and 3**.

Therefore, this chapter explores the potential of ubiquitous CPPs to be labelled with the long-lived PET isotope zirconium-89 for the synthesis of new, alternative PET tracer for the direct labelling of cells. For this, the most commonly used TAT peptides was equipped with the DFO chelator, both via a cleavable disulfide linker and via a non-cleavable linker to examine and probe the suitability for cell labelling. In addition, two versions of the MPG peptide also coupled to DFO via a non-cleavable linker, one with a nuclear localisation sequence (NLS) in the 27 amino acid sequence and one without (**Δ**NLS), were also investigated. MPG, unlike TAT, belongs to the class of amphipathic CPPs and has shown to be taken up into cells independent of the endosomal pathway or any kind of receptor i.e. via direct translocation. MPG is a fusion peptide combining a hydrophobic domain derived for the fusion sequence of the HIV-1 gp41 protein with the NLS of the large T antigen of SV40 [58]. The rationale behind the choice and design of the different CPPs used was to: 1) use known ^{89}Zr-DFO-chemistry with high possible specific activities in combination with versatile CPPs for cell labelling, 2) use TAT as a hydrophilic CPP that has been used in clinical trials and has shown to be rapidly taken up into cells to investigate whether zirconium-89 can be deposited intracellularly similar to the Oxine-approach by applying different linker strategies between ^{89}Zr-DFO and TAT, 3) use a different class of peptides, i.e. already tested amphipathic CPPs to facilitate and ensure a direct interaction with the lipophilic cell membrane similar to the Oxine-approach but at the same time ensure water-solubility and 4) compare the CPP-approaches directly to the Oxine-approach in terms of cell labelling and post-labelling properties. Both the choice of peptide and linker strategy was based on a thorough literature search and screening.

Figure 5.2 and **Table 5.3** give an overview of the CPPs tested for ^{89}Zr-labelling, their structures and some of their properties. This chapter had the following objectives:

I. To probe the selected CPPs for ^{89}Zr-labelling and establish a reliable synthesis route including their quality control for the final product that can be used for cell labelling in direct comparison to [^{89}Zr]Zr-Oxine

II. To investigate some of the *in vitro* characteristics of the ^{89}Zr-labelled CPPs

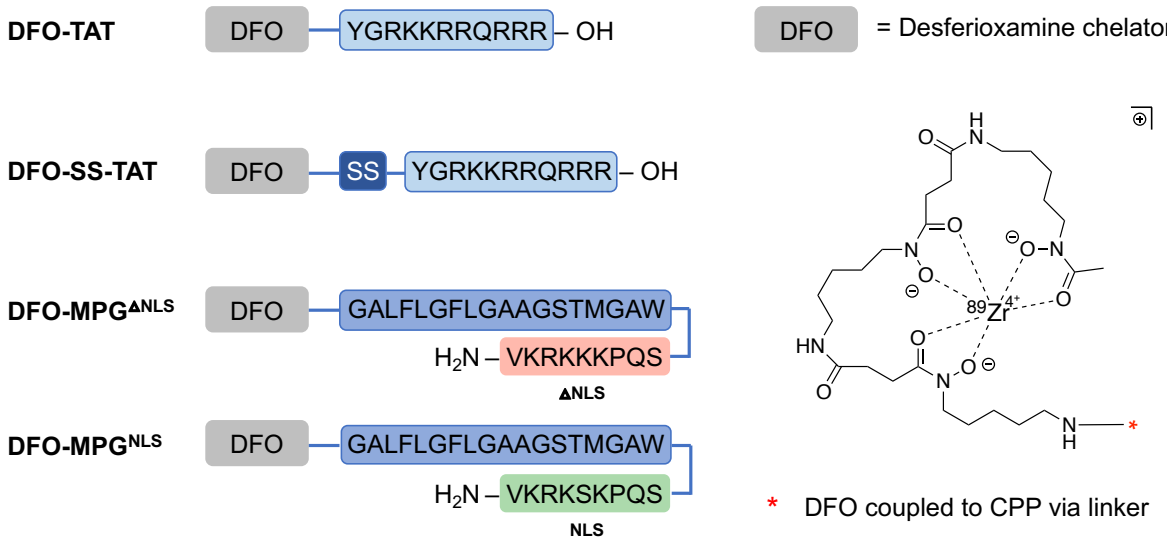

Figure 5.2 Schematic overview of CPPs tested for ^{89}Zr-labelling. Sequences are shown in amino acid single-letter codes with the C-terminus of the peptide carrying a carboxylic acid group (-OH) or an amide group (-NH_2). The chemical structure of the cargo (^{89}Zr-labelled chelator) is shown with the attachment point to the CPP via a linker indicated with a red asterisk. The details of the linker chemistry can be found in the materials and methods section of this chapter.
NLS = with nuclear localisation sequence; **Δ**NLS = without nuclear localisation sequence; -SS- = cleavable disulfide linker
Y = tyrosine, G = Glycine, R = Arginine, K = Lysine, Q = Glutamine, A = Alanine, L = Leucine, F = Phenylalanine, S = Serine, T = Threonine, M = Methionine, W = Tryptophan, V = Valine

Table 5.3 Characteristics of tested CPPs.

Peptide	Amino acid sequence	*CPP class	Charge	**MW
DFO-TAT	YGRKKRRQRRR	cationic	+8	2201.3
DFO-SS-TAT	YGRKKRRQRRR	cationic	+8	2308.3
DFO-MPG$^{\Delta NLS}$	GALFLGFLGAAGSTMGAWSQ PKSKRKV	amphipathic	+5	3405.9
DFO-MPG^{NLS}	GALFLGFLGAAGSTMGAWSQ PKKKRKV	amphipathic	+6	3446.9

* CPP = cell penetrating peptide

** MW = molecular weight [g/mol]

5.7 Materials and Methods

All chemicals, unless otherwise noted, were purchased from commercial sources (Sigma-Aldrich/Merck) and used without further purification. All water used was ultrapure (>18.2 MΩcm^{-1}). Zirconium-89 was supplied as Zr^{4+} in a 1 M oxalic acid (PerkinElmer) and was produced at the BV cyclotron Amsterdam via the $^{89}Y(p,n)^{89}Zr$ reaction on natural ^{89}Y-targets. Sep Pak C-18 cartridges (Waters Corp.) were each activated with 5 mL of EtOH and 10 mL of water.

Peptide Synthesis

All peptides were prepared customized and purchased from Cambridge Research Biochemicals (CRB, Cambridge, UK), by solid-phase peptide synthesis (SPPS) using Fmoc chemistry, Tentagel XV RAM resin for C-terminal amides and Fmoc Tentagel resin preloaded with the first amino acid for C-terminal acids. For all peptides without a disulfide linker, DFO was introduced on the resin. The N-terminus of the peptide was first reacted with succinic anhydride and the free acid group was then activated with HBTU/HOBt/DIPEA to form an amide bond with DFO. For DFO linked via a disulphide

bridge to the peptide, DFO was first converted to DFO-SPDP by reacting DFO with *N*-succinimidyl 3-(2-pyridyldithio)propionate (SPDP). DFO-SPDP was then reacted with the cysteine group of the peptide in solution before final HPLC purification. Final cleavage from the resin was performed using standard procedures. The peptides were purified using preparative RP-HPLC until >90% purity. Peptides were analysed by analytical RP-HPLC using a ACE 3 μm C-18 300 Å 150 × 2.1 mm column (VWR International Ltd., Poole, United Kingdom). The net peptide content was determined by elemental analysis. Primary structures of the peptides are shown in **Figure 5.2** and **Table 5.3.** Quality control, analysis and net peptide content of all peptides can be found in the **Appendix 5.6**

^{89}Zr-radiolabelling of DFO and DFO-peptide conjugates, radiochemical yields (RCY) and purification of radiolabelled peptides

0.7-3.7 MBq of ^{89}Zr-oxalate was transferred into a 1.5 mL low-protein binding Eppendorf tube, followed by addition of 1 M sodium carbonate to neutralize the reaction mixture. This solution was incubated for 3 min at RT. Subsequently, 100 µL of HEPES buffer (0.5 M, pH 7.0) was added to the reaction vial. DFO (5-20 µg), DFO-TAT (5-20 µg), DFO-SS-TAT (5-20 µg), DFO-MPG$^{\Delta NLS}$ and DFO-MPG^{NLS} (5-20 µg) was added to the reaction vial. The solution was then allowed to react at room temperature for 60-120 min. The reactions were monitored via ITLC and confirmed by HPLC as described in more detail below.

The crude ^{89}Zr-labelled peptide solution was diluted with ultrapure water and loaded onto an activated Sep-Pak C18 light cartridge. The cartridge was washed with 10 mL of water, and the ^{89}Zr-labelled peptide was eluted with 500 µL ethanol (10 mM HCl). The ethanol was completely evaporated under heat and the purified ^{89}Zr-labelled peptide was formulated in phosphate-buffered saline (PBS) for subsequent cell labelling.

All radiochemical yields (RCYs) were determined from an aliquot of the reaction solution before purification, expressed as the amount of activity in the product related to the starting activity as a percentage [%] utilised in the synthesis based on ITLC. The recovery of labelled peptide after C18 cartridge purification was determined from the amount of

^{89}Zr-labelled peptide eluted from the C18 cartridge divided by the amount of ^{89}Zr-labelled peptide added to the C18 cartridge after the washing step with water. The final specific activity of the labelled peptides was calculated by dividing the amount of activity isolated with the purified ^{89}Zr-DFO-peptide conjugates by the initial mass of DFO-peptide conjugate added to the initial radiolabelling reaction. In addition, the integrity of ^{89}Zr-labelled peptides was confirmed by RP-HPLC.

Synthesis of [^{89}Zr]Zr-Oxine

[^{89}Zr]Zr-Oxine was synthesised according to a newly established procedure published literature [59] as previously described in chapter 3. The final product contains 50 µg 8-hydroxyquinoline (oxine) whereby a fraction of this solution is taken for cell labelling (see details in chapter 6, materials and methods).

Radio-Thin Layer Chromatography (TLC)

Instant thin layer chromatography (ITLC) analysis for[^{89}Zr]Zr-Oxine was performed as described in chapter 4. In addition ITLC-SG paper (Macherey-Nagel) cut into 1 x 9 cm strips was also used for ITLC analysis of ^{89}Zr-labelled peptide conjugates which were developed in 0.1 M sodium citrate solution (pH 5). [^{89}Zr]Zr-DFO was developed in both 0.05 M EDTA solution (pH 7) and 0.1 M sodium citrate solution (pH 5). ^{89}Zr-labelled DFO and DFO-peptide conjugates remain at the origin (R_f < 0.1) while free, unchelated Zirconium-89 migrate with the solvent front (R_f > 0.9). [^{89}Zr]Zr-Oxine migrates with the respective mobile phase (R_f > 0.9) whereas unchelated Zirconium-89 migrated remains at the origin of the TLC plate (R_f < 0.1).

Analytical radio-High Performance Liquid Chromatography (HPLC)

Reversed Phase HPLC analysis of unchelated Zirconium-89 and ^{89}Zr-labelled peptides was performed on an Agilent 1200 Technologies HPLC equipped with a G1212B Binary Pump SL, an autosampler, column compartment (50°C oven temperature) and multi-wavelength diode-array detector followed by an in-line LabLogic detector (PosiRAM™, LabLogic; Sheffield, UK) using a C18 analytical column (Gemini®, 250 mm × 4.6 mm × 5 µm, 110 Å , Phenomenex). LabLogic Laura™ radiochromatography software was used for HPLC data collection and analysis. Solvents (HPLC grade) were degassed and a mobile phase of acetonitrile containing 0.1% TFA (A) and water containing 0.1% TFA (B) at a flow rate of 1.0 ml/min was used with the following gradients:

Gradient 1: 0.0-0.4 min 2% A, 0.4-11.2 min 2-70% A, 11.2-11.7 min 70-100% A, 11.70-12.00 min 100-2% A, 12.00-15.00 min 2 % A.

Gradient 2: 0.0-5.0 min 5% A, 5.0-15.0 min 5-70% A, 15.0-18.0 min 70-100% A, 18.0-20.0 min 100%-5% A

LogD determination

The partition coefficient (logD) of the purified [^{89}Zr]Zr-labelled peptides, [^{89}Zr]Zr-DFO and [^{89}Zr]Zr-Oxine and also neutralized, unchelated zirconium-89 in 1 M oxalic acid as delivered from the cyclotron was determined by measuring the distribution of the radioactivity in equal volumes of 1-octanol and PBS. Briefly, 10-20 µL aliquots (not more than 100 kBq) of the radiolabelled compound was loaded into an Eppendorf tube containing 500 µL of PBS and 500 µL of 1-octanol (Merck). After vigorous mixing for 3 minutes at room temperature, samples were centrifuged at 1000 g for 5 minutes to ensure complete separation of the solvents. 100-µL aliquots of each layer were taken and pipetted into separate 1.5 mL Eppendorf tubes. The samples were then counted in a Triathler well-counter (HIDEX, Turku, Finland) and the logD calculated as counts in

octanol/counts in PBS solution. Three independent experiments were performed in triplicates (n = 3).

Stability of ^{89}Zr-labelled DFO and DFO-peptide conjugates

RP HPLC was also used to study the chemical and radiochemical stability of ^{89}Zr-labelled DFO-peptide conjugates in ethanol directly after C18 purification of the peptides. The integrity of the ^{89}Zr-chelate and stability of the compound was analysed directly after synthesis and then every day by RP-HPLC.

Statistical analysis

Statistical analysis was performed using GraphPad Prism 8.0; (GraphPad Software Inc, La Jolla, USA). Results are presented as mean ± standard deviation (SD) or median [range] as appropriate. Means between two groups were compared using Student's two-tailed t test, whereas one-way ANOVA was used for comparison when more than two groups were compared. p-values <0.05 were considered statistically significant.

5.8 Results

All radiosynthesis were performed using [^{89}Zr]Zr(oxalate)$_4$ as a starting compound delivered from the cyclotron, both for the synthesis of ^{89}Zr-labelled CPPs and [^{89}Zr]Zr-Oxine. The CPPs tested for labelling were prepared by solid phase peptide synthesis at >90% purity and a total of 4 peptides were used for radiolabelling. ^{89}Zr-labelled CPPs were synthesised in a two-step procedure via a C18 cartridge purification step at a mean radiochemical yield >95 % (n = 6; **Table 5.4**) as indicated by thin layer chromatography and additionally confirmed by high performance liquid chromatography. The [^{89}Zr]Zr(oxinate)$_4$ complex was synthesised in an aqueous solution in a rapid kit formulation whereby [^{89}Zr]Zr(oxalate) was added to a premixed kit solution (**Fig. 5.3**) at a mean radiochemical yield of 92.3 % ± 1.2 (SD, n = 6) (**Table. 5.4**) as indicated by thin layer chromatography. [^{89}Zr]Zr(oxinate)$_4$ was used without further purification for subsequent experiments. Unchelated, free and neutralised zirconium-89 stays at the origin and does not move with ethylacetate as the mobile phase (**Fig. 5.4**).

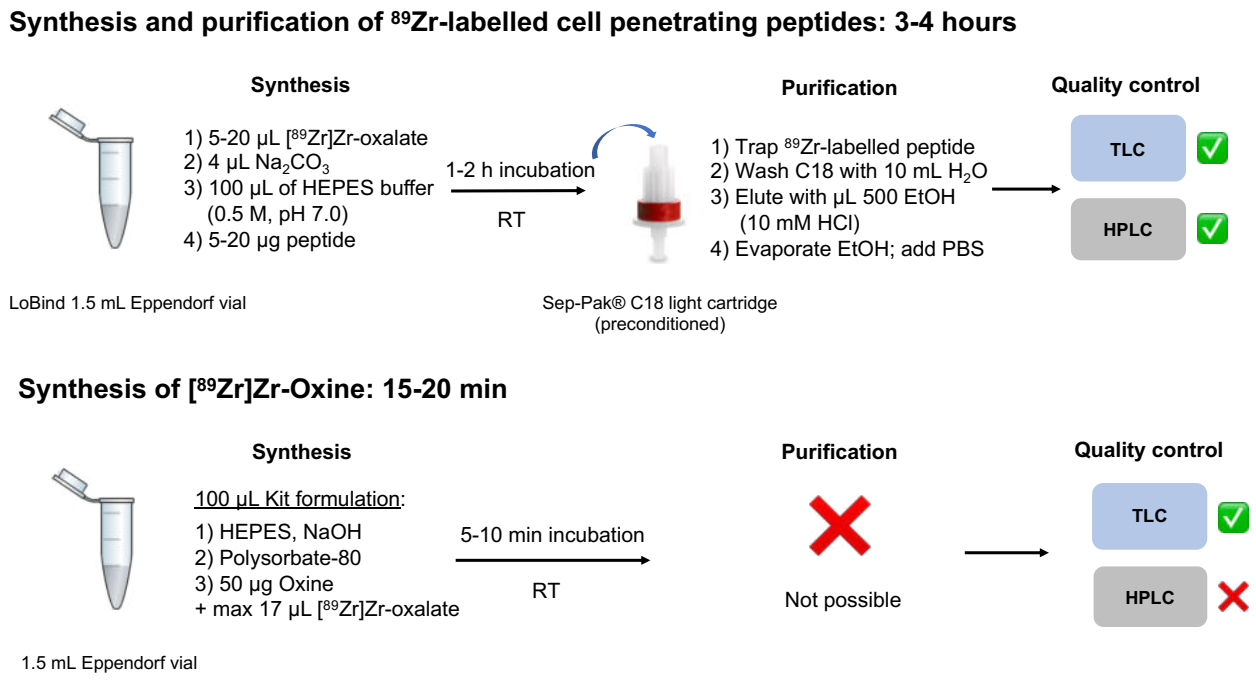

Figure 5.3 Overview of the radiosynthesis steps of ^{89}Zr-labelled CPPs and [^{89}Zr]Zr-Oxine. TLC = thin layer chromatography; HPLC = high performance liquid chromatography

Table 5.4 Radiochemical yields and range of specific activities of all tested and synthesised compounds. N = 6 and SD for all compounds tested in a direct comparison.

Compound	*Radiochemical yield (RCY) [%]	**Specific activity [MBq/µg]
[^{89}Zr]Zr-DFO-TAT	96.4 ± 3.0	[0.11-0.37]
[^{89}Zr]Zr-DFO-SS-TAT	98.3 ± 0.4	[0.18-0.27]
[^{89}Zr]Zr-DFO-MPG$^{\Delta NLS}$	98.1 ± 1.1	[0.07-0.26]
[^{89}Zr]Zr-DFO-MPG^{NLS}	95.0 ± 3.2	[0.11-0.19]
[^{89}Zr]Zr-Oxine	92.3 ± 1.2	[0.03-0.05]

* Mean radiochemical yield as determined by iTLC for all peptide synthesis carried out

** Range of specific activities for all peptide synthesis carried out

SD = standard deviation

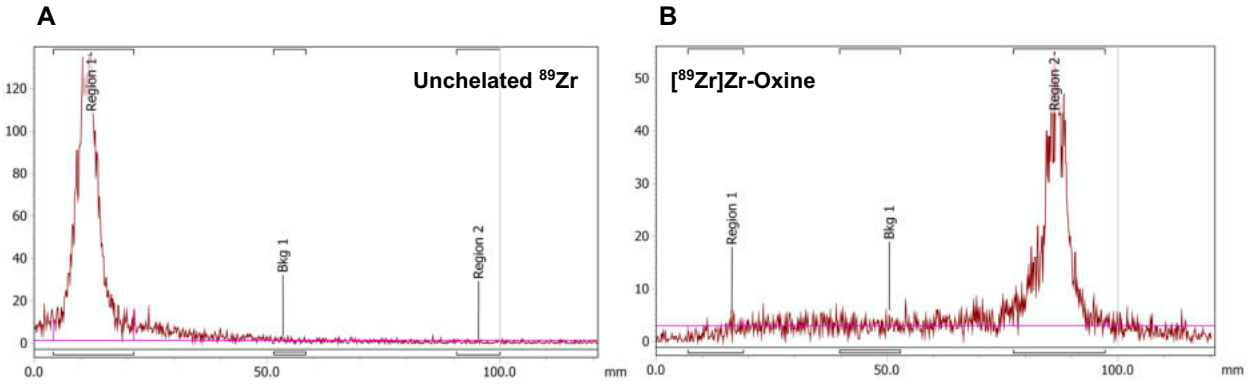

Figure 5.4 ITLC chromatograms of (**A**) unchelated, neutralised $^{89}Zr^{4+}$ as delivered from the cyclotron in 1 M oxalic acid and of (**B**) [^{89}Zr]Zr-Oxine. ITLCs were run in ethylacetate.

All ^{89}Zr-labelled CPPs showed an excellent recovery of >90% after C18 purification (**Table 5.5**). ^{89}Zr-labelled MPG peptides showed a more noticeable loss of tracer in the synthesis vial and also in pipette tips compared to ^{89}Zr-labelled TAT peptides which is also reflected in the more than 10% lower total activity recovery at the end of synthesis.

Table 5.5 Recovery after purification and loss of tracer during synthesis. N = 6 and SD for all compounds tested in a direct comparison.

Compound	Recovery after C18 purification [%]	Loss of tracer in synthesis vial [%] *	Loss of tracer in pipette tips [%] **	Total activity recovery [%] ***
[^{89}Zr]Zr-DFO-TAT	93.7 ± 3.4	1.3 ± 1.0	0.7 ± 1.0	83.3 ± 5.2
[^{89}Zr]Zr-DFO-SS-TAT	94.0 ± 1.8	0.6 ± 0.2	0.2 ± 0.1	86.6 ± 5.9
[^{89}Zr]Zr-DFO-MPG$^{\Delta NLS}$	94.4 ± 2.9	10.1 ± 5.8	3.9 ± 2.4	67.7 ± 13.9
[^{89}Zr]Zr-DFO-MPG^{NLS}	92.8 ± 2.8	6.9 ± 2.5	4.2 ± 2.6	70.5 ± 6.0
[^{89}Zr]Zr-Oxine	n/a	n/a	2.6 ± 0.6	n/a

* Remaining activity in vial when transferring the whole reaction mixture

** Activity sticking to pipette tips when pipetting or mixing the whole reaction solution

*** Activity in the final purified product compared to the starting activity used for synthesis

ITLC could be used for all ^{89}Zr-labelled CPPs to determine their radiochemical yield after synthesis and their integrity post-purification in terms of ^{89}Zr-chelation, however this was not sufficient to determine the overall radiochemical purity. ITLC chromatograms of both the ^{89}Zr-labelled DFO chelator only (**Fig. 5.5**) and the ^{89}Zr-labelled CPPs (**Fig. 5.6**) revealed that [^{89}Zr]Zr-DFO cannot be differentiated from [^{89}Zr]Zr-DFO-CPPs. In all cases, the unchelated zirconium-89 moves with the solvent front, whereas [^{89}Zr]Zr-DFO and the [^{89}Zr]Zr-DFO-CPPs remain at the origin. Although different solvents resulted in a slightly different peak shape of [^{89}Zr]Zr-DFO (**Fig. 5.5**) it was not possible to develop an ITLC solvent system in which [^{89}Zr]Zr-DFO can be differentiated from [^{89}Zr]Zr-DFO-CPPs in terms of the R_f-value on the TLC plate. Therefore, additional analytical HPLC methods were developed to be able to detect different retention times for [^{89}Zr]Zr-DFO and [^{89}Zr]Zr-DFO-CPPs but also to analyse all ^{89}Zr-labelled CPPs (**Fig. 5.7** and **Fig. 5.8**).

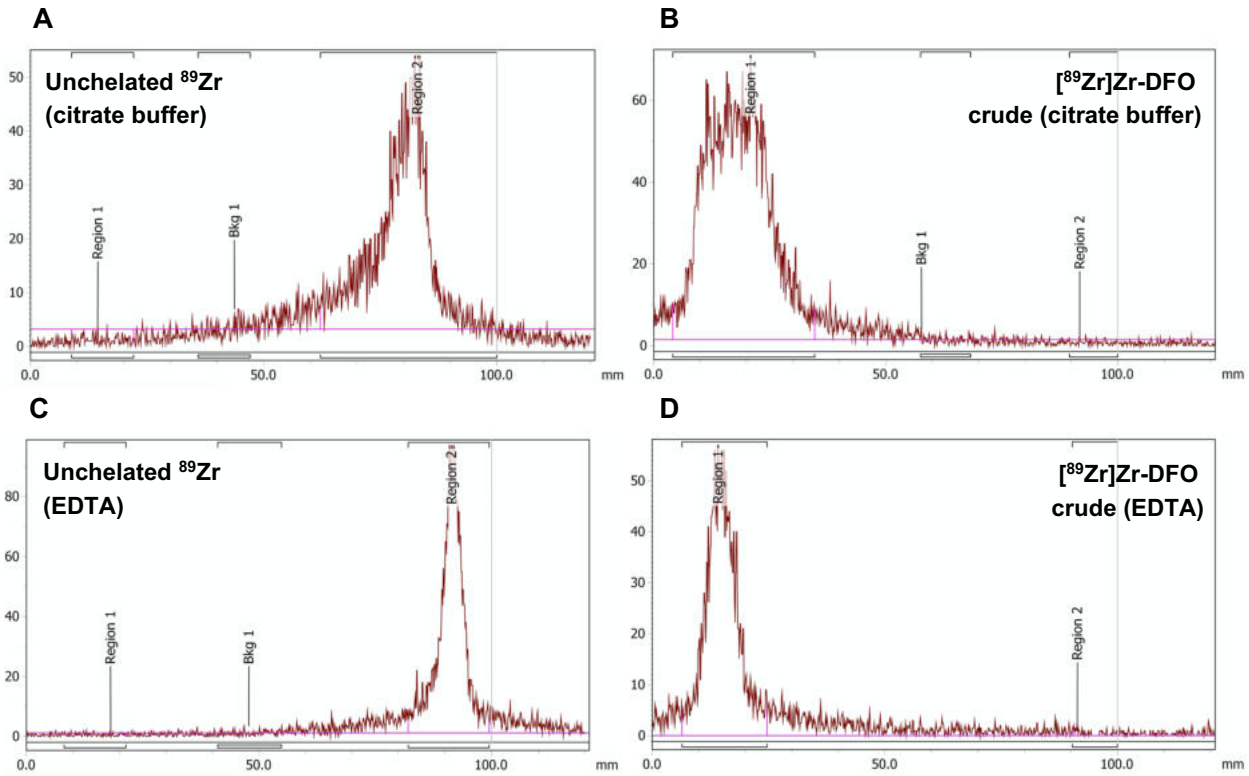

Figure 5.5 ITLC radiochromatograms of (**A**) unchelated, neutralised $^{89}Zr^{4+}$ as delivered from the cyclotron in 1 M oxalic acid developed in 0.1 M citrate buffer (pH 5), (**B**) [^{89}Zr]Zr-DFO developed in 0.1 M citrate buffer (pH 5), (**C**) unchelated, neutralised $^{89}Zr^{4+}$ as delivered from the cyclotron in 1 M oxalic acid developed in 50 mM EDTA solution (pH 7) and (**D**) [^{89}Zr]Zr-DFO developed in 50 mM EDTA solution (pH 7).

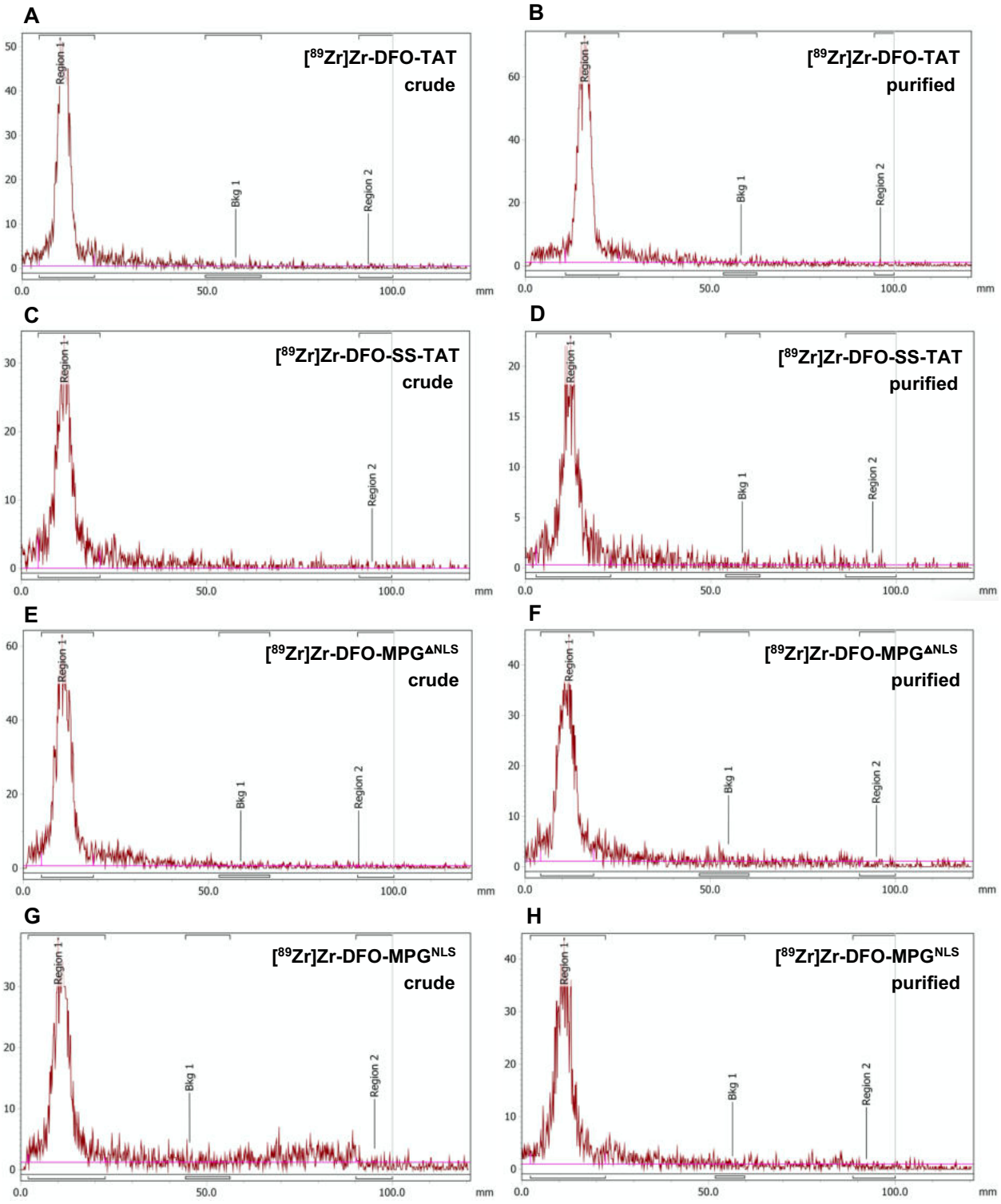

Figure 5.6 ITLC radiochromatograms of all ^{89}Zr-labelled CPPs investigated. (**A**, **C**, **E**, **G**) analysis of crude reaction mixture and (**B**, **D**, **F**, **H**) analysis of all ^{89}Zr-labelled CPPs after C18 purification. All compounds were developed in 0.1 M citrate buffer (pH 5).

At the time of the first [^{89}Zr]Zr-DFO-TAT peptide synthesis, the radio-HPLC was not yet set up to undertake quality control hence only ITLC was used. HPLC was set up during the labelling and use of the other CPPs and HPLC for [^{89}Zr]Zr-DFO-TAT, as shown in **Fig. 5.7 A** and **Fig. 5.8 C,** was done retrospectively past the expiration date and actual use of the peptide for further applications**. Fig. 5.7** shows clear and pure peaks for all ^{89}Zr-labelled peptides and [^{89}Zr]Zr-DFO. In addition, unchelated zirconium-89 shows smearing along the column throughout the HPLC run as comparison. Using gradient 1, both [^{89}Zr]Zr-DFO-TAT and [^{89}Zr]Zr-DFO-SS-TAT showed the same retention time similar to the two ^{89}Zr-labelled MPG peptides that could clearly be distinguished from the ^{89}Zr-labelled TAT peptides with a ~3 min longer retention time. However, the retention time of [^{89}Zr]Zr-DFO and the two ^{89}Zr-labelled TAT peptides, [^{89}Zr]Zr-DFO-TAT and [^{89}Zr]Zr-DFO-SS-TAT, did only marginally differ and could not properly be separated with gradient 1 meaning that the chromatogram, as shown in **Fig. 5.7 A** and **B,** do not provide information about whether the ^{89}Zr-labelled DFO chelator is still attached to the TAT peptide or if the peptide did undergo degradation whereby the DFO chelator may have split from the peptide which can happen to succinic acid linker after long-term storage as is the case of most CPPs investigated in this work with the exception of [^{89}Zr]Zr-DFO-SS-TAT. It was therefore necessary to probe different gradients in order to be able to clearly distinguish between [^{89}Zr]Zr-DFO and ^{89}Zr-labelled TAT peptides. **Fig. 5.8** shows that the application of gradient 2 was able to clearly distinguish the [^{89}Zr]Zr-DFO (**Fig. 5.8 A**) from [^{89}Zr]Zr-DFO-TAT and [^{89}Zr]Zr-DFO-SS-TAT (**Fig. 5.8 C, D**) with a difference in retention time of ~8 min. However, it became most obvious that the [^{89}Zr]Zr-DFO-TAT seems to have degraded after long-term storage of approximately one year after its first use. [^{89}Zr]Zr-DFO-TAT is expected to have a similar retention time to [^{89}Zr]Zr-DFO-SS-TAT, given that they differ only in terms of the disulfide linker, and the chromatogram of [^{89}Zr]Zr-DFO-TAT shows two peaks that can be ascribed to both [^{89}Zr]Zr-DFO-TAT and [^{89}Zr]Zr-DFO with a retention time of 11.4 min and 3.2 min, respectively. At the time when [^{89}Zr]Zr-DFO-TAT was first used, HPLC analysis was not available until experiments with [^{89}Zr]Zr-DFO-TAT had already been completed and other ^{89}Zr-labelled CPPs were investigated. All HPLC analysis for [^{89}Zr]Zr-DFO-SS-TAT were continued using gradient 2 thereafter. As it could be already observed with gradient 2, unchelated zirconium-89 also smears

along the column (**Fig. 5.8 B**) with only a minor detectable peak at around 5 min (**Fig. 5.8 B**). **Fig. 5.9 A** shows the chromatogram of [^{89}Zr]Zr-DFO-SS-TAT directly after purification and before further use whereas **Fig. 5.9 B** shows the HPLC analysis of the purified [^{89}Zr]Zr-DFO-SS-TAT that was stored in ethanol after C18 cartridge purification for 48 hours. Storage did not significantly affect the integrity of [^{89}Zr]Zr-DFO-SS-TAT as shown in the radiochemical purity after 48 hours.

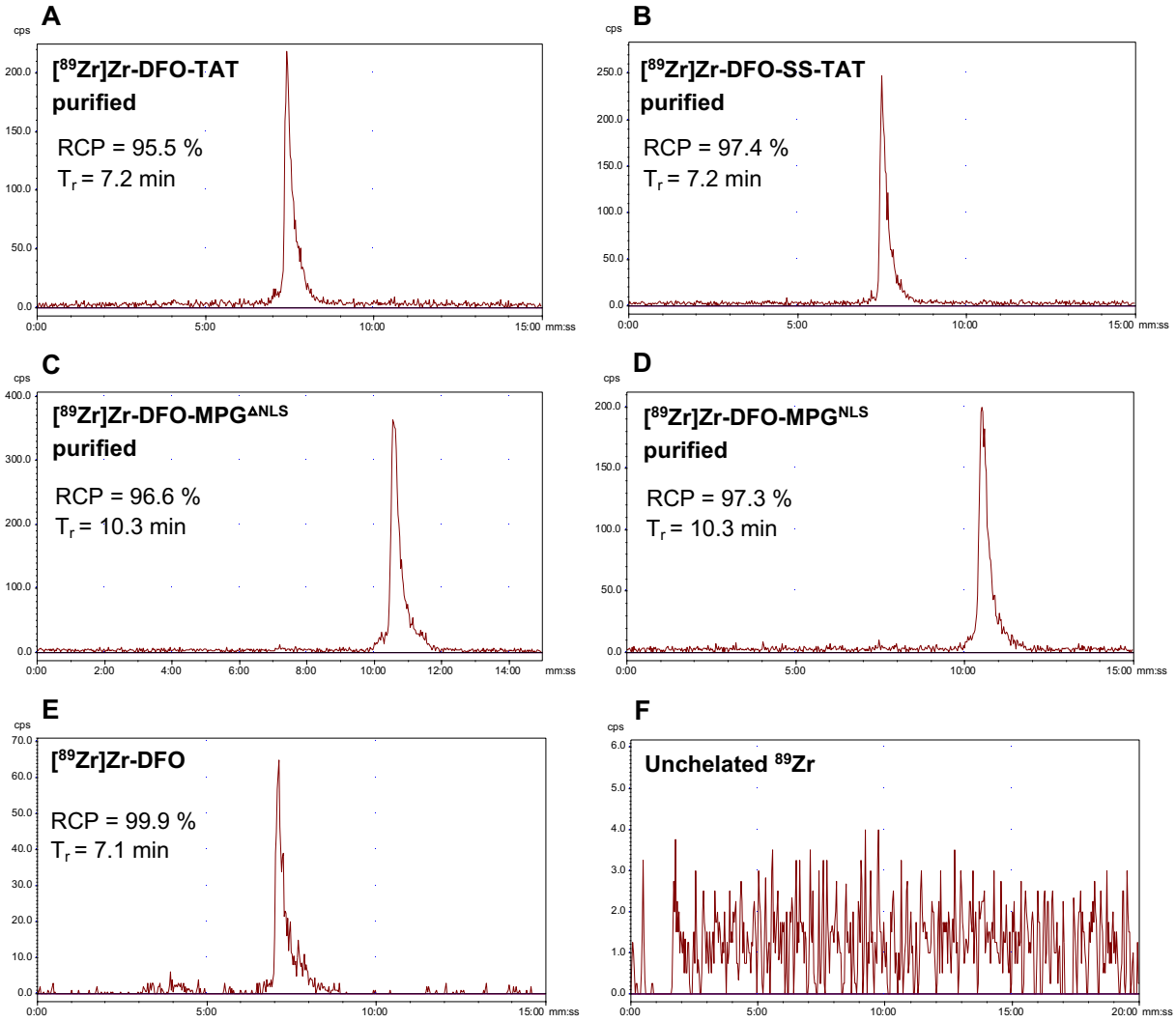

Figure 5.7 HPLC radiochromatograms of all ^{89}Zr-labelled investigated using gradient 1. [^{89}Zr]Zr-DFO-TAT and [^{89}Zr]Zr-DFO-SS-TAT show a very similar retention time compared to [^{89}Zr]Zr-DFO, whereas the ^{89}Zr-labelled MPG peptides can clearly be distinguished from [^{89}Zr]Zr-DFO. RCP: Radiochemical purity, T_r = Retention time

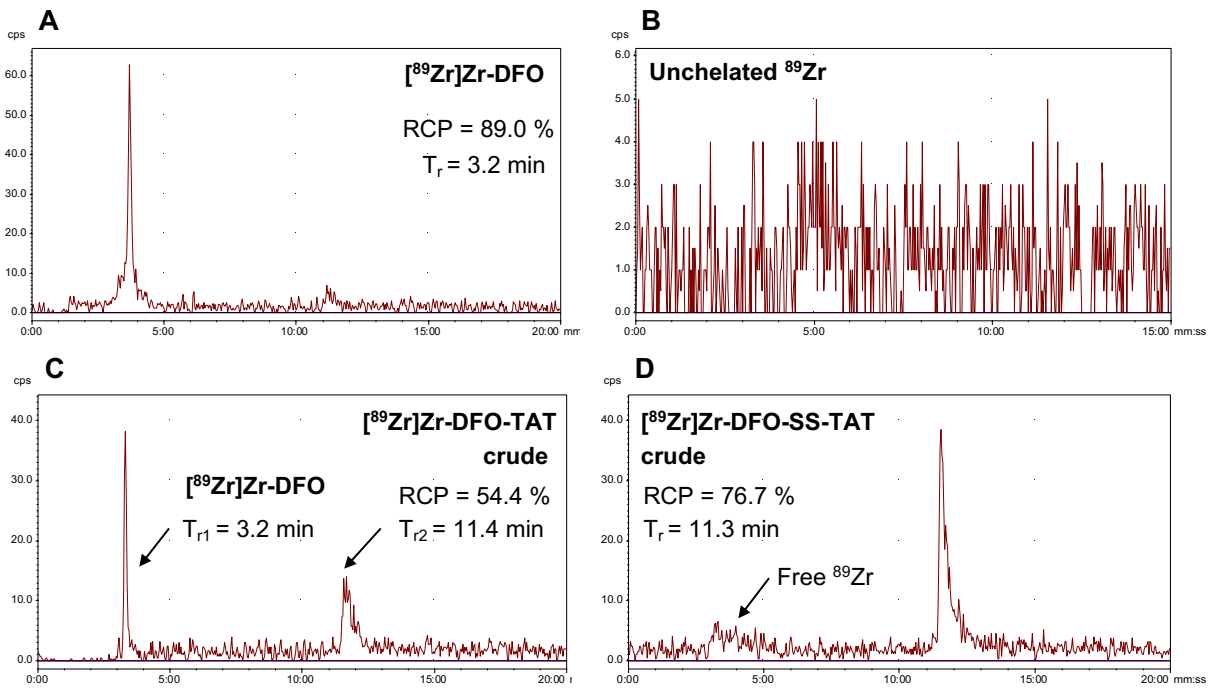

Figure 5.8 HPLC chromatograms of ^{89}Zr-labelled TAT peptides and [^{89}Zr]Zr-DFO using gradient 2. [^{89}Zr]Zr-DFO can clearly be distinguished from the ^{89}Zr-labelled TAT peptides however [^{89}Zr]Zr-DFO-TAT showed already degradation after long-term storage.
RCP: Radiochemical purity, T_r = Retention time

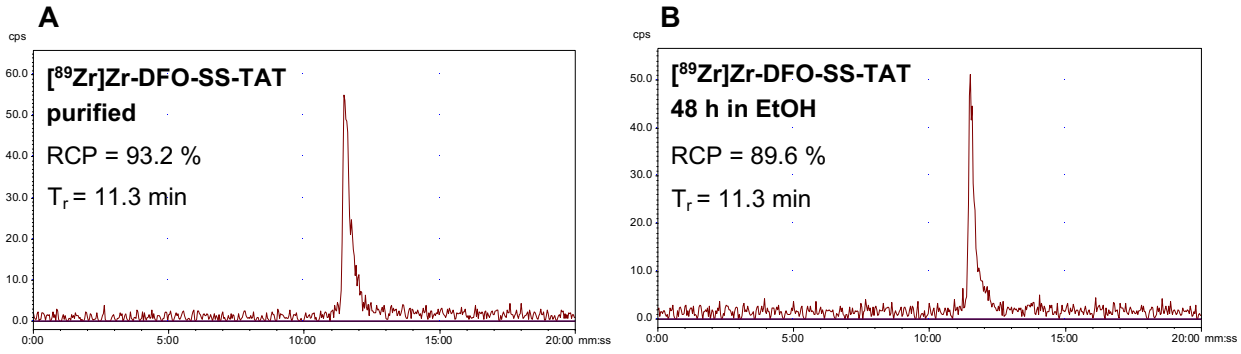

Figure 5.9 HPLC radiochromatograms of ^{89}Zr-labelled TAT peptides using gradient 2. (**A**) ^{89}Zr-labelled DFO-SS-TAT directly after purification and (**B**) stored in ethanol for 48 h after elution from the C18 cartridge. RCP: Radiochemical purity, T_r = Retention time

Fig. 5.10 shows the HPLC analysis of both the ^{89}Zr-labelled DFO-MPG$^{\Delta NLS}$ and DFO-MPG^{NLS} peptide using gradient 1 before (**Fig. 5.10 A, B**) and after C18 cartridge purification (**Fig. 5.10 C, D**). [^{89}Zr]Zr-DFO-MPG$^{\Delta NLS}$ and [^{89}Zr]Zr-DFO-MPG^{NLS} could be stored in ethanol for 48 hours to be used at a later time point without affecting the integrity ^{89}Zr-labelled MPG peptides (**Fig. 5.10 E, F**). This is especially useful when the tracer is needed a few days later after synthesis but can be preserved in a sterile solution.

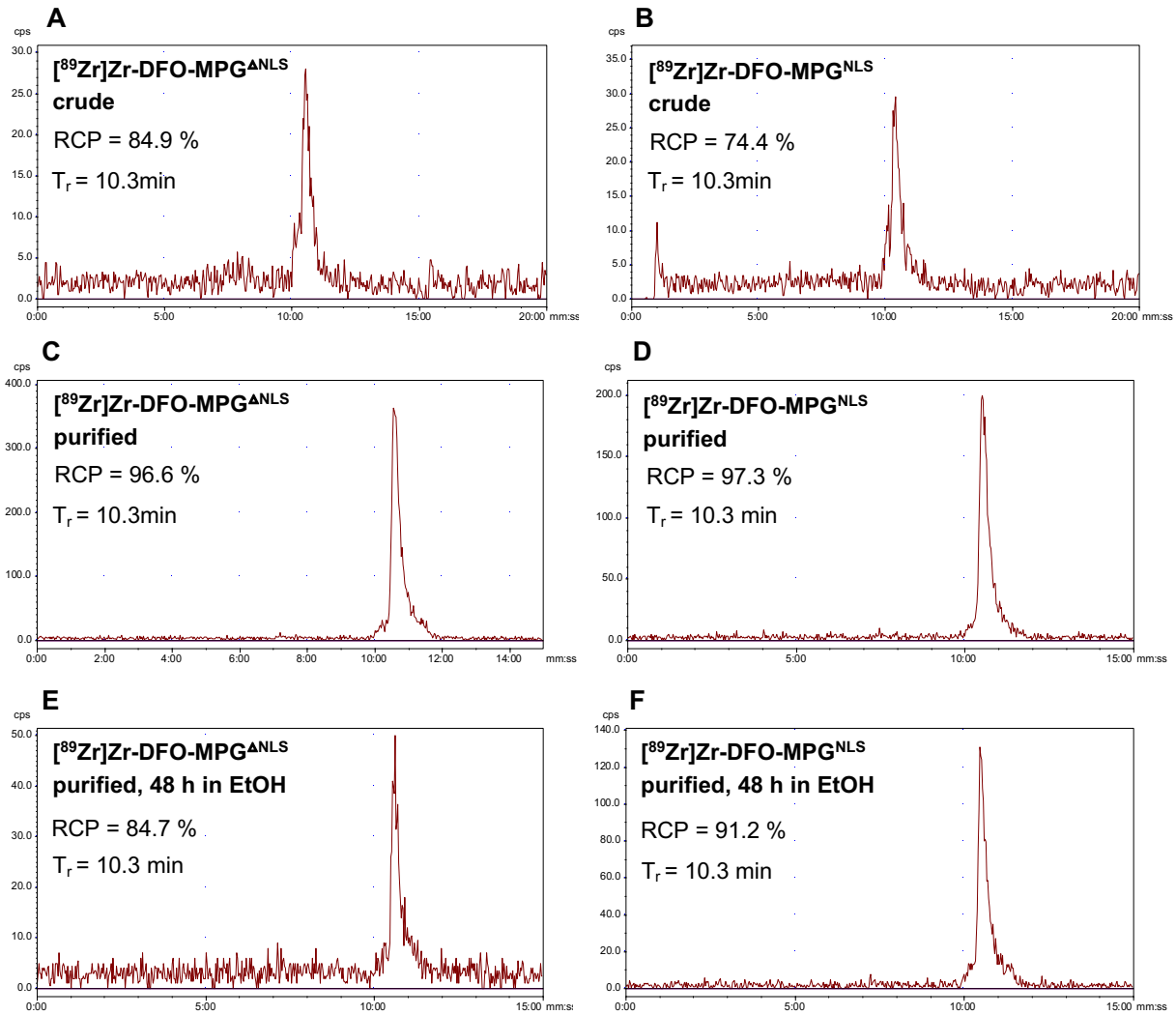

Figure 5.10 HPLC radiochromatograms of ^{89}Zr-labelled MPG peptides using gradient 1. (**A**, **B**) crude reaction solutions before C18 cartridge purification, (**C**, **D**) purified ^{89}Zr-labelled MPG peptides and (**E**, **F**) ^{89}Zr-labelled MPG peptides stored in ethanol for 48 h after C18 cartridge purification. RCP: Radiochemical purity, T_r = Retention time

LogD values were obtained by analysing the distribution of radioactivity between a two-phase system of n-octanol and PBS. The results and values are summarised in **Table 5.6**. A high to moderate hydrophilicity could be observes for neutralised, unchelated zirconium-89 in 1 M oxalic acid as delivered from the cyclotron. [^{89}Zr]Zr-DFO and all the peptides investigated had a negative logD value indicating good water solubility and hydrophilic behaviour. There was a significant difference in the logD value of ^{89}Zr-labelled TAT-peptides and MPG-peptides ($p<0.01$) which is in accordance with their different physicochemical properties with TAT being a cationic, highly charged (+8) peptide and MPG being a amphipathic peptide with a partial hydrophobic backbone explaining the less hydrophilic properties compared to TAT reflected in the logD value. The ^{89}Zr-labelled chelator DFO, [^{89}Zr]Zr-DFO, alone showed one of the most hydrophilic properties based on its logD value that is lower than all other peptides and also compared to ^{89}Zr-labelled TAT peptides that and, despite carrying a charge of +8 compared to +1 for [^{89}Zr]Zr-DFO, showed slightly lower hydrophilicity. [^{89}Zr]Zr-Oxine in comparison was the only compound with a positive logD value significantly different from all other compounds ($p<0.0001$), clearly indicating a decreased water solubility and a hydrophobic character of the tracer which is in agreement with what has been reported in literature about oxine-metal chelates.

Table 5.6 LogD values for all investigated CPPs including ^{89}Zr-compounds in comparison.

Compound	Charge of complex	*$logD_{Octanol/PBS}$ value
'free' ^{89}Zr (Oxalate)	-4	-2.90 ± 0.04
[^{89}Zr]Zr-DFO	+1	-2.64 ± 0.02
[^{89}Zr]Zr-DFO-TAT	+9	-2.22 ± 0.49
[^{89}Zr]Zr-DFO-SS-TAT	+9	-2.25 ± 0.49
[^{89}Zr]Zr-DFO-MPG$^{\Delta NLS}$	+6	-1.27 ± 0.06
[^{89}Zr]Zr-DFO-MPG^{NLS}	+7	-1.47 ± 0.23
[^{89}Zr]Zr-Oxine	0	0.16 ± 0.02

*2 independent experiments using triplicates each

5.9 Discussion

Despite the fact that the discovery of cell penetrating peptides dates to a similar time to when PET was first conceived as a medical imaging modality, the use of cell penetrating peptides as imaging agents combined with PET has not been widely explored to date [60]. One of the main reasons for this can be associated with the lack of specificity of standalone cell penetrating peptides for the target cells, and the reported instability of some CPPs *in vivo* [10]. Therefore, only a few studies have investigated CPPs as *in vivo* imaging agents in conjunction with radionuclides. Cell penetrating peptides that are anchored to a target specific moiety, e.g. antibodies, allow intracellular targets to be made accessible via the link to CPPs, such as [^{89}Zr]Zr-DFO-anti-γH2AX-TAT has demonstrated for the imaging of DNA damage whereby the TAT peptide was attached to the anti- γH2AX antibody [51],[53]. Yet, the non-specificity of cell penetrating peptides can also be used as an asset for cell labelling where the ideal tracer is taken up rapidly by a vast number of different cell types with a high labelling efficiency independent of the incubation temperature yielding a homogeneously labelled cell population.

This work describes the radiolabelling of 4 different CPPs which includes their route of synthesis and *in vitro* characterisation in comparison to the state-of-the-art [^{89}Zr]Zr-Oxine which has been used in the cell labelling arena for the past 5 years. As described in chapter 3 in more detail, several synthesis strategies have been investigated for [^{89}Zr]Zr-Oxine, some of which are very cumbersome and require many steps to yield a complex that is highly water insoluble and sticks to vials and pipette tips resulting in significant tracer loss and impairing its use for cell labelling. It was not until recently that Man et al. developed a so called ‘kit formulation’ for the synthesis of [^{89}Zr]Zr-Oxine [59] that overcomes some of the previously encountered problems with other synthesis strategies. This kit formulation employs a premixed solution that contains the ligand oxine and the surfactant polysorbate-80 which can be mixed in a simple procedure with the zirconium-89 solution as produced from the cyclotron (in 1 M oxalic acid) or alternatively with [^{89}Zr]$ZrCl_4$ that can be obtained via QMA cartridge ion exchange from [^{89}Zr]Zr-$(oxalate)_4$. Polysorbate-80 ensures that the formed [^{89}Zr]Zr-Oxine complex is homogenously distributed in aqueous solution including reduced surface adhesion and

stickiness of [^{89}Zr]Zr-Oxine and therefore tracer loss. Oxine acts as ionophore during cell labelling applications that can carry radiometals across the cell membrane via a fast and passive diffusion through the cell membrane and oxine-complexes have been described as metastable that dissociate inside cells [61]. Therefore, oxine-metal complexes can be seen as a very simple cell labelling and metal-delivery platform with the completion of radiosynthesis within less than 15 min. However, these lipophilic complexes cannot be purified via any cartridge system as it is very commonly practiced for many clinical grade radiotracers that are produced using automated synthesis modules. In addition, [^{89}Zr]Zr-Oxine and also other oxine-metal complexes have a very limited specific activity [59] where a significant amount of excess ligand (oxine) is needed. In addition, metal complexes with oxine and derivates have shown to be cytotoxic [62],[63]. **Table 5.6** summarises some of the advantages and disadvantages of [^{89}Zr]Zr-Oxine and ^{89}Zr-labelled DFO-CPPs in a direct comparison considering several factors.

Table 5.6 Head to head comparison between [^{89}Zr]Zr-Oxine and ^{89}Zr-labelled CPPs.

	[^{89}Zr]Zr-Oxine	**[^{89}Zr]Zr-DFO-CPP**
***Cost**	£	££-£££
Synthesis time	15 min	~ 3 h
Purification of tracer	n/a	SepPak C18 light cartridge
Quality control	ITLC	ITLC, HPLC
****Cytotoxicity*****	++ [64],[65]	+ [66],[67]
****Water solubility**	+	+++
****Specific activity**	+ (< 5 MBq/µg)	+++ (up to 1000 MBq/µg)*****

*Cost: £ = low, ££ = medium, £££ = high

**Properties: + = low, ++ = medium, +++ = high (based on literature descriptions)

***qualitative values for cytotoxicity based on literature

****value is based on ^{89}Zr-DFO chelation described in literature

Peptides in comparison, such as the CPPs used in this work, have a high translational potential given the many clinically applicable peptides for imaging and even therapy [68]. Peptides can be synthesised and purified under good manufacturing practice (GMP) compliant conditions using both TLC and HPLC as a means of quality control, and can be used as an accurate measurement of the quality of the labelled product. HPLC can elucidate information about peptide integrity that TLC cannot provide, as demonstrated during this work using [^{89}Zr]Zr-DFO-TAT. However, compared to [^{89}Zr]Zr-Oxine, the ^{89}Zr-labeling and full tracer synthesis takes much longer which is mostly attributed to the purification step and the extra HPLC quality control step which can be compensated for with the long half-life of zirconium-89 but shorter lived isotopes would suffer specific activity due to radioactive decay. Although the ^{89}Zr-labelled CPPs showed good water solubility, especially the MPG peptides, they exhibited a certain degree of stickiness to vials and pipette tips given their partly hydrophobic character. However, this was similar to the adherence of [^{89}Zr]Zr-Oxine. Ideally, the radio synthesis should not result in a significant loss of tracer in vials. Depending on the type of amino acids used the cost of the synthesis and production of the peptide can be much higher compared to oxine, tropolone or other much more affordable ligands. Despite their potential for clinical translation, the cost-benefit plays a significant role in the decision-making process for optimised clinical practice. However, this may be offset by the very expensive nature of cell based therapies, and if an imaging tool can be used to reduce the use of such agents in patients where they are not efficacious, there may be a significant cost benefit in favour of their use.

Another decisive advantage of DFO-conjugated CPPs is that, DFO is a FDA approved chelator that is frequently used for the labelling of antibodies for immuno-PET and DFO is known to be able to reach remarkable specific activities with zirconium-89 [69] that exceed [^{89}Zr]Zr-Oxine by at least two magnitudes. The use of DFO as a chelator may therefore allow for the modulation of the required activity and cold peptide mass for any subsequent application. For instance, the synthesis of [^{89}Zr]Zr-Oxine requires 0.34 µmol of oxine with an upper limit of [^{89}Zr]Zr(oxalate)$_4$ that can be used for synthesis whereas 2.90-4.54 nmol of CPP was used in this work reaching radiochemical yields of >90% although the upper and lower limits of chelation and labelling were not tested but

values based on literature for the chelation of zirconium-89 with DFO indicate that much higher specific activities can be reached compared to [^{89}Zr]Zr-Oxine as indicated in Table 5.6. Therefore, it can be anticipated that a very low cold mass is sufficient to label with a high amount of zirconium-89 which needs to be further evaluated for cell labelling purposes.

Although the logD value can be generally regarded as an indicator of the interaction of the compound with the cell membrane, and therefore indirectly measures cellular uptake, it does not necessarily provide accurate direct data on whether a compound is actually taken up into cells [70]. One of the best examples are CPPs themselves that have shown to be taken up by cells while being highly charged and soluble in water, such as the TAT peptide. For direct cell labelling applications, the interaction of the compound with the cell membrane is however of high importance.

In summary, CPPs are a versatile platform for the development of a plethora of functional and targeted peptides that can also be applied for imaging. The next chapter explores the application of the ^{89}Zr-labelled CPPs described and characterized in this chapter for direct cell labelling.

5.10 Appendix

5.10.1 Net peptide contents after synthesis

Table 5.7 CPPs investigated in this work together with their net peptide content after synthesis and final purification via RP-HPLC.

Peptide	Amino acid sequence	*NPC [%]	**MW	Charge
DFO-TAT	YGRKKRRQRRR	57.3	2201.3	+8
DFO-SS-TAT	YGRKKRRQRRR	63.4	2308.3	+8
DFO-MPG$^{\Delta NLS}$	GALFLGFLGAAGSTMGAWSQPKSKRKV	82.3	3405.9	+5
DFO-MPG^{NLS}	GALFLGFLGAAGSTMGAWSQPKKKRKV	75.9	3446.9	+6

* NPC = net peptide content

** MW = molecular weight [g/mol]

5.10.2 Quality control of all synthesised CPPs

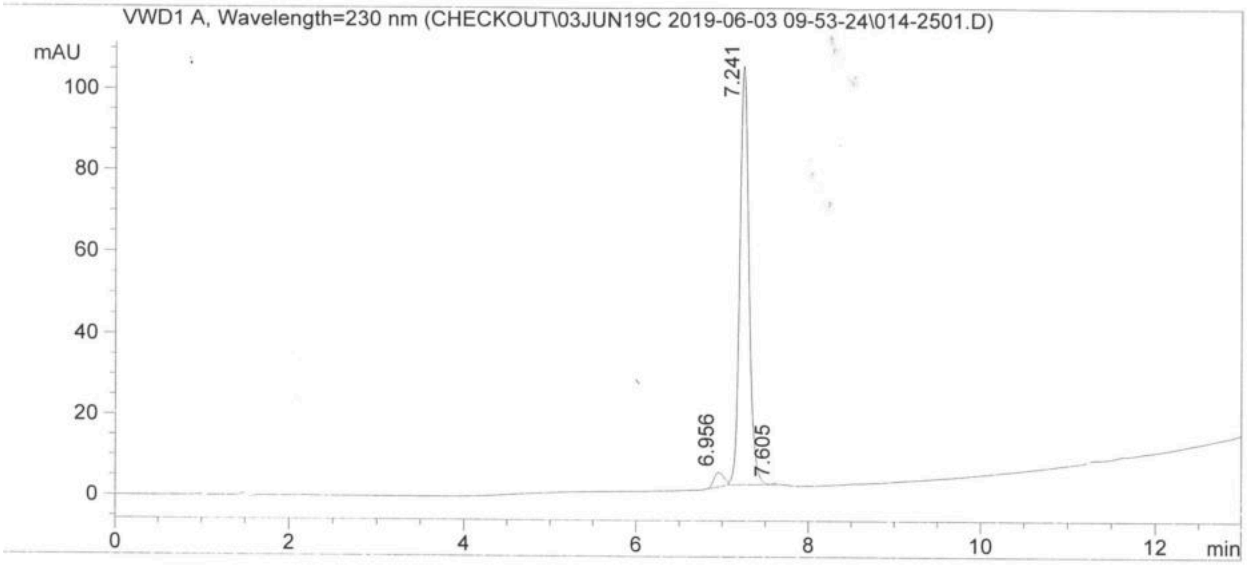

Figure 5.11 Analytical HPLC chromatogram of DFO-TAT using gradient 1.

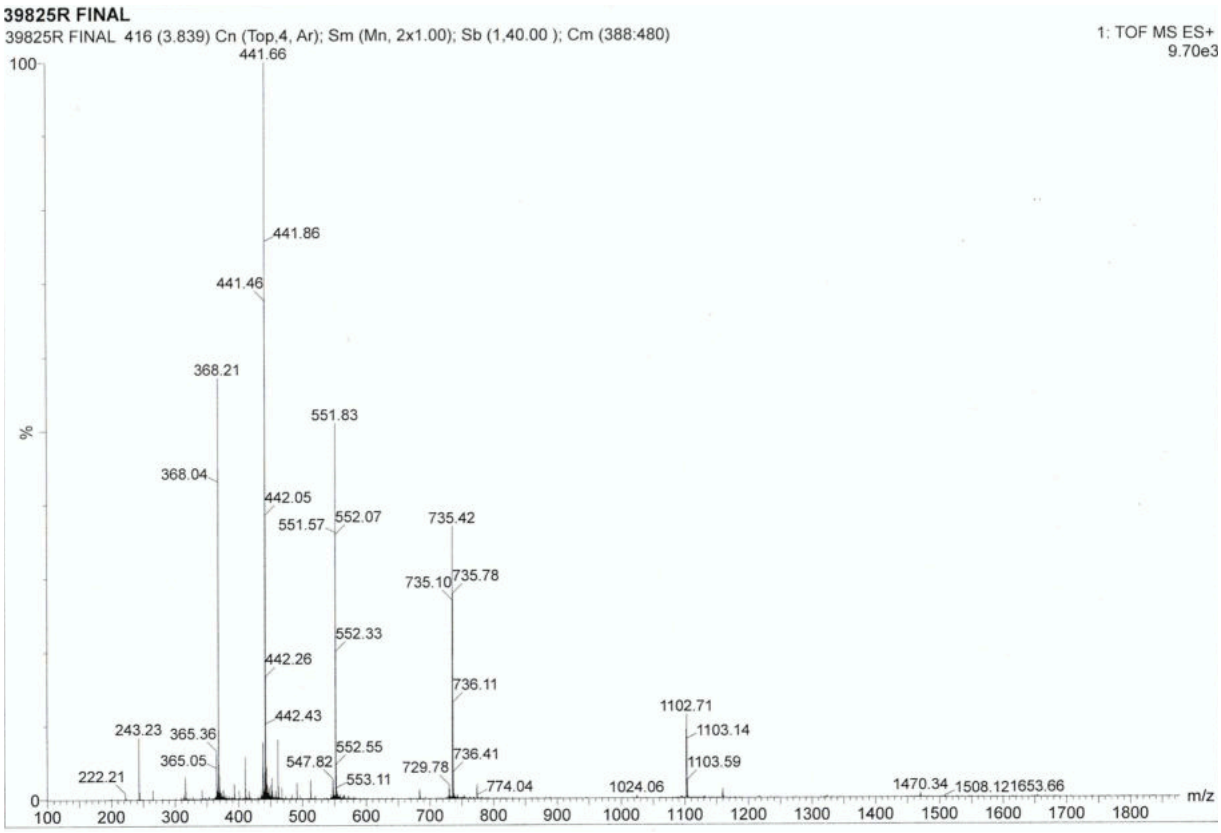

Figure 5.12 Mass spectrum of synthesised and purified DFO-TAT. Target MW = 2201.3. Observed MW: 1102.7 (2+), 735.1 (3+), 551.6 (4+), 441.5 (5+), 368.0 (6+).

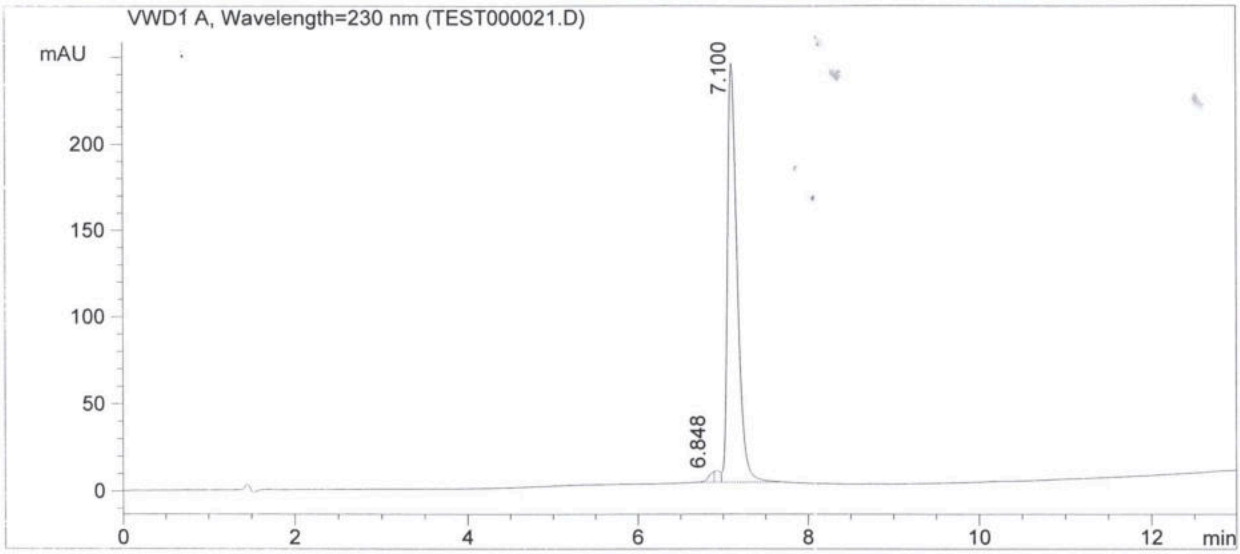

Figure 5.13 Analytical HPLC chromatogram of DFO-SS-TAT using gradient 1.

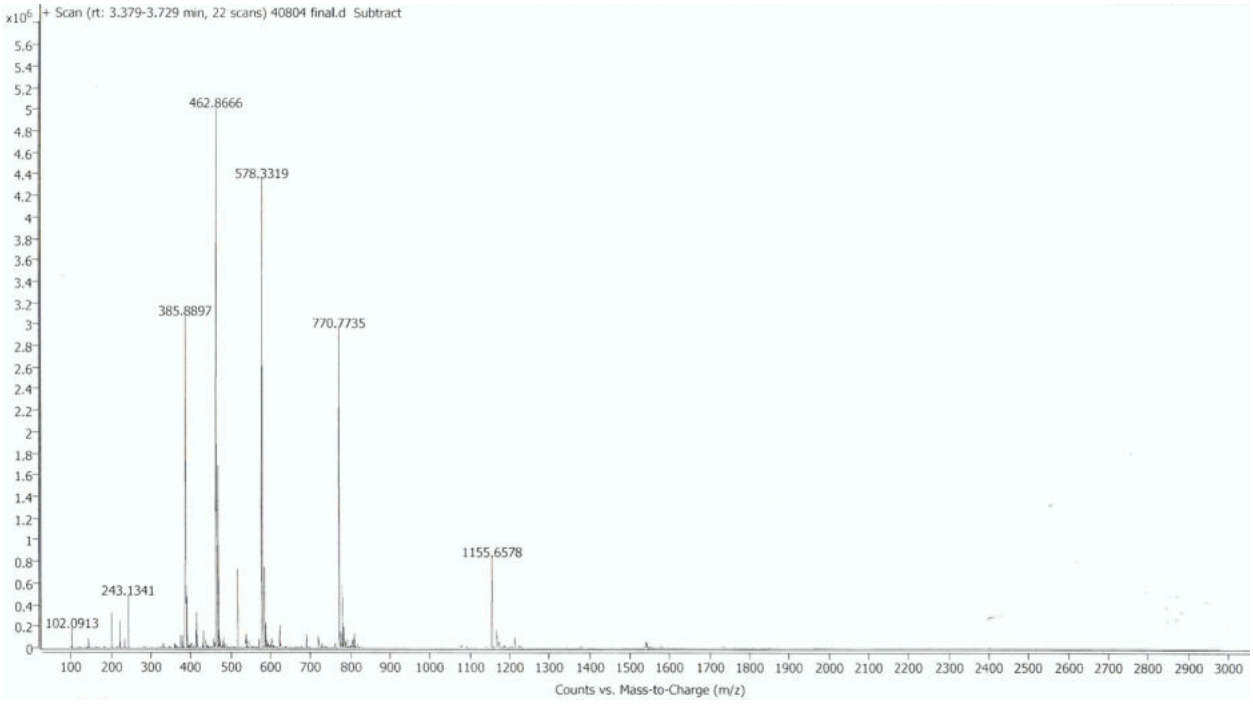

Figure 5.14 Mass spectrum of synthesised and purified DFO-SS-TAT. Target MW = 2208.3. Observed MW: 1155.6 (2+), 770.8 (3+), 578.3 (4+), 462.9 (5+), 385.9 (6+).

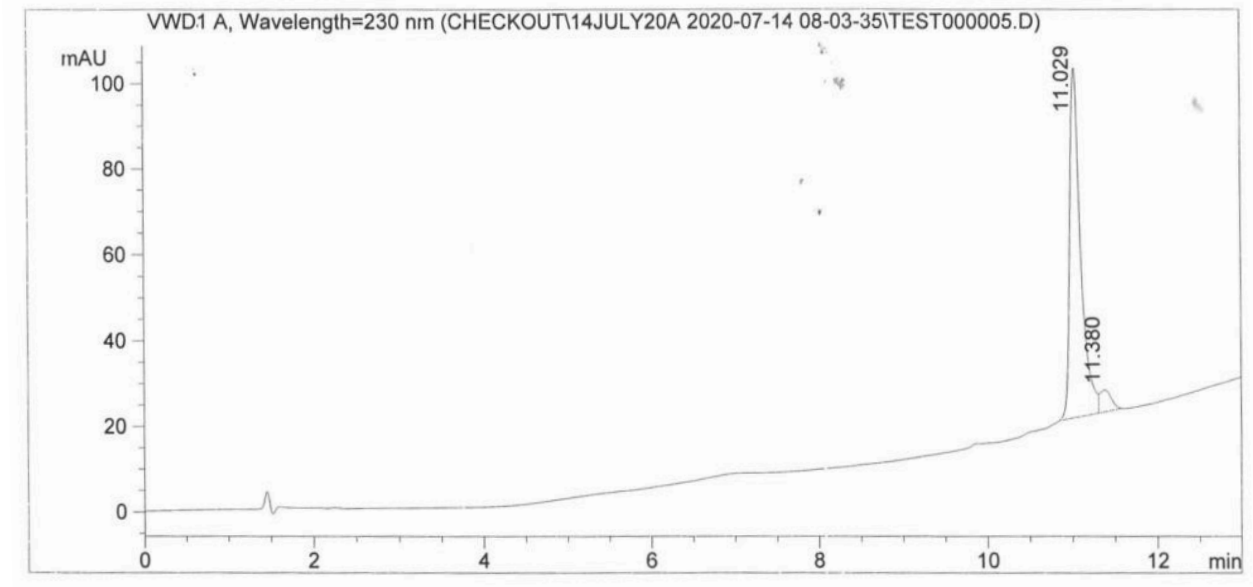

Figure 5.15 Analytical HPLC chromatogram of DFO-MPG$^{\Delta NLS}$ using gradient 1.

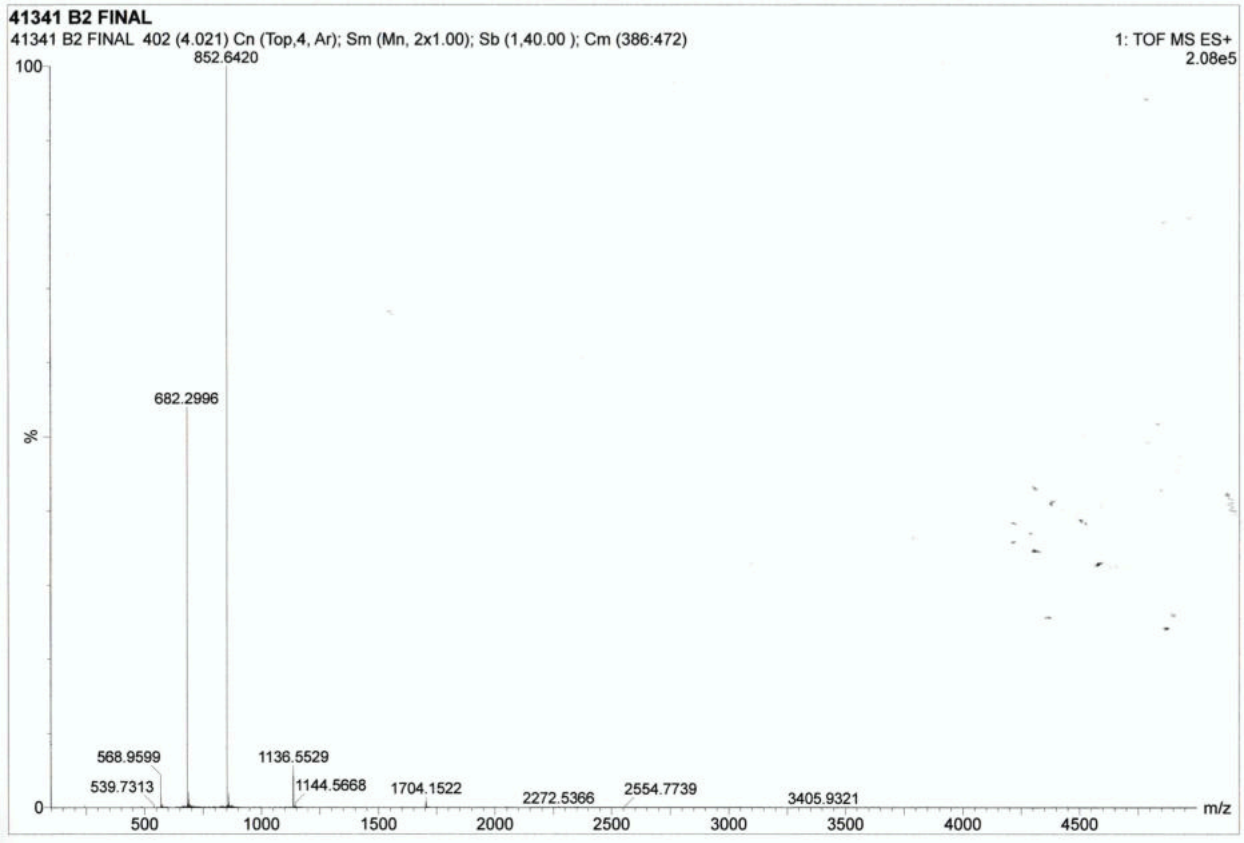

Figure 5.16 Mass spectrum of synthesised and purified DFO-MPG$^{\Delta NLS}$. Target MW = 3405.9. Observed MW: 1136.5 (3+), 852.6 (4+), 682.3 (5+).

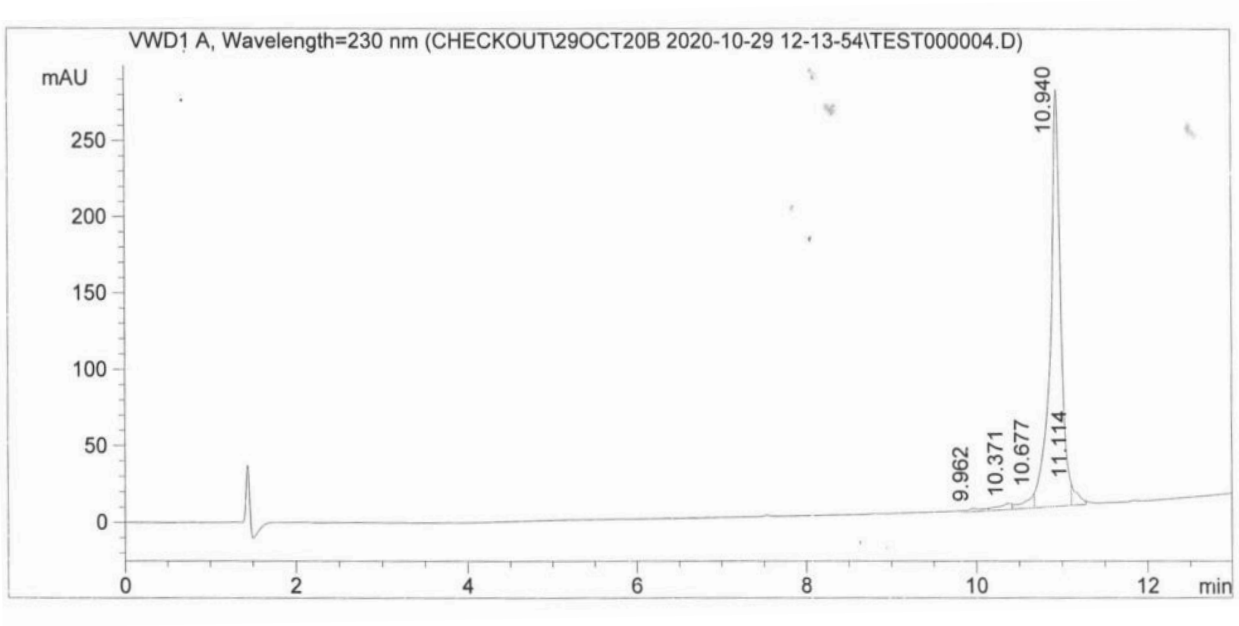

Figure 5.17 Analytical HPLC chromatogram of DFO-MPG^{NLS} using gradient 1.

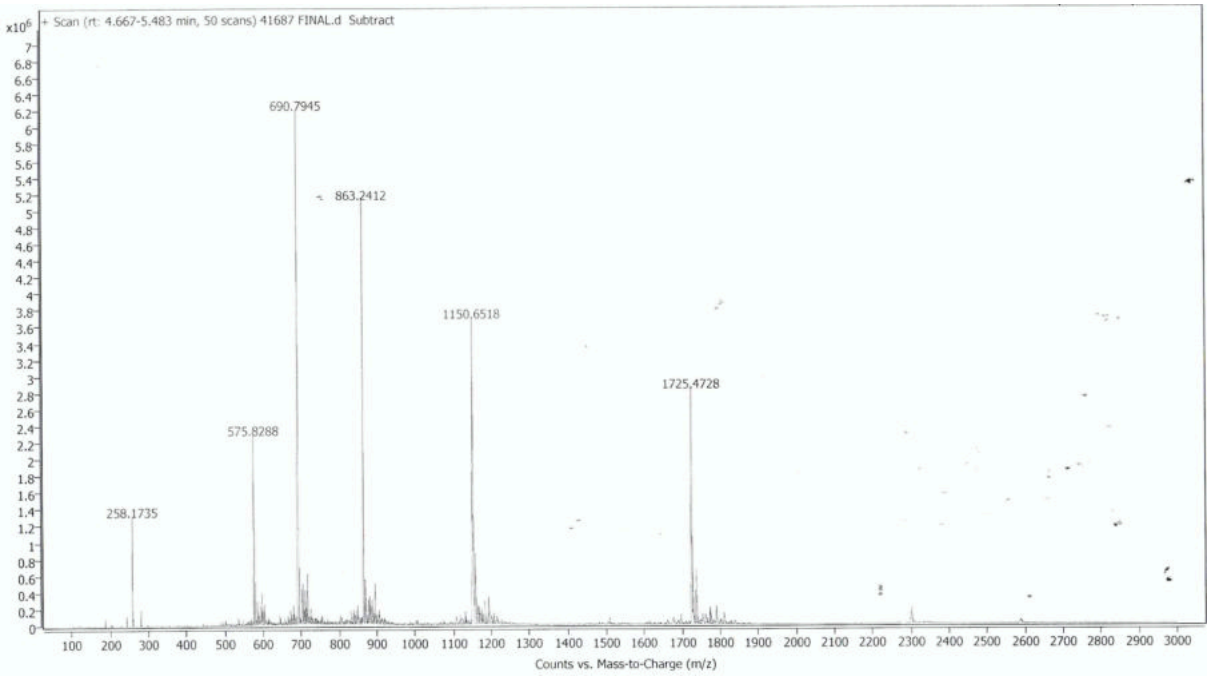

Figure 5.18 Mass spectrum of synthesised and purified DFO-MPG^{NLS}. Target MW = 3446.9. Observed MW: 1725.5 (2+), 1150.6 (3+), 863.2 (4+), 690.8 (5+), 575.8 (6+).

5.11 References

1. Frankel AD, Pabo CO. Cellular uptake of the tat protein from human immunodeficiency virus. *Cell*. 1988;55(6):1189-1193.
2. Green M, Loewenstein PM. Autonomous functional domains of chemically synthesized human immunodeficiency virus tat trans-activator protein. *Cell*. 1988;55(6):1179-1188.
3. Joliot A, Pernelle C, Deagostini-Bazin H, Prochiantz A. Antennapedia homeobox peptide regulates neural morphogenesis. *Proc Natl Acad Sci U S A*. 1991;88(5):1864-1868.
4. Derossi D, Joliot AH, Chassaing G, Prochiantz A. The third helix of the Antennapedia homeodomain translocates through biological membranes. *J Biol Chem*. 1994;269(14):10444-10450.
5. Järver P, Langel Ü. Cell-penetrating peptides-A brief introduction. *Biochim Biophys Acta - Biomembr*. 2006;1758(3):260-263.
6. Xie J, Bi Y, Zhang H, et al. Cell-Penetrating Peptides in Diagnosis and Treatment of Human Diseases: From Preclinical Research to Clinical Application. *Front Pharmacol*. 2020;11.
7. Van Nguyen T, Shin MC, Min KA, Huang Y, Oh E, Moon C. Cell-penetrating peptide-based non-invasive topical delivery systems. *J Pharm Investig*. 2018;48(1):77-87.
8. El-Andaloussi S, Holm T, Langel U. Cell-Penetrating Peptides: Mechanisms and Applications. *Curr Pharm Des*. 2005;11(28):3597-3611.
9. Heitz F, Morris MC, Divita G. Twenty years of cell-penetrating peptides: From molecular mechanisms to therapeutics. *Br J Pharmacol*. 2009;157(2):195-206.
10. Habault J, Poyet JL. Recent advances in cell penetrating peptide-based anticancer therapies. *Molecules*. 2019;24(5).
11. Mueller J, Kretzschmar I, Volkmer R, Boisguerin P. Comparison of cellular uptake using 22 CPPs in 4 different cell lines. *Bioconjug Chem*. 2008;19(12):2363-2374.

12. Fretz MM, Penning NA, Al-Taei S, et al. Temperature-, concentration- and cholesterol-dependent translocation of L- and D-octa-arginine across the plasma and nuclear membrane of CD34+ leukaemia cells. *Biochem J*. 2007;403(2):335-342.
13. Kosuge M, Takeuchi T, Nakase I, Jones AT, Futaki S. Cellular internalization and distribution of arginine-rich peptides as a function of extracellular peptide concentration, serum, and plasma membrane associated proteoglycans. *Bioconjug Chem*. 2008;19(3):656-664.
14. Lundberg M, Wikström S, Johansson M. Cell surface adherence and endocytosis of protein transduction domains. *Mol Ther*. 2003;8(1):143-150.
15. Palm-Apergi C, Lönn P, Dowdy SF. Do cell-penetrating peptides actually penetrate cellular membranes? *Mol Ther*. 2012;20(4):695-697.
16. Richard JP, Melikov K, Vives E, et al. Cell-penetrating peptides: A reevaluation of the mechanism of cellular uptake. *J Biol Chem*. 2003;278(1):585-590.
17. Koren E, Torchilin VP. Cell-penetrating peptides: Breaking through to the other side. *Trends Mol Med*. 2012;18(7):385-393.
18. Maiolo JR, Ferrer M, Ottinger EA. Effects of cargo molecules on the cellular uptake of arginine-rich cell-penetrating peptides. *Biochim Biophys Acta - Biomembr*. 2005;1712(2):161-172.
19. Vasconcelos L, Pärn K, Langel Ü. Therapeutic potential of cell-penetrating peptides. *Ther Deliv*. 2013;4(5):573-591.
20. Singh T, Murthy ASN, Yang HJ, Im J. Versatility of cell-penetrating peptides for intracellular delivery of siRNA. *Drug Deliv*. 2018;25(1):1996-2006.
21. Herce HD, Garcia AE, Litt J, et al. Arginine-rich peptides destabilize the plasma membrane, consistent with a pore formation translocation mechanism of cell-penetrating peptides. *Biophys J*. 2009;97(7):1917-1925.
22. Herce HD, Garcia AE, Cardoso MC. Fundamental molecular mechanism for the cellular uptake of guanidinium-rich molecules. *J Am Chem Soc*. 2014;136(50):17459-17467.
23. Järver P, Mäger I, Langel Ü. In vivo biodistribution and efficacy of peptide mediated delivery. *Trends Pharmacol Sci*. 2010;31(11):528-535.

24. Alves ID, Goasdoué N, Correia I, et al. Membrane interaction and perturbation mechanisms induced by two cationic cell penetrating peptides with distinct charge distribution. *Biochim Biophys Acta - Gen Subj*. 2008;1780(7-8):948-959.
25. Gräslund A, Madani F, Lindberg S, Langel Ü, Futaki S. Mechanisms of cellular uptake of cell-penetrating peptides. *J Biophys*. 2011.
26. Young JL, Dean DA. Electroporation-Mediated Gene Delivery. *Adv Genet*. 2015;89:49-88.
27. Chow YT, Chen S, Wang R, et al. Single cell transfection through precise microinjection with quantitatively controlled injection volumes. *Sci Rep*. 2016;6.
28. Dunaevsky A. The gene-gun approach for transfection and labeling of cells in brain slices. *Methods Mol Biol*. 2013;1018:111-118.
29. Vivès E, Schmidt J, Pèlegrin A. Cell-penetrating and cell-targeting peptides in drug delivery. *Biochim Biophys Acta - Rev Cancer*. 2008;1786(2):126-138.
30. Nakase I, Tanaka G, Futaki S. Cell-penetrating peptides (CPPs) as a vector for the delivery of siRNAs into cells. *Mol Biosyst*. 2013;9(5):855-861.
31. Nakase I, Akita H, Kogure K, et al. Efficient intracellular delivery of nucleic acid pharmaceuticals using cell-penetrating peptides. *Acc Chem Res*. 2012;45(7):1132-1139.
32. Liu BR, Huang YW, Lee HJ. Mechanistic studies of intracellular delivery of proteins by cell-penetrating peptides in cyanobacteria. *BMC Microbiol*. 2013;13(1).
33. Lindgren M, Rosenthal-Aizman K, Saar K, et al. Overcoming methotrexate resistance in breast cancer tumour cells by the use of a new cell-penetrating peptide. *Biochem Pharmacol*. 2006;71(4):416-425.
34. Santra S, Yang H, Stanley JT, et al. Rapid and effective labeling of brain tissue using TAT-conjugated CdS:Mn/ZnS quantum dots. *Chem Commun*. 2005;(25):3144-3146.
35. Lewin M, Carlesso N, Tung CH, et al. Tat peptide-derivatized magnetic nanoparticles allow in vivo tracking and recovery of progenitor cells. *Nat Biotechnol*. 2000;18(4):410-414.

36. Cosgrave L, Devocelle M, Forster RJ, Keyes TE. Multimodal cell imaging by ruthenium polypyridyl labelled cell penetrating peptides. *Chem Commun*. 2010;46(1):103-105.
37. Bargh JD, Isidro-Llobet A, Parker JS, Spring DR. Cleavable linkers in antibody-drug conjugates. *Chem Soc Rev*. 2019;48(16):4361-4374.
38. Neugebauer U, Pellegrin Y, Devocelle M, et al. Ruthenium polypyridyl peptide conjugates: Membrane permeable probes for cellular imaging. *Chem Commun*. 2008;(42):5307-5309.
39. Goswami D, Vitorino HA, Alta RYP, et al. Deferasirox-TAT(47-57) peptide conjugate as a water soluble, bifunctional iron chelator with potential use in neuromedicine. *BioMetals*. 2015;28(5):869-877.
40. Alta RYP, Vitorino HA, Goswami D, et al. Mitochondria-penetrating peptides conjugated to desferrioxamine as chelators for mitochondrial labile iron. *PLoS One*. 2017;12(2).
41. Polyakov V, Sharma V, Dahlheimer JL, Pica CM, Luker GD, Piwnica-Worms D. Novel Tat-peptide chelates for direct transduction of technetium-99m and rhenium into human cells for imaging and radiotherapy. *Bioconjug Chem*. 2000;11(6):762-771.
42. Bullok KE, Dyszlewski M, Prior JL, Pica CM, Sharma V, Piwnica-Worms D. Characterization of novel histidine-tagged Tat-peptide complexes dual-labeled with 99mTc-tricarbonyl and fluorescein for scintigraphy and fluorescence microscopy. *Bioconjug Chem*. 2002;13(6):1226-1237.
43. Nguyen QT, Olson ES, Aguilera TA, et al. Surgery with molecular fluorescence imaging using activatable cell-penetrating peptides decreases residual cancer and improves survival. *Proc Natl Acad Sci U S A*. 2010;107(9):4317-4322.
44. Xia B, Yan X, Fang WW, et al. Activatable Cell-Penetrating Peptide Conjugated Polymeric Nanoparticles with Gd-Chelation and Aggregation-Induced Emission for Bimodal MR and Fluorescence Imaging of Tumors. *ACS Appl Bio Mater*. 2020;3(3):1394-1405.

45. Olson ES, Whitney MA, Friedman B, et al. In vivo fluorescence imaging of atherosclerotic plaques with activatable cell-penetrating peptides targeting thrombin activity. *Integr Biol (United Kingdom)*. 2012;4(6):595-605.
46. Jiang T, Olson ES, Nguyen QT, Roy M, Jennings PA, Tsien RY. Tumor imaging by means of proteolytic activation of cell-penetrating peptides. *Proc Natl Acad Sci U S A*. 2004;101(51):17867-17872.
47. Barnett EM, Elangovan B, Bullok KE, Piwnica-Worms D. Selective cell uptake of modified Tat peptide-fluorophore conjugates in rat retina in ex vivo and in vivo models. *Investig Ophthalmol Vis Sci*. 2006;47(6):2589-2595.
48. Hedegaard SF, Derbas MS, Lind TK, et al. Fluorophore labeling of a cell-penetrating peptide significantly alters the mode and degree of biomembrane interaction. *Sci Rep*. 2018;8(1).
49. Birch D, Christensen MV, Staerk D, Franzyk H, Nielsen HM. Fluorophore labeling of a cell-penetrating peptide induces differential effects on its cellular distribution and affects cell viability. *Biochim Biophys Acta - Biomembr*. 2017;1859(12):2483-2494.
50. Cornelissen B, Kersemans V, Darbar S, et al. Imaging DNA damage in vivo using γH2AX-targeted immunoconjugates. *Cancer Res*. 2011;71(13):4539-4549.
51. Knight JC, Topping C, Mosley M, et al. PET imaging of DNA damage using89Zr-labelled anti-γH2AX-TAT immunoconjugates. *Eur J Nucl Med Mol Imaging*. 2015;42(11):1707-1717.
52. Knight JC, Mosley MJ, Bravo LC, et al. 89Zr-anti-gH2AX-TAT but not 18F-FDG allows early monitoring of response to chemotherapy in a mouse model of pancreatic ductal adenocarcinoma. *Clin Cancer Res*. 2017;23(21):6498-6504.
53. Poty S, Mandleywala K, O'Neill E, Knight JC, Cornelissen B, Lewis JS. 89Zr-PET imaging of DNA double-strand breaks for the early monitoring of response following α- And β-particle radioimmunotherapy in a mouse model of pancreatic ductal adenocarcinoma. *Theranostics*. 2020;10(13):5802-5814.
54. Bhorade R, Weissleder R, Nakakoshi T, Moore A, Tung CH. Macrocyclic chelators with paramagnetic cations are internalized into mammalian cells via a HIV-tat derived membrane translocation peptide. *Bioconjug Chem*. 2000;11(3):301-305.

55. Guo YM, Liu M, Yang J Le, et al. Intercellular imaging by a polyarginine derived cell penetrating peptide labeled magnetic resonance contrast agent, diethylenetriamine pentaacetic acid gadolinium. *Chin Med J (Engl)*. 2007;120(1):50-55.
56. Lei Y, Tang H, Yao L, Yu R, Feng M, Zou B. Applications of mesenchymal stem cells labeled with tat peptide conjugated quantum dots to cell tracking in mouse body. *Bioconjug Chem*. 2008;19(2):421-427.
57. Chen LJ, Zhao X, Yan XP. Cell-Penetrating Peptide-Functionalized Persistent Luminescence Nanoparticles for Tracking J774A.1 Macrophages Homing to Inflamed Tissues. *ACS Appl Mater Interfaces*. 2019;11(22):19894-19901.
58. Morris MC, Deshayes S, Heitz F, Divita G. Cell-penetrating peptides: from molecular mechanisms to therapeutics. *Biol Cell*. 2008;100(4):201-217.
59. Man F, Khan AA, Carrascal-Miniño A, Blower PJ, T.M. de Rosales R. A kit formulation for the preparation of [89Zr]Zr(oxinate)4 for PET cell tracking: White blood cell labelling and comparison with [111In]In(oxinate)3. *Nucl Med Biol*. 2020;90-91:31-40.
60. Jamous M, Haberkorn U, Mier W. Synthesis of peptide radiopharmaceuticals for the therapy and diagnosis of tumor diseases. *Molecules*. 2013;18(3):3379-3409.
61. Gawne P, Man F, Fonslet J, et al. Manganese-52: applications in cell radiolabelling and liposomal nanomedicine PET imaging using oxine (8-hydroxyquinoline) as an ionophore. *Dalt Trans*. 2018;47(28):9283-9293.
62. Barilli A, Atzeri C, Bassanetti I, et al. Oxidative stress induced by copper and iron complexes with 8-hydroxyquinoline derivatives causes paraptotic death of HeLa cancer cells. *Mol Pharm*. 2014;11(4):1151-1163.
63. Gupta R, Luxami V, Paul K. Insights of 8-hydroxyquinolines: A novel target in medicinal chemistry. *Bioorg Chem*. 2021;108.
64. Reis DC, Pinto MCX, Souza-Fagundes EM, et al. Investigation on the pharmacological profile of antimony(III) complexes with hydroxyquinoline derivatives: Anti-trypanosomal activity and cytotoxicity against human leukemia cell lines. *BioMetals*. 2011;24(4):595-601.

65. Tardito S, Barilli A, Bassanetti I, et al. Copper-dependent cytotoxicity of 8-hydroxyquinoline derivatives correlates with their hydrophobicity and does not require caspase activation. *J Med Chem*. 2012;55(23):10448-10459.
66. Tünnemann G, Ter-Avetisyan G, Martin RM, Stöckl M, Herrmann A, Cardoso MC. Live-cell analysis of cell penetration ability and toxicity of oligo-arginines. *J Pept Sci*. 2008;14(4):469-476.
67. Cardozo AK, Buchillier V, Mathieu M, et al. Cell-permeable peptides induce dose- and length-dependent cytotoxic effects. *Biochim Biophys Acta - Biomembr*. 2007;1768(9):2222-2234.
68. Wang XY, Wang YH, Song Z, et al. Recent progress in functional peptides designed for tumor-targeted imaging and therapy. *J Mater Chem C*. 2021;9(11):3749-3772.
69. Pandya DN, Bhatt N, Yuan H, et al. Zirconium tetraazamacrocycle complexes display extraordinary stability and provide a new strategy for zirconium-89-based radiopharmaceutical development. *Chem Sci*. 2017;8(3):2309-2314.
70. Arnott JA, Planey SL. The influence of lipophilicity in drug discovery and design. *Expert Opin Drug Discov*. 2012;7(10):863-875.

Chapter 6

Direct cell labelling with ^{89}Zr-labelled cell penetrating peptides

6.1 Contributions and collaborators

All synthesis, cell labelling procedures and post-labelling analysis were undertaken by myself. Cell culture was also managed by myself except where mentioned in the materials and method section when the cell source and initial culturing of the cells pre-labelling was provided by one of our collaborators.

6.1 Introduction and chapter objectives

As mentioned and elaborated in detail in the previous chapter, cell penetrating peptides (CPPs) are versatile peptides for various applications. They can serve as a shuttle for the delivery of different kinds of cargo that would not be able to traverse the cell membrane and be take up into cells. Previous approaches for direct cell labelling approaches have mostly resorted to lipophilic radiometal complexes that can passively cross the cell membrane and deposit the radiolabel in the cell of interest. The synthesis of these tracers is often simple, however the lipophilicity and other chemical properties of these tracers often hamper their clinical translatability and not all radioisotopes are suitable for direct cell labelling with the aim to longitudinally track cells *in vivo* over an extended period of time. Apart from only two recent studies that explored the cell surface labelling using the DFO chelator [1],[2], zirconium-89 has vastly emerged as one of the most promising radiometals for intracellular cell labelling due to its residualizing properties in cells as highlighted in the various cell tracking studies described in chapter 2. This work is the first to explore the direct cell labelling approach using highly water-soluble ^{89}Zr-labelled cell penetrating peptides as a platform to deposit zirconium-89 intracellularly for potential longitudinal cell tracking *in vivo*. The work described in this chapter had the following objectives:

I. To label Jurkat T-cells as a model cell line with ^{89}Zr-labelled CPPs to investigate the cellular uptake and labelling efficiency under different conditions in comparison to [^{89}Zr]Zr-Oxine

II. To investigate the cellular retention of zirconium-89 in cells over 24 hours and beyond in Jurkat T-cells and other cell types labelled with both [^{89}Zr]Zr-Oxine and ^{89}Zr-labelled CPPs in a direct comparison

III. To investigate the intracellular fate of zirconium-89 in cells post-labelling with both [^{89}Zr]Zr-Oxine and ^{89}Zr-labelled CPPs in a direct comparison

6.2. Materials and Methods

All chemicals, unless otherwise noted, were acquired from Sigma-Aldrich and used without further purification. Human serum was purchased frozen from Sigma-Aldrich. All water used was ultrapure (>18.2 MΩcm^{-1}). Zirconium-89 was supplied as Zr^{4+} in a 1 M oxalic acid (PerkinElmer) and was produced at the BV cyclotron Amsterdam via the ^{89}Y(p,n)^{89}Zr reaction in a cyclotron on natural ^{89}Y-targets. Activity measurements were made using a CRC-55t dose calibrator (Capintec Inc. Florham Park, NJ) with a calibration factor of 493 for Zirconium-89. Gamma counting was performed using a Wizard 1480 automatic gamma counter (Perkin Elmer, Waltham, MA, USA) as well as a Triathler well counter (HIDEX, Turku, Finland) was used to measure the radioactivity of samples retrieved from labelling experiments. All human biological samples were ethically sourced and their research use was in accord with the terms of the informed consents under an Institutional Review Board/Ethics Committee (IRB/EC) approved protocol (REC reference: 17/NE/0168, IRAS project ID: 222704). All donors provided written, informed consent.

Cell culture

Jurkat cells, a human lymphoblast cell line (ATCC, TIB-152TM, LGC), was cultured in Roswell Park Memorial Institute medium (RPMI, Gibco), supplemented with 10 % (v/v) fetal bovine serum (ThermoFischer), 200 U/l penicillin, 0.1 g/l streptomycin, 10 mM HEPES and 2 mM L-glutamate. Jurkat cells were maintained in suspension in a standard humidified CO_2 incubator (5 % CO_2 v/v).

PBMCs were obtained from heparinised blood, processed and extracted via Ficoll-Paque gradient centrifugation, as described in the methods in chapter 3. Frozen PBMC samples were thawed quickly in a 37 °C water bath, diluted with PBS in a 50 mL Falcon tube and spun down at 500 g for 8 min. The cell pellet was resuspended in warm, RPMI cell medium supplemented with 10 % (v/v) fetal bovine serum (Thermo Fischer), 200 U/l penicillin, 0.1 g/l streptomycin. Cells were cultured in 6-well plates for a few hours or maximum overnight in suspension in a standard CO_2 incubator (5 % CO_2 v/v) to separate out the monocytes from the PMBCs by plate adherence. Monocytes stick to the plastic plate and the remaining monocyte depleted cell populations could be pipetted as cell suspension into 1.5 mL Eppendorf tubes for further use and cell labelling.

T-cells: T-cells were provided by Dr Zoya Georgieva from the Department of Clinical Neuroscience (Clifford Albutt Building). The isolation of highly pure human T-cells was achieved via the Pan T-cell isolation kit (Miltenyi Biotec, Germany). In short, non-target cells, i.e., monocytes, neutrophils, eosinophils, B cells, stem cells, dendritic cells, NK cells, granulocytes, or erythroid cells were labelled by using a cocktail of biotin-conjugated antibodies. The cocktail contained antibodies against CD14, CD15, CD16, CD19, CD34, CD36, CD56, CD123, and CD235a (Glycophorin A). Subsequently, non-target cells were magnetically labelled with the Pan T-cell MicroBead Cocktail. Isolation of highly pure T-cells is achieved by depletion of magnetically labelled cells. For further cell culture, either before or after cell labelling, cells were resuspended in warm RPMI cell medium supplemented with 10 % (v/v) fetal bovine serum (Thermo Fischer), 200 U/l penicillin, 0.1 g/l streptomycin. Cells were cultured in 12-well plates overnight in suspension in a standard CO_2 incubator (5 % CO_2 v/v).

Sheep MSCs: Sheep MSCs were provided by William Hotham from the Department of Veterinary Medicine, (Addenbrooke's hospital). Bone marrow was aspirated from the medullary cavity of the distal femur and collected into 2,000U/ml sterile Heparin (Sigma, UK) dilutes in PBS (Sigma, UK) at 4 ^{o}C. The marrow was passed through a 70 µm cell strainer (Miltenyi, UK), before undergoing two rounds of centrifugation (300 g, 5 minutes at room temperature). The supernatant was discarded and the pellet re-suspended in standard culture media. Standard culture media consisted of MEM Alpha (Invitrogen, UK), supplemented with 10% FCS (First Link, UK), 1% penicillin/streptomycin (Sigma, UK),

1% Glutamax (Thermofisher, USA), 5µg/ml ascorbic acid (Sigma, UK) and 50ng/ml Human Fibroblast Growth Factor Beta (Peprotech, USA). Cells were initially plated in T75 flasks and after a first passage they were cultured in T175 flasks. Upon reaching 80% confluence, cells were passaged using trypLE (Life Technologies, USA). The cells were incubated with trypLE for 10 minutes before mild agitation to detach the cells. The cell containing trypLE was then collected and centrifuged at 300 g for 5 minutes. The supernatant was discarded, the cells re-suspended in culture media or PBS and counted with a haemocytometer. A certain fraction of the cultured cells were taken for cell labelling experiments (see 'cell labelling' section).

^{89}Zr-radiolabelling and purification of peptides

Details of the synthesis, purification and quality control (TLC, HPLC) are provided in the previous chapter (**chapter 5**, materials and methods section).

[^{89}Zr]Zr-Oxine synthesis

Details of the synthesis and quality control of [^{89}Zr]Zr-Oxine are provided in the previous chapter (**chapter 5**, materials and methods section).

Cell labelling with unchelated zirconium-89, [^{89}Zr]Zr-DFO, [^{89}Zr]Zr-Oxine and ^{89}Zr-labelled CPPs

Cell labelling (general): Cells were washed with PBS (Ca^{2+}/Mg^{2+} free) and re-suspended at a density of ~ 5×10^6/mL in 200-300 µL PBS at room temperature in either a 1.5 mL Eppendorf tube or a 1.5 mL LoBind Eppendorf tube in case of using peptides. 151-669 kBq [^{89}Zr]Zr(oxalate)$_4$, 97-844 kBq [^{89}Zr]Zr-DFO (1-5 µg DFO, 1.8-8.9 nmol) as a control**,** 94-902 kBq [^{89}Zr]Zr-Oxine (2-10 µg oxine, 13.8-68.9 nmol) and 60-954 kBq ^{89}Zr-labelled peptides **(**1-5 µg, 0.5-1.5 nmol) were added to the cell suspension and incubated for 10-30 min at different temperatures (RT, 4 °C and 37 °C) with gently swirling the cell suspension every 5 min. The total volume for cell labelling was consistently 500 µL. Following the incubation, cell suspensions were centrifuged at 500 g for 5 min, cells were

pelleted, and supernatants kept aside. The cell pellets were resuspended in PBS, centrifuged again and washings combined with the previous supernatants (SN). Final cell pellets (CP) were resuspended in 500 µL appropriate complete cell culture medium, transferred to a new 1.5 mL Eppendorf tube and measured in a gamma counter. Cell labelling efficiency (LE [%]) was calculated using the following equation:

$$LE\% = 100 \times \frac{A_{CP}}{A_{CP} + A_{SN}}$$

A_{CP}: Activity retained in cell pellet; A_{SN}: Activity of combined supernatants

Cellular retention of the radiotracer and viability

Retention of the radiotracer: 1.0-2.5 × 10^6 of the labelled cells (see 'cell labelling' above) were added to a 6-well or 12-well cell culture plate and appropriate cell culture medium was added. The cells were then incubated for 24 h at 37 °C. Thereafter, cell suspensions were centrifuged at 500 g for 5 min, the supernatant was removed, and the cells were resuspended in PBS (500 µL) and centrifuged again at 500 g for 5 min. The cells were re-suspended in complete cell culture medium (0.5 mL) appropriate for each cell type (see section 'cell culture'). The cell suspension and the supernatant were then taken to be γ-counted to determine the cell-associated radioactivity at each time point and subsequently the retention expressed as percentage [%] compared to the initial cell-associated activity directly post-labelling was calculated. For cellular retention experiments over several days, the labelled cell suspension was again transferred to a 6-well or 12-well cell culture plate to be cultured in the CO_2 incubator.

Viability: The number of live cells was counted using Trypan Blue (0.4 %) and cell viability was expressed as the proportion of live cells [%] within a population and sample. Viability as well as cell count was quantified in each cell sample on a haemocytometer.

Subcellular localisation of zirconium-89 in different cells

The subcellular localisation of all tested ^{89}Zr-labelled tracer on cells was investigated using two different subcellular fractionation assay kits (NE-PER™ Nuclear and Cytoplasmic Extraction Kit and Subcellular Protein Fractionation Kit for Cultured Cells, both ThermoFisher) per the manufacturer's instructions (**Fig. 6.1**). In short, ^{89}Zr-labelled cells were washed twice with PBS to remove excess cell medium from cells in a 1.5 mL Eppendorf tube and the cell pellet was kept as dry as possible on ice. Different ice-cold buffers were added to the original cell pellet to extract cytosolic proteins, nuclear proteins and membrane bound proteins amongst others during different and successive centrifugation steps. The different extracts were kept until the end of the assay and each extract including the remaining cell fraction and the vial were γ-counted to determine the percentage of zirconium-89 associated with each extracted cell fraction compared to the total cell associated radioactivity in the cell pellet before extraction.

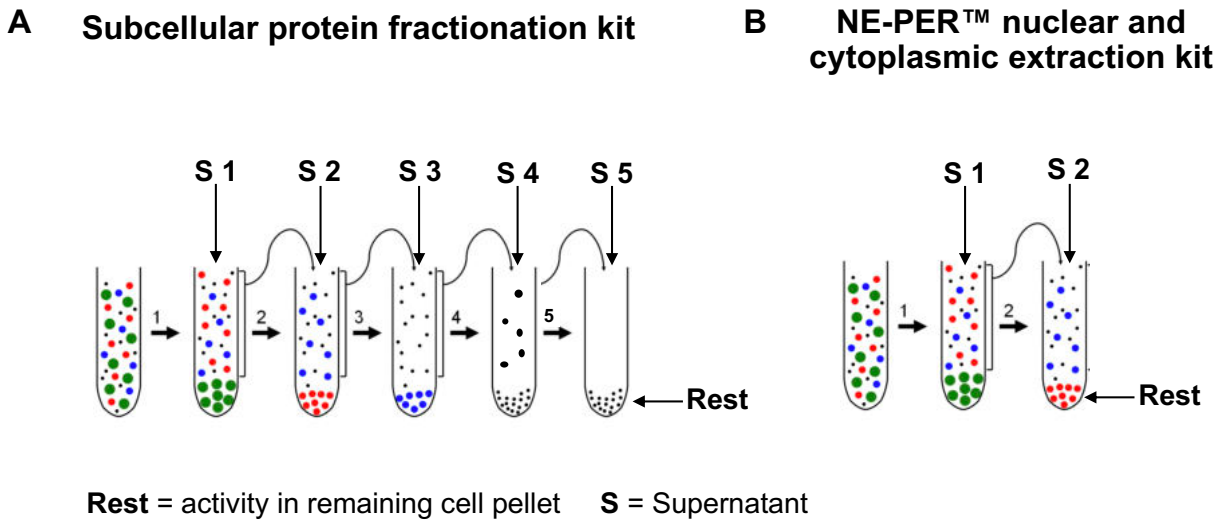

Figure 6.1 Overview of the assays used to determine the subcellular localisation of zirconium-89 in Jurkat T-cells post-labelling. (**A**) Subcellular protein fractionation kit with: S1 = cytoplasmic extract, S2 = membrane extract, S3 = soluble nuclear extract, S4 = chromatin bound nuclear extract, S5 = cytoskeletal extract and (**B**) NE-PER™ extraction kit with: S1 = cytoplasmic extract and S2 = nuclear extract. Rest = remaining, insoluble cell pellet components after all extractions (not specified by assay protocol or elsewhere).

Statistical analysis

Statistical analysis was performed using GraphPad Prism 8.0; (GraphPad Software Inc, La Jolla, USA). Results are presented as mean ± standard deviation (SD) or median [range] as appropriate. Means between two groups were compared using Student's two-tailed t test or two-way analysis of variance (ANOVA) was used to compare more than two groups. p-values <0.05 were considered statistically significant.

6.3 Results

[^{89}Zr]Zr-Oxine and all ^{89}Zr-labelled CPPs used in this chapter were synthesised according to the methods described in the previous chapter at a radiochemical yield >90%. ^{89}Zr-labelled CPPs were purified using a C18 cartridge before the cell labelling experiments. All cell labelling experiments were conducted under the same experimental conditions in regards to cell labelling and the methodology developed during this work. The first part of the results presents the data obtained using [^{89}Zr]Zr-DFO-TAT and [^{89}Zr]Zr-DFO-SS-TAT, whereas the second part of the results presents the data obtained using [^{89}Zr]Zr-DFO-MPG$^{\Delta NLS}$ and [^{89}Zr]Zr-DFO-MPG^{NLS} in a direct comparison to [^{89}Zr]Zr-Oxine. The second part of the results also includes the juxtaposition of all ^{89}Zr-labelled CPPs where appropriate. To afford the most accurate comparison between the different ^{89}Zr-labelled compounds a similar cold mass of the tracer was used for all cell labelling experiments. For this work 2-5 µg of Oxine and 2 µg of the respective peptide were used consistently for each cell labelling sample equalling to 27-68 µM and 1.2-1.8 µM respectively.

6.3.1 Jurkat cell labelling with [^{89}Zr]Zr-DFO-TAT and [^{89}Zr]Zr-DFO-SS-TAT

Cell labelling with [^{89}Zr]Zr-DFO-TAT

[^{89}Zr]Zr-DFO-TAT was first trialled for cell labelling with Jurkat T-cells. Cells were incubated at both 4 °C and 37 °C in comparison (**Fig. 6.2 A**) and a significant difference ($p<0.05$) between the two incubation temperatures in terms of labelling efficiency could be observed with higher labelling efficiencies achieved at 4 °C. [^{89}Zr]Zr-DFO-TAT was rapidly taken up into Jurkat T-cells and no significant difference ($p = 0.94$) in the achieved cell labelling efficiency after a 10, 20, or 30 min incubation time was noticed (**Fig. 6.2 B**). [^{89}Zr]Zr-DFO-TAT showed a significantly higher labelling efficiency compared to [^{89}Zr]Zr-DFO alone ($p<0.0001$) but which was significantly lower compared to [^{89}Zr]Zr-Oxine ($p<0.0001$, **Fig. 6.2 C**). Similar to [^{89}Zr]Zr-DFO, unchelated [^{89}Zr]Zr-(oxalate)$_4$ as a control

was hardly taken up into cells (<1%) indicating that Oxine and TAT could significantly increase cell uptake of zirconium-89.

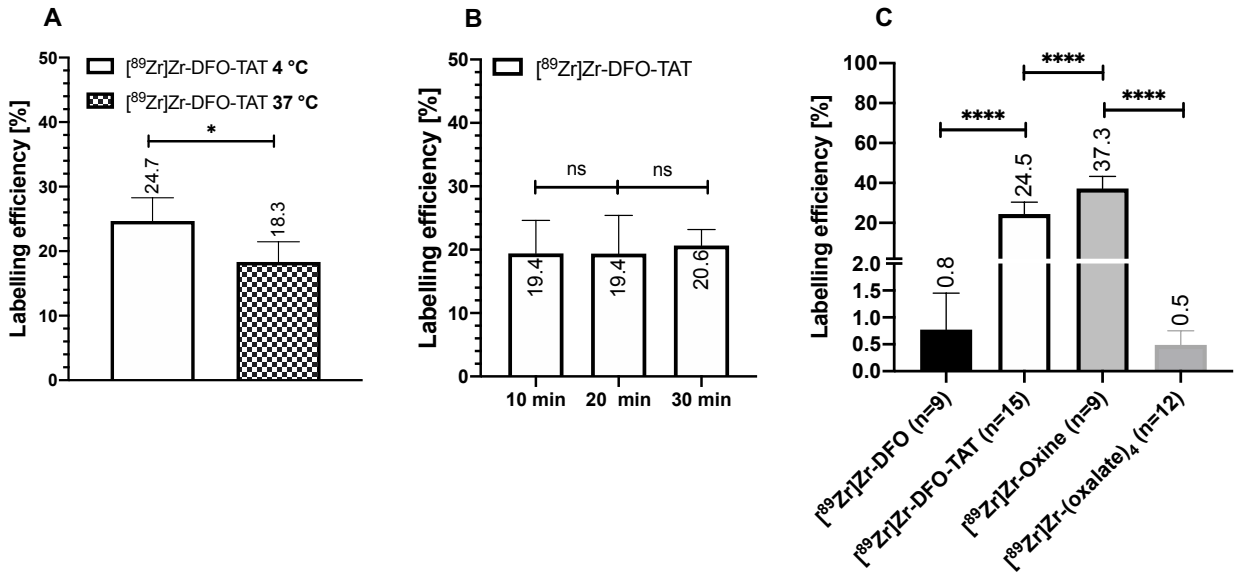

Figure 6.2 Labelling of Jurkat T-cells with [^{89}Zr]Zr-DFO-TAT. (**A**) Significantly higher labelling efficiency at 4 °C versus 37 °C (n = 6). (**B**) Non-significant difference in the labelling efficiency at different incubation times at 4 °C (n = 3). (**C**) Comparative labelling efficiencies of [^{89}Zr]Zr-DFO (at 4 °C), [^{89}Zr]Zr-DFO-TAT (at 4 °C), [^{89}Zr]Zr-Oxine (at RT) and [^{89}Zr]Zr-(oxalate)$_4$ (at RT).
ns = non-significant, * p<0.05, **** p<0.000; a non-linear scale has been used for clarity

Cell labelling with [^{89}Zr]Zr-DFO-TAT and cellular retention of zirconium-89 in Jurkat T-cells over 24 hours

Jurkat T-cells were labelled with [^{89}Zr]Zr-DFO-TAT at both 4 °C and 37 °C and cultured for 24 hours. The cellular retention of zirconium-89 was examined at different time points post-labelling. A rapid cellular efflux of radioactivity could be observed already at 1 hour post-labelling where more than 50% of the initial cell-associated activity was lost compared to the activity directly after the labelling (**Fig. 6.3 A**). At 24 hours post-labelling less than 20% of the initial cell associated radioactivity remained in the cells. The incubation temperature during cell labelling with [^{89}Zr]Zr-DFO-TAT did not have an impact on the cellular retention of radioactivity over 24 hours and very similar efflux kinetics could

be observed. In addition, ^{89}Zr-labelled cells were kept at 4 °C for 5 hours post-labelling to investigate whether the temperature post-labelling has an effect on cellular efflux (**Fig. 6.3 B**). The cellular retention 1 hour post-labelling was significantly higher than compared to labelled cells kept at 37 °C post-labelling. The cellular efflux could be delayed up to 3 hours post-labelling when the same efflux trend could be observed compared to cells kept at 37 °C and the cell associated activity decreased to less than 50% of the initial cell bound activity post-labelling. There was no significant change in viability of ^{89}Zr-labelled cells after 24 hours ($p = 0.13$) compared to unlabelled cells. The next section presents cell labelling data using a modified TAT peptide whereby a disulfide bond was introduced between the DFO chelator and the TAT peptide resulting in [^{89}Zr]Zr-DFO-SS-TAT. Disulfide bonds can be cleaved by intracellularly abundant glutathione levels compared to the extracellular space and thus have the potential to increase the retention of the delivered cargo, in this case zirconium-89 (**Fig. 6.3 C**).

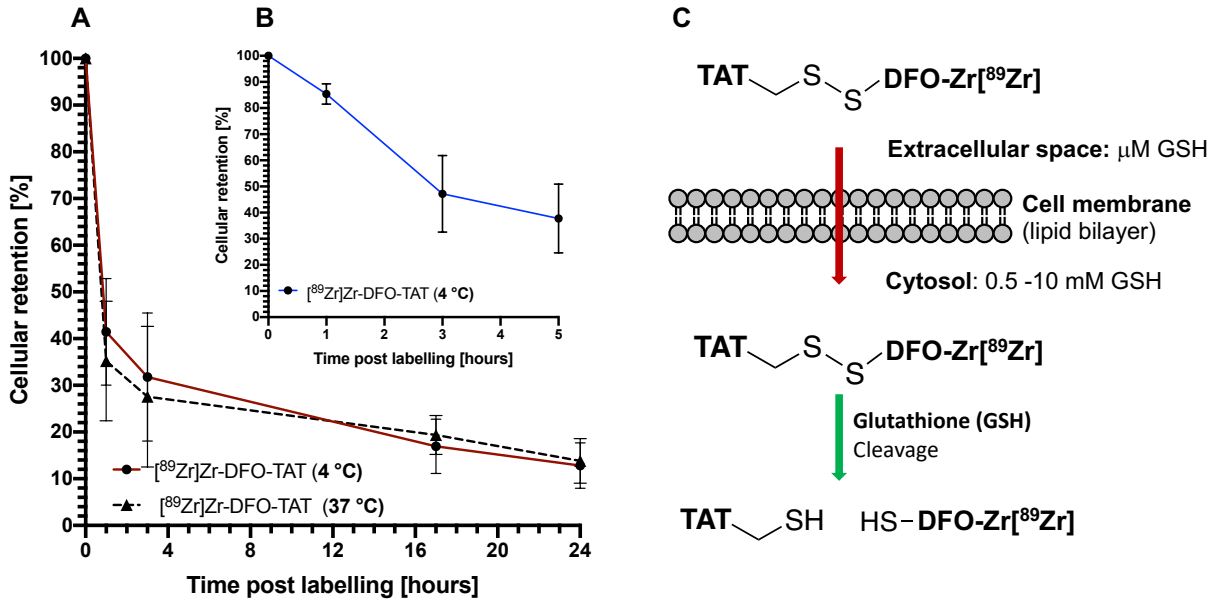

Figure 6.3 Cellular retention of [^{89}Zr]Zr-DFO-TAT over 24 hours in Jurkat T-cells. (**A**) Cellular retention of [^{89}Zr]Zr-DFO-TAT over 24 h, with labelling at 37 °C (n = 12) and at 4 °C (n = 6) and maintained at 37 °C post-labelling. (**B**) Cellular retention of [^{89}Zr]Zr-DFO-TAT over 5 h with labelling at 4 °C and maintained at 4 °C post-labelling (n = 3). (**C**) Proposed mechanism for potentially improved cellular retention of ^{89}Zr-conjugates via glutathione mediated intracellular disulfide bond cleavage.

Cell labelling with [^{89}Zr]Zr-DFO-SS-TAT

In order to investigate a potential improvement in cellular retention of zirconium-89 via TAT-mediated cell uptake, Jurkat T-cells were labelled with [^{89}Zr]Zr-DFO-SS-TAT at different incubation temperatures and times. [^{89}Zr]Zr-DFO-SS-TAT generally showed a very similar behaviour to [^{89}Zr]Zr-DFO-TAT and trend in terms of cell labelling: a significant difference ($p<0.05$) between the incubation at 4 °C and 37 °C could be observed with higher cell labelling efficiencies achieved at 4 °C (**Fig. 6.4 A**). All further cell labelling experiments with [^{89}Zr]Zr-DFO-SS-TAT were undertaken at 4 °C whereas labelling with [^{89}Zr]Zr-Oxine was undertaken at room temperature (RT) as described and undertaken in previous studies. [^{89}Zr]Zr-DFO-SS-TAT was rapidly taken up into Jurkat T-cells with no significant difference ($p = 0.96$) in the achieved cell labelling efficiency after a 10, 20 or 30 min of incubation time could be noticed (**Fig. 6.4 B**). [^{89}Zr]Zr-DFO-SS-TAT overall showed significantly higher labelling efficiencies ($p<0.01$) compared to [^{89}Zr]Zr-DFO-TAT (**Fig. 6.4 C**). There was no significant difference in the labelling efficiencies ($p = 0.10$) achieved with [^{89}Zr]Zr-DFO-SS-TAT compared to [^{89}Zr]Zr-Oxine.

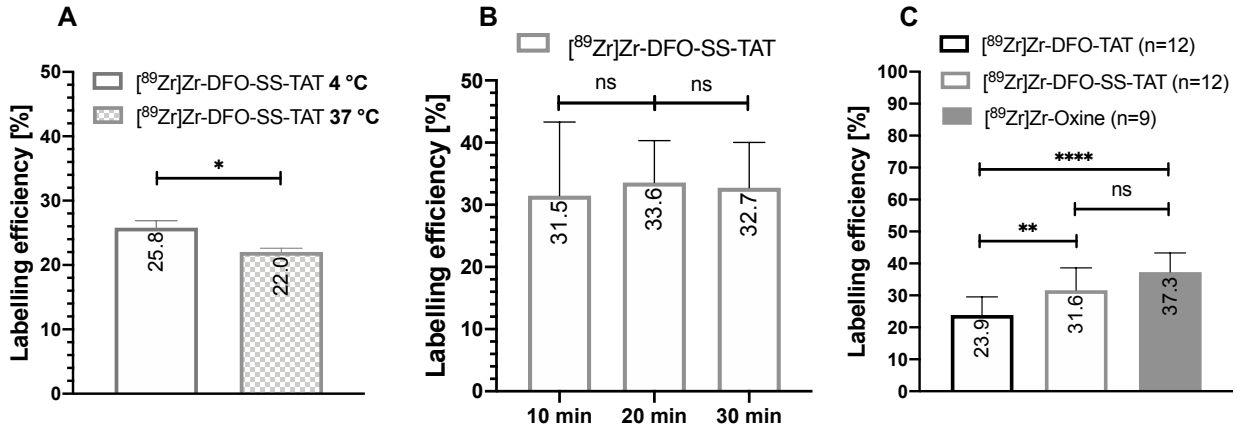

Figure 6.4 Labelling of Jurkat T-cells with [^{89}Zr]Zr-DFO-SS-TAT. (**A**) Significant difference in the labelling efficiency at 4 °C versus 37 °C. (**B**) Non-significant difference in the labelling efficiency at different incubation times 4 °C. (**C**) Comparative labelling efficiencies of [^{89}Zr]Zr-DFO-TAT (at 4 °C), [^{89}Zr]Zr-DFO-SS-TAT (at 4 °C) and [^{89}Zr]Zr-Oxine (at RT).
ns = non-significant, * $p<0.05$, ** $p<0.01$, **** $p<0.0001$

Cell labelling with [^{89}Zr]Zr-DFO-SS-TAT and cellular retention of zirconium-89 in Jurkat T-cells over 24 hours

In a direct comparison with [^{89}Zr]Zr-DFO-TAT, Jurkat T-cells were labelled with [^{89}Zr]Zr-DFO-SS-TAT at 37 °C and cultured for 24 hours at 37 °C to examine the effect of the disulfide bond and possible cleavage via glutathione on the cellular retention of activity. Cells labelled with [^{89}Zr]Zr-DFO-SS-TAT showed a noticeable increase in cellular retention at 1 hour post-labelling that was ~17 % higher ($p < 0.0001$) compared to [^{89}Zr]Zr-DFO-TAT at 24 hours post-labelling (**Fig. 6.5 A**). Nonetheless, a sharp decrease in cell associated activity to ~50% of the initial cell-associated activity was observed for cells labelled with [^{89}Zr]Zr-DFO-SS-TAT already at 1 hour post-labelling which was similar to what could be observed with [^{89}Zr]Zr-DFO-TAT. This result is supported by previous work described in literature for Jurkat T-cells labelled with a ^{99m}Tc-TAT conjugate maintained at different temperatures post-labelling. As a control, Jurkat T-cells were also labelled with unchelated zirconium-89 and [^{89}Zr]Zr-DFO and examined for cellular retention over 24 hours post-labelling (**Fig. 6.5 B**).

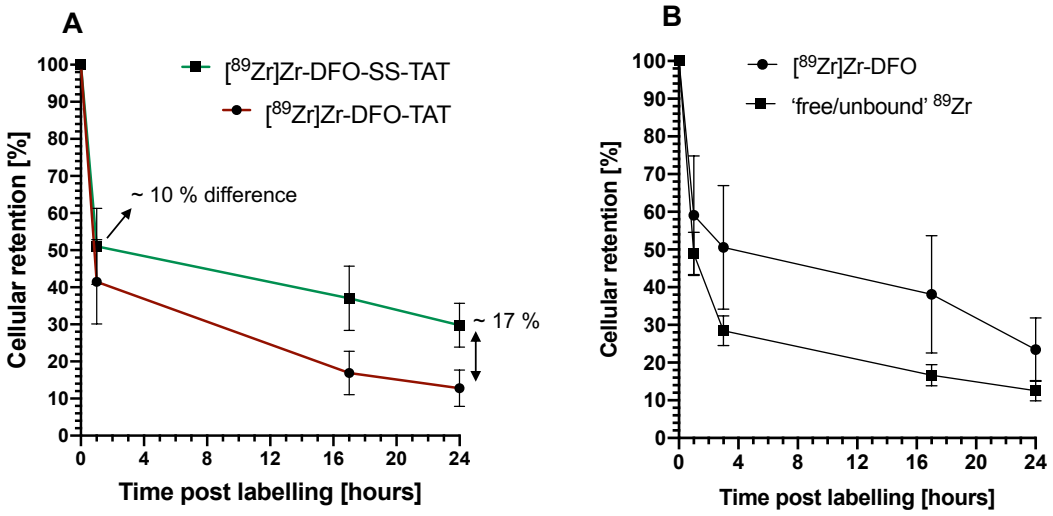

Figure 6.5 Cellular retention of [^{89}Zr]Zr-DFO-SS-TAT over 24 hours in Jurkat T-cells. (**A**) Cellular retention of both [^{89}Zr]Zr-DFO-TAT (n = 12) and [^{89}Zr]Zr-DFO-SS-TAT (n = 12) over 24 h with cell labelling at 37 °C and kept at 37 °C post-labelling. (**B**) Cellular retention of [^{89}Zr]Zr-DFO and unchelated [^{89}Zr]Zr-(oxalate)$_4$ over 24 hours as a control with cell labelling at 4 °C and maintained at 37 °C post-labelling.

Both unchelated zirconium-89 and [^{89}Zr]Zr-DFO did not achieve high labelling efficiencies as shown in **Fig. 6.5 B** resulting in very low cell specific activities overall compared to ^{89}Zr-labelled TAT-conjugates (**Table 6.1**). Nevertheless, unchelated zirconium-89 and [^{89}Zr]Zr-DFO exhibited similar efflux kinetics of the cell bound radioactivity post-labelling over 24 hours with less than 30 % of the initial cell bound radioactivity remaining at 24 hours post-labelling. Cell labelling and subsequent culturing over 24 hours with the respective ^{89}Zr-compound did not significantly affect the cell viability measured at 24 hours post-labelling compared to unlabelled cells in all cases.

Table 6.1 Cell specific activities post-labelling and relative viability at 24 hours post-labelling of [^{89}Zr]Zr-DFO-TAT, [^{89}Zr]Zr-DFO-SS-TAT, [^{89}Zr]Zr-DFO and unchelated [^{89}Zr]Zr.

Tracer	Range of cell specific activity [kBq/10^6 cells]	*Relative viability [%]
[^{89}Zr]Zr-DFO-TAT	4.4-33.0	90.7 ± 6.5
[^{89}Zr]Zr-DFO-SS-TAT	5.6-34.0	95.4 ± 3.3
[^{89}Zr]Zr-DFO	0.1-0.4	93.5 ± 4.7
Free/unchelated [^{89}Zr]Zr	0.2-1.4	92.8 ± 2.2

*Relative viability compared to unlabelled cells as a control (100 % viability) cultured and treated the same as labelled cells at 37 °C.

6.3.2 [^{89}Zr]Zr-DFO-MPG$^{\Delta NLS}$ and [^{89}Zr]Zr-DFO-MPG^{NLS} in direct comparison to [^{89}Zr]Zr-Oxine

Cell labelling with [^{89}Zr]Zr-DFO-MPG$^{\Delta NLS}$

^{89}Zr-labelled MPG$^{\Delta NLS}$ as an amphipathic cell penetrating peptide without a nuclear localisation sequence (NLS) was investigated for cell labelling first in Jurkat T-cells in direct comparison to [^{89}Zr]Zr-Oxine. Both [^{89}Zr]Zr-Oxine and [^{89}Zr]Zr-DFO-MPG$^{\Delta NLS}$ showed rapid cell uptake independent of the incubation time (**Fig. 6.6 A** and **B**) similar to what has been described in literature for the labelling of Vγ9Vδ2 T-cells with [^{89}Zr]Zr-

Oxine. While the uptake of [^{89}Zr]Zr-Oxine into cells differed significantly depending on the incubation temperature (**Fig. 6.6 C**), the labelling efficiencies achieved with [^{89}Zr]Zr-DFO-MPG$^{\Delta NLS}$ were independent of the incubation temperature during cell labelling (**Fig. 6.6 D**). The results obtained for Jurkat T-cells labelled with [^{89}Zr]Zr-Oxine at different temperatures are in contrast to what has been reported in literature for the labelling of Vγ9Vδ2 T-cells where a non-significant difference in the labelling efficiency for different incubation temperatures could be observed [4].

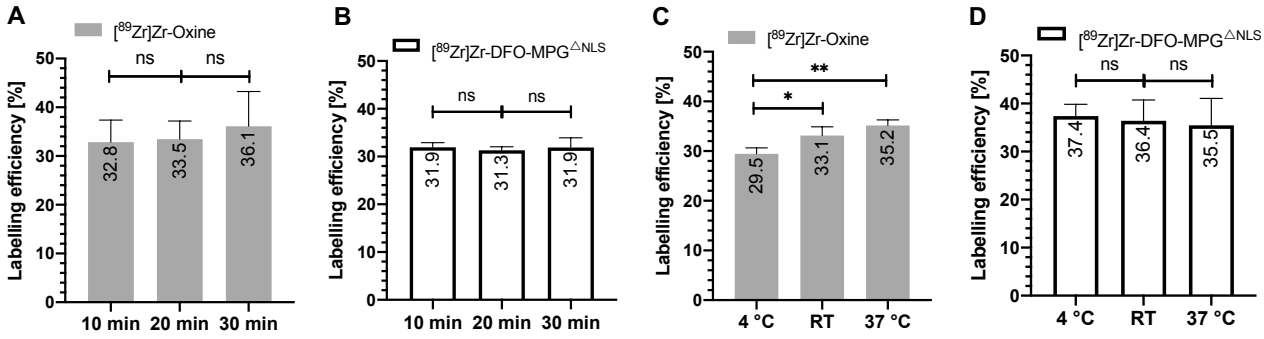

Figure 6.6 (A, C) Labelling of Jurkat T-cells with [^{89}Zr]Zr-Oxine and (B, D) [^{89}Zr]Zr-DFO-MPG$^{\Delta NLS}$ and [^{89}Zr]Zr-Oxine. (**A**) Cell labelling at room temperature at different incubation times with [^{89}Zr]Zr-Oxine (p = 0.74) and (**B**) [^{89}Zr]Zr-DFO-MPG$^{\Delta NLS}$ (p = 0.88). Cell labelling at different incubation temperatures for 10-15 min with (**C**) [^{89}Zr]Zr-Oxine and (**D**) [^{89}Zr]Zr-DFO-MPG$^{\Delta NLS}$ (p = 0.91). ns = non-significant, * p<0.05, ** p<0.01

Cell labelling with [^{89}Zr]Zr-DFO-MPG$^{\Delta NLS}$ and cellular retention of zirconium-89 in Jurkat T-cells over 24 hours

As a next step, the cellular retention of [^{89}Zr]Zr-DFO-MPG$^{\Delta NLS}$ was examined in direct comparison to [^{89}Zr]Zr-Oxine over 24 hours which is summarised in **Fig. 6.6 A**. The cellular retention and efflux profile of both tracers in Jurkat T-cells was very similar with only minor differences in the cell-associated radioactivity at 24 hours post-labelling. A noticeable amount of initial cell bound activity (~20-30 %) was lost at 1 h post-labelling whereas less radioactivity was lost over the following 23 hours during cell culture. A closer examination of two independently conducted cell labelling experiments using [^{89}Zr]Zr-

DFO-MPG$^{\Delta NLS}$ from the overall results as depicted in **Fig. 6.7 A** shows that the loss of cell associated activity over 24 hours can be vastly attributed to the loss of radioactivity at a very early time point post-labelling with relatively little loss of cell bound activity up to 24 hours post-labelling (**Fig. 6.7 B**). This could also be confirmed in a separate experiment whereby Jurkat T-cells were labelled with [^{89}Zr]Zr-DFO-MPG$^{\Delta NLS}$ at both 4 °C and 37 °C to examine the effect of the incubation temperature on the cellular retention. There was hardly any difference between the cellular retention of [^{89}Zr]Zr-DFO-MPG$^{\Delta NLS}$ when incubated with cells at 4 °C compared to 37 °C and most of the initial cell associated activity was lost at 1 hour post-labelling (**Fig. 6.7 C**). The loss of cell associated activity from cells labelled with [^{89}Zr]Zr-Oxine at earlier timepoints seems to be a commonly encountered phenomenon as this could be observed in other previously published studies where up to more than 40 % of cell associated activity was lost during the first 24 hours post-labelling [4],[5].

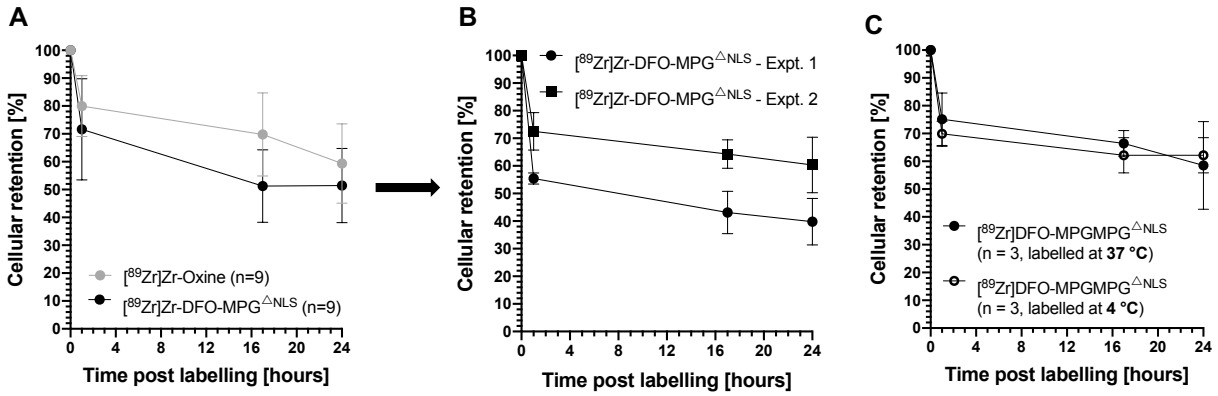

Figure 6.7 Cellular retention of [^{89}Zr]Zr-DFO-MPG$^{\Delta NLS}$ in Jurkat T-cells over 24 hours. (**A**) Overall cellular retention of [^{89}Zr]Zr-DFO-MPG$^{\Delta NLS}$ in Jurkat T-cells labelled at RT in comparison to [^{89}Zr]Zr-Oxine. (**B**) Detailed depiction of two labelling experiments taken out of the overall summary data from plot A with [^{89}Zr]Zr-DFO-MPG$^{\Delta NLS}$ (n = 3 each) showing the initial sharp drop in cell associated activity at 1 h post-labelling. (**C**) Two separate labelling experiments examining the cellar retention of [^{89}Zr]Zr-DFO-MPG$^{\Delta NLS}$ in cells labelled at 4 °C and 37 °C in comparison.

Although an initial loss of cell associated activity 1 hour post-labelling could still be noticed in the case of [^{89}Zr]Zr-DFO-MPG$^{\Delta NLS}$ and which could also be observed for [^{89}Zr]Zr-Oxine in comparison, the use of ^{89}Zr-labelled MPG for cell labelling could decisively improve the overall cellular retention of zirconium-89 not only at 1 hour post-labelling but also up to 24 hours post-labelling compared to TAT (**Fig. 6.8**). There was no significant difference in the cellular retention at 24 hours post-labelling for [^{89}Zr]Zr-DFO-MPG$^{\Delta NLS}$ compared to [^{89}Zr]Zr-Oxine ($p = 0.24$) and both tracers achieved significantly higher cellular retention ($p<0.0001$) compared to [^{89}Zr]Zr-DFO-TAT and [^{89}Zr]Zr-DFO-SS-TAT. Although the introduction of the disulfide bond in [^{89}Zr]Zr-DFO-SS-TAT significantly increased the cellular retention of zirconium-89 over 24 hours compared to [^{89}Zr]Zr-DFO-TAT, the cell associated activity at 24 hours was still less than 30% of the initial cell bound activity directly post-labelling.

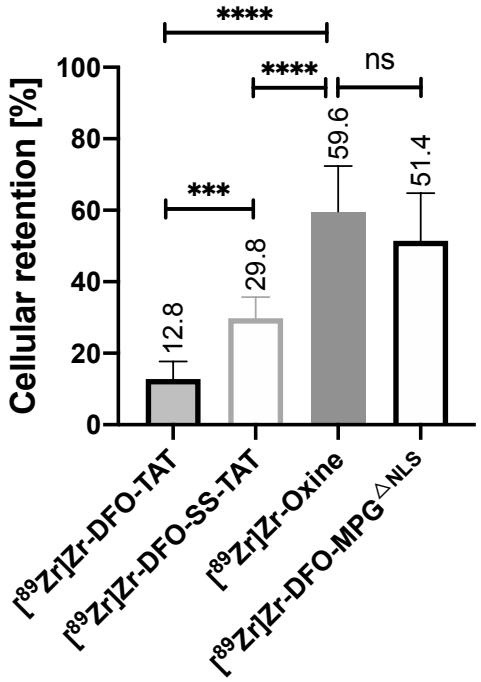

Figure 6.8 Cellular retention of all ^{89}Zr-labelled compounds tested over 24 hours in Jurkat T-cells. Difference in the cellular retention at 24 h post-labelling for all tested ^{89}Zr-tracer.
ns = non-significant, *** $p<0.001$, **** $p<0.0001$

Cellular retention of zirconium-89 over 24 hours and viability post labelling in different cell types

[^{89}Zr]Zr-DFO-MPG$^{\Delta NLS}$ and [^{89}Zr]Zr-Oxine were further tested in direct comparison for their cellular retention over 24 hours post-labelling in different cell types (**Fig. 6.9 A**). There was a clear and noticeable difference in cellular retention of both [^{89}Zr]Zr-DFO-MPG$^{\Delta NLS}$ and [^{89}Zr]Zr-Oxine depending on the cell type with PBMCs showing the highest retention of cell bound radioactivity over 24 hours and Jurkat T-cells together with sheep MSCs showed the lowest retention of radioactivity over 24 hours compared to all other cell types. [^{89}Zr]Zr-DFO-MPG$^{\Delta NLS}$ showed significantly higher retention in PBMCs ($p<0.05$) and sheep MSCs ($p<0.05$) at 24 h and a non-significant difference in cellular retention in human T-cells and Jurkat T-cells compared to [^{89}Zr]Zr-Oxine. All ^{89}Zr-labelled cells remained viable throughout the experiment up to 24 hours post-labelling which was similar to unlabelled control cells (**Fig. 6.9 B**).

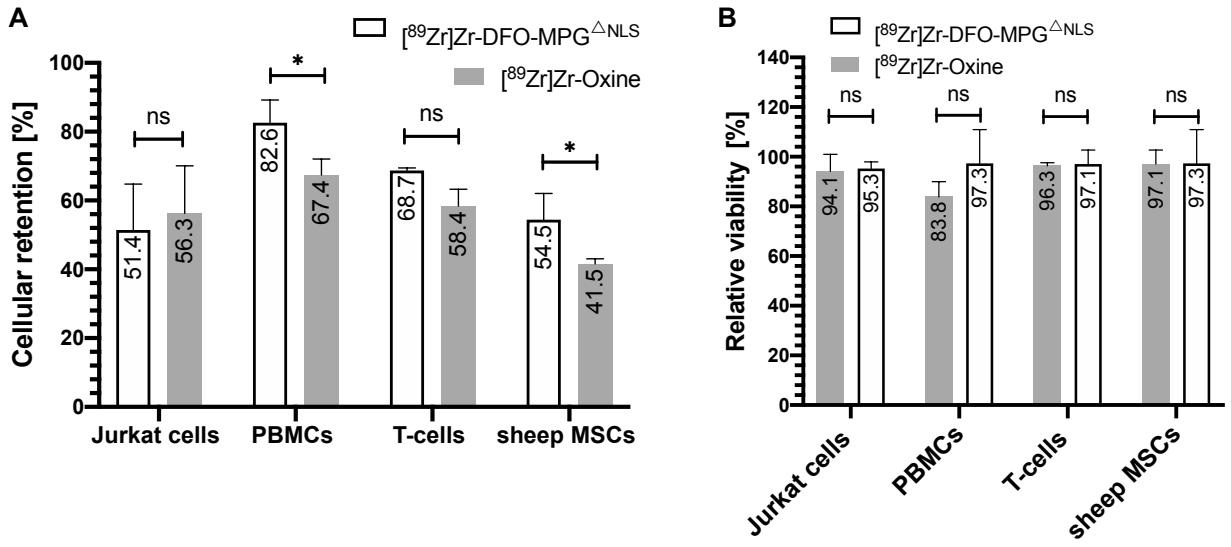

Figure 6.9 Cellular retention of [^{89}Zr]Zr-DFO-MPG$^{\Delta NLS}$ in direct comparison to [^{89}Zr]Zr-Oxine in different cell types at 24 hours post-labelling. (**A**) Cellular retention of zirconium-89 in Jurkat T-cells (n = 12), PBMCs (n = 3), human T-cells (n = 3) and sheep MSCs (n = 3) after 24 hours post-labelling in cell culture and (**B**) relative viability of Jurkat T-cells (n = 12), PBMCs (n = 3), T-cells (n = 3) and sheep MSCs (n = 3) labelled with [^{89}Zr]Zr-DFO-MPG$^{\Delta NLS}$ and [^{89}Zr]Zr-Oxine as shown in plot **A** compared to unlabelled cells as a control. ns = non-significant, * $p<0.05$

Relatively low cell specific activities were choosen (**Table 6.2**), equivalent to doses used in previously published cell labelling studies with [^{89}Zr]Zr-Oxine, where no significant impact on cell viability and functionality was observed [6]–[8].

Table 6.2 Cell specific activities [kBq/10^6 cells] achieved for different cell types labelled with both [^{89}Zr]Zr-Oxine and [^{89}Zr]Zr-DFO-MPG$^{\Delta NLS}$. ^{89}Zr-labelled cells were maintained in culture for 24 hours post-labelling to examine the cellular retention of radioactivity as shown in **Fig. 6.9 A**.

Specific activities [kBq/10^6 cells]	Jurkat T-cells	PBMCs	T-cells	Sheep MSCs
[^{89}Zr]Zr-Oxine	31.6 ± 10.9	16.1 ± 6.1	6.6 ± 5.0	27.8 ± 0.2
[^{89}Zr]Zr-DFO-MPG$^{\Delta NLS}$	9.7 ± 7.5	19.3 ± 9.3	11.8 ± 3.8	14.9 ± 2.8

Cell labelling with [^{89}Zr]Zr-DFO-MPG$^{\Delta NLS}$ and [^{89}Zr]Zr-DFO-MPG^{NLS}

In addition to the MPG$^{\Delta NLS}$ peptide without a nuclear localisation sequence, the MPG^{NLS} peptide carrying a nuclear localisation sequence was tested for cell labelling on Jurkat T-cells. The overall comparison of all cell labelling results combined with [^{89}Zr]Zr-Oxine, [^{89}Zr]Zr-DFO-MPG$^{\Delta NLS}$ and [^{89}Zr]Zr-DFO-MPG^{NLS} is shown in **Fig. 6.10 A**. Both [^{89}Zr]Zr-DFO-MPG$^{\Delta NLS}$ and [^{89}Zr]Zr-DFO-MPG^{NLS} similar labelling efficiencies ($p = 0.75$) than [^{89}Zr]Zr-Oxine at room temperature after a 15-20 min incubation period with the respective tracer. Compared to the ^{89}Zr-labelled TAT-conjugates, ^{89}Zr-labelled MPG-conjugates could achieve significantly higher labelling efficiencies with average labelling efficiencies of ~40 % (**Fig. 6.10 B**).

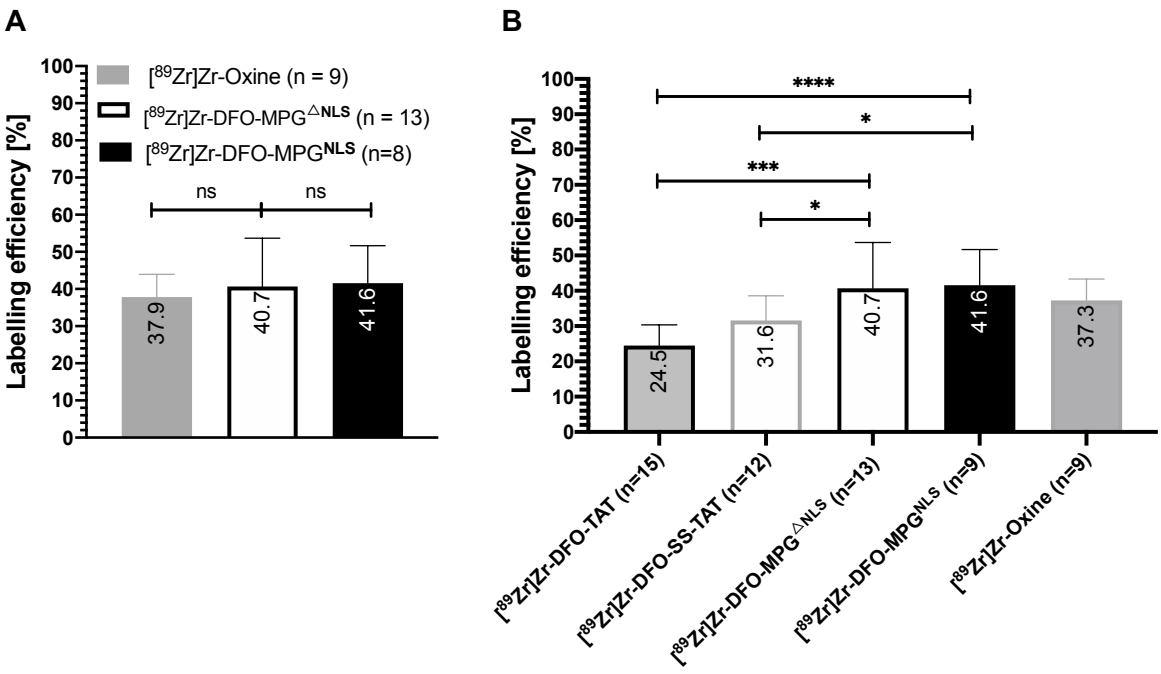

Figure 6.10 Cell labelling efficiencies of all ^{89}Zr-tracer in Jurkat T-cells in comparison. (**A**) Labelling efficiencies of [^{89}Zr]Zr-Oxine, [^{89}Zr]Zr-DFO-MPG$^{\Delta NLS}$ and [^{89}Zr]Zr-DFO-MPG^{NLS} achieved with a 15-20 min incubation at RT. (**B**) Overall summary of the labelling efficiencies achieved with all ^{89}Zr-labelled cell penetrating peptides tested on Jurkat T-cells.
ns = non-significant, * p<0.05, *** p<0.001, **** p<0.0001

Cellular retention of zirconium-89 over 4 days and viability post labelling in Jurkat T-cells

[^{89}Zr]Zr-Oxine, [^{89}Zr]Zr-DFO-MPG$^{\Delta NLS}$ and [^{89}Zr]Zr-DFO-MPG^{NLS} were also tested for their long-term retention in Jurkat T-cells beyond 24 hours (**Fig. 6.11 A**). Notably, almost 40% of the radioactivity was lost during the first 24 hours post-labelling followed by a rather slow and much smaller loss of radioactivity from Jurkat T-cells over the following days up to day 4. There was no noticeable difference in the cellular retention of [^{89}Zr]Zr-DFO-MPG$^{\Delta NLS}$ and [^{89}Zr]Zr-DFO-MPG^{NLS} over 4 days indicating that the MPG peptide with or without the NLS sequence does not affect the long-term retention in these cells. Up to day 2 there was no noticeable difference in the retention of both [^{89}Zr]Zr-MPG peptides and [^{89}Zr]Zr-Oxine, however from day 2 to 4 a slightly increased loss of

radioactivity from cells labelled with [^{89}Zr]Zr-Oxine could be observed. There was no significant difference (p = 0.06) in the cellular retention of all tracers at 4 days post-labelling. ^{89}Zr-labelled cells stayed viable throughout the course of the experiment without a significant loss of viability (p = 0.39) compared to unlabelled cells after 4 days (**Fig. 6.11 B**). The cell specific activities post-labelling ranged from 14.9 to 32.2 kBq/10^6 (**Table 6.3**).

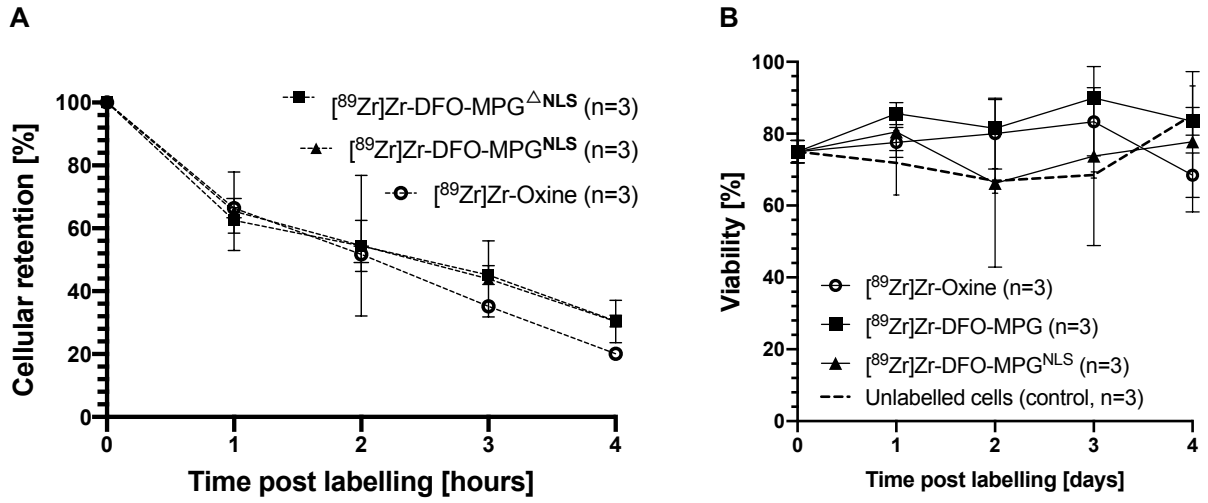

Figure 6.11 Cellular retention of [^{89}Zr]Zr-DFO-MPG$^{\Delta NLS}$ and [^{89}Zr]Zr-DFO-MPG^{NLS} in Jurkat T-cells over 4 days. (**A**) Cellular retention of all tracer over 4 days and (**B**) viability of ^{89}Zr-labelled cells over 4 days compared to unlabelled cells as control.

Table 6.3 Cell specific activities [kBq/10^6 cells] after labelling of Jurkat T-cells.

	[^{89}Zr]Zr-Oxine	[^{89}Zr]Zr-DFO-MPG$^{\Delta NLS}$	[^{89}Zr]Zr-DFO-MPG^{NLS}
Cell specific activity [kBq/10^6 cells]	32.2 ± 1.0	14.9 ± 1.0	16.0 ± 4.1

Intracellular localisation of zirconium-89 in Jurkat T-cells post-labelling

Two different intracellular localisation assays were undertaken in order to investigate the intracellular localisation of [^{89}Zr]Zr-Oxine, [^{89}Zr]Zr-DFO-MPG$^{\Delta NLS}$ and [^{89}Zr]Zr-DFO-MPG^{NLS} in Jurkat T-cells post-labelling at different time points, to acquire a detailed insight into the subcellular distribution of each tracer. Firstly, a subcellular protein fractionation kit was used for the extraction of five different cell compartments as previously described [7] to analyse cells at ~2-4 hours post-labelling (**Fig. 6.12**). Subsequently, a shorter assay which assessed a smaller number of subcellular compartments was used to compare the subcellular localisation of [^{89}Zr]Zr-Oxine, [^{89}Zr]Zr-DFO-MPG and [^{89}Zr]Zr-DFO-MPG^{NLS} in Jurkat T-cells at different time points post-labelling (**Fig. 6.13**). Due to the fast cellular efflux kinetics of TAT, this assay was not investigated for [^{89}Zr]Zr-DFO-TAT and [^{89}Zr]Zr-SS-DFO-TAT.

The initial subcellular localisation assay at 2-4 hours post-labelling (**Fig. 6.12**) revealed that [^{89}Zr]Zr-Oxine-labelling of Jurkat T-cells led to an accumulation of almost 50% of the total cell-associated activity in the cytoplasmic fraction of cells while more than 30% of the total cell-associated activity could be found in nuclear compartments with additional ~12% that accumulated in the cell membrane. These results are in line with previously obtained data using the same subcellular protein fractionation assay for CAR T-cells labelled with [^{89}Zr]Zr-Oxine as described previously [7]. The results obtained with [^{89}Zr]Zr-Oxine are in sharp contrast to the results obtained with [^{89}Zr]Zr-DFO-MPG$^{\Delta NLS}$ and [^{89}Zr]Zr-DFO-MPG^{NLS} where more than 80 % of the cell-associated activity accumulated in compartments other than the cytoplasm, nucleus and membrane. Around 10 % of the cell-associated activity accumulated in cytoskeletal proteins and there was little noticeable difference in the subcellular localisation between [^{89}Zr]Zr-DFO-MPG$^{\Delta NLS}$ and [^{89}Zr]Zr-DFO-MPG^{NLS}. Compared to [^{89}Zr]Zr-Oxine, there was almost no membrane-associated radioactivity when using [^{89}Zr]Zr-DFO-MPG$^{\Delta NLS}$ and [^{89}Zr]Zr-DFO-MPG^{NLS}.

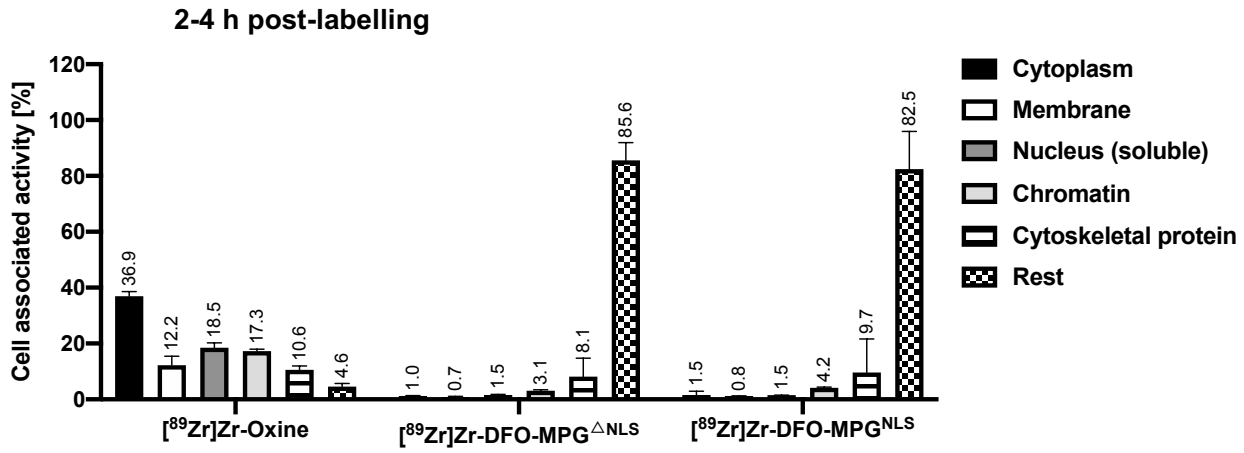

Figure 6.12 Subcellular protein fractionation assay with ^{89}Zr-labelled Jurkat T-cells undertaken at 2-4 hours post-labelling (n = 3).

The NE-PER™ extraction assay largely confirmed the differential subcellular localisation of zirconium-89 using [^{89}Zr]Zr-Oxine compared to [^{89}Zr]Zr-DFO-MPG peptides as was shown with the subcellular extraction assay described above. While the majority of the radioactivity following [^{89}Zr]Zr-Oxine cell labelling could be found in the cytoplasm at 2-4 hours post-labelling, most of the radioactivity was found to be in compartments other than the cytoplasm and the nucleus when using [^{89}Zr]Zr-DFO-MPG$^{\triangle NLS}$ and [^{89}Zr]Zr-DFO-MPG^{NLS} for cell labelling (**Fig. 6.13 A**). Although [^{89}Zr]Zr-DFO-MPG^{NLS} has a nuclear localisation sequence, less than 2 % of the total cell-associated radioactivity was found in the nucleus which was even slightly less than could be observed with [^{89}Zr]Zr-DFO-MPG$^{\triangle NLS}$. The results obtained with the NE-PER™ extraction assay at 2-4 hours post-labelling are in line with the results obtained with the subcellular localisation protein fractionation assay where the cytoplasmic fraction and cytoskeletal protein fraction account for the overall radioactivity in the cytoplasm and the soluble nuclear fraction together with the chromatin fraction account for the overall radioactivity in the nucleus. There was one main noticeable difference between the results obtained from both assays: whereas the subcellular fractionation assay (**Fig. 6.12**) showed that the overall radioactivity in the cytoplasm achieved with [^{89}Zr]Zr-Oxine was ~10% less than could be observed with the NE-PER™ extraction assay (**Fig. 6.13 A**), the subcellular fractionation

assay at 2-4 hours post-labelling (**Fig. 6.12**) showed that the overall and combined radioactivity in the cytoplasm achieved with [^{89}Zr]Zr-DFO-MPG$^{\Delta NLS}$ and [^{89}Zr]Zr-DFO-MPG^{NLS} was between 5-15 times higher compared to the results obtained with the NE-PER™ extraction assay (**Fig. 6.13 A**). Over the course of 4 days the subcellular localisation of zirconium-89 changed slightly in the case of [^{89}Zr]Zr-Oxine: the cytoplasm-associated radioactivity decreased 10% over 48 hours compared to 2-4 hours post-labelling (**Fig. 6.13 B**) and remained at ~45% up to day 4 post-labelling (**Fig. 6.13 C**). In the same example, the accumulation of radioactivity in compartments other than the cytoplasm and the nucleus increased ~15% up to day 4 post-labelling while the radioactivity in the nucleus remained constant throughout the course of the experiment. In the case of [^{89}Zr]Zr-DFO-MPG$^{\Delta NLS}$ and [^{89}Zr]Zr-DFO-MPG^{NLS}, there were no noticeable changes in the subcellular localisation of radioactivity over 4 days with >90 % of the cell-associated activity found in compartments other than the cytoplasm and nucleus. Only less than 3 % of the cell-associated radioactivity accumulated in the nucleus in the case of [^{89}Zr]Zr-DFO-MPG^{NLS}.

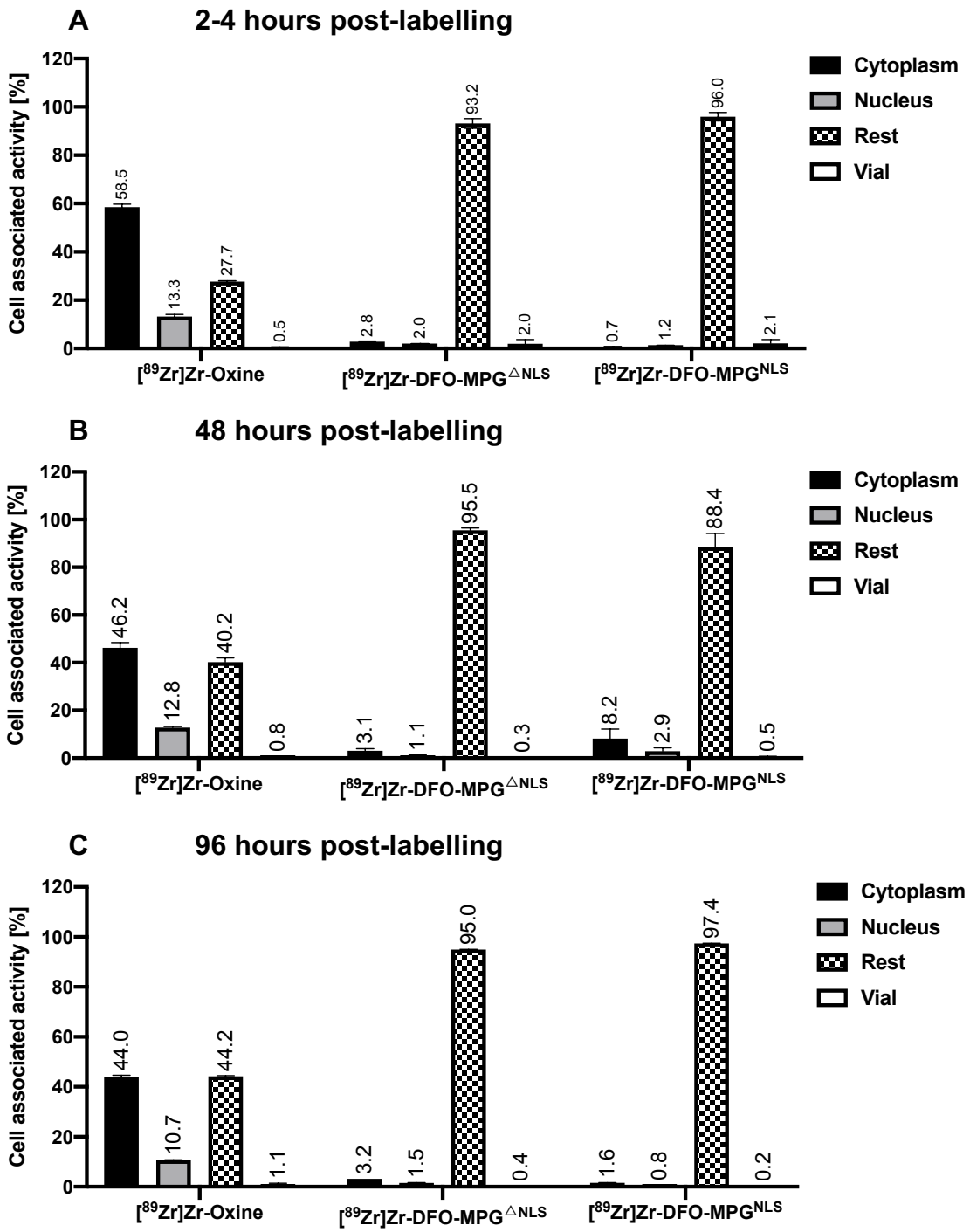

Figure 6.13 NE-PER™ extraction assay with ^{89}Zr-labelled Jurkat T-cells at different timepoints post-labelling using [^{89}Zr]Zr-Oxine, [^{89}Zr]Zr-DFO-MPG$^{\Delta NLS}$ and [^{89}Zr]Zr-DFO-MPG^{NLS}. The subcellular localisation was analysed at (**A**) 2-4 hours post-labelling, (**B**) 48 hours post-labelling and (**C**) 96 hours (4 days) post-labelling.

6.4 Discussion

Direct cell labelling has a long history of use in clinical practice with the application of SPECT tracers for white blood scintigraphy. With the advent of cell therapies for a range of diseases, cell imaging and tracking has gained even more importance as a tool to understand the biodistribution and localisation of cells that impact on the overall efficacy but also to identify potential side effects from both on- and off-target toxicities. With the development and optimisations of PET and the emergence of different PET tracers for both direct and indirect cell labelling via gene reporters, PET has gained a lot of momentum in recent years. Despite the superior sensitivity and advances in this technology, a PET approach analogous to the SPECT approach for direct cell labelling has not been translated into clinical practice up to today. The recent development of a kit formulation for the synthesis and use of [^{89}Zr]Zr-Oxine for direct cell labelling [9] is likely to facilitate the implementation into clinical studies. This also highlights the importance of the tracer itself and the sythesis for its application for direct cell labelling which has been discussed in detail in the previous chapter. Other important factors in the evaluation and development of tracer for cell labelling are: labelling efficiency, cellular retention over the desired imaging period and radiobiology, i.e. the effect of the radiolabel on cellular function and viability. The ideal tracer for this purpose would be a compound that is rapidly taken up into cells independent of the cell type and one in which cell labelling is ideally independent of the incubation temperature and possible at room temperature with no significant impact on cell viability and overall functionality.

This chapter has evaluated the use of ^{89}Zr-labelled cell penetrating peptides (CPPs) as described in more detail in the previous chapter for direct cell labelling in comparison to the state-of-the-art [^{89}Zr]Zr-Oxine. Some of the major beneficial properties of CPPs are hydrophilicity, versatility with various existing peptides that can be modified with chelators and linkers for radioisotope labelling, as well as the applicability in various areas of imaging with the potential of a GMP compliant synthesis of the tracer.

The cell labelling efficiencies achieved with [^{89}Zr]Zr-Oxine in different cell types, as described in the literature and summarised in chapter 2, show that these can vastly vary

depending on the cell type used. The labelling efficiencies achieved during this work are in line with previously published results using T-cells [4]. However, previous studies do not describe the amount of oxine used for each cell labelling batch in detail and mostly indicate the amount of radioactivity instead. Some studies may have used higher amounts of oxine for cell labelling and slightly different labelling conditions, e.g. different vial and cell concentration. Therefore, literature values and the values found for labelling efficiencies in this study cannot be directly compared. However, the tracer mass added to cells plays an important role in cellular uptake.

In this work the concentration of tracer and chemical mass was kept to a minimum to prevent cell death and effects on cellular function. Concentrations in the µM range used here can be regarded as very low which is decisive to keep the cytotoxicity of the cold mass of the tracer, e.g. oxine or the respective CPP, as low as possible. At the same time sufficient ligand, in this case oxine and the DFO-peptide conjugate, needs to be available for mediating efficient cellular uptake. Passive diffusion through the lipid bilayer, as is the case for oxine and the MPG peptide as interacting ligands with the cell membrane, follows a concentration gradient [10] which seems to be a favourable tracer property for efficient cellular uptake. In the case of the TAT peptide the mechanism of cell uptake has been controversially discussed whereby different uptake mechanisms have been described in the literature ranging from direct membrane translocation at low extracellular peptide concentrations to energy-dependent and endocytosis-mediated uptake at high peptide concentrations [11]. TAT as a cationic peptide has also been described as a peptide that can be trapped in endosomes upon cellular uptake [12] which may render cellular uptake and availability of the tracer in the cytosol due to lysosomal degradation. The uptake of other CPPs have been shown to be dependent on the peptide-to-cell ratio rather than on peptide concentration [13]. Especially during this work, both the ^{89}Zr-labelled MPG and TAT peptide have shown to be taken up into cells at 4 °C indicating an energy-independent mechanism (e.g. passive diffusion) that rules out endocytosis-mediated cell uptake. It is therefore important to consider the uptake mechanism of the respective compound as well as different tracer concentrations when evaluating the labelling efficiency in a direct cell labelling approach as this can have a significant impact on the overall cell labelling. During this work it was not possible to investigate the relationship

between tracer concentration and the impact on cell uptake as only a very small amount of the DFO-CPP conjugates were available. This work did not investigate the elucidation of the uptake mechanism for each approach but could be done in conjunction with fluorochromes attached to the CPPs and fluorescent microscopy could provide an insight into the uptake. Nevertheless, studies have also shown that the cargo, such as a fluorochrome, can influence the cellular uptake [14] and is therefore to be used with careful consideration in the evaluation of cellular uptake mechanism.

In order to label cells most economically with a tracer, a high cell labelling efficiency is desirable to avoid wasting a lot of surplus tracer that does not get taken up by cells. Theoretically speaking, this is not necessarily for DFO-peptide conjugates where high cellular activities can be reached despite having low labelling efficiencies. The DFO chelator is a very versatile chelator which can be labelled with a wide range of activities and specific activities of up to 1000 MBq/µmol chelator [15] providing the possibility to tune the cell specific activity with a given labelling efficiency, even if significantly lower compared to [^{89}Zr]Zr-Oxine. This is one major advantage of DFO-conjugates compared to [^{89}Zr]Zr-Oxine where only a limited specific activity can be achieved during the synthesis [9]. The coordination of zirconium-89 with DFO is rather suboptimal in terms of stability as the $^{89}Zr^{4+}$ demands octacoordination to form stable complexes, while the three hydroxamate groups of DFO only offer hexacoordination, resulting in additional binding of water molecules. However, this instability is not necessarily an issue for intracellular labelling purposes where unchelated $^{89}Zr^{4+}$ can bind to intracellular proteins and is described as residualizing isotope [16].

All ^{89}Zr-labelled CPPs assessed here achieved good labelling efficiencies, with the MPG peptide as the most promising candidate achieving slightly higher labelling efficiencies compared to [^{89}Zr]Zr-Oxine. This work largely evaluated the ^{89}Zr-tracers on Jurkat T-cells with the exception of PBMCs, human T-cells and sheep MSCs that were investigated for cellular retention of zirconium-89 at 24 hours post-labelling. In order to validate the universal applicability of ^{89}Zr-labelled CPPs, different cell types would need to be used. Likewise and as summarised in chapter 2, the labelling efficiency varies quite significantly depending on the cell type and needs to be re-evaluated in each cell line especially in regards to the maximum cell specific activity that cells can tolerate post-

labelling and that does not cause significant damage to cells. This work did not demonstrate and neither investigate if the MPG approach is able to achieve higher cell specific activities as the cellular activities were kept to a minimum and in the same range as described in chapter 4 where no significant damage to cells has been observed also as has been described in literature. Reaching similar cell specific activities with different cell labelling approaches is challenging however this was roughly achieved during this work. Just because in some cases higher cell specific activities were reached with the Oxine approach does not mean that this approach is superior to the MPG approach but rather reflects that more activity was added and that more radioactivity entered the cell with similar labelling efficiencies of both tracers. The superiority of MPG over Oxine in terms of the maximum achievable cell specific activity has to be investigated separately.

One of the most important prerequisites for longitudinal cell imaging using a direct cell labelling approach is the label retention over at least the intended imaging time. The TAT peptide as one of the most frequently used CPP can be used as a versatile platform for the development of various compounds. However, this work showed that although a good labelling efficiencies of >20 % could be achieved, the rapid cellular efflux over time with less than 20% of the initial cell-associated activity remaining in cells after 24 hours is not a well-suited property for longitudinal cell imaging. To improve the cellular retention of ^{89}Zr-labelled TAT peptide a disulfide bond between the DFO chelator and the TAT peptide was introduced which significantly improved the retention at 24 hours post-labelling but not sufficiently to allow for long-term cell tracking. Previous *in vitro* studies have shown that only ~8% of a disulfide bond construct was intracellularly cleaved after one hour by glutathione (GSH) [17], which can explain why the cellular retention of [^{89}Zr]Zr-DFO-SS-TAT was only ~10% higher at one hour post-labelling compared to [^{89}Zr]Zr-DFO-TAT. The rate limiting step in this cleavage is GSH activity which seems to be much slower than the efflux kinetics of labelled TAT conjugates. Nevertheless, TAT peptides are well-suited shuttle systems for the intracellular delivery of imaging agents and an intracellular target similar to that exploited for the imaging of DNA damage with [^{89}Zr]Zr-DFO-anti-γH2AX-TAT [18] may be needed to trap the TAT-conjugate intracellularly.

One noticeable observation during this work was the fact that there was a significant loss of cell-associated radioactivity at already one hour post-labelling, both in the case of [^{89}Zr]Zr-Oxine and [^{89}Zr]Zr-MPG$^{\Delta NLS}$ despite the more promising cellular retention long-term. This highlights the importance of efficient washing steps and methods to remove excess tracer that is not internalised and possibly adheres to the lipid cell membrane, either inside the membrane or outside through hydrophobic interactions. This excess of tracer may be washed off when cells are transferred back into cell culture medium or *in vivo*. Most studies which have made use of tracer for the intracellular labelling of cells, in particular using lipophilic tracers such as [^{89}Zr]Zr-Oxine or [^{111}In]In-Oxine/[^{111}In]In-Tropolone, did not investigate the cellular retention at early time points directly after labelling. However, this is very important for both preclinical and clinical cell imaging studies where injected cells would release the radioisotope *in vivo*, as observed *in vitro* as part of this work. Zirconium-89, unlike indium-111 does accumulate in the bone and may significantly impact on the quality of the imaging and create background signal that could make it hard to distinguish labelled cells from the background when this is very close to the detection limit. Cellular retention studies need to be carefully investigated especially in terms of the interpretation of results and the predicted behaviour *in vivo* as this can be completely different. *In vitro* cellular retention does not accurately reflect the conditions *in vivo* where cells are contained within a very different microenvironment and the loss of cells and activity during pipetting and centrifugation can lower the overall cell retention and additionally impact on cell viability directly. *In vitro* experiments may therefore reflect different results as encountered *in vivo*. However, *in vitro* assessment is required in order to stratify which tracer are best suited for longitudinal *in vivo* cell tracking.

Only few studies that involved the intracellular labelling of cells with zirconium-89 and also other radioisotopes have investigated the subcellular localisation post-labelling [7],[19]. Interestingly, this work has shown that ^{89}Zr-labelled MPG peptides with and without a nuclear localisation sequence intracellularly stick to compartments other than the nucleus and cytosol which is very much in contrast to the cell labelling results obtained using [^{89}Zr]Zr-Oxine. Although there was no significant difference in the overall cellular retention over several days when using [^{89}Zr]Zr-Oxine compared to [^{89}Zr]Zr-MPG peptides which indicated that the subcellular localisation does not seem to have an effect

on the retention of cell-associated radioactivity, it can nevertheless be very important and insightful to investigate the subcellular localisation as this can also help in the design of intracellularly targeted radiopharmaceuticals for diagnosis and therapy. Surprisingly, this work could also show that the ^{89}Zr-labelled MPG peptide with a nuclear localisation sequence did not show an increased accumulation of radioactivity in the nucleus compared to the MPG peptide without the nuclear localisation sequence. One explanation for this could be that the nuclear localisation sequence was not very efficient using the ^{89}Zr-labelled DFO-MPG construct described in this work. This is in contrast to what is reported in a previous study where both MPG$^{\Delta NLS}$ and MPG^{NLS} were used to transport fluorescently labelled siRNA into HS-68 human fibroblasts [20]. At only one hour post-labelling, siRNA could be clearly detected in in the nucleus when using MPG^{NLS} as a shuttle. Given both the positron range and also the range of the high gamma emission (909 keV) during zirconium-89 decay, which are several magnitudes higher than the cell diameter, the radiation doses to certain cell organelles will most likely be similar, whether the radioactivity accumulates close to the nucleus or in the cytosol. Despite giving an insight into the intracellular localisation of the radioactivity and in this case also revealing differences between ^{89}Zr-tracer, the cellular fractionation assays used in this work and in general also involve limitations. Firstly, the results can be heavily influenced by pipetting mistakes and a spill over of cellular fractions after centrifugation into the next pipetting step is likely. Furthermore, the extraction buffer mainly dissolve the soluble part of the target compartment in the cell, however insoluble components may not be properly dissolved and dependent on the ^{89}Zr-species, the radioactivity may stick to insoluble cell components. Similarly, the intracellular localisation with radiolabelled cells only reflects the localisation of zirconium-89 itself and not necessarily the ^{89}Zr-tracer used for cell labelling. In addition, in order to validate that a certain cellular compartment is extracted with the assay a control experiment whereby the cell fractions are analysed for example with a western blot is needed. Overall, the assays gave an interesting insight into the subcellular localisation of zirconium-89 but have an inherent inaccuracy in combination with radiotracers. On the opposite, these assays allow the use of radioactivity whereas other methods may not permit the use of radioactivity.

One major advantage of CPPs in general and with localisation sequences in particular, is the possibility to tune the intracellular behaviour and the deliberate delivery of imaging agents and radionuclides to a specific location inside the cell. For example, the mechanism by which MPG delivers active macromolecules does not involve the endosomal pathway and therefore allows the controlled release of the cargo into the cytosol or nucleus only depending on the peptide sequence [21]. Unlike with [^{89}Zr]Zr-Oxine, cell labelling using CPPs offers the possibility to control and navigate the intracellular localisation of imaging agents which is especially important if the radionuclide is not supposed to accumulate in certain organelles. CPPs are therefore a valuable platform for the design of tracer to suit very specific applications but similarly have a very broad applicability in diverse areas of research.

6.5 References

1. Bansal A, Pandey MK, Demirhan YE, et al. Novel 89Zr cell labeling approach for PET-based cell trafficking studies. *EJNMMI Res*. 2015;5(1).
2. Lee SH, Soh H, Chung JH, et al. Feasibility of real-time in vivo 89Zr-DFO-labeled CAR T-cell trafficking using PET imaging. *PLoS One*. 2020;15(1).
3. Polyakov V, Sharma V, Dahlheimer JL, Pica CM, Luker GD, Piwnica-Worms D. Novel Tat-peptide chelates for direct transduction of technetium-99m and rhenium into human cells for imaging and radiotherapy. *Bioconjug Chem*. 2000;11(6):762-771.
4. Man F, Lim L, Volpe A, et al. In Vivo PET Tracking of 89 Zr-Labeled Vγ9Vδ2 T Cells to Mouse Xenograft Breast Tumors Activated with Liposomal Alendronate. *Mol Ther*. 2019;27(1):219-229.
5. Patrick PS, Kolluri KK, Zaw Thin M, et al. Lung delivery of MSCs expressing anti-cancer protein TRAIL visualised with 89Zr-oxine PET-CT. *Stem Cell Res Ther*. 2020;11(1):256.
6. Asiedu KO, Koyasu S, Szajek LP, Choyke PL, Sato N. Bone marrow cell trafficking analyzed by 89Zr-oxine positron emission tomography in a murine transplantation model. *Clin Cancer Res*. 2017;23(11):2759-2768.

7. Weist MR, Starr R, Aguilar B, et al. PET of adoptively transferred chimeric antigen receptor T Cells with 89Zr-Oxine. *J Nucl Med*. 2018;59(10):1531-1537.
8. Man F, Lim L, Volpe A, et al. In Vivo PET Tracking of 89 Zr-Labeled Vγ9Vδ2 T Cells to Mouse Xenograft Breast Tumors Activated with Liposomal Alendronate. *Mol Ther*. 2019;27(1):219-229.
9. Man F, Khan AA, Carrascal-Miniño A, Blower PJ, T.M. de Rosales R. A kit formulation for the preparation of [89Zr]Zr(oxinate)4 for PET cell tracking: White blood cell labelling and comparison with [111In]In(oxinate)3. *Nucl Med Biol*. 2020;90-91:31-40.
10. Brodin B, Steffansen B, Nielsen CU. Passive diffusion of drug substances: the concepts of flux and permeability. In: *Molecular Biopharmaceutics*. 2002:18.
11. Li Z, Zhang Y, Zhu D, et al. Transporting carriers for intracellular targeting delivery via non-endocytic uptake pathways. *Drug Deliv*. 2017;24:45-55.
12. LeCher JC, Nowak SJ, McMurry JL. Breaking in and busting out: Cell-penetrating peptides and the endosomal escape problem. *Biomol Concepts*. 2017;8(3-4):131-141.
13. Hällbrink M, Oehlke J, Papsdorf G, Bienert M. Uptake of cell-penetrating peptides is dependent on peptide-to-cell ratio rather than on peptide concentration. *Biochim Biophys Acta - Biomembr*. 2004;1667(2):222-228.
14. Hedegaard SF, Derbas MS, Lind TK, et al. Fluorophore labeling of a cell-penetrating peptide significantly alters the mode and degree of biomembrane interaction. *Sci Rep*. 2018;8(1).
15. Pandya DN, Bhatt N, Yuan H, et al. Zirconium tetraazamacrocycle complexes display extraordinary stability and provide a new strategy for zirconium-89-based radiopharmaceutical development. *Chem Sci*. 2017;8(3):2309-2314.
16. Liapis V, Tieu W, Rudd SE, et al. Improved non-invasive positron emission tomographic imaging of chemotherapy-induced tumor cell death using Zirconium-89-labeled APOMAB®. *EJNMMI Radiopharm Chem*. 2020;5(1).
17. Feener EP, Shen WC, Ryser HJP. Cleavage of disulfide bonds in endocytosed macromolecules. A processing not associated with lysosomes or endosomes. *J Biol Chem*. 1990;265(31):18780-18785.

18. Knight JC, Topping C, Mosley M, et al. PET imaging of DNA damage using 89Zr-labelled anti-γH2AX-TAT immunoconjugates. *Eur J Nucl Med Mol Imaging*. 2015;42(11):1707-1717.
19. Griessinger CM, Maurer A, Kesenheimer C, et al. 64Cu antibody-targeting of the T-cell receptor and subsequent internalization enables in vivo tracking of lymphocytes by PET. *Proc Natl Acad Sci U S A*. 2015;112(4):1161-1166.
20. Simeoni F, Morris MC, Heitz F, Divita G. Insight into the mechanism of the peptide-based gene delivery system MPG: Implications for delivery of siRNA into mammalian cells. *Nucleic Acids Res*. 2003;31(11):2717-2724.
21. Deshayes S, Gerbal-Chaloin S, Morris MC, et al. On the mechanism of non-endosomial peptide-mediated cellular delivery of nucleic acids. *Biochim Biophys Acta - Biomembr*. 2004;1667(2):141-147.

Chapter 7

Contribution to knowledge, limitations and future directions

One never notices what has been done;
One can only see what remains to be done.
Marie Curie (1867 – 1934)

7.1 Contribution to knowledge

The establishment of this project and the use of zirconium-89 for the work described in this thesis has not only contributed to the knowledge in this field, as will be described below, but has also benefitted the local research on the Cambridge Biomedical Campus and has helped to advance and broaden the use of PET on site in addition to carbon-11, fluorine-18 and gallium-68. This work has also enabled research collaboration with the VU University Medical Center (VUMC) Amsterdam and also Memorial Sloan Kettering Cancer Centre (MSKCC) New York where previous knowledge and expertise with zirconium-89 has helped and contributed to the successful set-up of the project and the following work that could build on this transfer of knowledge.

My project has also laid the foundation for future clinical work with the experience of zirconium-89 gained during this project, assisting in the knowledge regarding handling, waste management, radiation safety and risk assessment. During this project I have established radioactive cell culture in a sterile environment in our lab which has also opened other avenues of research. Most importantly, I have also expanded my own knowledge and expertise working with a multidisciplinary team of academics, clinicians and industry partners, which has been a great privilege. This is the first time that I have used my previously gained expertise in different radiochemistry labs to set up a lab and infrastructure for the work with zirconium-89 which was both holistic and at the same time challenging but overall an extremely exciting and rewarding experience. I owe the success of the project and my personal and academic growth to my supervisor Prof Ferdia Gallagher who always trusted me and my ideas and especially in some of the most challenging situations.

Detection limit and phantom work

The sensitivity and detection limits are of pivotal interest in the cell tracking and imaging arena. Given the potential that molecular imaging has in being able to answer important questions in the development of cell therapies, respective imaging approaches need to be carefully validated in general, but also in terms of their sensitivity. The work

conducted during this thesis has investigated for the first time the *in vitro* detection limit of T-cells directly labelled with [^{89}Zr]Zr-Oxine on both clinical PET/CT and PET/MRI devices, as compared to other cell tracking studies that have examined the detection limit either *in vitro* or *in vivo* on microPET systems. This work showed that cells in the order of 10^4 with a cell specific activity as low as 15.4 kBq/10^6 cells could still be detected which has important implications for cell labelling studies in patients, particularly when using radiosensitive cells (e.g. T-cells), which require detection of low cell numbers while minimising radiation dose per cell. This work can be used as a guideline for prospective clinical studies where both the radiation dose to cells and the body are a concern and need to be as low as possible, but where the limitations of detection need to be considered at the same time.

^{89}Zr-labelling of cell penetrating peptides (CPPs)

This work has shown that CPPs can also be used in conjunction with the radioisotope zirconium-89 utilising known labelling chemistry of the DFO chelator. ^{89}Zr-labelled CPPs are water soluble compounds that can be formulated in aqueous buffers without the use of DMSO and can be purified post-labelling compared to [^{89}Zr]Zr-Oxine with the potential to be transferred onto an automated synthesis module. For instance, other radiolabelled peptides such as ^{68}Ga-DOTATATE are well established in clinical practice and can be synthesised under GMP conditions on automated modules. For the direct cell labelling approach using zirconium-89 there is no available tracer that can be manufactured under GMP compliant conditions. ^{89}Zr-labelled peptides investigated in this work could pave the way for the first peptide-based approach for direct cell labelling with a clinically applicable, GMP compliant synthesis route.

Cell labelling work with ^{89}Zr-labelled CPPs

This work is the first to show that ^{89}Zr-labelled DFO can be utilised for intracellular cell labelling via conjugation to different cell penetrating peptides. The MPG peptide has emerged as the most promising competitor to the state-of-the-art tracer [^{89}Zr]Zr-Oxine

with short incubation times needed for efficient cellular uptake. In some cell types ^{89}Zr-labelled MPG has shown superiority in the cellular retention over [^{89}Zr]Zr-Oxine with a significant 10-15 % higher cellular retention which shows encouraging results for future investigations. The major advantages of [^{89}Zr]Zr-DFO-MPG over [^{89}Zr]Zr-Oxine are: the water solubility of [^{89}Zr]Zr-DFO-MPG; the high specific activity of DFO that can be achieved with zirconium-89; the additional purification step after synthesis; and the potential to transfer the synthesis to an automated synthesis module.

7.2 Limitations during the PhD

There were several limitations and obstacles that the project had to face and that were partly required first steps that needed to be tackled, even beyond the timeline of the PhD:

First, there was no previous use of long-lived isotopes for research purposes on site and the infrastructure for this work had to be initiated and grew during the course of the project. The logistics for zirconium-89 as a long-lived isotope had to be established and this is inherently different from the use of short-lived radioisotopes in terms of radiation safety and waste management, which had to be undertaken separately with special care and specific procedures. The long half-life and risk of contamination associated with zirconium-89 results in other limitations: specific analysis techniques and instrumentation are required such as centrifuges, plate reader, flow cytometry or HPLC; and certain procedures like cell culture cannot easily be used in combination with radioactivity when instruments are used by other researchers not working with radioactivity, and some instruments cannot be shared with researchers working with short-lived isotopes such as carbon-11 and fluorine-18 in the case of HPLC analysis for example. Dedicated equipment for this kind of work with zirconium-89 is and was therefore indispensable.

The most severely imposed limitation during this project was without doubt the emergence of the coronavirus that entailed lockdowns and time away from the lab for many months, but especially working under strict social distancing rules and restrictions during the time when lab work resumed. Overall, almost 30% of the time of this PhD

project was affected by coronavirus restrictions which is elaborated in more detail in the Covid research impact statement attached to this thesis.

7.3 Future work and directions

Detection limit and phantom work

Future work is aimed at extending the cellular detection limit work described in this thesis in chapter 4 which explored theoretical detection limits of ^{89}Zr-labelled cells for *in vitro* imaging experiments with respect to cell number, specific activity, and cell density. However, *in vivo* cell tracking presents several additional challenges compared to *in vitro* experiments. Factors limiting the detectability of ^{89}Zr-labelled cells in clinical studies include: the heterogeneous distribution and density of cells in tumours; non-specific tracer accumulation by normal tissue; limited counting statistics due to the low injected activity and positron fraction of zirconium-89; and the higher level of photon attenuation, scatter and random coincidences encountered in patients. To estimate how the detection limit might change *in vivo*, and expand upon the findings presented in chapter 4, future work will include fusing *in silico* or *in vitro* data representing ^{89}Zr-labelled cells with images acquired from clinical PET examinations. To achieve this, spherical gel suspensions of ^{89}Zr-labelled cells with a range of cell specific activities, cell numbers and sizes, will be imaged on the GE SIGNA PET/MR scanner and the resulting raw data will be inserted into the raw data from whole-body [^{18}F]-FDG PET/MR patient examinations. This approach has the advantage of assessing the detection limit within clinically-realistic images, and comparing with the ground truth regarding the location, contrast and size of the lesions, as well as parameters that effect detectability, such as specific activity and labelled cell density. Additionally, a physical phantom (i.e. a National Electrical Manufacturers Association Image Quality phantom (NEMA IQ)) containing ^{89}Zr-filled spheres will be used to explore different lesion contrasts as a function of lesion size.

Additionally, phantoms are routinely used in molecular imaging to assess scanner performance. However, traditional phantoms with fillable shapes do not replicate human anatomy. 3D-printed phantoms have overcome this by creating phantoms which replicate

human anatomy. Colleagues from the Nuclear Medicine Department in Cambridge have recently demonstrated for the first time the feasibility of creating resin-based, radioactive 3D-printed phantoms using the PET radionuclide fluorine-18 [1]. I have also started investigating the use of radioactive 3D printing with zirconium-89 which is not described in this thesis. In collaboration we have undertaken initial 3D printing using zirconium-89 mixed directly with the resin and future work is aimed to take this work forward and expand the use of other radiometals for 3D printing together with subsequent imaging of printed shapes. This could enable us to print anatomically accurate objects such as an irregular tumour with compartments containing different concentrations of zirconium-89 or small precise objects as test spheres or rods that would be difficult using fillable voids and phantoms. This work could also be used to optimise imaging parameters and reconstruction algorithms for ^{89}Zr-imaging - specifically in regard to partial volume correction and point spread function correction algorithms. Low activity long-lived isotopes (e.g. germanium-68, sodium-22) are commonly used to obtain high statistics measurements without exposing operators to high radiation doses [2],[3]. However, this solution, while practical, results in non-optimal PSF models, as the positron range does not exactly correspond to that of the isotopes used in clinical studies.

Cell labelling work with zirconium-89

Following the initial cell labelling work undertaken during the work for this thesis there are several important and interesting points that remain to be investigated for a better understanding of direct cell labelling approaches, some of which are listed below.

To accurately quantify labelled cells on images, the homogenous labelling of a specific cell subpopulation for injection is of pivotal importance. For example, if the tracer accumulates inside cells via passive diffusion through the cell membrane a concentration-dependent uptake takes place, where the uptake into each single cell is difficult to control. Analysing the single cell uptake of tracers added to cells could not only help to establish a better cell labelling protocol by informing on whether cell labelling is homogeneously or heterogeneous, but could better inform on signal accumulation in the target lesion and the correlation with the respective cell number. Similar work has previously been

undertaken using radioluminescence microscopy (RLM) described in chapter 1 [4],[5]. RLM can quantify how many radioactive molecules are present within individual cell with high sensitivity and has the advantage that differences in cell labelling can be visualised. RLM has not been undertaken with zirconium-89 as a PET isotope and would be interesting to investigate for [^{89}Zr]Zr-Oxine as well as other new approaches. To get an idea about the radioactivity on subdivided cell populations or single cells, a cell sorting device can also be used for such investigations when equipped with a radioactive detector.

The impact of cell proliferation on label retention is a very important question in the direct cell labelling arena, where cell proliferation contributes to label and signal dilution. Given the complex nature of cell proliferation and division it is likely that this can impact on the radiolabel retention. The long-term cellular retention of a tracer could be significantly influenced if cell proliferation has an effect on the label retention. While Jurkat T-cells and other tumour cell lines are highly proliferative cell lines, human immune cells do not proliferate without stimulation and they often proliferate slowly compared to the half-life of the tracer used. This could be investigated by labelling cells with and without an inhibitor of proliferation.

Similarly, the intracellular label retention can be influenced by the stability of the tracer and the ^{89}Zr-species inside the cell. Although zirconium-89 has been described as a residualizing isotope that binds to intracellular proteins, it is not clear as to which chemical form zirconium-89 is retained within the cell. HPLC or TLC analysis could be used to investigate whether unchelated zirconium-89 is retained in cells. This could be especially interesting when comparing [^{89}Zr]Zr-Oxine to [^{89}Zr]Zr-MPG peptides given their differential subcellular localisation as shown in chapter 6. In this respect it would also be interesting to investigate the retention of radioactivity in dead cells compared to live cells labelled with both [^{89}Zr]Zr-Oxine and [^{89}Zr]Zr-MPG peptides, to investigate whether the release of cell-associated activity is determined by cell death and if this is different in the presence of [^{89}Zr]Zr-MPG.

As shown in chapter 4, ~10^4 cells can be visualised in vitro using clinical PET/CT and PET/MRI when the cell specific activity was ~28 kBq/10^6 cells. This chapter also showed

that detection is influenced by both cell specific activity and the cell number. The cell labelling work using [^{89}Zr]Zr-MPG has not investigated the upper limit of cell specific activities that can be reached in comparison to [^{89}Zr]Zr-Oxine and therefore this cannot be commented on at this point without further investigation. Cells labelled with [^{89}Zr]Zr-Oxine have been focused around low cell specific activities where no damage to cells has been observed according to literature and the activities were in the range of the in vitro detection limit found in chapter 4. Although the focus of this work was not to investigate different cell specific activities and compare [^{89}Zr]Zr-Oxine and [^{89}Zr]Zr-MPG, similar cell specific activities could be reached which is always dependent on the absolute activity added to cells and this can vary also between tracers. However, even with the cell specific activities reached during this work and assuming that 1% of injected cells make it to the tumour in a patient that is injected with ca. 10^6-10^8 cells, 10^4-10^6 cells labelled with [^{89}Zr]Zr-MPG and a cell specific activity around 20 kBq/10^6 cells could still be visualized according to the data obtained in chapter 4. This scenario will need to be tested *in vivo* where radioactive decay, cell dilution and background signal will influence cell detection and its lower limits.

Lastly, even though the results of the previous chapter suggested that the subcellular localisation of radioactivity was different for [^{89}Zr]Zr-Oxine compared to [^{89}Zr]Zr-MPG peptides, this did not have an effect on the overall retention of cell-associated activity over several days. Nevertheless, in the case of ^{89}Zr-labelled peptides it would be interesting to investigate in more detail the localisation of zirconium-89 inside the cell using different approaches. For this a labelling approach using non-radioactive zirconium could be used together with subsequent cell analysis post-labelling via secondary ion mass spectrometry (NanoSIMS) which is able to detect zirconium in single cells and is recognised as a powerful technique for visualizing molecular architectures in the fields of neurobiology and cell biology [6].

In vivo animal work and translational work

In preparation for *in vivo* animal work in an appropriate animal model cells will need to undergo radiobiological and functional examination post-labelling. Following the work described in chapter 6, the next step would be to investigate different cell specific activities and doses on cells and their impact on cell viability and functionality over several days in culture, including the cellular retention of the radiolabel over the course of the experiment. Functional factors which could be explored include: DNA damage, cytotoxicity, antigen expression, proliferation, activation and cytokine production (IFN-γ and IL-2).

A first *in vivo* evaluation of the cell labelling approaches described in this thesis could use a proof-of-concept comparative imaging study. This could entail a simple biodistribution and imaging study of Jurkat cells labelled with both [^{89}Zr]Zr-Oxine and [^{89}Zr]Zr-MPG peptides in NSG mice over several days. Alternatively, a CD19^{+} tumour model with ^{89}Zr-labelled CD19-targeting CAR T-cells could be an appropriate model to demonstrate a head-to-head comparison of cells labelled with different ^{89}Zr-tracer in terms of their performance and migration *in vivo*. It would also be interesting to investigate whether cells labelled via cell penetrating peptides cause bone uptake due to the release of radioactivity from dead cells or if the radioactive species released from cells have a different excretion and biodistribution *in vivo*.

Eventually, the overarching aim of future work is the translation of direct cell labelling with zirconium-89 for *in vivo* human imaging. To date, no study has reported the use of ^{89}Zr-labelled cells and the initial evaluation could be undertaken using similar established protocols for the use of indium-111 scintigraphy. The recent development of a kit formulation for the synthesis of [^{89}Zr]Zr-Oxine could also facilitate this together with a possible head-to-head comparison with ^{111}In-labelled cells in terms of radiobiology.

7.4 References

1. Gillett D, Marsden D, Ballout S, et al. 3D printing 18F radioactive phantoms for PET imaging. *EJNMMI Phys*. 2021;8(1).
2. Panin VY, Kehren F, Michel C, Casey M. Fully 3-D PET reconstruction with system matrix derived from point source measurements. *IEEE Trans Med Imaging*. 2006;25(7):907-921.
3. Alessio AM, Stearns CW, Tong S, et al. Application and evaluation of a measured spatially variant system model for PET image reconstruction. *IEEE Trans Med Imaging*. 2010;29(3):938-949.
4. Gallina ME, Kim TJ, Vasquez J, Tuerkcan S, Abbyad P, Pratx G. Single-cell analysis of radiotracers' uptake by fluorescence microscopy: direct and droplet approach. In: *Imaging, Manipulation, and Analysis of Biomolecules, Cells, and Tissues XV*. Vol 10068. ; 2017:100680Y.
5. Türkcan SC, Pratx G. Radioluminescence Microscopy: Measuring the Heterogeneous Uptake of Radiotracers in Single Living Cells. *Biophys J*. 2014;106(2):401a-402a.
6. Agüi-Gonzalez P, Jähne S, Phan NTN. SIMS imaging in neurobiology and cell biology. *J Anal At Spectrom*. 2019;34(7):1355-1368.